UNIVERSITY OF CALIFORNIA SAN DIEGO

SAN DIEGO STATE UNIVERSITY

From Bismuth Nitrogen Molecules to Silver Nanoparticles: A Bottom-up Approach to Materials Chemistry and Applications

A dissertation submitted in partial satisfaction of the
requirements for the degree Doctor of Philosophy

in

Chemistry

by

Nobuyuki Yamamoto

Committee in charge:

University of California San Diego

Professor John Crowell
Professor William Trogler

San Diego State University

Professor Miriam Bennett, Chair
Professor David Pullman, Co-Chair
Professor Carl Carrano
Professor Milton Torikachvili

2019

The Dissertation of Nobuyuki Yamamoto is approved, and it is acceptable in quality and form for publication on microfilm and electronically:

_____

_____

_____

_____

_____
Co-chair

_____
Chair

University of California San Diego

San Diego State University

2019

DEDICATIONS

To our beautiful home Earth.

TABLE OF CONTENTS

LIST OF FIGURES

LIST OF SCHEMES

LIST OF TABLES

ACKNOWLEDGEMENTS

First and foremost, I would like to thank my advisors, Dr. Miriam Bennett and Dr. David Pullman, for providing me an opportunity to pursue research projects and training me to become a skilled chemist for this long journey to obtain my doctoral degree. The techniques I've learned in Dr. Bennett's lab involving air-free chemistry are truly fascinating. I really appreciate that her research allowed me to have hands-on experience on single-crystal X-ray diffractometer. Solving structures on the instrument became more like my hobby. I see it as much as solving a puzzle.

I would like to equally acknowledge Dr. David Pullman for developing my knowledge in nanoscience. He gave me a good deal of flexibility to explore exciting and unusual nanoscale phenomena that could be helpful in our solar cell project. He also taught me that besides making molecules, chemists can also be mini-engineers and make special scientific instruments with features that are difficult or impossible to find in commercial units.

I would like to thank Dr. Steven Barlow for teaching me a skill to visualize the "small world" by using electron microscopy techniques. I did not realize how beautiful small matters can appear. These techniques allowed me to open a gate to see things beyond the scope of my eyes.

The teaching experience was a fun part during graduate school. It was pleasure for me to see how undergraduate students grow their knowledge. I would like to thank Dr. Diane Smith and Dr. Karen Peterson for having me as a CHEM 201 TA for five semesters consecutively. The drama we had gone

through during qualitative analysis each semester is now a great memory of mine.

There are many others I must thank for their contributions. Dr. Laurence Beauvais and his undergrads carried on a portion of my project necessary to complete my degree and worked remotely at Point Loma University. Dr. Jing Gu let me store some of my air-sensitive samples in her drybox until the completion of my research. My samples were happy to be in the right home. A fellow graduate student, Aaron Nash, whom I see much like a mobile encyclopedia, could answer all my chemistry related questions right away. His broad knowledge always impressed me. Savannah DeLorenzo was very friendly and respectful to everyone. She is someone that you would want to have as a co-worker. Clemente Andre Inocente from College of Sciences STS Department, who closely worked with me to troubleshoot computer problems related to the departmental X-ray diffractometer.

Chapter 2 contains material that is currently being prepared for publication. Yamamoto, N.; Gilley, R. N.; Wilson, R. J.; Bennett, M. V. “Synthesis and Reactivity of the Unprecedented Bismuth-Nitrogen Cubanes Capped with Metals: $[Bi_4(NSnMe_3)_4Cl_6]^{2-}$ and $[Bi_4N_4(GaCl_3)_4]\cdot 6MeCN$”. *Manuscript in preparation*. The dissertation author was the primary researcher for the data presented. Soon after I joined Dr. Bennett’s laboratory group, Robert Gilley, who was an undergraduate student succeeded in the synthesis of $[Bi_4(NSnMe_3)_4Cl_6]^{2-}$ cluster. He left much work for me to complete characterization when he left for his job and then his Ph.D. work. His

enthusiasm motivated me to produce something that goes beyond the cluster. I would like to thank a former JDP student, Dr. Robert Wilson, who was always thinking ahead of me, and I was able to absorb the habit. He taught a whole process related to single-crystal X-ray diffraction, starting from cutting the crystals, operation, and all the way until structural solutions. He collected the structure of $[Bi_4(NSnMe_3)_4Cl_6]^{2-}$ cubane and helped with my learning to do it myself. Kaley Dane was an undergraduate researcher who was most efficient undergraduate student I have met. She contributed to the preparation of the starting materials. I would like to thank Professor David Pullman for offering me guidance on the use on Raman spectrometer, Professor Dale Chatfield for assistance collecting the mass spectrum and use of the ESI mass spectrometer, Professor Laurance Beauvais for use of the diffuse reflectance spectrometer, and SDSU Department of Geological Sciences for the use of powder X-ray diffractometer.

Chapter 5 contains material that is currently being prepared for publication. Yamamoto, N.; Nash, A. G.; Baker, S.; Bennett, M. V. “Investigation of the Reactivity of $[Bi_2Cl_9]^{3-}$ with $(Me_3Si)_3P$”. *Manuscript in preparation*. The dissertation author was the primary researcher for the data presented. Aaron Nash began investigating the reaction of $[Bi_2Cl_9]^{3-}$ with $(Me_3Si)_3P$. I would like to thank Dr. Beauvais for the use of diffuse reflectance spectrophotometer, Aaron Nash and Stig Baker for growing crystals of arylbismuth halide complexes, and SDSU Department of Geological Sciences for the use of powder X-ray diffractometer.

Chapter 6 contains material that is currently being prepared for publication. Yamamoto, N.; Torres, M. Z.; Harris, D.; Pullman, D. P. “Seedless, one-pot synthesis of infrared-absorbing silver nanoparticles”. *Manuscript in preparation*. The dissertation author was the primary researcher for the data presented. I thank a fellow graduate student in Dr. Pullman’s group, Martha Torres, for her contribution in the computational calculations, which will be included in the manuscript, to aid in the interpretation of silver nanoparticles I have prepared. Debra Harris is an undergraduate researcher who patiently adhered to my guidance to prepare the nanoparticles and assessed the reproducibility. Besides chemistry, she is very talented at cleaning and organizing the lab neatly. I would like to thank PURE Bioscience of El Cajon, CA for partial support of this work.

Lastly, I can never forget to say thank you to my family members, especially, my parents Yoko and Shiro for their profound support outside of my research. Without their love, my achievement would not have been possible.

VITA

2007	Undergraduate research assistant, Advisor: Dr. Steve Bachofer Saint Mary's College of California
2007	Bachelor of Science, Chemistry Saint Mary's College of California
2008-2010	Research Assistant, Advisor: Dr. Chul Kim California State University, East Bay
2011-2019	Research Assistant, Advisors: Dr. Miriam Bennett; Dr. David Pullman San Diego State University
2019	Doctor of Philosophy, Chemistry University of California San Diego San Diego State University

Manuscripts in Preparation

Yamamoto, N.; Gilley, R. N.; Wilson, R. J.; Bennett, M. V. "Synthesis and Reactivity of the Unprecedented Bismuth-Nitrogen Cubanes Capped with Metals: $[Bi_4(NSnMe_3)_4Cl_6]^{2-}$ and $[Bi_4N_4(GaCl_3)_4]\cdot 6MeCN$"

Yamamoto, N.; Nash, A. G.; Baker, S.; Bennett, M. V. "Investigation of the Reactivity of $[Bi_2Cl_9]^{3-}$ with $(Me_3Si)_3P$"

Yamamoto, N.; Torres, M. Z.; Harris, D.; Pullman, D. P. "Seedless, one-pot synthesis of infrared-absorbing silver nanoparticles"

DeLorenzo, S. C.; **Yamamoto, N.**; Wilson, R. J.; Dew, A.; Shoukry, M.; Beauvais, L. G.; Bennett, M. V. "Synthesis of $[Co_5Cl_{10}(THF)_6]_n$ and $[Mn_9Cl_{18}(THF)_{14}]_n$"

DeLorenzo, S. C.; Nguyen, M. P.; Wilson, R. J.; **Yamamoto, N.**; O'Brien, J. R.; Bennett, M. V. "Self Assembly of $[X_3Co(II)\cdot N(SnMe_3)_3]^{1-}$ (X = Cl, Br): Characterization and Investigation of Magnetic Anisotropy"

Williams, N.; Chen, X.; Yang, Y.; Nash, A.; Tran, I.; **Yamamoto, N.**; Beard, M.; Gu, J. "Covalent Interfaces of the Active Site of the [FeFe] Hydrogenase on Silicon Photoelectrode for Hydrogen Production"

Presentations (*Presented by author in bold*)

Yamamoto, N.; Pullman, D. P. “Seedless, one-pot synthesis of infrared-absorbing silver nanoparticles” 256th American Chemical Society National Meeting, Boston, MA; August 2018

Yamamoto, N.; Pullman, D. P. "Enhancement of solar cell activity by the attachment of silver nanoparticles" Student Research Symposium, San Diego State University, San Diego, CA; March 2016

Yamamoto, N.; Gilley, R. N.; Wilson, R. J.; Bennett, M. V. “Synthesis and reactivity of two unprecedented bismuth-nitrogen cubanes” 248th American Chemical Society National Meeting, San Francisco, CA; August 2014

Yamamoto, N.; Nash, A. G.; Gilley, R. N.; Wilson, R. J.; Bennett, M. V. “Synthesis of bismuth nitride and phosphide clusters and nanoparticles” 243rd American Chemical Society National Meeting, San Diego, CA; March 2012

Yamamoto, N.; Kim, C. “Structural and Dynamic Determination on cB box RNAs” California State University Program for Education & Research in Biotechnology Symposium, Anaheim, CA; January 2011

Yamamoto, N.; Bachofer, S. J. “Characterization of Tetradecyl Trimethyl Ammonium (TTA^+) 2,4-, 2,6-, and 3,5-Difluorobenzoate” 19th Annual American Chemical Society Undergraduate Research Symposium, Sonoma State University, Rohnert Park, CA; May 2007

Fields of Study

Major Field: Chemistry (Inorganic)

Studies in Inorganic Synthesis and Characterization
Professor Miriam Bennett

Studies in Nanoparticle Synthesis and Characterization
Professor David Pullman

ABSTRACT OF THE DISSERTATION

From Bismuth Nitrogen Molecules to Silver Nanoparticles: A Bottom-up Approach to Materials Chemistry and Applications

by

Nobuyuki Yamamoto

Doctor of Philosophy in Chemistry

University of California San Diego, 2019
San Diego State University, 2019

Professor Miriam Bennett, Chair
Professor David Pullman, Co-Chair

Two main projects are described in this dissertation. In the first, high-nuclearity bismuth-nitrogen complexes were synthesized as potential precursors to nanomaterials. In the second, a one-pot, seedless approach of producing triangular silver nanoplates of controllable size was developed for light-harvesting applications.

The synthesis of the bismuth-nitrogen cubane complex, $[Bi_4(NSnMe_3)_4Cl_6]^{2-}$, from the reaction between $[Bi_2Cl_9]^{3-}$ and $(Me_3Sn)_3N$ is presented. This is the first report of a bismuth-nitrogen cubane complex where

the nitrogen sites of the Bi_4N_4 cube are solely bound to metal atoms. The reaction of $[Bi_4(NSnMe_3)_4Cl_6]^{2-}$ with $GaCl_3$ produces $[Bi_4N_4(GaCl_3)_4]$, which represents a rare transformation of a high-nuclearity compound directly to another through a metal exchange process. The reactions of $[Bi_4(NSnMe_3)_4Cl_6]^{2-}$ with other metal halides ($AlCl_3$, $InCl_3$, $BiCl_3$, $[Bi_2Cl_9]^{3-}$, and $[GaCl_4]^{1-}$) were also investigated, and the results suggest that similar transformations also occur. The technique of hot injection was then used with the complexes $[Bi_4(NSnMe_3)_4Cl_6]^{2-}$ and $[Bi_4N_4(GaCl_3)_4]$ to explore whether they could serve as precursors to form bismuth-nitride containing nanoparticles. The resulting particles were characterized by scanning electron microscopy, which showed that the sizes were in fact in the micrometer range. The reactions to produce bismuth-nitrogen cubane complexes were adopted for synthesizing bismuth-phosphide complexes from $[Bi_2Cl_9]^{3-}$ and $(Me_3Si)_3P$.

The final two chapters are devoted to the synthesis and application of silver nanoparticles. A new method of producing triangular silver nanoplates of tunable size is presented. These nanoplates can absorb or scatter light throughout the visible and infrared regions of light. Notably, these nanoplates are stable for long periods of time at room temperature and have capping agents that are easily displaced, which is important in potential applications. They can also be produced in large quantity. In preliminary work aimed toward functionalizing solar cells with the nanoparticles, 4-aminobenzene diazonium complex, a bifunctional linker molecule was synthesized and characterized.

Chapter 1: Bismuth-Nitrogen and Silver Nanoparticles

Chemistry: Bottom-up Approach to Materials and Application

Challenge and Goal of Our Renewable Energy

Electricity is a vital means to support life. Since humans have implemented its use in various applications in the 19th century, the production of electricity from burning fossil fuels (coal, petroleum, and natural gas) has contributed to a tremendous amount of greenhouse gas. The average temperature on Earth has been increasing ever since the dawn of the fossil fuel age and is expected to surge up to 4 °C by 2100. However, the increase in temperature can be reduced to 1 °C if we are able to mitigate the greenhouse gas emissions.[1] Thus, it is crucial to find alternative energy sources that are environmentally friendly.

The demand for new energy sources has generated research initiatives in areas such as, wind, solar, and biofuels. Biofuels, such as jatropha, corn, and algae, are an attractive alternative to biofuels because they can be carbon neutral, given that CO_2 uptake by the crops and the emissions of CO_2 by combustion of these fuels are theoretically equal to each other. However, the production costs can be quite high, and requirements for arable land can cause large increases in the price of food. It is crucial to seek low-cost, maintenance-free, and high-throughput energy sources to meet our goals of finding new energy sources and reducing greenhouse gas emissions. Nuclear power could be an alternative due to energy efficiency; however, toxicity and disposal problems pose significant problems which could lead to a disaster.

Solar energy has emerged as a popular choice in the past decades, with various countries providing subsidies for the installation of household and

business solar panels. More and more households started to cover the rooftop with solar panels at an affordable cost. As the technology advances, the solar cells are found in a different format: (i) solar paint which can convert the entire exterior of buildings into a solar generator and (ii) flexible cells which can apply, for instance, on a roof top of a car. The energy acquired from the sunlight can induce chemical conversions (e.g. CO_2 to CH_4 and H_2O to H_2). This transformation can perform to store potential energy which can release as an electricity through the reverse process when needed. The system is so called a fuel cell. If these efficient energy transfers can be met, we would achieve a true replacement of fossil fuels.

One of the bottlenecks for the commercial solar cells; however, is the energy conversion rate. The average performance of commercially available solar panels is approximately 20% efficiency at most.[2] In fact, silicon based solar cells have been used over the decades; yet, the energy conversion rate has not increased significantly. Majority of energy input is wasted and transferred into the heat energy. It is imperative to discover a new type of material for the solar cell application or, alternatively, make a modification to the silicon solar cells that can minimize the loss of energy absorbed from the sunlight and improve the solar cell performance.

Bismuth Nitride as a Potential Component of Hot-Carrier Solar Cells

The major source of photocurrent loss among solar cells is attributed to thermalization in the lattice by photo-excited electrons.[3] However, this loss can

be minimized if these electrons can transport energy faster than it proceeds to thermalization. A system which adopts the concept is called hot-carrier solar cells (HCSC).[4] Studies have shown that HCSCs are promising for next generation photovoltaics. The theoretical power conversion could reach as high as ~60%.[4,5] One of the key components in the HCSCs is heavy atoms. The presence of these atoms in the material means HCSCs are less prone to lattice vibrations. As a result, these allow for faster photon energy transfer and reduce energy lost to heat generation in the lattice, leading to a higher energy conversion overall.

Recently, König *et al.* published a theoretical calculation on next generation hot-carrier solar cells.[6] Density functional calculations on H-terminated diatomic molecules were used as a model to accurately predict phononic properties of material candidates. One of the candidates discussed was bismuth nitride (BiN). Their calculations suggest that the bandgap is ~1.4 eV, that is approximately 900 nm. Since the bandgap is a minimum energy required to excite electrons from a valance band to a conduction band, it is hoped that BiN-based HCSCs can be used to convert photon energy in the visible and near-infrared light region. Among novel hot-carrier solar cell materials which have been studied, lead selenide (PbSe) nanoparticles have drawn attention due to the easy preparation from molecular precursors (lead acetate trihydrate and trioctylphosphine selenide) and the straightforward application on silicon- and titanium dioxide substrates.[7,8] The photo conversion efficiencies have improved in the recent years: 1.3% in 2006,[9] 6% in 2014,[10]

and 9.8% in 2018.[11] The results for lead-chalcogenide systems prepared via a bottom-up approach was intriguing and indicates that other candidates could exist. Bismuth would be a less toxic alternative. Indeed, compounds like Bi_2S_3[12] and BiOI[13] are potentially useful in photovoltaic applications. We found inspiration from studies like these to investigate the synthesis of bismuth-nitrogen precursor molecules, especially high nuclearity complexes, for nanoparticle and solar cell applications. While BiN itself is highly unstable to spontaneous disproportionation to Bi metal and N_2 gas, we were interested in learning whether molecules containing Bi-N bonds could be synthesized and then used in making mixed-metal bismuth nitrides or surfactant stabilized nanoparticles of BiN.[14]

Early Studies in Bismuth Nitride Chemistry

The first reports on bismuth-nitride (BiN) date to the early 20th century. The first synthesis of BiN involved alkali metal amides solubilized in liquid ammonia and bismuth halides (bromide and iodide) (Scheme 1.1a).[15] Both reactants are soluble while the BiN product is isolated as a precipitate. Thus, the strategy allowed purification and analysis, leading to identification of the compositions. The dry solid was found to be explosive upon heating or upon contact with water or dilute acids. Indeed, the reaction often resulted in explosions. Slow decomposition to metallic bismuth was also confirmed under air. In addition, BiN solid was found to be shock-sensitive, and the explosion

was concomitant with a release of nitrogen gas.[16] Bismuth nitride is capable of oxidizing hydrazines according to scheme 1.1b.[17]

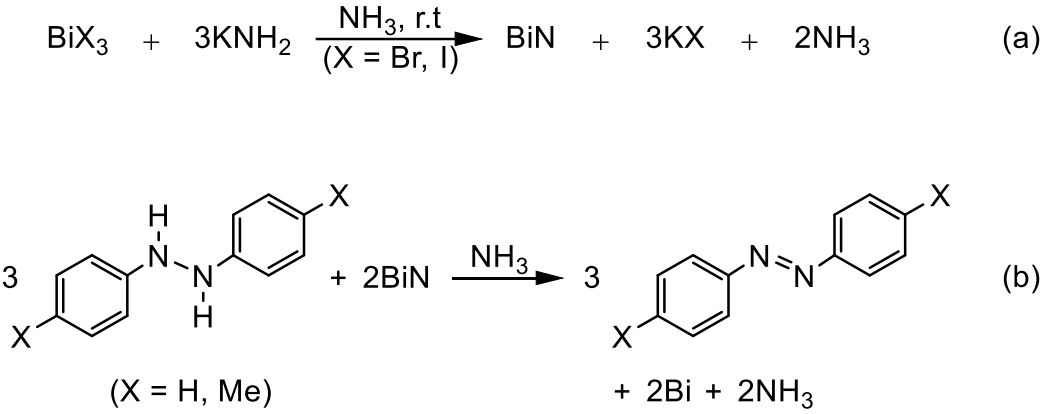

Scheme 1.1. The first reported preparation of bismuth nitride (a). The first application of bismuth nitride as a nitridizing agent (b).

Single-Source Precursors Clusters to BiN

Polynuclear molecules are recognized as building blocks in the formation of minerals,[18] biominerals,[19–21] and man-made materials.[22] Molecules containing pre-formed bonds between the desired elements which can be used to synthesize the material are called single source precursors (SSPs). These types of molecules have been used as convenient precursors of semiconducting materials and nanomaterials.[23–40]

Chemical vapor deposition (CVD)[23–25] and spin coating[26] are methods which afford uniform films on a variety of substrates with thickness ranging from atomically thin to a few microns. The advantage of these two strategies is that the byproduct(s), typically volatile ligands, dissociate from the SSPs and are

isolated by the gas flow or under the vacuum, so the resulting film is found in a pure form.

A solution-phase application of SSPs has been demonstrated in the synthesis of nanoparticles. These nanoparticles are prepared using hot-injection method, in which the SSPs in a solution are rapidly injected to a stirred hot solution of surfactants (Figure 1.1).[41–46] This scheme allows the motif of precursor molecules to thermally achieve homogeneous nucleation while the surfactant molecules prevent the aggregation during the particle growth (Figure 1.2). The resulting colloidal particles are typically found in 1 – 10 nm sizes, and these are so called quantum dots (QDs). The optical and electronic properties are distinct from the bulk and are depended on the particle sizes. The aliquots may be removed at intervals during the growth to larger sizes. Thus, QDs can be engineered to meet for specific applications in one-pot synthesis. These examples include cadmium selenide (CdSe),[41,45,47–49] zinc sulfide (ZnS),[50–53] and indium phosphide (InP) QDs.[54–56] Accessing BiN materials through SSPs may be a plausible approach to particles which are less susceptible to disproportionation Bi metal and N_2.

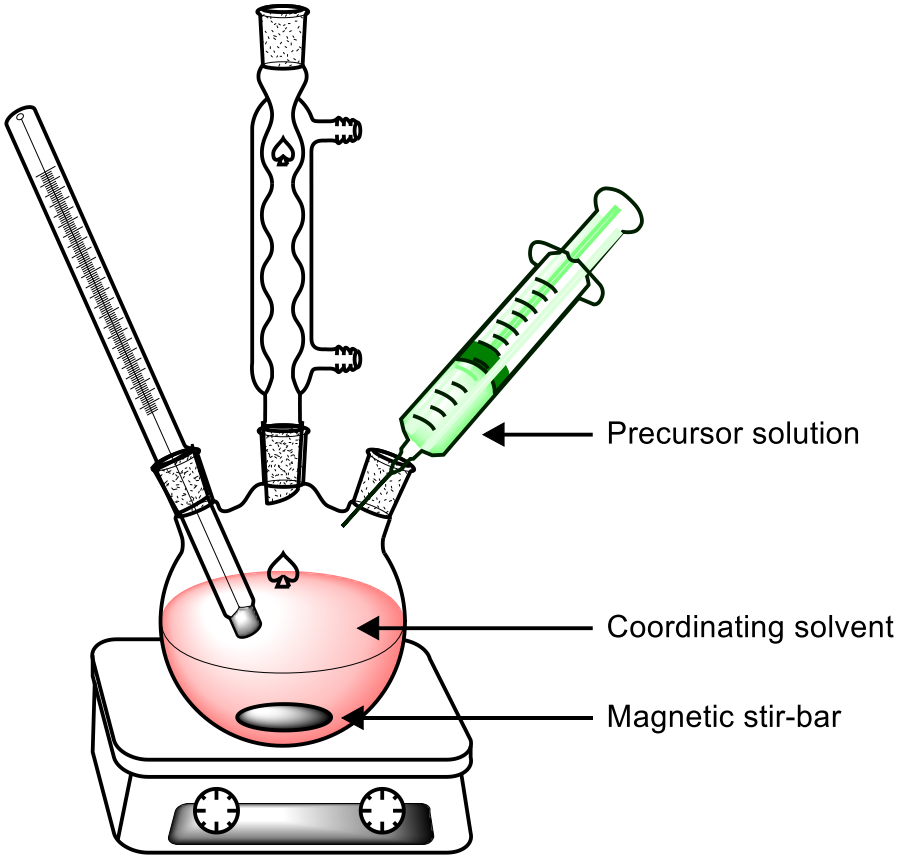

Figure 1.1. A general apparatus setup of hot injection experiment.

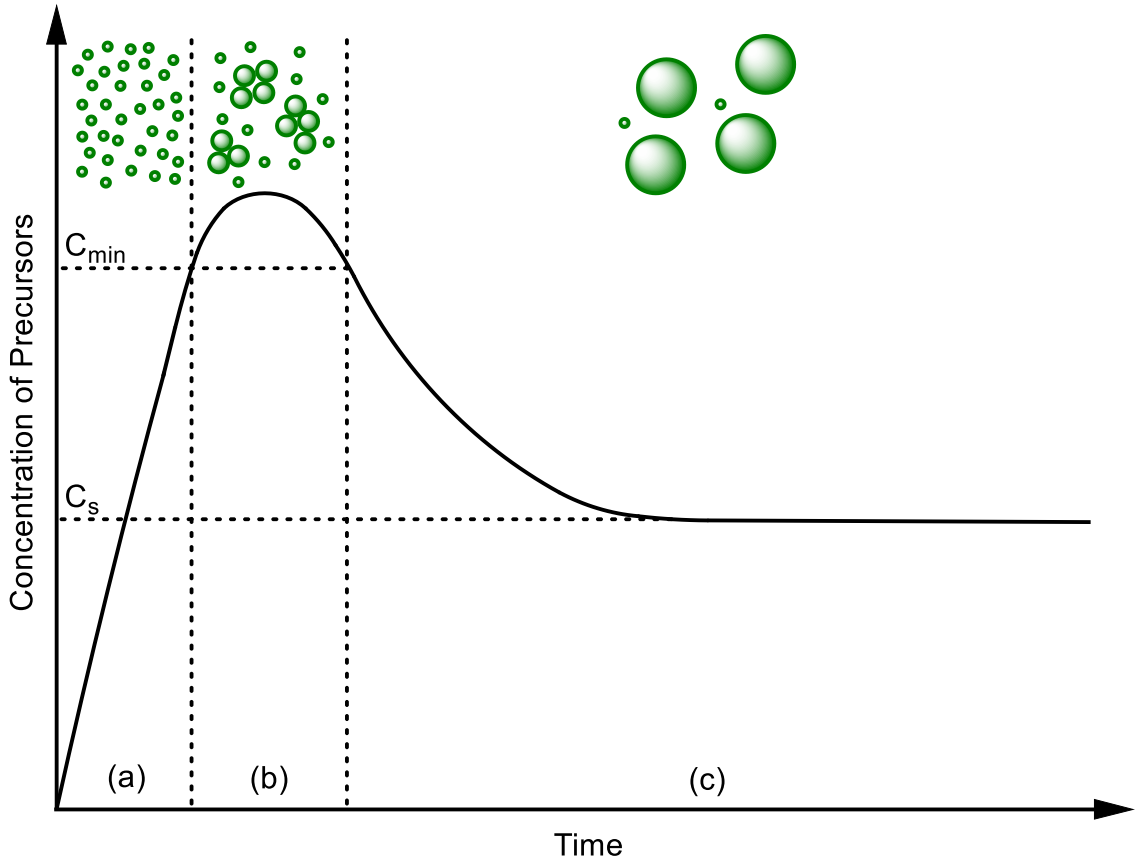

Figure 1.2. A process of nanoparticle growth from precursor molecules. (a) precursor molecules (b) nucleation (c) growth (C_s = equilibrium solute concentration; C_{min} = nucleation concentration).

Recent Studies in Bismuth-Nitrogen Oligomers

In the literature there are handful of reports of bismuth-nitrogen oligomers synthesized via numerous routes. One type of synthesis to access oligomers is the salt metathesis of alkali amides and bismuth trichloride. These cases include: (i) the formation of the dimeric complex: $[(RHN)Bi(\mu\text{-}NR)]_2$ (**1**) (R = 2,6-diisopropylphenyl) (Scheme 1.2(1));[57] (ii) the formation of the dimer $\{[(Me_3Si)_2N]Bi[\mu\text{-}N(SiMe_3)]\}_2$ (**2**) (Scheme 1.2(2));[58] and (iii) the formation of the bismuth amide, $Bi(NHR')_3$ (**3**) (R' = 2,6-dimethylbenzene) (Scheme 1.2(3)).[59] The monomeric bismuth amide **3** can undergo spontaneous condensation to a tetrameric complex: $[Bi_3(\mu\text{-}NR')_4(NHR')]$ (**4**) (Scheme 1.2(4)).[59] Another dimer, $[ClBi(\mu\text{-}NTer)]_2$ (**6**), is formed from the base catalyzed condensation of $[(TerNH)BiCl_2]$ (**5**) (Scheme 1.2(5) and (6)).[60]

The highest nuclearity bismuth-nitrogen complexes are tetramer with a Bi_4N_4 cubane core: $[pyOBi(\mu_3\text{-}NCy)]_4$ (**7**) (Cy = cyclohexyl, py = 2-pyridyl) (Scheme 1.3(7)).[61] The driving force of the synthesis is an amine elimination which coincides with alkyl amide and cationic bismuth generations, resulting in Bi-N bond formation. Another example of a tetramer was a bimetallic cubane composed of $Li_2Bi_2N_4$ core where *t*-butyl groups adopt the nitrogen sites and tetrahydrofuran (THF) ligands are bound to lithium atoms: $[Bi_2(N^tBu)_4]Li_2{\cdot}2THF$ (**8**) (Scheme 1.3(8)).[62] The strategy involves base catalyzed reaction, using ^{t}BuNHLi, amine elimination, and followed by structural rearrangement.

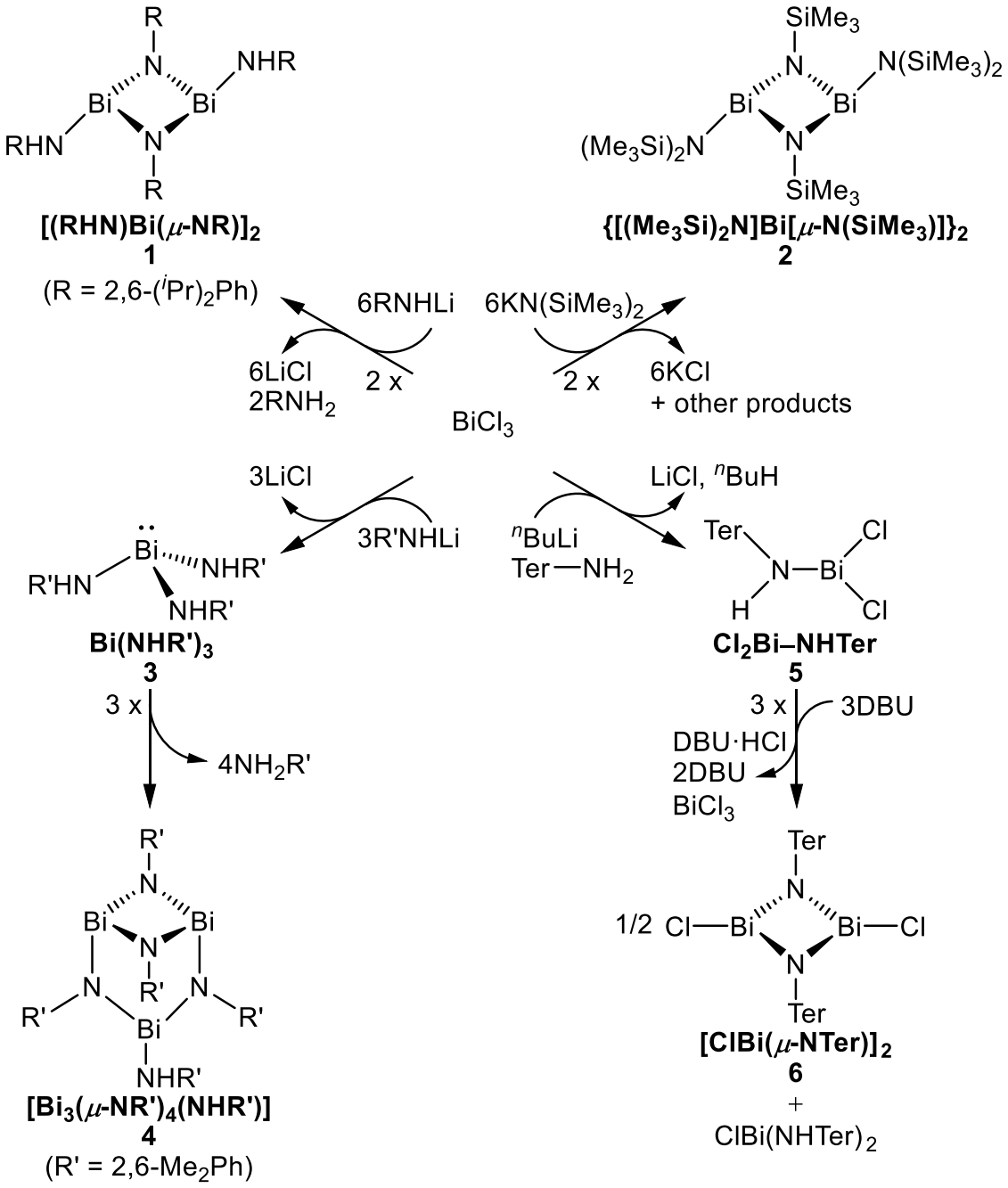

Scheme 1.2. Bismuth-nitrogen oligomer syntheses (Ter = 2,6-$Mes_2C_6H_3$, Mes = 2,4,6-$Me_3C_6H_2$; DBU = 1,8-diazabicyclo[5.4.0]undec-7-ene).

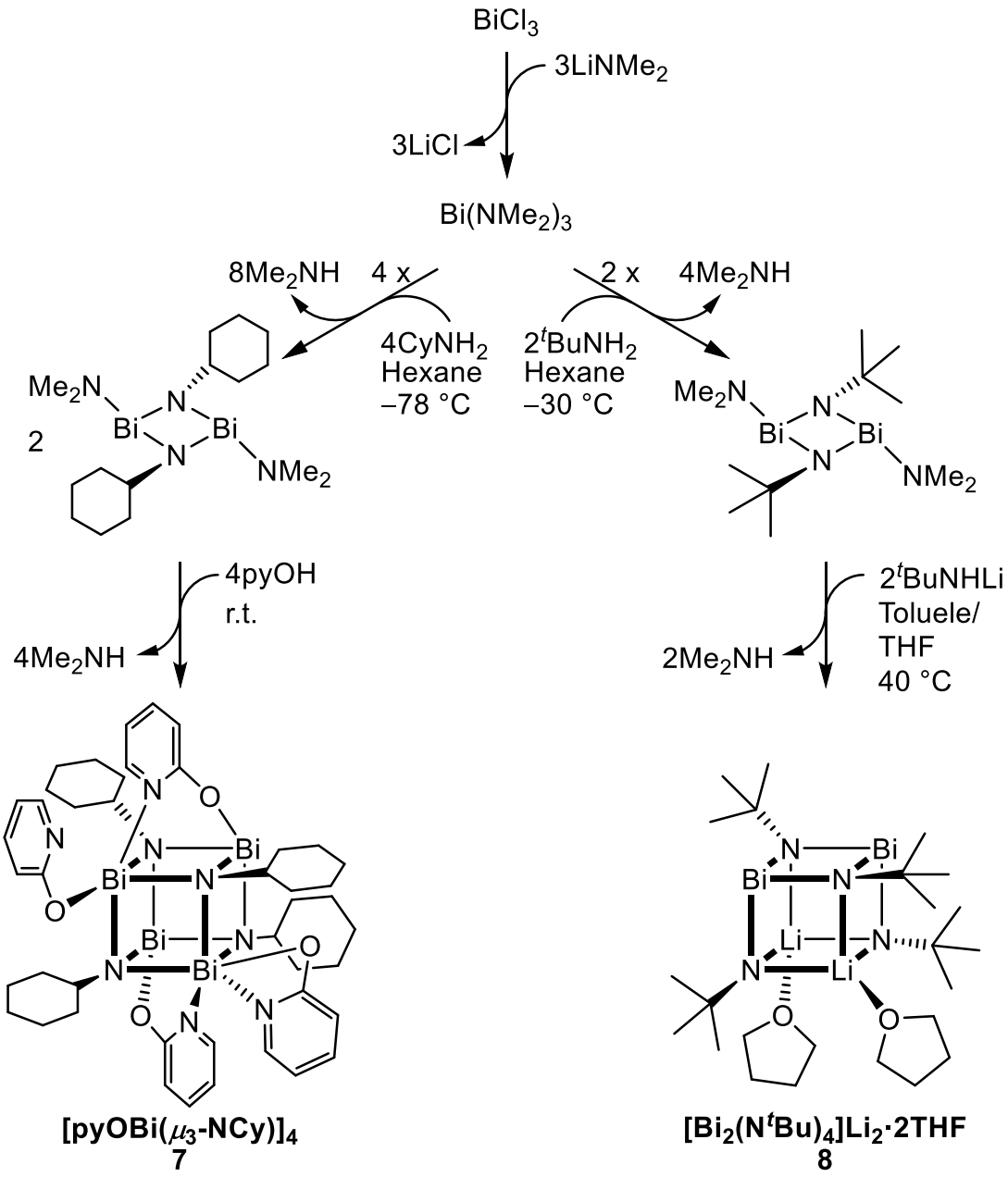

Scheme 1.3. A bismuth-nitrogen cubane with support of organic ligands (**7**) and a cubane formed in a bimetallic fashion (**8**) (Cy = cyclohexyl, py = 2-pyridyl).

Tris(trimethylstannyl)amine as a Molecular Nitride Source

The molecule tris(trimethylstannyl)amine, $(Me_3Sn)_3N$, presents itself as a convenient nitrogen source to chemical species. The $(Me_3Sn)_3N$ can be regarded as carrying a built-in base since an elimination of $Me_3Sn–$ group can result in a reactive Lewis base, $[(Me_3Sn)_2N]^-$. The Lewis base can then attack on a Lewis acidic metal. The successive eliminations of $Me_3Sn–$ groups could lead to a higher order of M–N bonds, metal-imides or -nitrides.

There have been several reports on metal-nitride complexes derived from $(Me_3Sn)_3N$. These examples include: $[Cp^*TaN(Cl)]_3$ (**9**),[63] $[Cp^*TiCl(\mu\text{-}NSnMe_3)]_2$ (**10**),[64] $[MeB(\mu\text{-}NSnMe_3)]_2$ (**11**),[65] $[MeB(\mu\text{-}NSnMe_3)]_4$ (**12**),[65] $[(Cl_3Ga)_3N]^{3-}$ (**14**),[66] $[Fe_4N_2Cl_{10}]^{4-}$ (**15**),[67] $[Fe_{10}N_8Cl_{12}]^{5-}$ (**16**),[67] and $[Fe_{14}N_8(NSnMe_3)_4Cl_{12}]^{4-}$ (**17**).[68] Among the iron-nitride complexes (**15**) – (**17**), the reaction routes are predicted by the molar ratio of the reactants. The strategy that affords these metal-nitride products is governed by the thermodynamic process through the formation of a stable byproduct, tristrimethylstannyl halide (Me_3SnX; X = Br, Cl) (Scheme 1.4 and 1.5). The elimination of Me_3SnX is called dehalostannylation. When a formation of bismuth-nitrogen imides or nitrides is considered, it is crucial to favorably drive the dehalostannylation process as evidenced by these literature reports.

While $(Me_3Sn)_3N$ can act as a suitable reagent for the nitride source, a periodic trend may seek the alternatives such as $(Me_3Si)_3N$ and $(Me_3Ge)_3N$. To our knowledge, there have not been examples of metal-nitride clusters that are formed through $(Me_3Si)_3N$ and $(Me_3Ge)_3N$ thus far. The plausible explanation

can be drawn from the relative bond dissociation energies (BDEs) of $Me_3E–N$ (E = Si, Ge, Sn) and $Me_3E–X$ (X = Br, Cl) (Scheme 1.6).[69] Among these reactant and product pairs, $Me_3Sn–Cl$ strongly favors towards the product while others are likely to stay at an equilibrium. Thus, the reaction of bismuth-chloride complexes and $(Me_3Sn)_3N$ are reasonable approach for preparing Bi-N oligomers.

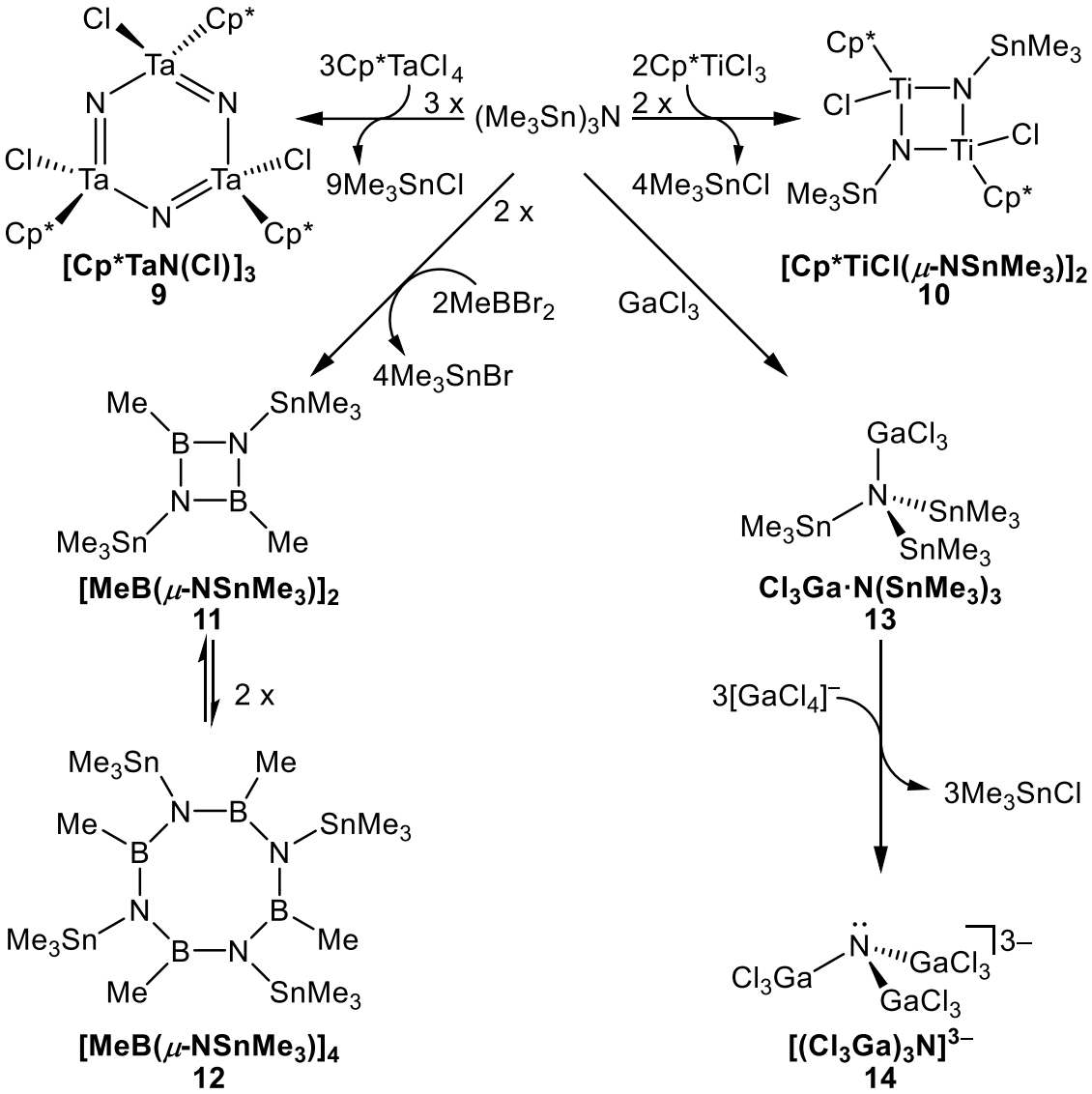

Scheme 1.4. $(Me_3Sn)_3N$ as a precursor for forming molecular-nitride complexes. (Cp* = pentamethylcyclopentadiene). Solvents are omitted for clarity.

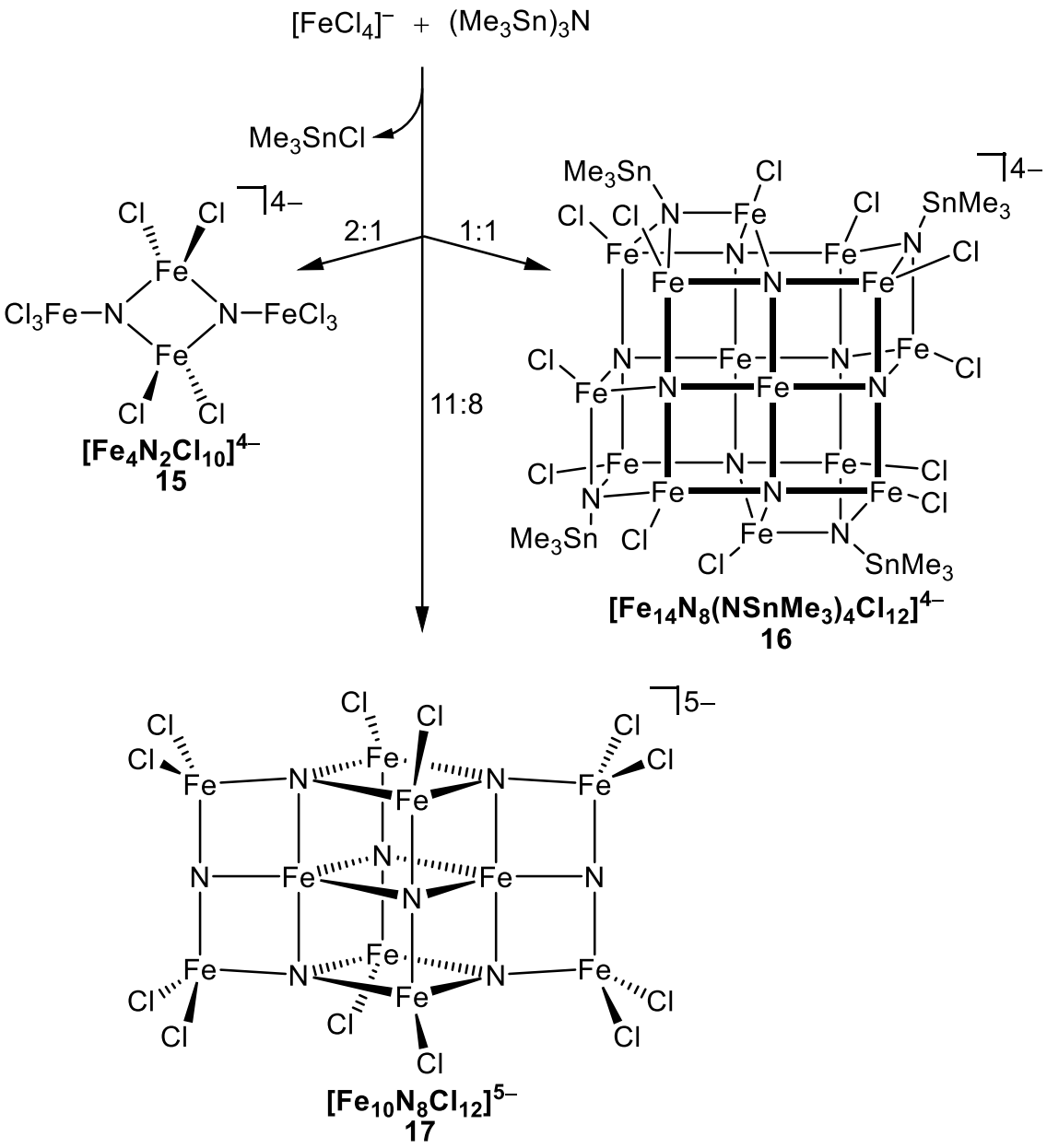

Scheme 1.5. Stoichiometrically controlled reaction of $[FeCl_4]^-$ and $(Me_3Sn)_3N$ leading to three iron-nitride clusters.

$$Me_3Si{-}N > Me_3Ge{-}N > Me_3Sn{-}N \quad (a)$$

$$Me_3Si{-}Cl > Me_3Ge{-}Cl \approx Me_3Sn{-}Cl \quad (b)$$

$$Me_3Si{-}N \approx Me_3Si{-}Cl > Me_3Si{-}Br \quad (c)$$

$$Me_3Sn{-}Cl > Me_3Sn{-}Br \geq Me_3Sn{-}N \quad (d)$$

Scheme 1.6. Relative bond dissociation energies of Me_3EN (E = Si, Ge, Sn) and Me_3EX (X = Br, Cl).

Silver: Overview of Silver Applications

In daily life, we encounter silver in a variety of forms, ranging in size from single ions to the bulk, with nanoparticles occupying an intermediate region of size and having distinct properties and applications. Before discussing these distinct properties and applications, a brief overview of the common uses of silver ions and bulk metal will be presented.

Prior to the widespread use of antibiotics, solutions of silver nitrate were used as antimicrobial agents. A classic example was putting drops of silver nitrate in baby's eyes to prevent infection. Silver salts also serve as supplements in antibiotics owing to silver ions' inhibition effect on bacterial growth. Similarly, the antimicrobial effect is found useful for the application in footwear, insoles, air filters, door handles, bandages, etc. Silver can terminate the bacterial activities through multiple functions: (1) altering the structure and function of bacterial membranes (2) binding to bacterial DNA, and (3) binding to metabolic enzymes.

Silver's lustrous appearance has also of course attracted its use in jewelry, coins, dishes, utensils, and mirrors. Silver also has the highest thermal and electrical conductivities among common materials,[70] accounting for its use in electronic components. As examples, silver thermal grease is used at the interface between electronic chips and heat sinks to improve heat transfer, and silver paste is used electrodes on solar cells to efficiently transfer the current.

Silver Nanoparticles (AgNPs): History – Early use of AgNPs

Research involving silver and gold nanoparticles in the past few decades represents a major and still growing division of nanotechnology, but the use of these nanoparticles in fact dates back many centuries. The 4th century Lycurgus cup crafted by Roman artisans displays distinctive colors depending on the positions of the light source. When illuminated outside the cup, the color appears opaque green, and translucent reddish purple as the light is transmitted inside (Figure 1.3a and b).[71] Modern research concludes that the presence of silver and gold nanoparticles suspended in the glass gives rise to strong absorption and scattering of the light, resulting in dichroic effects.[72] These nanoparticles were also found in stained glass at chapels during the Medieval era. A majority of the red color found in these stained glasses arose from the incorporation of gold nanoparticles into the glass, and the yellow from the silver nanoparticles (Fig. 1.3c).[73,74] These historical artifacts were examples of unintentional nanoengineering well before humans were aware of the nature of atomic, molecular, and nanoscale matter.

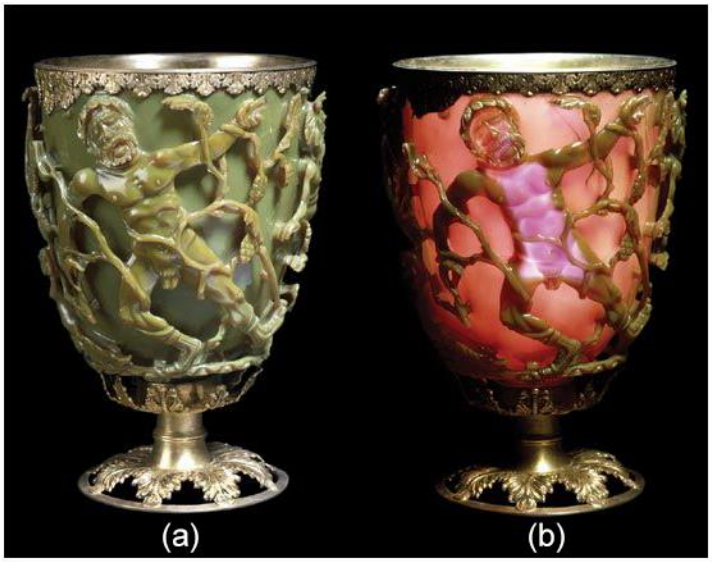

(c)

Figure 1.3. Light reflected outside the Lycurgus cup (a). Light illuminated inside the Lycurgus cup (b) (Photo credit: Trustees of the British Museum). Stained glass window from the Sainte-Chapelle, Paris, France (c) (Photo credit: Centre des Monuments Nationaux).

Early Investigation and Development on Au/AgNPs

Alchemists in the 17th century had some knowledge of producing colloidal gold, which they referred to as “drinkable gold”[75] and which was thought to bring immortality.[76] The first detailed investigation, however, was reported by Michael Faraday much later, in 1857.[77] His method was to chemically reduce gold chloride solutions with phosphorus. The resulting ruby-color colloidal solution was stabilized by gelatin surfactants and other macromolecules. Upon addition of salts to the colloidal solution, the color underwent a wide variety of changes from red to blue and sometimes faded. He was aware that these colored solutions possessed distinctive optical properties compared to the bulk. The characteristic ruby color of his colloidal gold has remained unchanged ever since 1856 and is preserved at The Royal Institution of Great Britain.

The first scientific report on silver nanoparticles was given in the 1880’s by M. Carey Lea, an American chemist known mostly for his work in the chemistry of photography. These nanoparticles were prepared by the chemical reduction of $AgNO_3$ by iron(II) sulfate ($FeSO_4$) and were stabilized by citrate ions that served as a capping agent.[78,79] His method is remarkably similar to procedures still used today Carey Lea stated that the resulting particle colors were gold-yellow, reddish-brown, blue, or green depending on small variations in the synthetic procedure. The nanoparticles made by his procedure were referred to as Carey Lea silver sols. His work was reinvestigated in the 1960s. The analysis by transmission electron microscopy confirmed that these particles

had spherical shapes and were fairly monodisperse with a majority of particle sizes within the range of 4 to 6 nm.[80] Lea's procedure is remarkably similar to the modern synthesis of spherical silver nanoparticles carried out using silver nitrate ($AgNO_3$), trisodium citrate (Na_3Cit), and sodium borohydride ($NaBH_4$) as a reducing agent, which produces an average diameter of ~5 nm.[81–83] Today, the particles are called nanoparticles; in Lea's time, they were referred to as "Carey Lea silver sols".

Faraday and Lea attributed the origin of the vibrant colors, which were distinct from the bulk metal colors, to significantly small metal particles; however, they could not provide an explanation of the colors in terms of the interaction of the particles with light. The first scientist to offer such a rationale was Gustav Mie shortly after 1900. Mie applied Maxwell's equations, which describe the relationships between electric and magnetic fields and electric charge density and current, to the behavior of spherical metal nanoparticles that are exposed to an oscillating electric field.[84] Mie's theory provides mathematical relations between the wavelength-dependent absorption and scattering of light by metal particles that are smaller than the wavelength of incident light. His theory also incorporated the influence of the medium (e.g. air, water, etc.) surrounding the nanoparticles. In addition, the scattering coefficient of these nanoparticles can be solved since the extinction is based on the combination of scattering and absorption.

Plasmonic Nanoparticles

The strong absorption and scattering of light by metal nanoparticles has brought tremendous interest in their optical properties and potential applications. The free electrons in metals are highly polarizable, and when the frequency of incident light matches the resonance frequency of the free electrons, they undergo a collective oscillation that is called the surface plasmon resonance (SPR). The SPR found in metal nanoparticles is called a localized surface plasmon resonance (LSPR) because the electromagnetic field generated by the collectively oscillating electrons is localized at the nanoparticle's surface and in the region just outside the surface. Examples of metal nanoparticles that have been studies for LSPR are silver, gold, copper, platinum, palladium, and aluminum, among which silver and gold give the highest LSPR effect.[85]

The displacement of positive and negative charges in metal nanoparticles results in restoring forces by the Coulombic attraction and allows recurring oscillation as long as the incident light continues (Figure 1.4). The electric field near the surface is greatly enhanced, often by orders of magnitude, due to the resonance effect. Moreover, the effect rapidly falls off with distance.[86] Thus, this property gives an advantage for enhancing the spectroscopic signals attributed to molecules in close proximity to the surface. Application of the LSPR is therefore found in spectroscopic techniques, such as surface enhanced Raman spectroscopy (SERS) and surface enhanced fluorescence (SEF). The resonance wavelength is affected by multiple factors (i) size and shape of the nanoparticles (sphere, cube, triangular, rod, prisms, etc.), (ii)

dielectric constant of the metal, and (iii) dielectric constant of the surrounding medium (air, water, capping agent, etc.).[87–91]

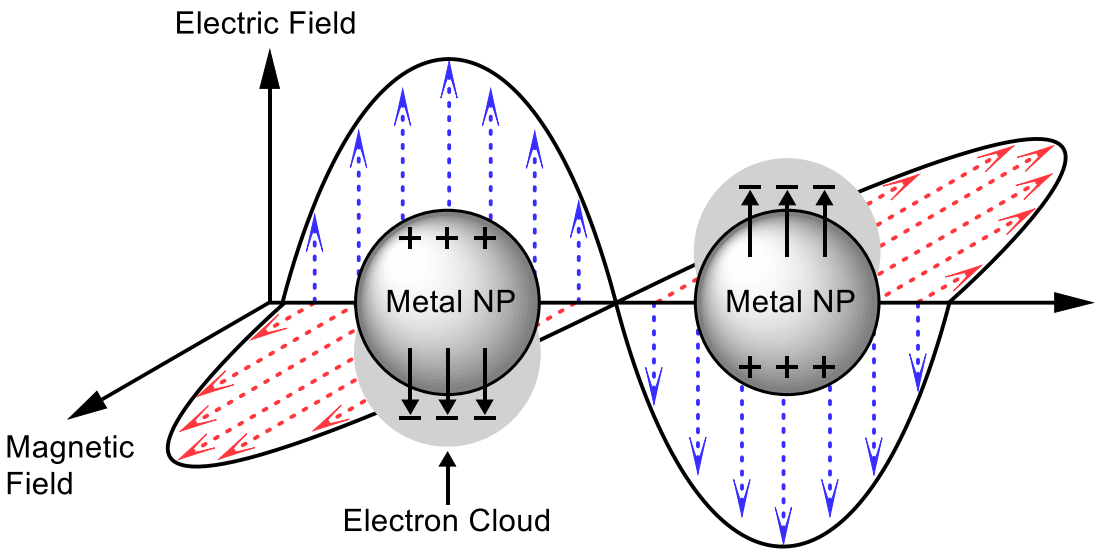

Figure 1.4. Collective oscillation of conducting electrons in metal nanoparticles under the incident light.

Synthesis of Silver Nanoparticles

The preparative strategy for AgNPs can be divided into two fundamental categories: top-down and bottom-up approaches. The top-down method initiates from silver in its bulk form, and the size reduction to nanoscale is accomplished by a variety of techniques: lithography,[92–94] laser ablation,[95–97] thermal decomposition,[98–100] mechanical milling,[101,102] etc.

By contrast, the bottom-up approach is accomplished typically by wet chemical techniques through reduction of a silver salt to elemental Ag and atom-by-atom assembly to nanosizes. Many different synthetic strategies have been reported in the literature for producing a broad range of shapes (spheres,

triangles, rods, cubes, decahedrons, discs, etc.). A few of the more common ones that are relevant to our work will be mentioned here. The most widely used synthesis is conducted by the addition of sodium borohydride ($NaBH_4$) into an aqueous solution of silver nitrate ($AgNO_3$)[103] that also contains trisodium citrate ($Na_3C_6H_5O_7$, or Na_3Cit for short) as a stabilizing agent.[104] This approach is straightforward, can be done at room temperature, and rapidly generates spherical AgNPs which appear bright yellow and are approximately 5 to 10 nm in diameter.[82,83] The citrate ion can also act as a reducing agent but not at room temperature. If a citrate solution is added to a boiling solution of $AgNO_3$, then the citrate can serve as both the reducing agent and the capping agent.[105] The supplied energy promotes the carboxylate groups in Cit^{3-} to participate as a reducer and releases CO_2. The solution is also yellow as with the borohydride method, but the resulting AgNPs are found to be more polydisperse and the shapes are non-uniform. Similarly, in the polyol method, if a solution of ethylene glycol and $AgNO_3$ is heated in the presence of O_2 to about 150 °C, AgNPs are produced.[106–108]

As mentioned earlier, the shape and the size of plasmonic metal nanoparticles play a significant role in determining their optical properties. While spherical AgNP synthesis is straightforward, anisotropic nanostructures such as rods, cubes, polyhedra, discs, etc. require additional techniques. A typical strategy uses the reduction kinetics to control the morphologies of AgNPs. The anisotropic growth is established by a balance among several competing factors, including selective growth and etching of different crystalline facets that

is guided by the relative binding affinity of the capping agent for one facet as opposed to another. An example is the synthesis of triangular silver nanoplates in a one-pot setup. This synthesis is accomplished via the reduction of $AgNO_3$ by $NaBH_4$ in the presence of Na_3Cit and hydrogen peroxide (H_2O_2).[109] The role of H_2O_2 was to facilitate an oxidative etching during the growth of nanoplates. The final edge length and the UV-visible absorption maxima are dictated by the concentration of H_2O_2.[109]

Another approach to producing triangular silver nanoplates is to use a seeding method.[110] In this method, first, a solution of small spherical AgNP is prepared. Then, a small amount of $AgNO_3$ is introduced to the solution, along with a reducing reagent. The idea is to maintain low enough silver atom concentration that atoms will add to the seeds preferentially compared to forming new silver clusters. The advantage of this method is that there is better control of the final morphologies can be achieved due to isolation of the nucleation and growth steps. Evidence of the narrow size and shape distributions of the resulting nanoplates came from TEM micrographs and by the narrow width of the UV-visible absorption peak.

Overview of Subsequent Chapters

Chapter 2 and 3 present syntheses, properties, and reactivity related to novel bismuth-nitrogen high-nuclearity compounds. Chapter 4 is dedicated to the approach of these compounds to the materials. In Chapter 5, explorations of synthesizing bismuth-phosphorus compounds by adopting the scheme employed for the bismuth-nitrogen study. In addition, two newly produced arylbismuth halide complexes are reported.

Two chapters of this thesis is devoted to the synthesis and application of the silver nanoparticles. In Chapter 6, a new method of producing triangular silver nanoplates of tunable size and shape is presented. These nanoplates can absorb or scatter light in the visible and infrared, are stable at room temperature, have capping agents that are easily displaced (which is important in application), and can be produced in a sufficient quantity. In Chapter 7, we present preliminary results on the application of these nanoplates to enhance solar cell activity.

References

1. Future of Climate Change. https://19january2017snapshot.epa.gov/climate-change-science/future-climate-change_.html (accessed 4/5/2019).

2. Crystalline Silicon Photovoltaics Research. https://www.energy.gov/eere/solar/crystalline-silicon-photovoltaics-research (accessed 4/5/2019).

3. Bernardi, M.; Vigil-Fowler, D.; Lischner, J.; Neaton, J. B.; Louie, S. G. *Phys. Rev. Lett.* **2014**, *112*, 257402.

4. Ross, R. T.; Nozik, A. J. *J. Appl. Phys.* **1982**, *53*, 3813.

5. Green, M. A. *Physica E.* **2002**, *14*, 65.

6. König, D.; Casalenuovo, K.; Takeda, Y.; Conibeer, G.; Guillemoles, J. F.; Patterson, R.; Huang, L. M.; Green, M. A. *Physica E.* **2010**, *42*, 2862.

7. Tisdale, W. A.; Williams, K. J.; Timp, B. A.; Norris, D. J.; Aydil, E. S.; Zhu, X.-Y. *Science.* **2010**, *328*, 1543.

8. Talapin, D. V. *Science.* **2005**, *310*, 86.

9. Cui, D.; Xu, J.; Zhu, T.; Paradee, G.; Ashok, S.; Gerhold, M. *Appl. Phys. Lett.* **2006**, *88*, 183111.

10. Zhang, J.; Gao, J.; Church, C. P.; Miller, E. M.; Luther, J. M.; Klimov, V. I.; Beard, M. C. *Nano Lett.* **2014**, *14*, 6010.

11. He, J.; Tang, J. In *The International Photonics and Optoelectronics Meeting (POEM)*; OSA Technical Digest; Optical Society of America, **2018**; p PT4B.18.

12. Miller, N. C.; Bernechea, M. *APL Mater.* **2018**, *6*, 084503.

13. Hoye, R. L. Z.; Lee, L. C.; Kurchin, R. C.; Huq, T. N.; Zhang, K. H. L.; Sponseller, M.; Nienhaus, L.; Brandt, R. E.; Jean, J.; Polizzotti, J. A.; Kursumović, A.; Bawendi, M. G.; Bulović, V.; Stevanović, V.; Buonassisi, T.; MacManus-Driscoll, J. L. *Adv. Mater.* **2017**, *29*, 1702176.

14. Sun, W.; Holder, A.; Orvañanos, B.; Arca, E.; Zakutayev, A.; Lany, S.; Ceder, G. *Chem. Mater.* **2017**, *29*, 6936.

15. Franklin, E. C. *J. Am. Chem. Soc.* **1905**, *27*, 820.

16. Fischer, F.; Schröter, F. *Ber. Dtsch. Chem. Ges.* **1910**, *43*, 1465.

17. Schurman, I.; Fernelius, W. C. *J. Am. Chem. Soc.* **1930**, *52*, 2425.

18. Hazen, R. M.; Papineau, D.; Bleeker, W.; Downs, R. T.; Ferry, J. M.; McCoy, T. J.; Sverjensky, D. A.; Yang, H. *Am. Mineral.* **2008**, *93*, 1693.

19. Meldrum, F. C.; Cölfen, H. *Chem. Rev.* **2008**, *108*, 4332.

20. Navrotsky, A. *Proc. Natl. Acad. Sci. U.S.A.* **2004**, *101*, 12096.

21. Lowenstam, H. *Science.* **1981**, *211*, 1126.

22. Maniaki, D.; Pilichos, E.; Perlepes, S. P. *Front. Chem.* **2018**, *6*, 1.

23. Veith, M.; Altherr, A.; Wolfanger, H. *Chem. Vap. Deposition.* **1999**, *5*, 87.

24. Ouyang, T.; Loh, K. P.; Zhang, H.; Vittal, J. J.; Vetrichelvan, M.; Chen, W.; Gao, X.; Wee, A. T. S. *J. Phys. Chem. B.* **2004**, *108*, 17537.

25. Tedstone, A. A.; Lewis, E. A.; Savjani, N.; Zhong, X. L.; Haigh, S. J.; O'Brien, P.; Lewis, D. J. *Chem. Mater.* **2017**, *29*, 3858.

26. Erk, C.; Berger, A.; Wendorff, J. H.; Schlecht, S. *Dalton Trans.* **2010**, *39*, 11248.

27. Cumberland, S. L.; Hanif, K. M.; Javier, A.; Khitrov, G. A.; Strouse, G. F.; Woessner, S. M.; Yun, C. S. *Chem. Mater.* **2002**, *14*, 1576.

28. Gary, D. C.; Terban, M. W.; Billinge, S. J. L.; Cossairt, B. M. *Chem. Mater.* **2015**, *27*, 1432.

29. Bryan, J. D.; Gamelin, D. R. In *Progress in Inorganic Chemistry*; John Wiley & Sons, Ltd, **2005**; Vol. 54, pp 47.

30. Malik, M. A.; Afzaal, M.; O'Brien, P. *Chem. Rev.* **2010**, *110*, 4417.

31. van Embden, J.; Chesman, A. S. R.; Jasieniak, J. J. *Chem. Mater.* **2015**, *27*, 2246.

32. Fan, D.; Afzaal, M.; Mallik, M. A.; Nguyen, C. Q.; O'Brien, P.; Thomas, P. J. *Coord. Chem. Rev.* **2007**, *251*, 1878.

33. He, G.; Shynkaruk, O.; Lui, M. W.; Rivard, E. *Chem. Rev.* **2014**, *114*, 7815.

34. Knapp, C. E.; Carmalt, C. J. *Chem. Soc. Rev.* **2016**, *45*, 1036.

35. Lewis, D. J.; Kevin, P.; Bakr, O.; Muryn, C. A.; Malik, M. A.; O'Brien, P. *Inorg. Chem. Front.* **2014**, *1*, 577.

36. Masala, O.; Seshadri, R. *Annu. Rev. Mater. Res.* **2004**, *34*, 41.

37. Reiss, P.; Carrière, M.; Lincheneau, C.; Vaure, L.; Tamang, S. *Chem. Rev.* **2016**, *116*, 10731.

38. Seisenbaeva, G. A.; Kessler, V. G. *Nanoscale.* **2014**, *6*, 6229.

39. Shi, W.; Song, S.; Zhang, H. *Chem. Soc. Rev.* **2013**, *42*, 5714.

40. Wang, F.; Richards, V. N.; Shields, S. P.; Buhro, W. E. *Chem. Mater.* **2014**, *26*, 5.

41. Murray, C. B.; Norris, D. J.; Bawendi, M. G. *J. Am. Chem. Soc.* **1993**, *115*, 8706.

42. Murray, C. B.; Kagan, C. R.; Bawendi, M. G. *Annu. Rev. Mater. Sci.* **2000**, *30*, 545.

43. de Mello Donegá, C.; Liljeroth, P.; Vanmaekelbergh, D. *Small.* **2005**, *1*, 1152.

44. Park, J.; Joo, J.; Kwon, S. G.; Jang, Y.; Hyeon, T. *Angew. Chem. Int. Ed.* **2007**, *46*, 4630.

45. Williams, J. V.; Kotov, N. A.; Savage, P. E. *Ind. Eng. Chem. Res.* **2009**, *48*, 4316.

46. Timonen, J. V. I.; Seppälä, E. T.; Ikkala, O.; Ras, R. H. A. *Angew. Chem. Int. Ed.* **2011**, *50*, 2080.

47. Rosenthal, S.; Mcbride, J.; Pennycook, S.; Feldman, L. *Surf. Sci. Rep.* **2007**, *62*, 111.

48. Somers, R. C.; Bawendi, M. G.; Nocera, D. G. *Chem. Soc. Rev.* **2007**, *36*, 579.

49. Harrell, S. M.; McBride, J. R.; Rosenthal, S. J. *Chem. Mater.* **2013**, *25*, 1199.

50. Fang, X.; Zhang, L. *J. Mater. Sci. Technol.* **2006**, *22*, 721.

51. Fang, X.; Gautam, U. K.; Bando, Y.; Golberg, D. *J. Mater. Sci. Technol.* **2008**, *24*, 520.

52. Fang, X.; Zhai, T.; Gautam, U. K.; Li, L.; Wu, L.; Bando, Y.; Golberg, D. *Prog. Mater Sci.* **2011**, *56*, 175.

53. Wang, X.; Huang, H.; Liang, B.; Liu, Z.; Chen, D.; Shen, G. *Crit. Rev. Solid State Mater. Sci.* **2013**, *38*, 57.

54. Mushonga, P.; Onani, M. O.; Madiehe, A. M.; Meyer, M. *J. Nanomater.* **2012**, *2012*, 1.

55. Brichkin, S. B. *Colloid J.* **2015**, *77*, 393.

56. Koh, S.; Lee, D. C. *MRS Commun.* **2018**, *8*, 742.

57. Wirringa, U.; Roesky, H. W.; Noltemeyer, M.; Schmidt, H.-G. *Inorg. Chem.* **1994**, *33*, 4607.

58. Evans, W. J.; Rego, D. B.; Ziller, J. W. *Inorg. Chim. Acta.* **2007**, *360*, 1349.

59. James, S. C.; Norman, N. C.; Orpen, A. G.; Quayle, M. J.; Weckenmann, U. *J. Chem. Soc., Dalton Trans.* **1996**, 4159.

60. Michalik, D.; Schulz, A.; Villinger, A. *Angew. Chem. Int. Ed.* **2010**, *49*, 7575.

61. Bickley, J. F.; Bond, A. D.; García, F.; Jantos, K.; Lawson, G. T.; McPartlin, M.; Steiner, A.; Wright, D. S. *J. Chem. Soc., Dalton Trans.* **2002**, 4629.

62. Edwards, A. J.; Beswick, M. A.; Galsworthy, J. R.; Paver, M. A.; Raithby, P. R.; Rennie, M.-A.; Russell, C. A.; Verhorevoort, K. L.; Wright, D. S. *Inorg. Chim. Acta.* **1996**, *248*, 9.

63. Plenio, H.; Roesky, H. W.; Noltemeyer, M.; Sheldrick, G. M. *Angew. Chem. Int. Ed. Engl.* **1988**, *27*, 1330.

64. Bai, Y.; Roesky, H. W.; Schmidt, H.-G.; Noltemeyer, M. *Z. Naturforsch., B: Chem. Sci.* **1992**, *47*, 603.

65. Franz, T.; Hanecker, E.; Nöth, H.; Stöcker, W.; Storch, W.; Winter, G. *Chem. Ber.* **1986**, *119*, 900.

66. Wilson, R. J.; Jones, J. R.; Bennett, M. V. *Chem. Commun.* **2013**, *49*, 5049.

67. Bennett, M. V.; Stoian, S.; Bominaar, E. L.; Münck, E.; Holm, R. H. *J. Am. Chem. Soc.* **2005**, *127*, 12378.

68. Bennett, M. V.; Holm, R. H. *Angew. Chem. Int. Ed.* **2006**, *45*, 5613.

69. Basch, H. *Inorg. Chim. Acta.* **1996**, *252*, 265.

70. Rumble, J. R. *CRC Handbook of Chemistry and Physics, 99th Edition (Internet Version 2018)*; CRC Press: Boca Raton, FL.

71. Leonhardt, U. *Nat. Photonics.* **2007**, *1*, 207.

72. Barber, D. J.; Freestone, I. C. *Archaeometry.* **1990**, *32*, 33.

73. Schaming, D.; Remita, H. *Found. Chem.* **2015**, *17*, 187.

74. Delgado, J.; Vilarigues, M.; Ruivo, A.; Corregidor, V.; Silva, R. C. da; Alves, L. C. *Nucl. Instrum. Methods Phys. Res., Sect. B.* **2011**, *269*, 2383.

75. Charlier, P.; Poupon, J.; Huynh-Charlier, I.; Saliège, J.-F.; Favier, D.; Keyser, C.; Ludes, B. *BMJ.* **2009**, *339*, 1402.

76. Kauffman, G. B. *Gold Bull.* **1985**, *18*, 69.

77. Faraday, M. *Philos. Trans. Royal Soc.* **1857**, *147*, 145.

78. Pradeep, T.; Anshup *Thin Solid Films.* **2009**, *517*, 6441.

79. Lea, M. C. *Am. J. Sci.* **1889**, *37*, 476.

80. Frens, G.; Overbeek, J. Th. G. *Kolloid Z. Z. Polym.* **1969**, *233*, 922.

81. Dong, X.; Ji, X.; Jing, J.; Li, M.; Li, J.; Yang, W. *J. Phys. Chem. C.* **2010**, *114*, 2070.

82. Espinoza, M. G.; Hinks, M. L.; Mendoza, A. M.; Pullman, D. P.; Peterson, K. I. *J. Phys. Chem. C.* **2012**, *116*, 8305.

83. Baber, R.; Mazzei, L.; Thanh, N. T. K.; Gavriilidis, A. *RSC Adv.* **2015**, *5*, 95585.

84. Mie, G. *Ann. Phys.* **1908**, *330*, 377.

85. Rycenga, M.; Cobley, C. M.; Zeng, J.; Li, W.; Moran, C. H.; Zhang, Q.; Qin, D.; Xia, Y. *Chem. Rev.* **2011**, *111*, 3669.

86. Mayer, K. M.; Hafner, J. H. *Chem. Rev.* **2011**, *111*, 3828.

87. Fuchs, R. *Phys. Rev. B.* **1975**, *11*, 1732.

88. Genzel, L.; Martin, T. P.; Kreibig, U. *Z. Phys. B.* **1975**, *21*, 339.

89. Link, S.; El-Sayed, M. A. *J. Phys. Chem. B.* **1999**, *103*, 8410.

90. Link, S.; El-Sayed, M. A. *Int. Rev. Phys. Chem.* **2000**, *19*, 409.

91. Haes, A. J.; Haynes, C. L.; McFarland, A. D.; Schatz, G. C.; Van Duyne, R. P.; Zou, S. *MRS Bull.* **2005**, *30*, 368.

92. Gotschy, W.; Vonmetz, K.; Leitner, A.; Aussenegg, F. R. *Opt. Lett.* **1996**, *21*, 1099.

93. Haynes, C. L.; Van Duyne, R. P. *J. Phys. Chem. B.* **2001**, *105*, 5599.

94. Choi, D.-G.; Yu, H. K.; Jang, S. G.; Yang, S.-M. *J. Am. Chem. Soc.* **2004**, *126*, 7019.

95. Mafuné, F.; Kohno, J.; Takeda, Y.; Kondow, T.; Sawabe, H. *J. Phys. Chem. B.* **2000**, *104*, 8333.

96. Barcikowski, S.; Hahn, A.; Kabashin, A. V.; Chichkov, B. N. *Appl. Phys. A.* **2007**, *87*, 47.

97. Tsuji, T.; Thang, D.-H.; Okazaki, Y.; Nakanishi, M.; Tsuboi, Y.; Tsuji, M. *Appl. Surf. Sci.* **2008**, *254*, 5224.

98. Rast, L.; Stanishevsky, A. *Appl. Phys. Lett.* **2005**, *87*, 223118.

99. Navaladian, S.; Viswanathan, B.; Viswanath, R. P.; Varadarajan, T. K. *Nanoscale Res. Lett.* **2007**, *2*, 44.

100. Akhbari, K.; Morsali, A.; Retailleau, P. *Polyhedron.* **2010**, *29*, 3304.

101. Khakan, B.; Shahroozi, A.; Afsari, A.; Hosseini, S. R. *Powder Diffr.* **2017**, *32*, 93.

102. Baláž, M.; Daneu, N.; Balážová, Ľ.; Dutková, E.; Tkáčiková, Ľ.; Briančin, J.; Vargová, M.; Balážová, M.; Zorkovská, A.; Baláž, P. *Adv. Powder Technol.* **2017**, *28*, 3307.

103. Creighton, J. A.; Blatchford, C. G.; Albrecht, M. G. *J. Chem. Soc., Faraday Trans. 2.* **1979**, *75*, 790.

104. Lee, P. C.; Meisel, D. *J. Phys. Chem.* **1982**, *86*, 3391.

105. Turkevich, J.; Stevenson, P. C.; Hillier, J. *Discuss. Faraday Soc.* **1951**, *11*, 55. (Note: This method was developed specifically for gold nanoparticles, but it was later also applied to silver nanoparticle synthesis.)

106. Ducamp-Sanguesa, C.; Herrera-Urbina, R.; Figlarz, M. *J. Solid State Chem.* **1992**, *100*, 272.

107. Skrabalak, S. E.; Wiley, B. J.; Kim, M.; Formo, E. V.; Xia, Y. *Nano Lett.* **2008**, *8*, 2077.

108. Silvert, P.-Y.; Herrera-Urbina, R.; Tekaia-Elhsissen, K. *J. Mater. Chem.* **1997**, *7*, 293.

109. Zhang, Q.; Li, N.; Goebl, J.; Lu, Z.; Yin, Y. *J. Am. Chem. Soc.* **2011**, *133*, 18931.

110. Le Beulze, A.; Duguet, E.; Mornet, S.; Majimel, J.; Tréguer-Delapierre, M.; Ravaine, S.; Florea, I.; Ersen, O. *Langmuir.* **2014**, *30*, 1424.

Chapter 2: Synthesis and Reactivity of Stannyl- and Gallyl-Capped Bismuth Nitrogen Cubanes

Introduction

Bismuth-nitride (BiN) is a candidate for improving solar cell performance because it is expected to absorb sunlight from the visible to near-infrared light region which is ideal for maximizing solar cell efficiency.[1] In addition, due to the heavy nature of bismuth, photo-excited electrons can transfer the photocurrent before the energy is thermally dissipated. This effect is especially efficient in nanostructures.[2] Given the potential importance of bismuth and nitrogen in useful materials containing Bi-N bonds,[3,4] we were inspired to investigate the reactivity of $[Bi_2Cl_9]^{3-}$ with $(Me_3Sn)_3N$. The first investigation on bismuth-nitride (BiN) was initiated in early 20th century by Edward Franklin[5] and Iman Schurman *et al*. thereafter.[6] Their experiments concluded that BiN was is difficult to handle because it is shock sensitive and explosive under ambient conditions, and therefore, few examples of bismuth-nitrogen oligomers have been prepared. Pnictogen-nitrogen chemistry is dominated by phosphorus-nitrogen complexes. Among the rest of the pnictogen family, arsenic, antimony-, and bismuth-nitrogen oligomers, there are a decreasing number of known compounds as one proceeds down the periodic table. This lack of known compounds suggests a promising chemical space for discovering novel molecules in bismuth-nitrogen chemistry.

Aside from bismuth-pnictogen chemistry, bismuth-chalcogenides exhibit unique properties and applications. Bismuth(III) oxide (Bi_2O_3) is often used for fireworks called Dragon's Eggs, to trigger a spark effect, and its low toxicity is

preferred to the more toxic lead tetroxides.[7] Due to their exothermic decomposition, Bi_2O_3 nanoparticles have been studied as high-density energetic materials.[8] Owing to the high surface to volume ratio, the reaction sites are profoundly increased compared to the bulk and thus a rapid energy release can be achieved. Ternary and quaternary bismuth oxide materials are important in application ranging from ferroelectrics,[9] photoelectrics,[9] superconductors,[9] and catalysts.[9,10] Among other bismuth-chalcogenides, applications and studies in bioimaging for Bi_2S_3[11,12] and thermoelectric materials for Bi_2Se_3[13–15] and Bi_2Te_3[14–16] are reported. The Bismuth-chalcogenide uncapped cubanes, $(Bi_4Q_4)[AlCl_4]_4$ (Q = S,[17] Se,[17] Te[18]) have been synthesized and found to be stable. These syntheses presumably proceeded by the oxidation of elemental bismuth and chalcogens by $BiCl_3$ in the present of the strong Lewis acid $AlCl_3$ which promotes the abstraction of chloride ions (Scheme 2.1). Another report demonstrated use of ionic liquid containing Lewis acid EMIMBr-$AlCl_3$ (EMIM = 1-ethyl-3-methylimidazolium) in the presence of elemental bismuth and tellurium in molten salt reaction which afforded an infinite cationic framework, $[Pn_2Te_2Br](AlCl_4)$ (Pn = Sb, Bi) (Scheme 2.2).[19] These syntheses inspired us to react complex **1** with Lewis acids with the goal of preparing an uncapped bismuth-pnictogen cubane.

The initial attempts at preparing bismuth-nitrogen oligomers from a reaction of $BiCl_3$ and $(Me_3Sn)_3N$ resulted in an intractable polymeric product.[20] Given the success in using anionic precursors at synthesizing new metal-nitride containing soluble species,[21–23] we hypothesized that the dimeric complex,

$[Bi_2Cl_9]^{3-}$ could be starting material in the search for new high-nuclearity Bi-N species. The anion $[Bi_2Cl_9]^{3-}$ has an advantage over $BiCl_3$ because the reaction may proceed from more reactive terminal chlorides while the bridging chlorides stay intact to bismuth atoms which aids in a support for building a larger cluster. Additionally, it is a stronger Lewis acid. The stable counterions can allow crystallization of anions representative of portions of extended solids. As for the nitrogen source, tristrimethylstannyl amine is a convenient nitrogen anion source, given that it can afford thermodynamically stable trimethylstannyl chlorides by abstraction of Cl^- from $[Bi_2Cl_9]^{3-}$. The energetic factors of dissociation of Me_3Sn- group and the stability of Me_3SnCl can be seen from the relative bond dissociation energies based on computational calculations.[24] The equilibrium will strongly favor the formation of Me_3SnCl; thus, $(Me_3Sn)_3N$ has the advantage of forming metal-nitrogen bonds. When these two reagents react, a parallel production of a bismuth cation and a nitrogen anion favors formation of a Bi–N bond. The successive elimination of remaining Me_3Sn^+ and Cl^- can generate the Bi–N core in a high nuclearity complex. Additionally, we investigated another possible nitrogen source that could bind to bismuth. There is a report on tris(trimethylsilyl)phosphine, $(Me_3Si)_3P$, which was used as a source to form bismuth-phosphide.[25] The preparative method relied on the dehalosilylation of Me_3SiCl in a neat solution of $(Me_3Si)_3P$ and solid $BiCl_3$. We report our attempt to use tris(trimethylsilyl) amine, $(Me_3Si)_3N$ as a source of nitrogen.

Reaction of $(Me_3Sn)_3N$ and $[Bi_2Cl_9]^{3-}$ in acetonitrile (MeCN) led to an unprecedented tetrameric cubane structure, $[Bi_4(NSnMe_3)_4Cl_6]^{2-}$, which contains the Bi_4N_4 core where nitrogen sites are bound solely to metal atoms. Its distorted cubane core similar to that found for $[pyOBi(\mu_3\text{-}NCy)]_4$.[26] Each face of the cube was capped by chloride atoms bridging adjacent bismuth atoms. Investigations into the stability and reactivity of the $[Bi_4(NSnMe_3)_4Cl_6]^{2-}$ anion in MeCN and with $GaCl_3$ are reported. This chapter describes our exploration of the synthesis and characterizations of a novel bismuth-nitrogen cubane cluster, $[Bi_4(NSnMe_3)_4Cl_6]^{2-}$, and the subsequent reaction of the cluster with $GaCl_3$ to generate the neutral cubane, $[Bi_4N_4(GaCl_3)_4]$ by an unforeseen exchange process.

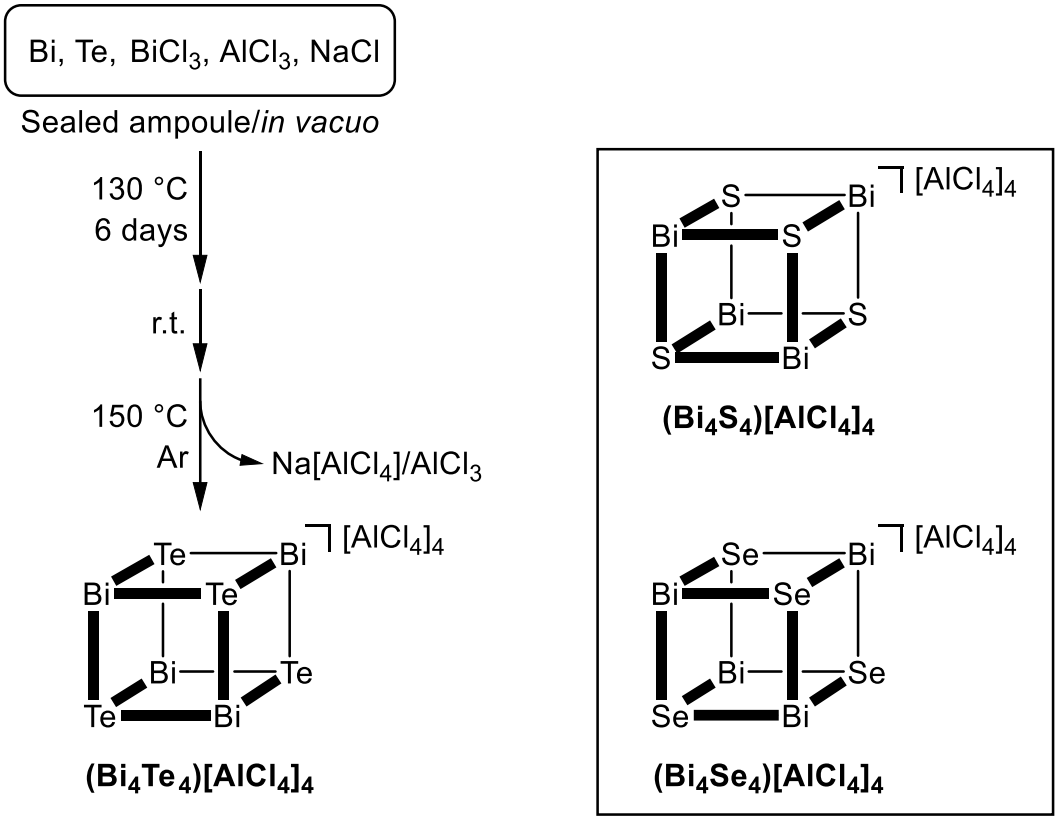

Scheme 2.1. Scheme for syntheses of uncapped cubane $(Bi_4Te_4)[AlCl_4]_4$ (left). Series of analogous bismuth-chalcogenide uncapped cubanes: $(Bi_4Q_4)[AlCl_4]_4$ (Q = S, Se) (right).

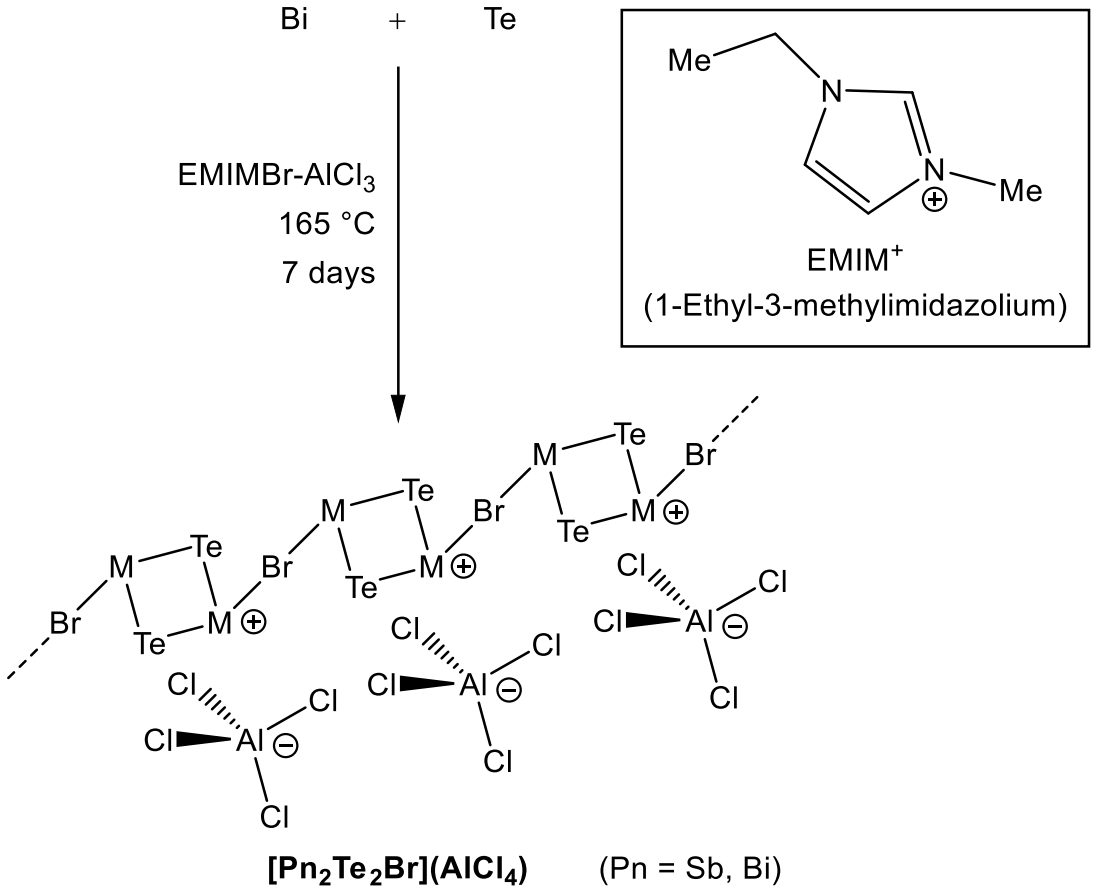

Scheme 2.2. Example of extended dimeric Pn_2Te_2 (Pn = Sb, Bi) cationic squares bridged via bromide ions. Only a segment of an extended layered structure is shown.

Experimental Section

Preparation of Compounds

Anhydrous tetrahydrofuran (THF), diethyl ether (Et_2O), hexane, dichloromethane, and toluene were purchased from EMD Drysolve. Acetonitrile (MeCN) was purchased from Burdick and Jackson. These solvents were stored over dried 4 Å molecular sieves for at least 18 hours before the use and were left in a nitrogen atmosphere. The sample preparation was conducted using a nitrogen gas filled dry-box and Schlenk techniques. The solid $(Me_3Sn)_3N$ was synthesized according to literature procedure and was stored in a −20 °C freezer.[27] The synthesis of $(Pr^n_4N)_3[Bi_2Cl_9]$ is described in Appendix.

$(Pr^n_4N)_2[Bi_4(NSnMe_3)_4Cl_6]$, $(Pr^n_4N)_2$1. A solution of $(Pr^n_4N)_3[Bi_2Cl_9]$ (0.62 g, 0.52 mmol) in 6 mL of MeCN was added dropwise to a solution of $(Me_3Sn)_3N$ (0.53 g, 1.0 mmol) in 6 mL of MeCN under magnetic stirring. The reaction mixture was stirred for 1 min, and then left undisturbed for 18 h. A suspension of a bright orange solution and orange precipitate was filtered through a nylon filter paper on a Hirsch funnel by vacuum filtration. The orange filtrate was recrystallized in a vapor diffusion setup with Et_2O diffusing into the solution, which afforded orange cubic shaped crystals along with orange powder (polymeric product (**2**); see Results and Discussion) after 3 days. The supernatant was decanted, and the powder was isolated mechanically by a pipet with successive aliquots of THF (5 x 10 mL) which helped disperse the

powder. The remaining crystals were crushed on a mortar-and-pestle to afford a fine yellow powder. The powder was washed with successive aliquots of THF (3 x 10 mL) and Et_2O (3 x 10 mL) onto a nylon filter paper on a Hirsch funnel by vacuum filtration. The solid was dried *in vacuo* overnight to afford 0.15 g (13 %) of fine powder. Analysis calcd for $C_{36}H_{92}Bi_4Cl_6N_6Sn_4$: C, 20.27; H, 4.35; N, 3.94. Found: C, 19.90; H, 4.67; N, 3.86. Absorption spectrum (solid state) λ_{max}: 313, 454 (sh) nm. Absorption spectrum (MeCN) λ_{max} (ε_M): 275 (23,900), 375 (sh) (1,690) nm. ^{1}H-NMR: 0.35 ppm, s, $J(^{119}Sn, ^1H)$ 58.0 Hz, $J(^{117}Sn, ^1H)$ 56.2 Hz. ES$^-$-MS (MeCN): *m*/*z* 1724 ($[Bi_4N_4(SnMe_3)_4Cl_5]^-$).

$[Bi_4N_4(GaCl_3)_4]$ (3). A suspension of $(Pr^n{}_4N)_2$**1** (0.17 g, 0.081 mmol) in 6 mL MeCN was added dropwise into a solution of $GaCl_3$ (0.096 g, 0.55 mmol) in 3 mL MeCN under magnetic stir. The reaction mixture was stirred for 1 min, and then left undisturbed for 3 days. The resulting solution was a pale green color and had a small amount of yellow precipitate, which may have originated from the unreacted $(Pr^n{}_4N)_2$**1**. The solution was filtered through a nylon filter paper on a Hirsch funnel by vacuum filtration. The filtrate was recrystallized in a vapor diffusion setup with Et_2O. Pale green needle and block shaped crystals were found after 14 days. These crystals were ground to a fine powder on a mortar-and-pestle and were washed with successive aliquots of MeCN (2 x 1 mL) and Et_2O (3 x 5 mL). The solid was dried *in vacuo* overnight and afforded 0.062 g (46 %) of product. Analysis calcd for $C_3H_{4.5}N_{5.5}Bi_4Ga_4Cl_{12}$: C, 2.17; H, 0.27; N,

4.65; Bi, 50.4; Ga, 16.8. Found: C, 2.09; H, 0.37; N, 4.10; Bi, 45.8; Ga, 12.2. Absorption spectrum (solid state) λ_{max}: 275, 320, 410 (sh), 518 nm.

Single Crystal X-ray Diffraction Experiment

Paratone oil and nylon loops were purchased from Hampton Research. A single crystal was selected under a polarized light microscope and was mounted on a nylon loop with support of paratone oil. The data collection was performed by using a Bruker Apex II diffractometer with a CCD detector equipped with a molybdenum sealed-tube X-ray source (λ = 0.71073 Å). The data was collected at 100 K. A scan rate of 0.5 deg/frame was used. The optimal strategy for collecting X-ray diffraction data was generated by Apex 2 software. The reflections were integrated by SAINT program and scaled by SADABS program. Space groups were assigned using SHELXTL.[28] The structure was solved by ShelXS with a direct method and was refined by ShelXL with a least-squares method on Olex2 software.[29] All pertinent crystallographic data are summarized in Table 2.1. Selected bond lengths and angles are presented in Table 2.2 and 2.3.

Other Characterization Methods

The ^{1}H-NMR data collection was carried out on 400 MHz Varian VNMRS at 30 °C. The samples were sealed in J. Young valve NMR tubes with Teflon coated screw caps under a nitrogen atmosphere. Solution UV-Vis spectroscopy was collected on a Jasco V-630 spectrophotometer with a quartz cuvette with an air-tight cap. The background scan was taken with anhydrous MeCN. Diffuse reflectance spectroscopy was acquired using a Jasco V-670 UV-Vis-NIR spectrophotometer equipped with a 60 mm integrating sphere. The background scan was taken with a nylon filter. A pulverized solid sample was evenly spread on a nylon filter for the sample scan. Infrared spectra were performed using a Perkin-Elmer RX I spectrometer with an attenuated total reflectance accessory. Raman spectra were collected using a Thermo Scientific DXR Raman microscope equipped with a 532 nm laser. The samples were placed in a Raman sample tube with well-sealed cap wrapped with a Parafilm under an inert atmosphere. Powder X-ray diffraction was performed with a Malvern Panalytical X'Pert Pro diffractometer with a Cu-K_{α} X-ray radiation source. The experimentally found peaks were referenced to previous reports on HighScore software. Transmission electron microscopy (TEM) morphographs were collected on FEI Tecnai 12 Transmission Electron Microscope. Formvar coated copper grids were used to hold the specimen. Particle size analysis was determined by using ImageJ software.

Table 2.1. Crystallographic data for $(Pr^n_4N)_2[Bi_4(NSnMe_3)_4Cl_6]$, $(Pr^n_4N)_2$**1**, and $[Bi_4N_4(GaCl_3)_4]\cdot 6MeCN$ (**3**).

	$(Pr^n_4N)_2$**1**	**3**
formula	$C_{36}H_{92}Bi_4Cl_6N_4Sn_4$	$C_{12}H_{18}Bi_4Cl_{12}Ga_4N_{10}$
formula weight, g/mol	2132.54	1842.56
T, K	100	100
crystal system	Monoclinic	Orthorhombic
space group	$P2_1/c$	*Pnma*
a, Å	12.1068 (9)	19.3221(9)
b, Å	23.8434(19)	16.6810(8)
c, Å	21.3314(16)	12.4629(6)
α, deg	90	90
β, deg	96.283(3)	90
γ, deg	90	90
V, Å^3	6120.7(8)	4016.9(3)
Z	4	4
crystal color	orange	pale green
ρ_{calc}, g/cm^3	2.314	3.047
2θ range, deg	2.10 to 27.48	1.94 to 36.36
GOF (F^2)	1.098	1.011
R_1/wR_2, %	6.00/11.31	3.29/4.72
largest peak/hole (e$^-$/Å^3)	5.975/−4.681	1.79/−1.78

Results and Discussion

Synthesis of (1)

The reaction is carried out in a 1:2 stoichiometric ratio of concentrated solutions of $(Pr^n_4N)_3[Bi_2Cl_9]$ and $(Me_3Sn)_3N$ in MeCN, which affords one equivalent of $[Bi_4(NSnMe_3)_4Cl_6]^{2-}$ (**1**) (Scheme 2.3). Immediately upon addition of $(Pr^n_4N)_3[Bi_2Cl_9]$ into $(Me_3Sn)_3N$ solution changes from colorless to bright yellow and further addition produces a bright orange solution with a fine yellow precipitate. The fine yellow powder is presumably a polymeric species and the cause of the low yield. A vapor diffusion of Et_2O into the orange filtrate affords orange cubic crystals of $(Pr^n_4N)_2$**1**.

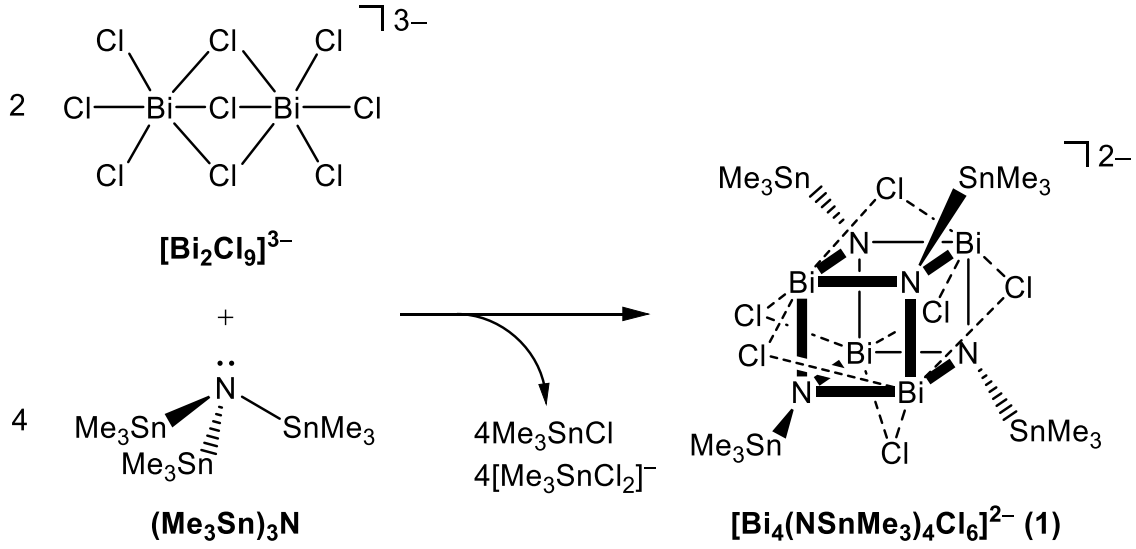

Scheme 2.3. Synthesis of $[Bi_4(NSnMe_3)_4Cl_6]^{2-}$ (**1**) in acetonitrile followed by elimination of trimethylstannyl monochloride and dichloride byproducts.

Synthesis of polymeric product (2)

The synthesis of polymer **2** is documented in a preparation of compound **1** (See Chapter 2: Synthesis of (**1**)). Briefly, a yellow precipitate is isolated from a solution of **1** by filtration through a nylon filter. The residue is washed with successive THF (3 x 5 mL) and Et_2O (3 x 5 mL). The solid is dried *in vacuo* overnight. Elemental analysis: C, 19.90; H, 4.67; N, 3.86; Bi, 66.48; Cl, 6.85; Sn, 11.43.

Properties of (1)

The ^{1}H-NMR spectrum of $(Pr^n_4N)_2$**1** in MeCN-d_3 revealed a characteristic peak at 0.35 ppm which corresponds to the Me_3Sn- groups (Figure 2.1). There are satellite peaks associated with this peak which comes from geminal tin-proton coupled peaks: $J_{^1H\text{-}^{117}Sn}$ = 56.2 Hz and $J_{^1H\text{-}^{119}Sn}$ = 58.0 Hz. Other peaks found at δ 0.95 ppm, δ 1.66 ppm, and δ 3.06 ppm are from the cations. A small peak at 0.62 ppm is attributed to $[Me_3SnCl_2]^{1-}$ which matches with a previous report.[23] The presence of $[Me_3SnCl_2]^{1-}$ may be due to the impurity or it could imply the equilibrium process in the solution state where dissociation of Me_3Sn- and Cl^- are responsible. Solution stability is monitored for 20-day period by ^{1}H-NMR (Figure 2.2). The spectrum remains moderately unchanged for 24 h. An increase in the integration area of $[Me_3SnCl_2]^{1-}$ coincides with an emergence of a broad peak at 0.39 ppm which implies a small degradation. After 20 days, an insoluble yellow powder is found on the bottom of the NMR tube. Upon heating a freshly prepared NMR sample at 60 °C for 2 days, a small presence of

tetramethyl tin is found at 0.06 ppm and the broad peak at 0.39 ppm is found (Figure 2.3). Insoluble yellow powder is also found on the bottom. The appearance of this broad peak is similar to the peak found in the solution stability test. This may suggest the degradation product is the same for the solution left at room temperature for 20 days, and we can conclude heat speeds up the process.

A thermolysis experiment of solid 1 was carried out to learn of the stability under solvent-free condition. A pulverized solid of **1** placed in a sealed quartz tube under vacuum was heated at 350 °C for 15 h, ramped to 400 °C, where it remained for 1 h, and then cooled to room temperature. The contents of the quartz tube were a greyish black metallic powder with silver metallic grains (0.1 x 0.1 x 0.1 mm^3). The PXRD data confirms the presence of metallic bismuth[30] and metallic tin[31] (Figure 2.4). When a pulverized solid of **1** was heated at 400 °C in air, the PXRD revealed the presence of bismuth oxychloride (Figure 2.5).[32]

Electrospray ionization mass spectrometry (ESI-MS) data collected for compound **1** in MeCN shows isotopic fragmentation patterns at 1724 *m/z* in a negative ion mode which is equivalent to the molecular ion peak for $[Bi_4(NSnMe_3)_4Cl_5]^-$, resulting from the loss of one Cl^- ion (Figure 2.6). The calculated splitting pattern overlaid perfectly to the experimental result. The finding is agreement with the solution stability found in the ^{1}H-NMR experiment.

The solution state UV-Vis spectrum of $(Pr^n_4N)_2$**1** in MeCN shows characteristic peaks at 275 nm (ε = 23,900 $cm^{-1}M^{-1}$) and 375 nm (1,690

$cm^{-1}M^{-1}$) (Figure 2.7). The latter absorption tails up to 500 nm which is responsible for an orange color of the solution. In fact, in other reported compounds containing bismuth nitrogen bonds, the color of the compounds is typically reported as yellow or orange.[26,33–35] Upon exposure to air, the peak centered at 375 nm gradually decays over 24 h (Figure 2.8) The change from yellow to colorless is quite noticeable. The solid state UV-Vis spectrum reveals a maximum absorbance at 313 nm and a shoulder at 454 nm (Figure 2.9) which tails to 700 nm and is responsible for an orange color of the solid. This peak disappears after the solid is exposed to air for 24 h. The color changed to faint green which is attributed to the peak in the UV region tailing to the visible spectrum (Figure 2.10).

The infrared spectrum from 3800 – 550 cm^{-1} exhibits vibrational signals which are dominated by the $(Pr^{n}{}_4N)^+$ cation (Figure 2.11). The key structural vibrational signals such as Bi-N, Bi-Cl, Sn-N, and Sn-C are expected to be below those wavenumbers due to the molecule containing heavy atoms. Raman spectra were collected; however, peak assignments below 200 cm^{-1} are not straightforward because the lattice modes can overwhelm the molecular peaks as described in the literature.[36–39] The Raman spectrum reveals several peaks which originate from Me_3Sn- moieties (Figure 2.12). The Me_3Sn peaks found at 1182, 527, 510 cm^{-1} are assigned to a symmetric bending mode of C−H, asymmetric-, and symmetric stretch modes of $Sn-C_3$, respectively. A sharp resonance found at 175 cm^{-1} may possibly due to Bi−Cl stretch, but a lack of data for similar known compounds complicates the analysis. Sample

scans on closely related compounds such as $BiCl_3$, $(Pr^n_4N)Cl$, and $(Me_3Sn)_3N$, were collected to aid in deducing spectroscopic features of $(Pr^n_4N)_2$**1**. Major peaks from each scan are assigned based on the literature reports on $BiCl_3$,[36] trimethyltin azide (Me_3SnN_3),[37,38] and a complex carrying Pr^n_4N cations;[39] however, the only peaks we could definitively assign were associated with the Me_3Sn moieties.

Binary bismuth-nitrogen complexes are known to be shock-sensitive;[40] however, the ternary complexes are believed to be stable.[3] Upon physical impact by a glass rod on the solid under a nitrogen atmosphere, the compound remained unchanged and thus formation of metallic bismuth, Me_3SnCl, or $[Me_3SnCl_2]^{1-}$ was not observed.

Properties of polymeric product (2)

The Raman spectrum of polymer **2** is collected and is compared to $(Pr^n_4N)_2$**1**. Our belief is that $(Pr^n_4N)_2$**1** is produced from a thermodynamic process, and the polymer **2** is a kinetic product; thus, the polymer may exhibit similar structural motifs as the cubane **1**. The vibrational signals from polymer **2** are almost identical to $(Pr^n_4N)_2$**1** (Figure 2.13). Solubility was tested with common solvents such as MeCN, THF, hexane, dichloromethane, ethyl ether, and toluene, but none of these solves can solubilize **2**.

Structure of (1)

The crystal of $(Pr^{n}_{4}N)_2$**1** is found in a monoclinic space group $P2_1/c$ with one formula in an asymmetric unit. The cubane structure consists of Bi_4N_4 core where each nitrogen atom is terminated by a Me_3Sn group (Figure 2.14). Each Sn site adopts a tetrahedral geometry. All six faces of the cubane are capped by chlorine atoms bridging adjacent bismuth atoms. The structure viewing along tin-, nitrogen-, and bismuth atoms at the corner of the cube displays a pseudo three-fold rotational symmetry (Figure 2.15). The Bi_4N_4 core is distorted because of the size difference between the Bi and N atoms: Bi–N–Bi = 99.4(8)°; N–Bi–N = 79.8(6)°. The average interatomic distance of Bi···Bi diagonally measured across each face of the cube is 3.409(15) Å. The previous reports in the literature shows the bond lengths of Bi–Bi are found in a range between 2.9 – 3.1 Å. The bond distances found in organobismuth compounds, Bi_2Ph_4[41] and Bi_2Mes_4 (Mes = mesityl),[42] are 2.990(2) Å and 3.087(3) Å. Homoatomic bismuth clusters, $[K([2.2.2]crypt)]_2(Bi_4)$[43] and $[K(2.2.2)crypt)]_3(Bi_{11})$ (crypt = cryptand)[44], are found in the distances of 2.950(7) and 2.98(4) Å. It is coherent that there is no direct Bi–Bi bond in the Bi_4N_4 cube, given that it is longer by 0.3 Å.

The core structure of **1** is comparable to a closely related structure bearing a Bi_4N_4 core, $[pyOBi(\mu_3\text{-}NCy)]_4$ (Cy = cyclohexyl, py = 2-pyridyl).[26] The core of the cube displays expected distortions on Bi–N–Bi and N–Bi–N angles with 100.3(34)° and 78.6(30)°, respectively. The average Bi–N bond length of **1** is 2.235(17) Å which does not significantly differ from 2.31(12) observed in

[pyOBi(μ_3-NCy)]$_4$; yet, the ranges are wider in the latter by comparing the standard deviation. The reason relates to the capping of 2-pyridinolate groups on bismuth atoms, and the two of which cap by forming a bridge between bismuth atoms. The last one coordinates on one bismuth site. The lack of equivalency on terminal atoms leads to deviations in the molecular geometries. The Sn-N and Sn-C bond lengths in 1 are 2.099(10) Å and 2.137(8) Å which only slightly changed from those found in the parent molecule $(Me_3Sn)_3N$ (2.04(3) Å and 2.18(8) Å).[45]

While each face is capped by bridging chlorides, each chloride is asymmetrically bonded to bismuth atoms, so these bonds can be divided into two categories: $Bi–Cl_{short}$ (3.05(4) Å); $Bi–Cl_{long}$ (3.23(9) Å). These types of asymmetric bridges are commonly found in bismuth chloride complexes. The two compounds, $(4\text{-MePyH})_4[Bi_2Cl_{10}]$ (Py = pyridine)[46] and $(NH_3(CH_2)_2NH_3)_2[Bi_2Cl_{10}]\cdot 4H_2O$,[47] possess $Bi–Cl_{long}$/$Bi–Cl_{short}$ pair in the distances of 2.9674(5)/2.8310(5) Å and 2.957(1)/2.872(2) Å. The $Bi–Cl_{long}$ in **1** is fairly long compared to $Bi–Cl_{terminal}$ bond lengths found in the literature ($Bi–Cl_{mean}$: 2.70(3) Å in $((Me_3)_2NH_2)[BiCl_6]Cl$;[48] 2.73(15) Å in $(Et_2H_2N)_3[BiCl_6]$);[49] however, the long interactions are typically observed in bismuth-chloride complexes containing bridging chlorides. A variety of Bi–(μ-Cl) linkages found in $((C_2H_5)_4N)_6[Bi_8Cl_{30}]$ shows the range of bridging between 2.544(9) – 3.207(8) Å.[50] This longest interatomic distance 3.207(8) Å only differs by 0.02 Å compared to $Bi–Cl_{long}$ found in **1**.

Investigation on $(Me_3Si)_3N$ as an alternative source of nitrogen

To demonstrate whether reactivity will follow a periodic trend in forming bismuth-nitrogen bonds, $(Me_3Si)_3N$ was tested for the reaction on $[Bi_2Cl_9]^{3-}$. Pure $(Me_3Si)_3N$ in CD_3CN has the silyl-coupled methyl-peak at 0.20 ppm for ^{1}H-NMR ($J_{^1H-^{29}Si}$ = 118.2 Hz) (Figure 2.16). Once the solution is mixed with $[Bi_2Cl_9]^{3-}$ for 2 days, the peak is unshifted. The peak of Me_3SiCl would be found at 0.44 ppm if dehalosilylation takes place.[51] This result is agreement with the energetic factor of Si–N and Sn–N discussed in Ch.2 introduction, given that the bond dissociation energy of Si–N is far greater than Sn–N.

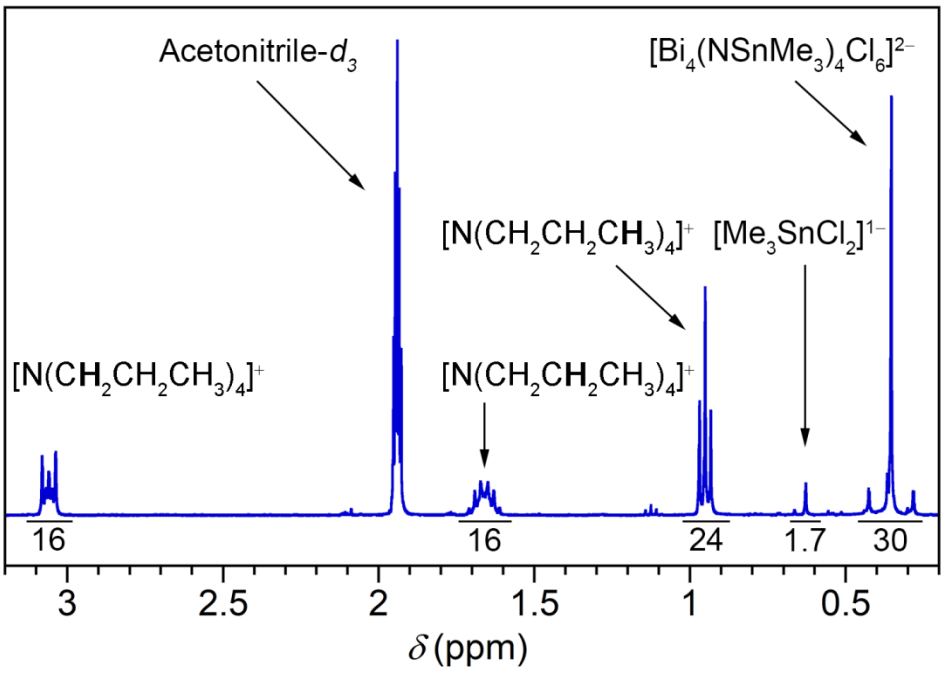

Figure 2.1. ^{1}H-NMR spectrum of $(Pr^n_4N)_2$**1** in CD_3CN. Immediately after the solution was prepared.

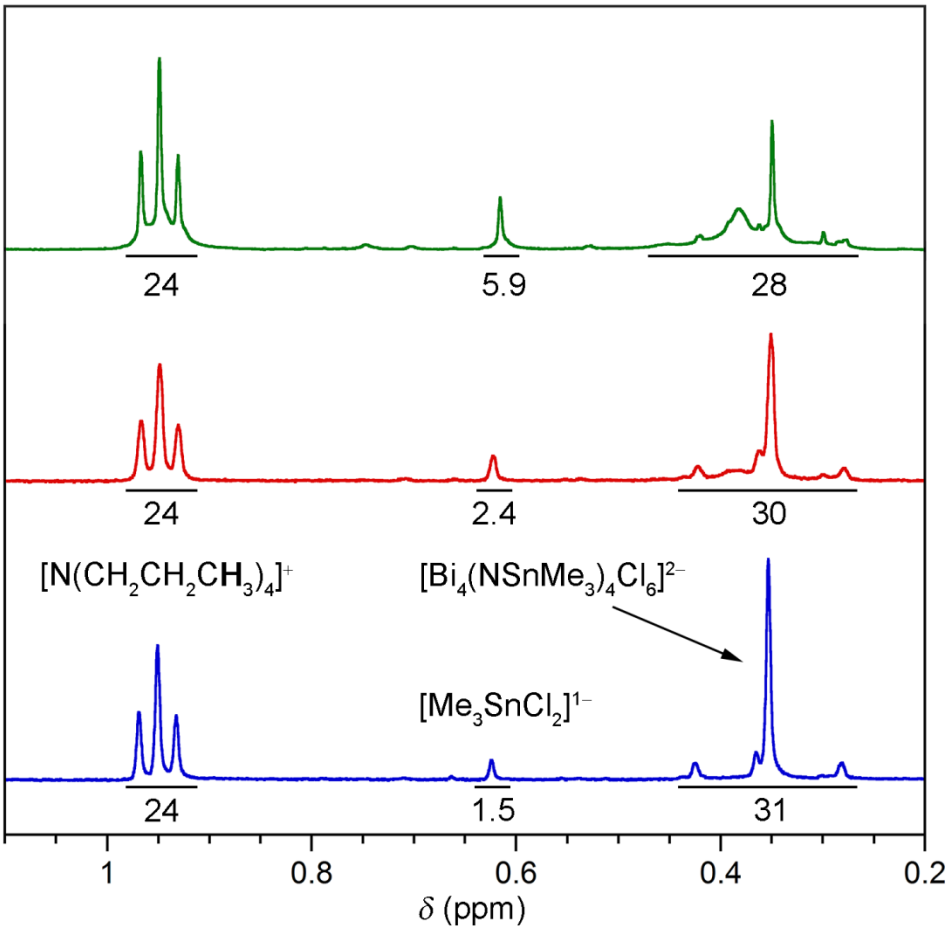

Figure 2.2. ^{1}H-NMR spectrum of $(Pr^{n}{}_{4}N)_{2}$**1** in $CD_{3}CN$. Solution stability monitored for 20 days. As-prepared (blue). 1 day (red). 20 days (green).

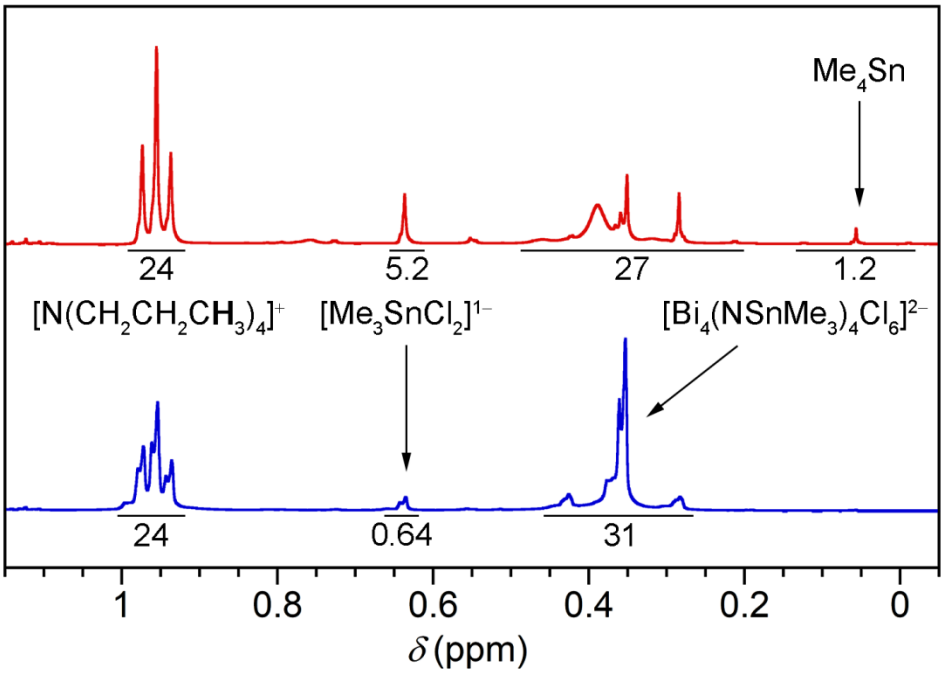

Figure 2.3. ^{1}H-NMR spectrum of $(Pr^{n}{}_{4}N)_{2}$**1** in $CD_{3}CN$. As-prepared (blue). Heated at 60 °C for 2 days (red).

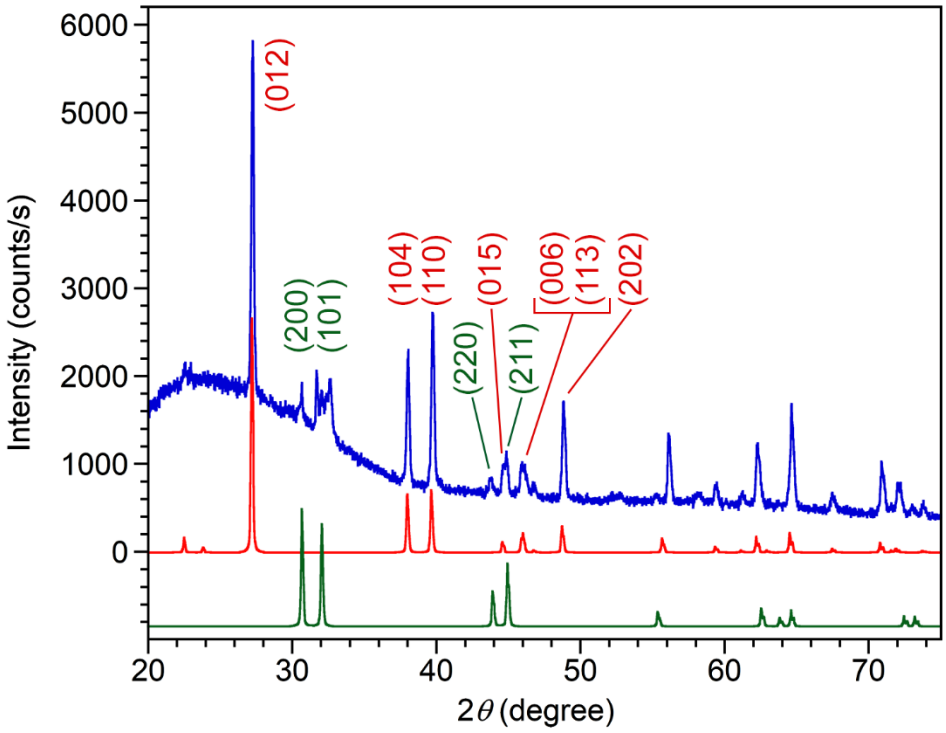

Figure 2.4. Powder X-ray diffraction data of $(Pr^{n}{}_{4}N)_{2}$**1** pyrolyzed in a vacuum-sealed glass tube (blue). Reference: metallic bismuth (red); metallic tin (green).

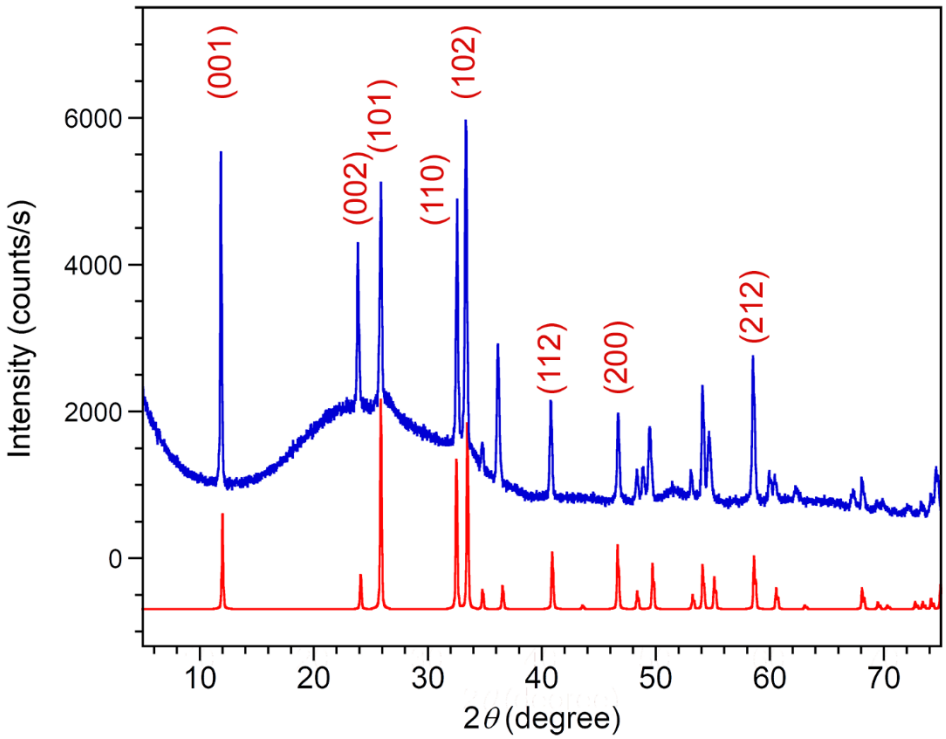

Figure 2.5. Powder X-ray diffraction data of $(Pr^{n}{}_{4}N)_{2}$**1** pyrolyzed under aerobic conditions (blue). Reference: bismuth oxychloride (red).

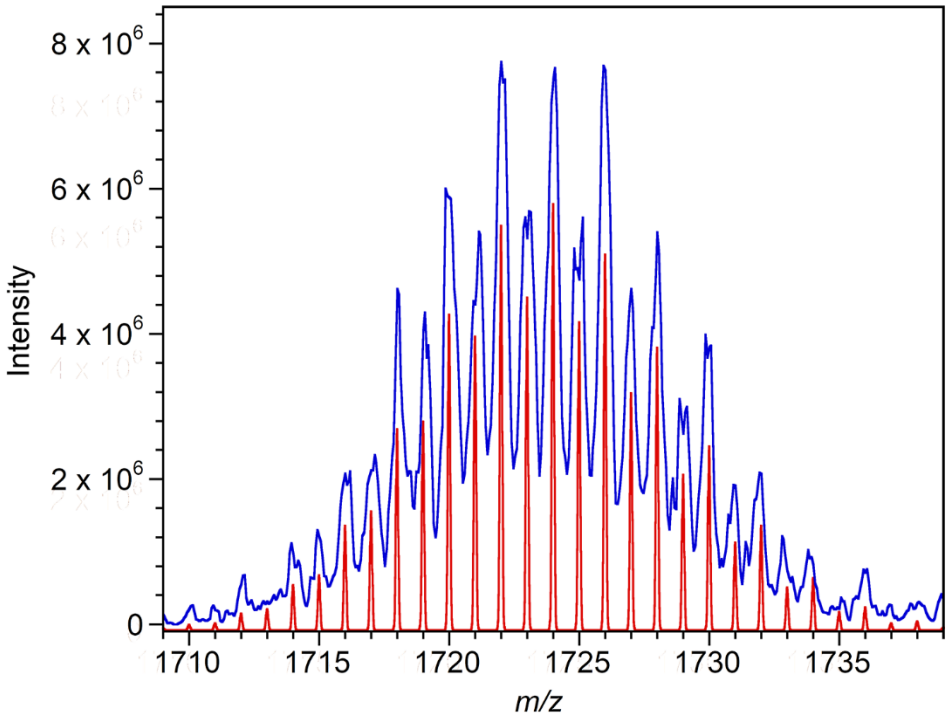

Figure 2.6. Isotopic fragmentation patters for $[Bi_4(NSnMe_3)_4Cl_5]^-$ in the ESI-MS of $(Pr^n{}_4N)_2$**1** in MeCN. Experimental data (blue). Calculated (red).

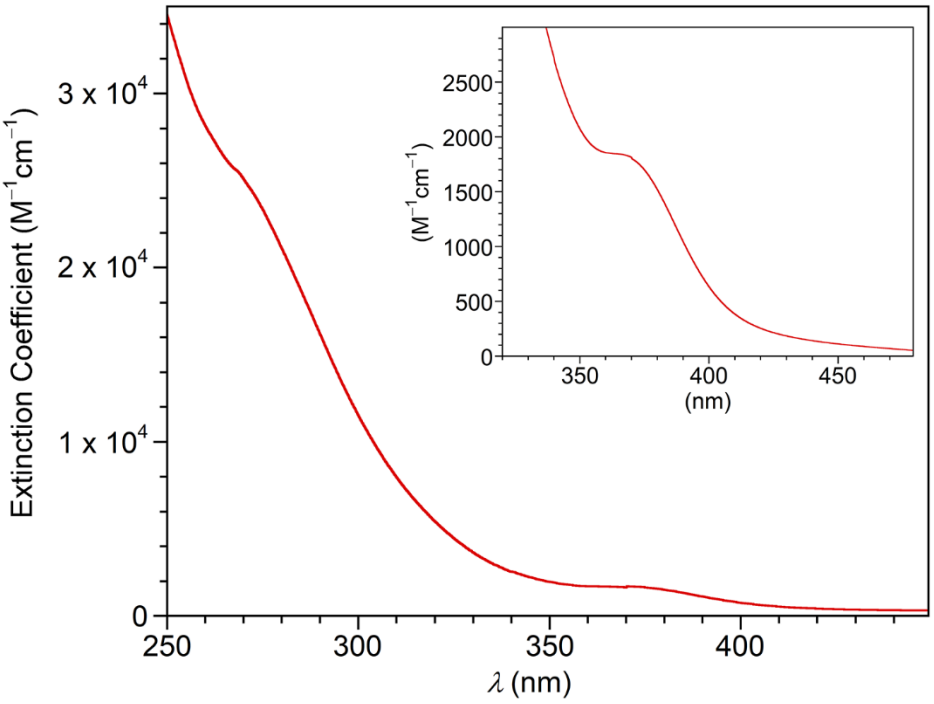

Figure 2.7. Solution state UV-Vis spectrum of $(Pr^{n}{}_4N)_2$**1** in MeCN.

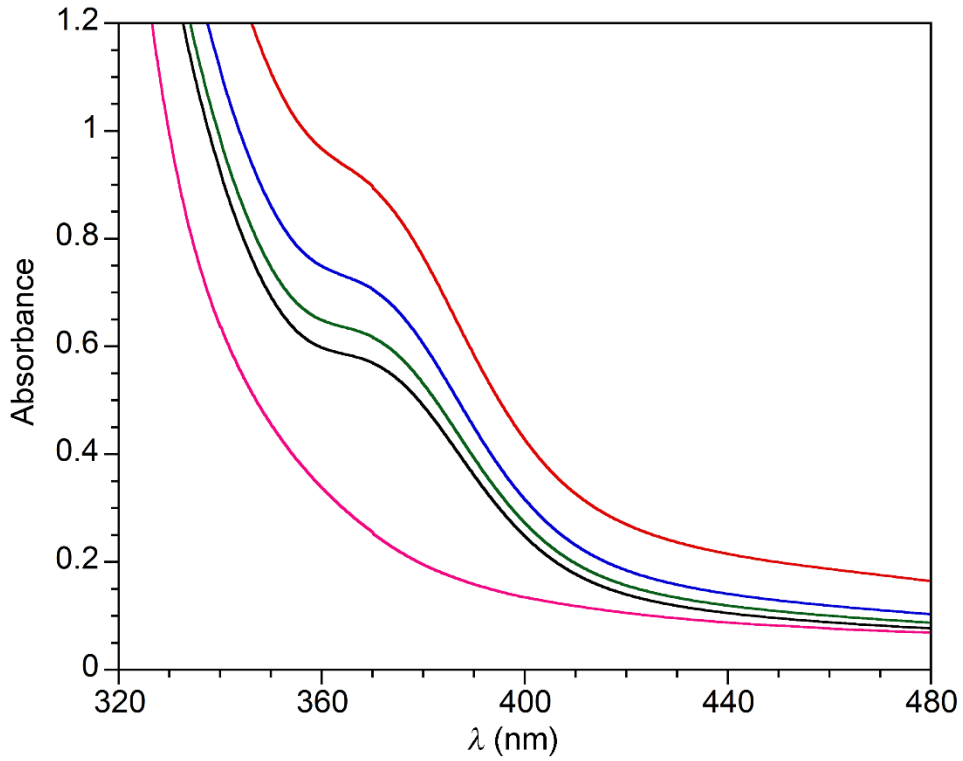

Figure 2.8. Solution state UV-Vis spectra of $(Pr^{n}{}_{4}N)_{2}$**1** in MeCN: before exposure to air (red) and after exposure to air for 5 min (blue), 10 min (green), 15 min (black), and 24 h (pink).

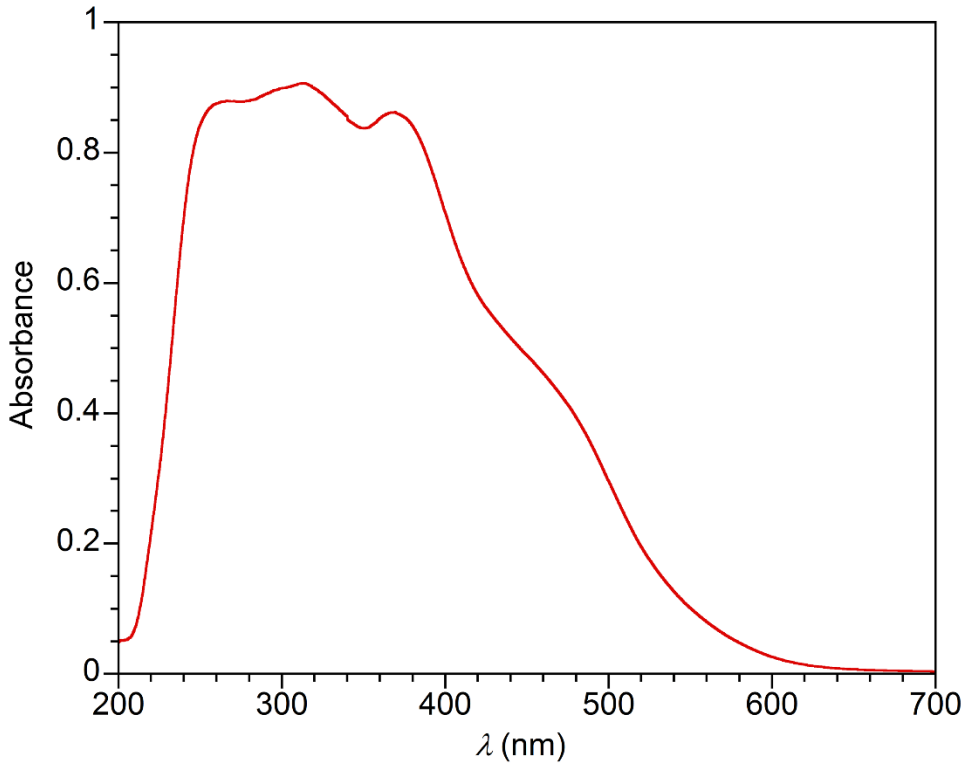

Figure 2.9. Diffuse reflectance UV-Vis spectrum of $(Pr^{n}{}_{4}N)_{2}$**1** before exposure to air.

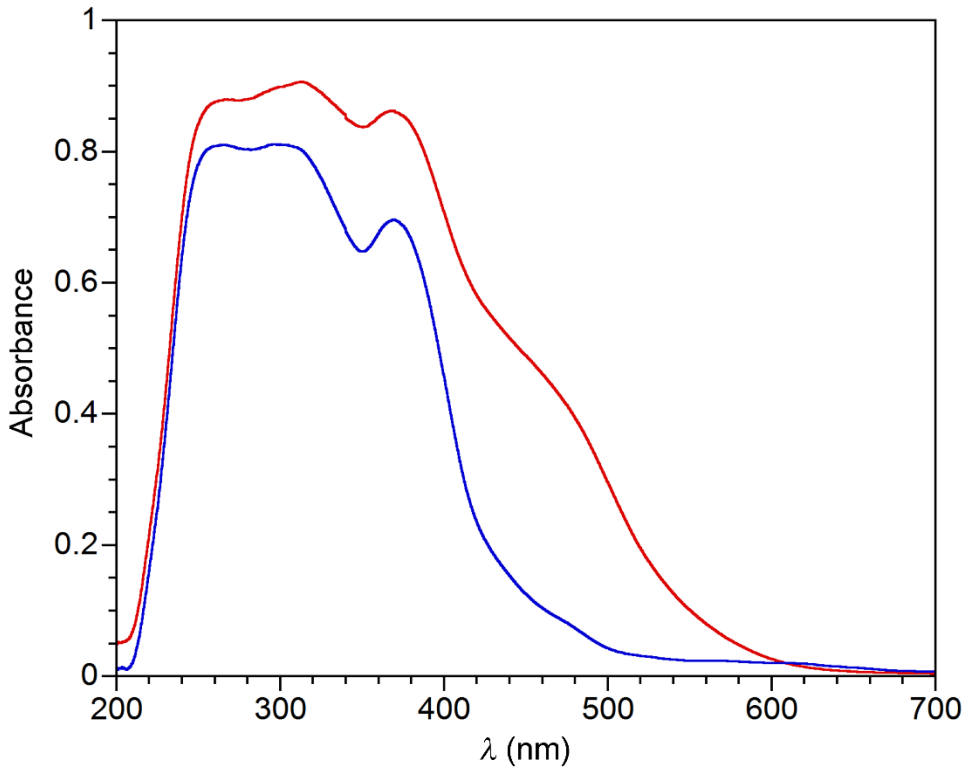

Figure 2.10. Diffuse reflectance UV-Vis spectra of $(Pr^{n}{}_{4}N)_{2}$**1**: before exposure to air (red) and after exposure to air for 24 h (blue).

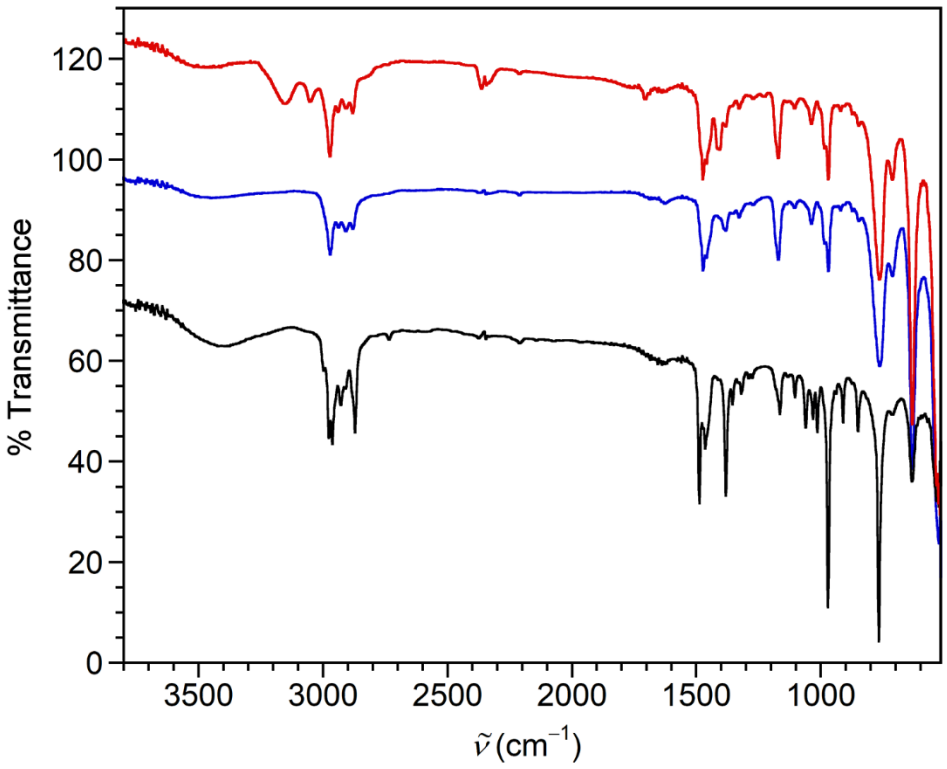

Figure 2.11. Infrared transmission spectra of ($Pr^n_4N)_2$**1**: immediately after post-exposure to air (red) and after exposure to air for 3 days (blue). The IR spectrum for tetrapropylammonium chloride is shown for reference (black). The spectra are offset for clarity.

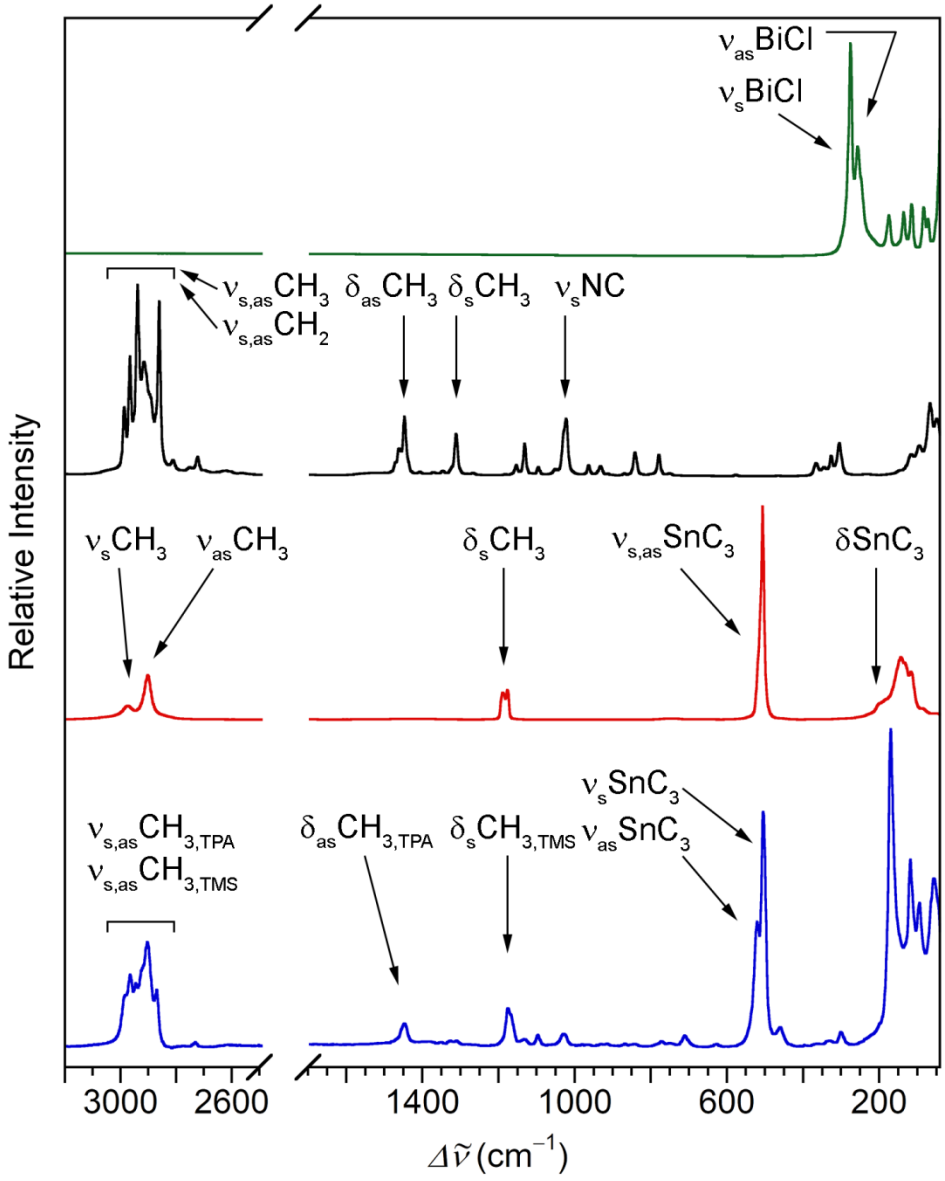

Figure 2.12. Raman spectra of $(Pr^n_4N)_2$**1** (blue), $(Me_3Sn)_3N$ (red), $(Pr^n_4N)Cl$ (black), and $BiCl_3$ (green). (TPA = tetrapropylammonium chloride; TMS = trimethylstannyl).

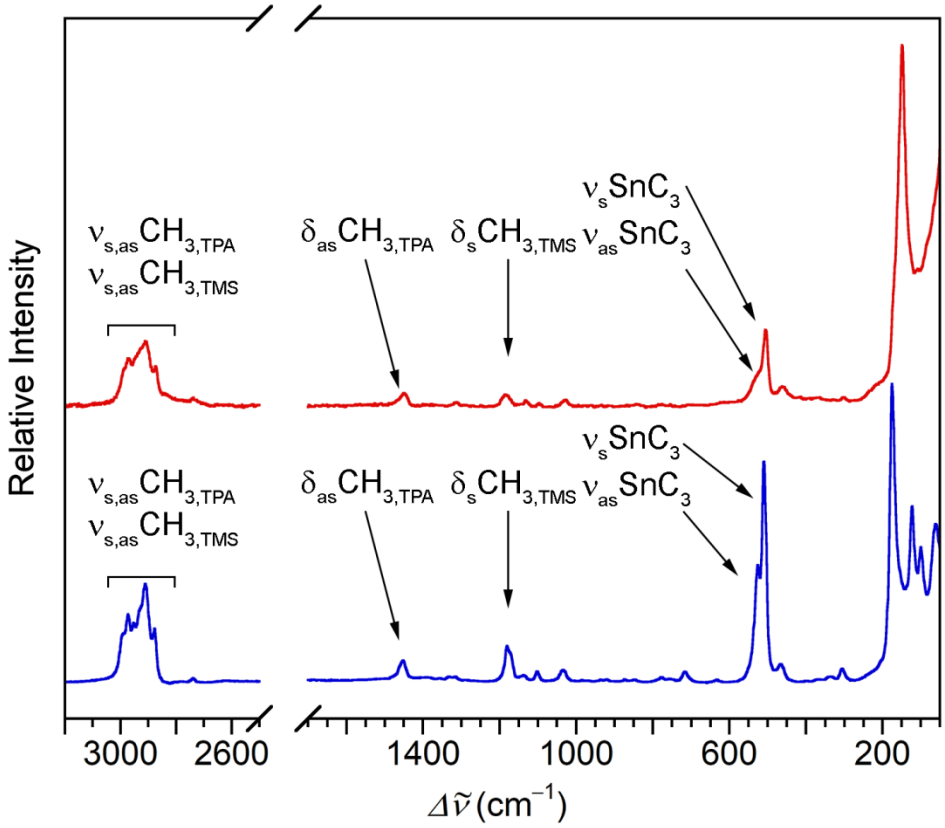

Figure 2.13. Raman spectra of $(Pr^{n}{}_{4}N)_{2}$**1** (blue) and a polymeric product **2** (red). (TPA = tetrapropylammonium chloride; TMS = trimethylstannyl).

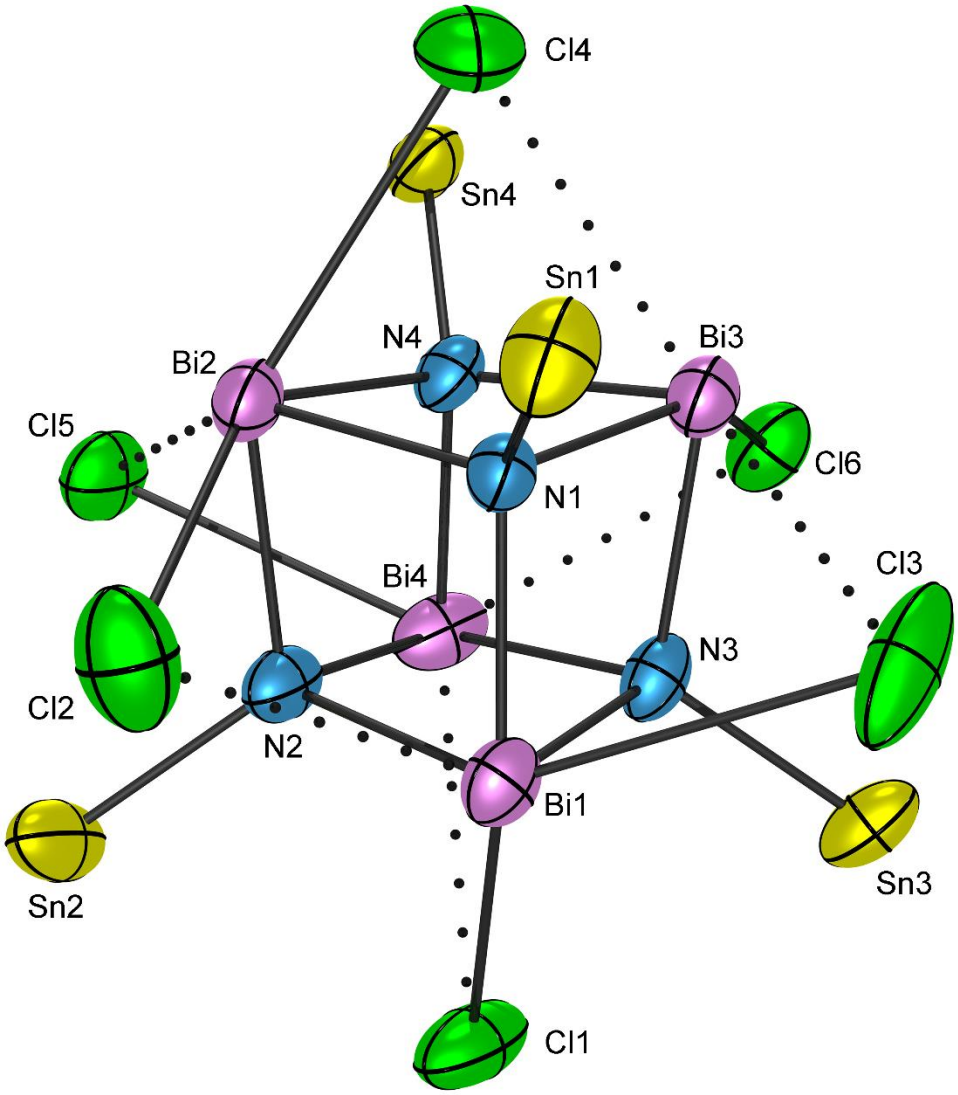

Figure 2.14. The X-ray crystal structure of $(Pr^{n}{}_{4}N)_{2}$**1**. The thermal ellipsoids are plotted at 50% probability level. The cations and methyl groups are omitted for clarity. The long-distance Bi–Cl interactions are drawn as dotted lines.

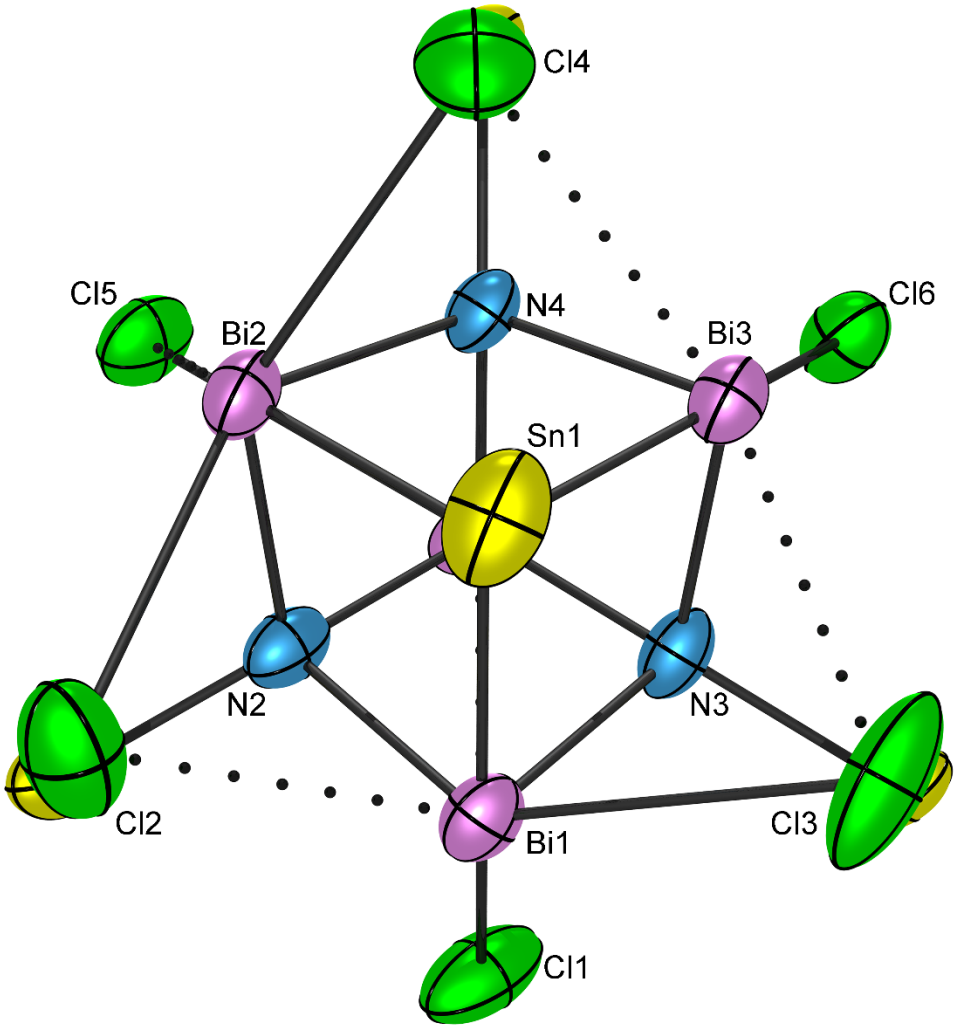

Figure 2.15. The X-ray crystal structure of $(Pr^{n}{}_{4}N)_{2}$**1** viewing diagonally going through Sn1, N1, and Bi4. A pseudo 3-fold symmetry of cubane is represented. The thermal ellipsoids are plotted at 50% probability level. The cations and methyl groups are omitted for clarity. The long-distance Bi-Cl interactions are drawn as dotted lines.

Table 2.2. Selected mean bond lengths (Å) and angles (°) for $(Pr^{n}_{4}N)_{2}$**1**.

Bi–N	2.235(17)	Bi–N–Bi	99.4(8)
Bi···Bi	3.409(15)	N–Bi–N	79.8(6)
N–N	2.867(16)	Bi–Cl–Bi	65.7(7)
$Bi–Cl_{short}$	3.047(35)	Bi–N–Sn	118(1)
$Bi–Cl_{long}$	3.233(89)	N–Sn–C	109(2)
Sn–N	2.099(10)	C–Sn–C	110(3)
Sn–C	2.137(8)		
$Cl···C_{Me_3Sn}$	3.609(64)		

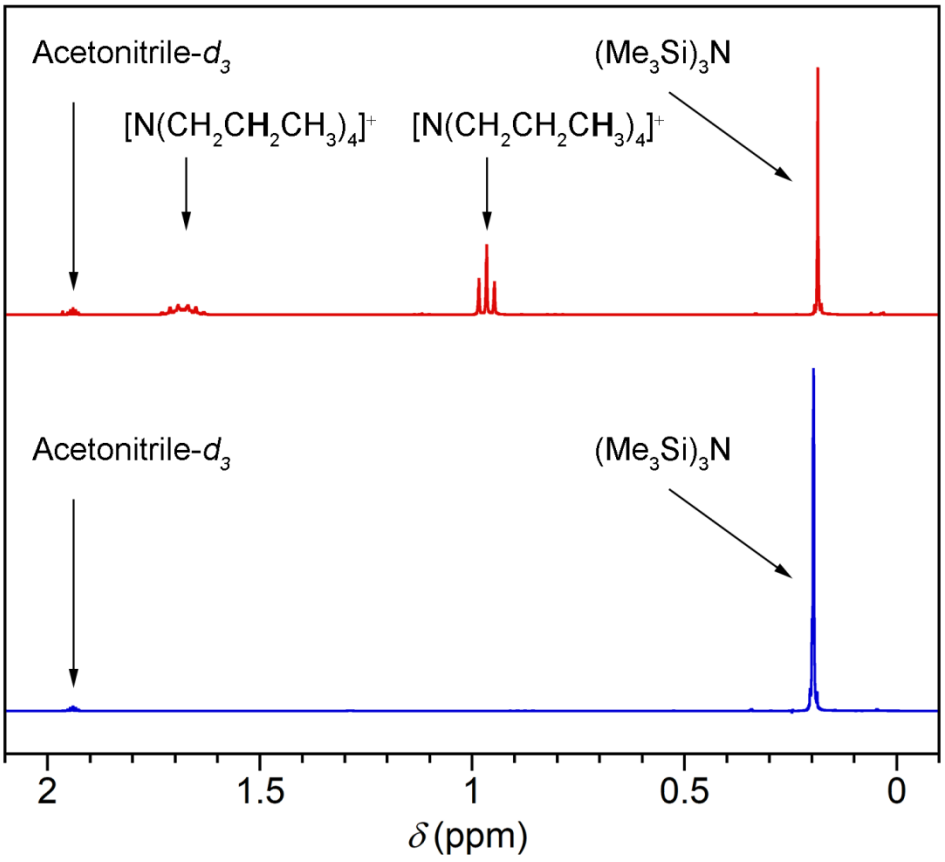

Figure 2.16. ^{1}H-NMR spectra of $(Me_3Si)_3N$ in CD_3CN. A spectrum of pure $(Me_3Si)_3N$ (blue) and 2 days after $(Pr_4N)_3[Bi_2Cl_9]$ is added (red).

Synthesis of (3)

Addition of a MeCN solution of $(Pr^n_4N)_2$**1** into a MeCN solution of $GaCl_3$ in a 1:6 ratio results in fading of the bright orange color of $(Pr^n_4N)_2$**1** to pale yellow (Scheme 2.4). Leaving this reaction mixture undisturbed for 72 h results in a solution that is pale green. Only a trace amount of undissolved solid (yellow) was found. The product solution was filtered by a vacuum filtration through a nylon filter. Vapor diffusion of Et_2O into the pale green filtrate affords pale green needle crystals after 14 days. The NMR scale reaction shows the elimination of Me_3SnCl which evolves at 0.66 ppm ($J_{^1H\text{-}^{117/119}Sn}$ = 64.0/66.6 Hz) in 3 days, so the product solution contains Me_3SnCl byproduct (Figure 2.17).[23] Given that all the six bridging chlorides are abstracted from complex **1**, $GaCl_3$ serves as a dual functionality: abstraction of chlorides and capping on nitrogen sties through adduct formation. The pale green color is nearly indistinguishable with colorless Me_3SnCl crystals, so the recrystallized product should be washed with MeCN which readily dissolves the byproduct. The compound **3** is mildly soluble in MeCN so the washing should be performed with a minimum volume.

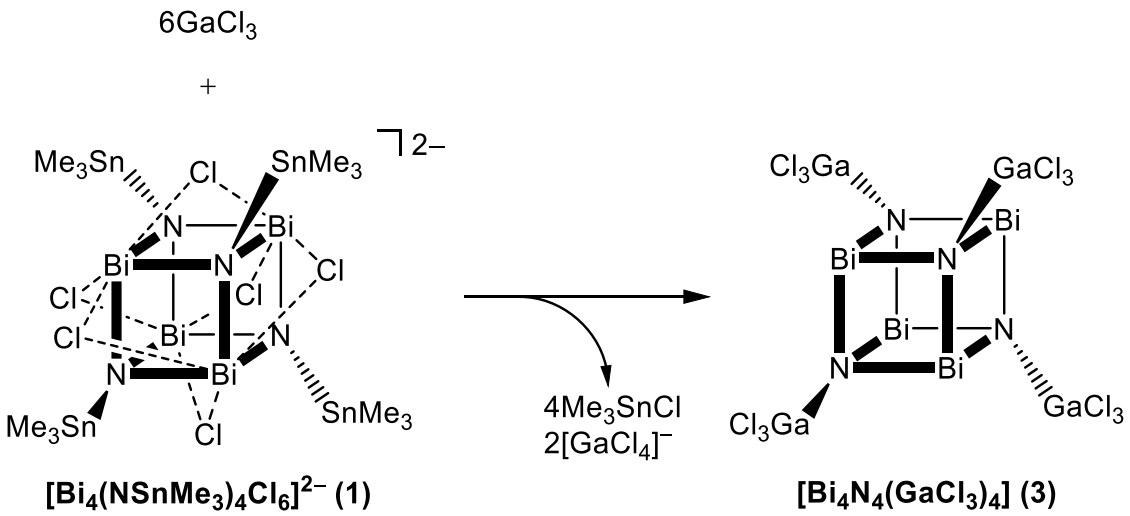

Scheme 2.4. Synthesis of $[Bi_4N_4(GaCl_3)_4]$ (**3**) in acetonitrile followed by elimination of trimethylstannyl monochloride and gallium tetrachloride ion.

Properties of (3)

The MeCN molecules are observed in ^{1}H-NMR spectrum at 1.97 ppm which is slightly shifted from the residual peak of CD_3CN at 1.94 ppm (Figure 2.18).[52] This is the only peak that is observed which confirms there are no byproducts associated with trimethyltin chlorides. The infrared spectrum also sees an indicative peak of MeCN at 2267 cm^{-1} (C≡N stretch) in the scan recorded in a nujol moll immediately after the exposure to air (Figure 2.19). The key features of the compound such as Bi–N, Ga–N, and Ga–Cl signals are not present within the spectral range. Once the solid is exposed to an atmosphere, new peaks appear at 3176 and 3050 cm^{-1} which are assigned to the O–H stretching modes of gallium oxyhydroxide (GaOOH) found in previous report.[53] The formation of the decomposition product which implies that $GaCl_3$ in the

structure is susceptible to hydration. The O–H signals from water are due to hygroscopic nature of the compound.

The solution UV-Vis spectrum of **3** in MeCN shows a characteristic peak at 367 nm, and the tail extends up to 450 nm (Figure 2.20). Exposure of the solution to air leads to the disappearance of the peak along with the color change to colorless, and peaks at 273 (sh) and 300 nm are found (Figure 2.21). A white precipitate deposits on the bottom of the cuvette which appears to be GaOOH based on the FTIR spectra. The diffuse reflectance UV-Vis-NIR spectrum features characteristic peak at 275, 320, 410 (sh), and 518 nm (Figure 2.22). The major contribution of absorption in the visible region is up to 475 nm such that the solid give a green color similarly to the solution UV-Vis data. The peaks located at 410 and 518 nm vanish upon exposure to air to afford a white product (Figure 2.23). The peaks between 1400 – 1700 cm^{-1} in the near-IR region are assigned to water.[54]

As a comparison to thermolysis experiment performed using solid **1**, a pulverized solid of **3** placed in a sealed quartz tube under vacuum and heated at 350 °C for 72 h. The contents of the quartz tube are transformed into a black powder. PXRD data confirms the presence of metallic bismuth (Figure 2.24).[30]

Structure of (3)

The neutral complex **3** crystallizes in the orthorhombic space group *Pnma* with a half of one formula unit in the asymmetric unit reflected by a mirror plane (Figure 2.25). The Ga atomic sites adopt tetrahedral geometries. The structure possesses a three-fold rotational symmetry viewing diagonally through Ga, N, and Bi atoms with respect to the corner of the cube (Figure 2.26). Six MeCN solvent molecules are found coordinated towards bismuth atoms in the crystal structure. The bond distances and angles in **3** are Bi–N 2.237(9) Å, Bi···Bi 3.414(6) Å, Bi–N–Bi 99.5(3)°, and N–Bi–N 79.6(3)°. These perfectly coincide with $(Pr^{n}{}_4N)_2$**1**: Bi–N 2.235(17) Å; Bi···Bi 3.409(15) Å; Bi–N–Bi 99.4(8)°; N–Bi–N 79.8(6)°. These nearly unchanged geometrical parameters are the evidence of rigidity of the cubane core structure. Only a minor deviation is observed for **3** with respect to the Bi_4N_4 core, so the comparison to the previous reports is analogues to the discussion presented for $(Pr^{n}{}_4N)_2$**1** (See Chapter 2 Structure of (**1**)).

The $GaCl_3$ capping each nitrogen site can be perceived as an adduct since the dehalostannylation leaves the lone-pair electrons on the nitrogen atoms. Thus, the Lewis acid and base reaction between $GaCl_3$ and $(Me_3Sn)_3N$ results in an adduct complex, $[Cl_3Ga{\cdot}N(SnMe_3)_3]$, which possesses the interatomic distances of Ga–N and Ga–Cl that are 1.950(8) Å and 2.18(1).[55] These bond lengths are comparable to those found in **3**: Ga–N 1.913(7) Å; Ga–Cl 2.183(8) Å.

The coordination of MeCN solvent molecules shows the mean $Bi\cdots N_{MeCN}$ distances of 2.97 (17) Å. The $Bi\cdots N_{MeCN}$ distances are far beyond the covalent bond of these two elements: $\Sigma r_{cov.}$ Bi–N 2.19 Å (Bi: 1.48(4) Å; N: 0.71(1) Å).[56] This coordination should be considered as weak interaction. The six MeCN molecules coordination to Bi atoms found in bismuth-oxide cluster, $[Bi_6O_4(OH)_4(OTf)_6(CH_3CN)_6]$ (OTf = triflate), have the range 2.63 – 2.90 Å with mean 2.78(9) Å.[57] In bismuth-crown ether cationic complexes, $[BiCl_2(15\text{-crown-}5)(CH_3CN)]^+$ and $[BiCl(18\text{-crown-}6)(CH_3CN)_2]^{2+}$, are found with MeCN coordination.[58] The former $Bi\cdots N_{MeCN}$ is found in the distance of 2.65(3) Å and the latter with 2.82(2) Å and 2.86(3) Å.

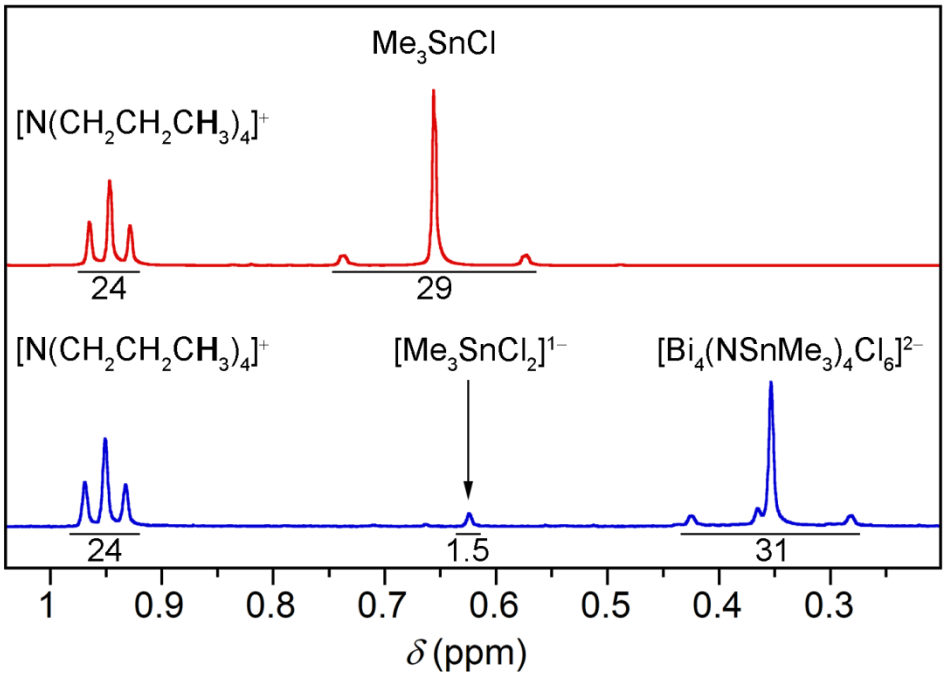

Figure 2.17. ^{1}H-NMR spectra of $(Pr^{n}_{4}N)_2$**1** + 6$GaCl_3$ in CD_3CN: before reaction of $(Pr^{n}_{4}N)_2$**1** (blue) and 3 days after addition of $GaCl_3$ (red).

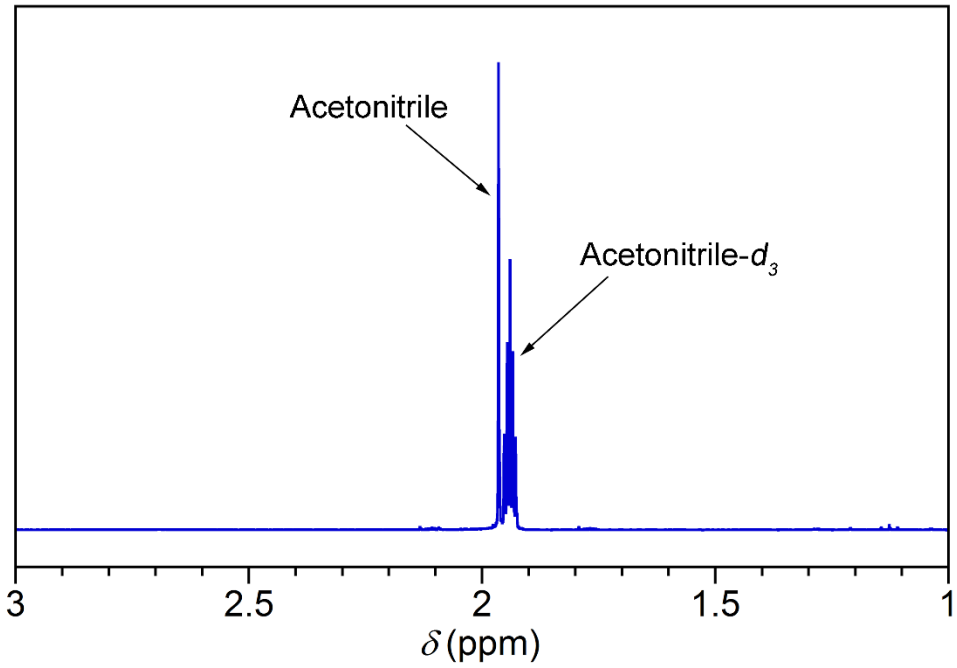

Figure 2.18. ^{1}H-NMR spectrum of **3** in CD_3CN. Non-deuterated MeCN peak is due to 1.5 MeCN solvent molecules found in **3** after drying *in vacuo*.

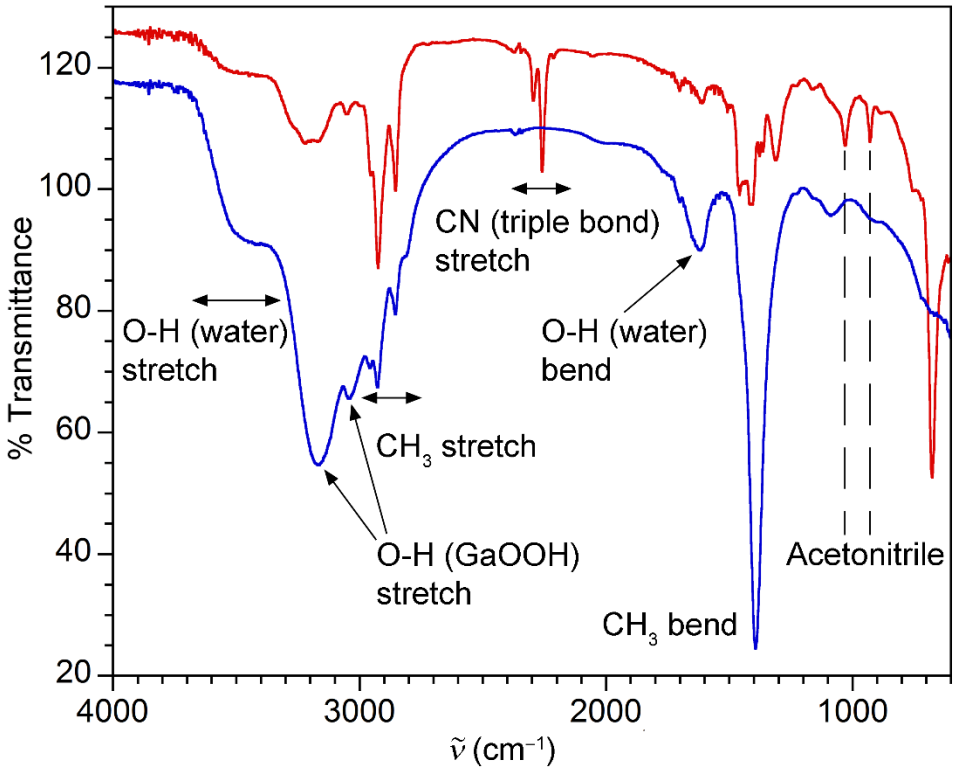

Figure 2.19. Infrared transmission spectra of **3**: immediately after exposure to air (red) and after exposure to air for 3 days (blue).

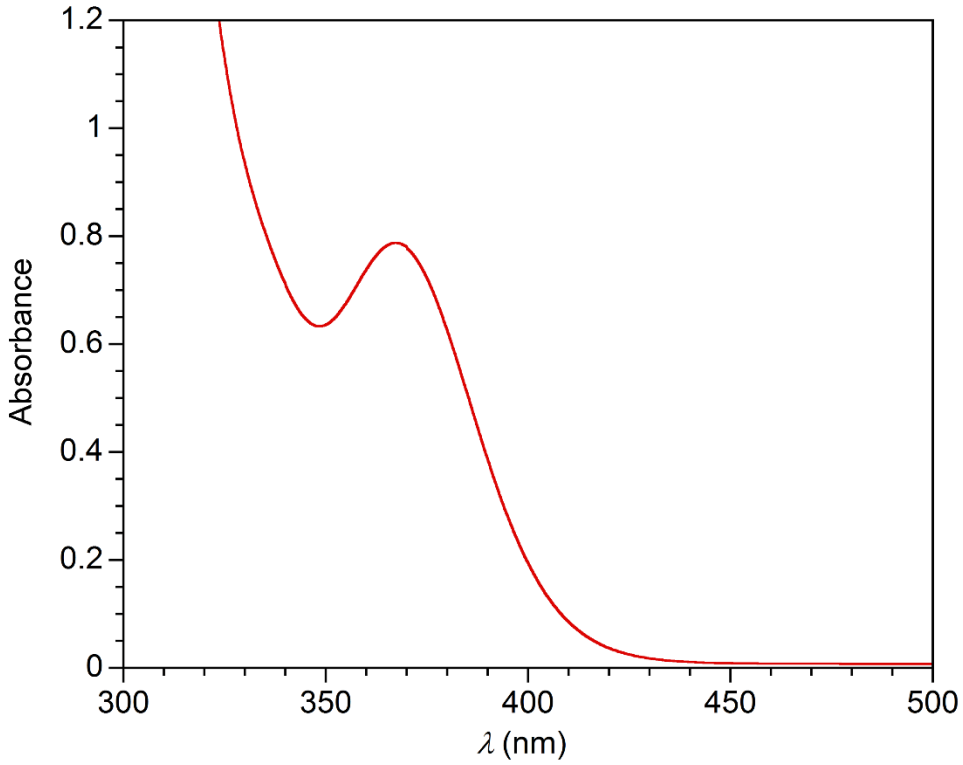

Figure 2.20. Solution state UV-Vis spectrum of **3** in MeCN.

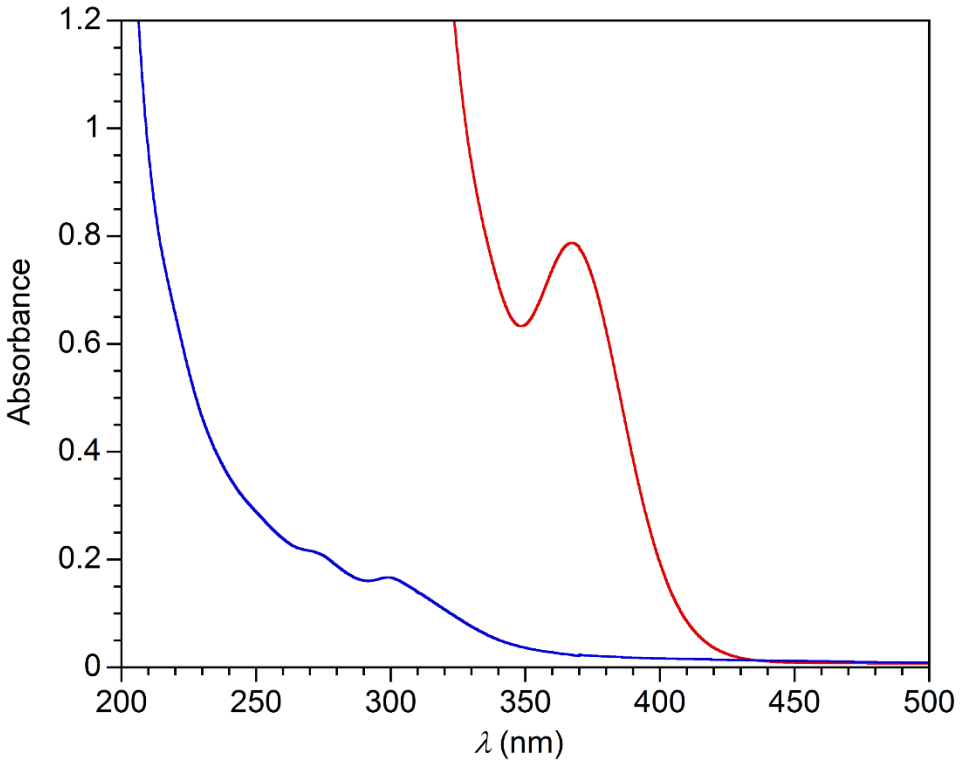

Figure 2.21. Solution state UV-Vis spectra of **3** in MeCN: before exposure to air (red) and after exposure to air for 2 days (blue).

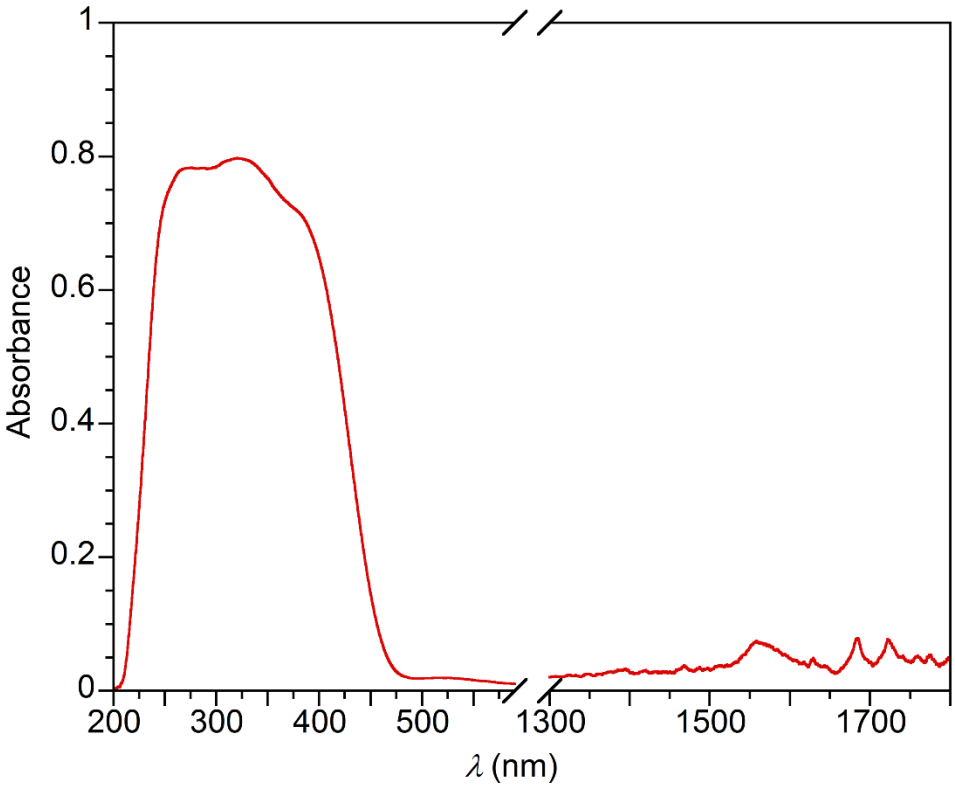

Figure 2.22. Diffuse reflectance UV-Vis spectrum of **3**.

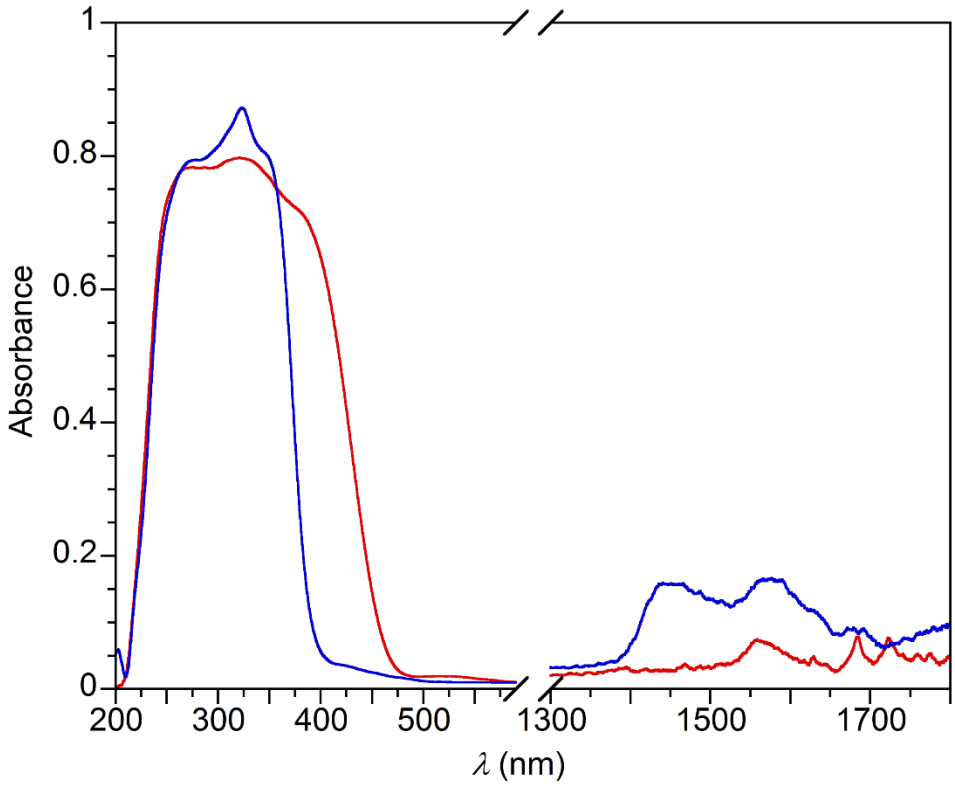

Figure 2.23. Diffuse reflectance UV-Vis spectra of **3**: as-prepared (red) and after exposure to air for 24 h (blue).

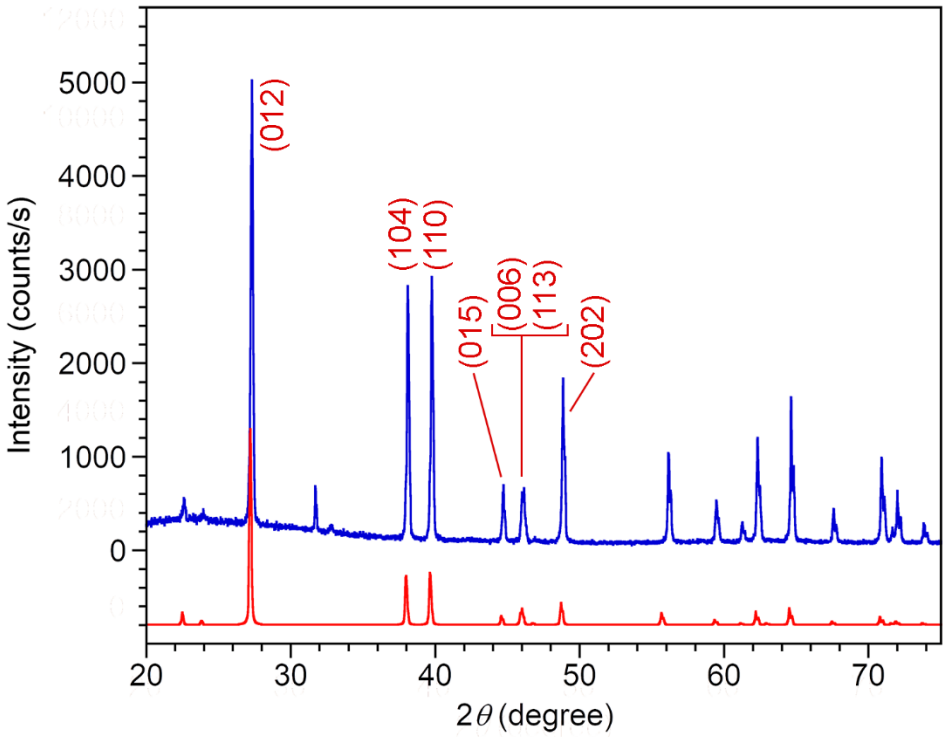

Figure 2.24. Powder X-ray diffraction data of **3** pyrolyzed in a vacuum-sealed glass tube (blue). Reference: metallic bismuth (red).

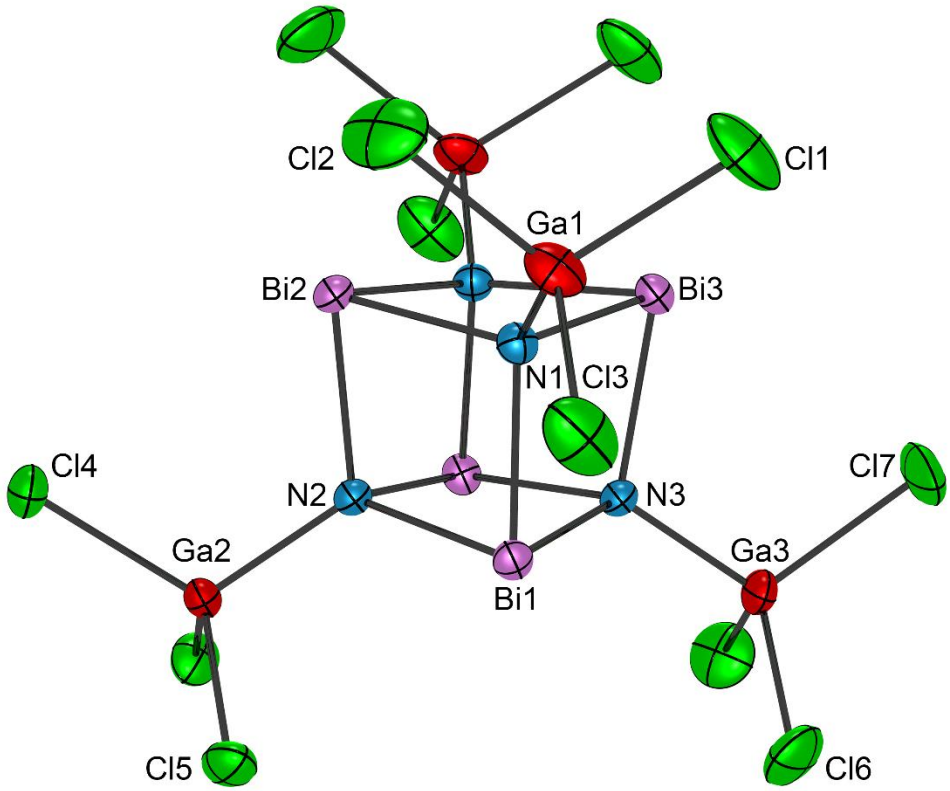

Figure 2.25. The X-ray crystal structure of **3**. The thermal ellipsoids are plotted at 50% probability level. The MeCN solvent molecules are omitted for clarity. A mirror plane bisects through Bi2, Bi3, N2, N3, Ga2, Ga3, Cl4, and Cl7.

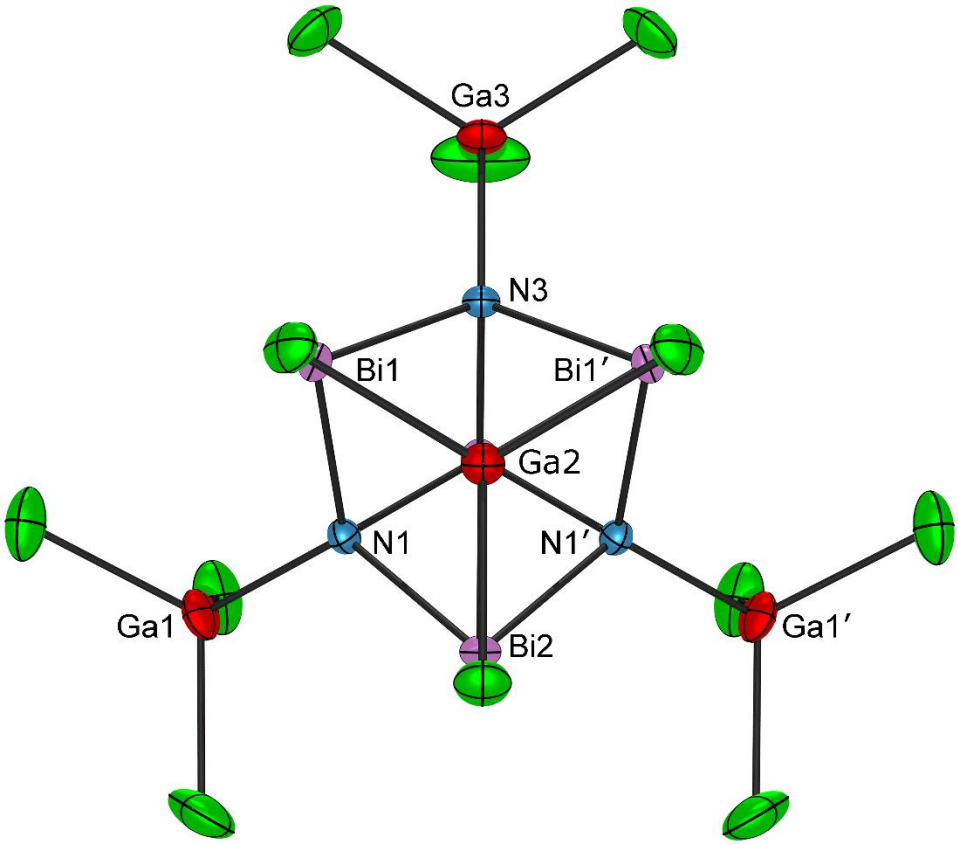

Figure 2.26. The X-ray crystal structure of **3** viewing diagonally through Ga2, N2, Bi3, representing the three-fold rotational symmetry. The thermal ellipsoids are plotted at 50% probability level. The MeCN solvent molecules are omitted for clarity.

Table 2.3. Selected mean bond lengths (Å) and angles (°) for **3**.

Bi–N	2.237(9)	Bi–N–Bi	99.5(3)
Bi–Bi	3.414(6)	N–Bi–N	79.6(3)
N–N	2.864(6)	Bi–N–Ga	118(1)
Ga–N	1.913(7)	N–Ga–Cl	109(2)
Ga–Cl	2.183(8)	Cl–Ga–Cl	110(1)
$Bi\cdots N_{MeCN}$	2.97(17)		

Conclusion

The reaction of anionic bismuth chloride, $[Bi_2Cl_9]^{3-}$ with $(Me_3Sn)_3N$ leads to the formation of bismuth-nitrogen bonds in a tetrameric Bi_4N_4 cubane: $[Bi_4(NSnMe_3)_4Cl_6]^{2-}$ (**1**). In this synthesis, we have demonstrated the use of $(Me_3Sn)_3N$ as a convenient nitrogen source for the synthesis of bismuth-nitrogen oligomers. The salt elimination of $Me_3SnCl/[Me_3SnCl_2]^{1-}$ was the key for producing Lewis basic nitrogen intermediate that was suitable for reacting with Lewis acidic bismuth halides. This Bi_4N_4 cubane is the first reported where the nitrogen sites are only bound to the metal. In addition, the characterization on a polymeric product **2** isolated in a synthesis of $(Pr^n_4N)_2$**1** revealed that the structure most likely consists of the same types of bonds as the cubane. Further reaction of $(Pr^n_4N)_2$**1** led to a metal-exchange process on Me_3Sn- moieties when reacted with $GaCl_3$ through dehalostannylation. A purely inorganic compound, $[Bi_4N_4(GaCl_3)_4]$ (**3**), is the first such reported.

Acknowledgements

Chapter 2 contains material that is currently being prepared for publication. Yamamoto, N.; Gilley, R. N.; Wilson, R. J.; Bennett, M. V. “Synthesis and Reactivity of the Unprecedented Bismuth-Nitrogen Cubanes Capped with Metals: $[Bi_4(NSnMe_3)_4Cl_6]^{2-}$ and $[Bi_4N_4(GaCl_3)_4]\cdot 6MeCN$”. *Manuscript in preparation*. The dissertation author was the primary researcher for the data presented. Soon after I joined Dr. Bennett’s laboratory group, Robert Gilley, who was an undergraduate student succeeded in the synthesis of $[Bi_4(NSnMe_3)_4Cl_6]^{2-}$ cluster. He left much work for me to complete characterization when he left for his job and then his Ph.D. work. His enthusiasm motivated me to produce something that goes beyond the cluster. I would like to thank a former JDP student, Dr. Robert Wilson, who was always thinking ahead of me, and I was able to absorb the habit. He taught a whole process related to single-crystal X-ray diffraction, starting from cutting the crystals, operation, and all the way until structural solutions. He collected the structure of $[Bi_4(NSnMe_3)_4Cl_6]^{2-}$ cubane and helped with my learning to do it myself. Kaley Dane was an undergraduate researcher who was most efficient undergraduate student I have met. She contributed to the preparation of the starting materials. I would like to thank Professor David Pullman for offering me guidance on the use on Raman spectrometer, Professor Dale Chatfield for assistance collecting the mass spectrum and use of the ESI mass spectrometer, Professor Laurance Beauvais for use of the diffuse reflectance spectrometer,

and SDSU Department of Geological Sciences for the use of powder X-ray diffractometer.

References

1. König, D.; Casalenuovo, K.; Takeda, Y.; Conibeer, G.; Guillemoles, J. F.; Patterson, R.; Huang, L. M.; Green, M. A. *Physica E.* **2010**, *42*, 2862.

2. Nozik, A. J. *Annu. Rev. Phys. Chem.* **2001**, *52*, 193.

3. Gäbler, F.; Kirchner, M.; Schnelle, W.; Schwarz, U.; Schmitt, M.; Rosner, H.; Niewa, R. *Z. Anorg. Allg. Chem.* **2004**, *630*, 2292.

4. Sun, Y.; Chen, X.-Q.; Yunoki, S.; Li, D.; Li, Y. *Phys. Rev. Lett.* **2010**, *105*, 216406.

5. Franklin, E. C. *J. Am. Chem. Soc.* **1905**, *27*, 820.

6. Schurman, I.; Fernelius, W. C. *J. Am. Chem. Soc.* **1930**, *52*, 2425.

7. Croteau, G.; Dills, R.; Beaudreau, M.; Davis, M. *Atmos. Environ.* **2010**, *44*, 3295.

8. Martirosyan, K. S. *J. Mater. Chem.* **2011**, *21*, 9400.

9. Mehring, M. *Coord. Chem. Rev.* **2007**, *251*, 974.

10. Huang, Z.-F.; Pan, L.; Zou, J.-J.; Zhang, X.; Wang, L. *Nanoscale.* **2014**, *6*, 14044.

11. Kinsella, J. M.; Jimenez, R. E.; Karmali, P. P.; Rush, A. M.; Kotamraju, V. R.; Gianneschi, N. C.; Ruoslahti, E.; Stupack, D.; Sailor, M. J. *Angew. Chem. Int. Ed.* **2011**, *50*, 12308.

12. Rabin, O.; Manuel Perez, J.; Grimm, J.; Wojtkiewicz, G.; Weissleder, R. *Nat. Mater.* **2006**, *5*, 118.

13. Sun, Y.; Cheng, H.; Gao, S.; Liu, Q.; Sun, Z.; Xiao, C.; Wu, C.; Wei, S.; Xie, Y. *J. Am. Chem. Soc.* **2012**, *134*, 20294.

14. Mishra, S. K.; Satpathy, S.; Jepsen, O. *J. Phys.: Condens. Matter.* **1997**, *9*, 461.

15. Ding, Z.; Viculis, L.; Nakawatase, J.; Kaner, R. B. *Adv. Mater.* **2001**, *13*, 797.

16. Zhao, X. B.; Ji, X. H.; Zhang, Y. H.; Zhu, T. J.; Tu, J. P.; Zhang, X. B. *Appl. Phys. Lett.* **2005**, *86*, 062111.

17. Beck, J.; Schlüter, S.; Zotov, N. *Z. Anorg. Allg. Chem.* **2004**, *630*, 2512.

18. Beck, J.; Dolg, M.; Schlüter, S. *Angew. Chem. Int. Ed.* **2001**, *40*, 2287.

19. Biswas, K.; Zhang, Q.; Chung, I.; Song, J.-H.; Androulakis, J.; Freeman, A. J.; Kanatzidis, M. G. *J. Am. Chem. Soc.* **2010**, *132*, 14760.

20. Wilson, R. J. Reactions of Stannylamines and Anionic Main Group Metal Halides: A Mild Route to Novel Main Group Metal-Nitrogen Compounds. Doctoral Dissertation, University of California, San Diego, **2013**.

21. Bennett, M. V.; Stoian, S.; Bominaar, E. L.; Münck, E.; Holm, R. H. *J. Am. Chem. Soc.* **2005**, *127*, 12378.

22. Bennett, M. V.; Holm, R. H. *Angew. Chem. Int. Ed.* **2006**, *45*, 5613.

23. Wilson, R. J.; Jones, J. R.; Bennett, M. V. *Chem. Commun.* **2013**, *49*, 5049.

24. Basch, H. *Inorg. Chim. Acta.* **1996**, *252*, 265.

25. Carmalt, C. J.; Cowley, A. H.; Hector, A. L.; Norman, N. C.; Parkin, I. P. *J. Chem. Soc., Chem. Commun.* **1994**, 1987.

26. Bickley, J. F.; Bond, A. D.; García, F.; Jantos, K.; Lawson, G. T.; McPartlin, M.; Steiner, A.; Wright, D. S. *J. Chem. Soc., Dalton Trans.* **2002**, 4629.

27. Sisido, K.; Kozima, S. *J. Org. Chem.* **1964**, *29*, 907.

28. Sheldrick, G. M. *Acta Crystallogr., Sect. A: Found. Crystallogr.* **2008**, *64*, 112.

29. Dolomanov, O. V.; Bourhis, L. J.; Gildea, R. J.; Howard, J. A. K.; Puschmann, H. *J. Appl. Crystallogr.* **2009**, *42*, 339.

30. Cucka, P.; Barrett, C. S. *Acta Cryst.* **1962**, *15*, 865.

31. Swanson, H. E.; Tatge, E. *Standard X-ray diffraction powder patterns*; U.S. Department of Commerce, National Bureau of Standards: Washington D.C., **1953**; Vol. 1.

32. Swanson, H. E.; Fuyat, R. K.; Ugrinic, G. M. *Standard X-ray diffraction powder patterns*; U.S. Department of Commerce, National Bureau of Standards: Washington D.C., **1955**; Vol. 4.

33. Edwards, A. J.; Beswick, M. A.; Galsworthy, J. R.; Paver, M. A.; Raithby, P. R.; Rennie, M.-A.; Russell, C. A.; Verhorevoort, K. L.; Wright, D. S. *Inorg. Chim. Acta.* 6.

34. Evans, W. J.; Rego, D. B.; Ziller, J. W. *Inorg. Chim. Acta.* **2007**, *360*, 1349.

35. Michalik, D.; Schulz, A.; Villinger, A. *Angew. Chem. Int. Ed.* **2010**, *49*, 7575.

36. Oertel, R. P.; Plane, R. A. *Inorg. Chem.* **1969**, *8*, 1188.

37. Müller, J. *Z. Naturforsch., B.* **2014**, *34*, 536.

38. Jiang, J.; Zhu, P.; Li, D.; Chen, Y.; Li, M.; Wang, X.; Liu, B.; Cui, Q.; Zhu, H. *RSC Adv.* **2016**, *6*, 98921.

39. Dhouib, I.; Feki, H.; Guionneau, P.; Mhiri, T.; Elaoud, Z. *Spectrochim. Acta, Part A.* **2014**, *131*, 274.

40. Fischer, F.; Schröter, F. *Ber. Dtsch. Chem. Ges.* **1910**, *43*, 1465.

41. Calderazzo, F.; Poli, R. *J. Chem. Soc., Dalton Trans.* **1984**, 2365.

42. Balázs, L.; Breunig, H. J.; Lork, E. *Z. Naturforsch. B Chem. Sci.* **2005**, *60*, 180.

43. Kuznetsov, A. N.; Fässler, T. F. *Z. Anorg. Allg. Chem.* **2002**, *628*, 2537.

44. Weinert, B.; Eulenstein, A. R.; Ababei, R.; Dehnen, S. *Angew. Chem. Int. Ed.* **2014**, *53*, 4704.

45. Appel, A.; Kober, C.; Neumann, C.; Nöth, H.; Schmidt, M.; Storch, W. *Chem. Ber.* **1996**, *129*, 175.

46. Adonin, S. A.; Gorokh, I. D.; Samsonenko, D. G.; Korol`kov, I. V.; Sokolov, M. N.; Fedin, V. P. *J. Struct. Chem.* **2017**, *58*, 718.

47. Chaabouni, S.; Kamoun, S.; Jaud, J. *J. Chem. Crystallogr.* **1998**, *28*, 209.

48. Herdtweck, E.; Kreusel, U. *Acta Crystallogr., Sect. C: Cryst. Struct. Commun.* **1993**, *49*, 318.

49. Liu, G.; Liu, J.; Zheng, X.; Liu, Y.; Yuan, D.; Zhang, X.; Gao, Z.; Tao, X. *CrystEngComm.* **2015**, *17*, 2569.

50. Zaleski, J.; Glowiak, T.; Jakubas, R.; Sobczyk, L. *J. Phys. Chem. Solids.* **1989**, *50*, 1265.

51. Tsurugi, H.; Hayakawa, A.; Kando, S.; Sugino, Y.; Mashima, K. *Chem. Sci.* **2015**, *6*, 3434.

52. Fulmer, G. R.; Miller, A. J. M.; Sherden, N. H.; Gottlieb, H. E.; Nudelman, A.; Stoltz, B. M.; Bercaw, J. E.; Goldberg, K. I. *Organometallics.* **2010**, *29*, 2176.

53. Ristić, M.; Popović, S.; Musić, S. *Mater. Lett.* **2005**, *59*, 1227.

54. Curcio, J. A.; Petty, C. C. *J. Opt. Soc. Am.* **1951**, *41*, 302.

55. Cheng, Q. m.; Stark, O.; Merz, K.; Winter, M.; Fischer, R. A. *J. Chem. Soc., Dalton Trans.* **2002**, 2933.

56. Cordero, B.; Gómez, V.; Platero-Prats, A. E.; Revés, M.; Echeverría, J.; Cremades, E.; Barragán, F.; Alvarez, S. *Dalton Trans.* **2008**, 2832.

57. Miersch, L.; Rüffer, T.; Lang, H.; Schulze, S.; Hietschold, M.; Zahn, D.; Mehring, M. *Eur. J. Inorg. Chem.* **2010**, 4763.

58. Schäfer, M.; Frenzen, G.; Neumüller, B.; Dehnicke, K. *Angew Chem. Int. Ed. Engl.* **1992**, *31*, 334.

Chapter 3: Reactivity Tests of $(Pr^n_4N)_2[Bi_4(NSnMe_3)_4Cl_6]$ with Variety of Metal Chlorides

Introduction

Metal exchange in single-source precursor molecules is a potential synthetic technique which would allow access to a library of precursors to materials. In chapter 2, the first substitution of capping groups as a means to synthesize new cubanes was presented. A search of pnictogen-nitrogen cubanes, Pn_4N_4 (Pn = P, As, Sb, Bi), in the Cambridge Structural Database (CSD) (v. 5.39)[1] and a study of their reactivity revealed that the exchange of capping Me_3Sn moieties so far remains unique. There is only one example of Bi_4N_4 cubane $[pyOBi(\mu_3\text{-}NCy)]_4$ (Cy = cyclohexyl, py = 2-pyridyl).[2] This complex does not undergo exchange of ligands on the nitrogen corners of the cube. Among imido cubanes, trialkyl- or triaryl-E (E = Si, Ge, Sn, Pb) are commonly found in the exocube. These complexes include: $[CpTi(\mu_3\text{-}NSnMe_3)]_4$,[3] $[Sn(\mu_3\text{-}NSnMe_3]_4$,[4] $[M(\mu_3\text{-}NGeMe_3)]_4$ (M = Sn, Ge, Pb),[4] $[Sn(\mu_3\text{-}NSiMe_3)]_4$,[5,6] $[M(\mu_3\text{-}NSiMe_3)]_4$ (M = Ge, Pb),[7] $[MeGa(\mu_3\text{-}NSiMe_3)]_4$,[8] $[i\text{-}BuAl(\mu_3\text{-}NSiPh_3)]_4$,[9] $[(THF)Mg(\mu_3\text{-}NSiPh_3)]_4$,[10] and $[LSm(\mu_3\text{-}NSiMe_3)]_4$ (L = silyl-linked bis-amidinate).[11] Bismuth-containing heterometal cubanes are found as neutral and cationic clusters: $\{[(CO)_4FeBi(\mu_3\text{-}M)]_4\}^{4-}$ (M = $Fe(CO)_3$),[12] $\{Bi[\mu_3\text{-}Co(CO)_3]\}_4$,[13] $\{Bi_4[Pd(PPh_2Me)_2]_4\}^{2+}$,[14] and $[Bi(\mu_3\text{-}Q)]^{4+}$ (Q = S,[15] Se,[15] Te[16]). None of the complexes in these reports have been utilized in substitution reactions of the R_3E groups. Among all these groups, the Me_3Sn seems the most likely to be a good leaving group.

As discussed in Chapter 2, reaction of $(Pr^n_4N)_2$**1** with gallium trichloride ($GaCl_3$) led to loss of Me_3SnCl and exchange of the Me_3Sn- moieties capping the cubane for $GaCl_3$, resulting in $[Bi_4N_4(GaCl_3)_4]$ (**2**) (Scheme 3.1). This dehalostannylation and exchange occurred without alteration of the Bi-N cubane core based on single-crystal X-ray diffraction. The strong Lewis acidity of $GaCl_3$ may have promoted the formation of thermodynamically stable adduct on the nitrogen sites; Bi_3N-$GaCl_3$ (only nitrogen-site is shown). We were interested to learn if $(Pr^n_4N)_2$**1** would undergo similar reactions in the presence of other metal-halides. The question arises as to how stable the $[Bi_4N_4]$ core is to substitution of a variety of other Lewis acids or whether the core can be altered to form new compounds. In this chapter, the reactivity of compound **1** with a variety of metal halides ($AlCl_3$, $InCl_3$, $BiCl_3$, $[Bi_2Cl_9]^{3-}$, and $[GaCl_4]^{1-}$), will be presented.

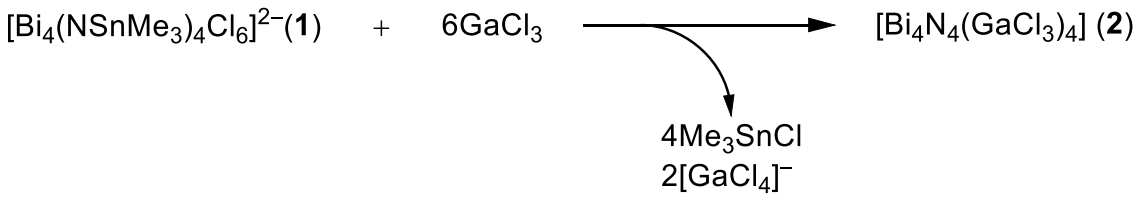

Scheme 3.1. A synthesis of **2** through dehalostannylation and Me_3Sn- substitution on $(Pr^n_4N)_2$**1** by $GaCl_3$.

Experimental Section

General Sample Preparations

Anhydrous tetrahydrofuran (THF) and diethyl ether (Et_2O) were purchased from EMD Drysolve. Acetonitrile (MeCN) was purchased from Burdick and Jackson. Deuterated acetonitrile (CD_3CN) was purchased from Cambridge Isotope Laboratories, Inc. These solvents were stored over dried 4 Å molecular sieves for at least 18 hours before the use and were left in a nitrogen atmosphere. $AlCl_3$ (Alfa Aesar, 99.999%), $InCl_3$ (J.T. Baker, 99.99%), and $BiCl_3$ (Alfa Aesar, 99.997%) were stored under a pure nitrogen gas environment and used as-received. All the reactions were carried out in a N_2 gas atmosphere in a drybox. The ^{1}H-NMR data collection was recorded on 400 MHz Varian VNMRS at 30 °C. The samples were sealed in J. Young valve NMR tubes. Once each spectrum was acquired, the NMR samples were stored in the N_2 gas atmosphere undisturbed in the NMR tubes. For the reaction with $AlCl_3$, the drybox was purged periodically with a nitrogen gas and was purged for 10 min once the reaction mixture was made. The inductively coupled plasma optical emission spectrometry (ICP-OES) data was collected on a Thermo Fisher Scientific iCAP 7000 Plus ICP-OES. The calibrations for Al, Bi, In, Ga, and Sn were plotted using standard solutions which were purchased from Sigma-Aldrich and diluted with 3 M HCl. The ICE-OES samples were obtained from the reactions worked in a larger scale based on the NMR scale, maintaining the concentrations of each reactant. The solid products found from

each reaction were collected by filtration, washed with 3 x 3 mL diethyl ether (Et_2O), and dried *in vacuo* overnight, except the product solution of reaction (**4**) was obtained by vapor diffusion of Et_2O into the solution, washed, and dried in the same manner as other reaction products. Powders were weighed under a N_2 atmosphere and then digested and diluted in 3 M HCl under aerobic conditions.

Preparation of NMR scale reactions

(**1**) Reaction of $(Pr^{n}{}_4N)_2$**1** with $AlCl_3$. An orange solution of $(Pr^{n}{}_4N)_2$**1** (0.025 g, 0.012 mmol) in 0.84 mL of CD_3CN was added to a stirred solution of $AlCl_3$ (0.010 g, 0.078 mmol) in 0.42 mL of CD_3CN (Scheme 3.2). A suspension of a pale yellow solid in a yellow mother liquor resulted. The reaction mixture was stirred for 1 min, and the yellow suspension was sealed in a NMR tube. A pale yellow solid and a greenish-yellow solution were found after 3 days. The solid was isolable by filtration and was found to be insoluble in THF and Et_2O.

$$[Bi_4(NSnMe_3)_4Cl_6]^{2-}(\mathbf{1}) \quad + \quad 6AlCl_3 \longrightarrow \text{Pale yellow solid} \quad + \quad Me_3SnCl$$

Scheme 3.2. Reaction (**1**): $(Pr^{n}{}_4N)_2$**1** with $6AlCl_3$ in CD_3CN.

(**2**) Reaction of $(Pr^{n}{}_4N)_2$**1** with $InCl_3$. An orange solution of $(Pr^{n}{}_4N)_2$**1** (0.030 g, 0.014 mmol) in 1.0 mL of CD_3CN was added to a stirred solution of $InCl_3$ (0.020 g, 0.090 mmol) in 0.52 mL of CD_3CN (Scheme 3.3). A suspension of a yellow solid in a light yellow mother liquor resulted. The reaction mixture was stirred for 1 min, and the suspension was sealed in a NMR tube. A pale yellow solid and a pale yellow solution were found after 3 days. The solid was isolable by filtration and was found to be insoluble in THF and Et_2O.

$$[Bi_4(NSnMe_3)_4Cl_6]^{2-}(\mathbf{1}) \quad + \quad 6InCl_3 \longrightarrow \text{Pale yellow solid} \quad + \quad Me_3SnCl$$

Scheme 3.3. Reaction (**2**): $(Pr^{n}{}_4N)_2$**1** with $6InCl_3$ in CD_3CN.

(**3**) Reaction of $(Pr^n_4N)_2$**1** with $BiCl_3$. An orange solution of $(Pr^n_4N)_2$**1** (0.023 g, 0.011 mmol) in 0.83 mL of CD_3CN was added to a stirred solution of $BiCl_3$ (0.022 g, 0.071 mmol) in 0.41 mL of CD_3CN (Scheme 3.4). A suspension of a pale yellow solid in a nearly colorless mother liquor resulted. The reaction mixture was stirred for 1 min, and the suspension was sealed in a NMR tube. A pale yellow solid and a pale greenish-yellow solution were found after 1 day. The solid was isolable by filtration and was found to be insoluble in THF and Et_2O.

$$[Bi_4(NSnMe_3)_4Cl_6]^{2-}(\mathbf{1}) \quad + \quad 6BiCl_3 \longrightarrow \text{Pale yellow solid} \quad + \quad Me_3SnCl$$

Scheme 3.4. Reaction (**3**): $(Pr^n_4N)_2$**1** with $6BiCl_3$ in CD_3CN.

(**4**) Reaction of $(Pr^n_4N)_2$**1** with $(Pr^n_4N)_3[Bi_2Cl_9]$. An orange solution of $(Pr^n_4N)_2$**1** (0.024 g, 0.011 mmol) in 0.81 mL of CD_3CN was added to a stirred solution of $(Pr^n_4N)_3[Bi_2Cl_9]$ (0.045 g, 0.035 mmol) in 0.40 mL of CD_3CN (Scheme 3.5). A negligible amount of a yellow solid in a yellow mother liquor resulted. The reaction mixture was stirred for 1 min, and the suspension was sealed in a NMR tube. No solid and a greenish-yellow solution were found after 1 day.

$$[Bi_4(NSnMe_3)_4Cl_6]^{2-}(\mathbf{1}) + 3(Pr^n_4N)_3[Bi_2Cl_9] \longrightarrow \begin{matrix}\text{Greenish-}\\ \text{yellow solution}\end{matrix} + [Me_3SnCl_2]^{1-}$$

Scheme 3.5. Reaction (**4**): $(Pr^n_4N)_2$**1** with $3(Pr^n_4N)_3[Bi_2Cl_9]$ in CD_3CN.

(**5**) Reaction of $(Pr^n_4N)_2$**1** with $(Pr^n_4N)[GaCl_4]$. An orange solution of $(Pr^n_4N)_2$**1** (0.031 g, 0.015 mmol) in 0.43 mL of CD_3CN was added to a stirred solution of $(Pr^n_4N)[GaCl_4]$ (0.037 g, 0.092 mmol) in 0.43 mL of CD_3CN (Scheme 3.6). A suspension of a yellow solid in a yellow mother liquor resulted. The reaction mixture was stirred for 1 min, and the suspension was sealed in a NMR tube. A yellow solid and a yellow solution were found after 3 days. The solid was isolable by filtration and was found to be insoluble in THF and Et_2O.

$$[Bi_4(NSnMe_3)_4Cl_6]^{2-}(\mathbf{1}) + 6(Pr^n_4N)[GaCl_4] \longrightarrow \text{Yellow solid} + [Me_3SnCl_2]^{1-}$$

Scheme 3.6. Reaction (**5**): $(Pr^n_4N)_2$**1** with $6(Pr^n_4N)[GaCl_4]$ in CD_3CN.

Results and Discussion

The ^{1}H-NMR spectra of reactions of (1) – (5)

The ^{1}H-NMR spectrum of the reaction mixtures for the reactions of $(Pr^{n}_{4}N)_2$**1** with $AlCl_3$, $InCl_3$, $BiCl_3$, $[Bi_2Cl_9]^{3-}$, and $[GaCl_4]^{1-}$) indicate that a change in the cuboidal anion occurs in every instance. The disappearance of Me_3Sn- peaks from compound **1** and the formation of Me_3SnCl indicates that exchange occurs. Samples of $(Pr^{n}_{4}N)_2$**1** which are pure by elemental analysis show a ^{1}H shift associated with terminal Me_3Sn- at 0.35 ppm with integration value of 31 where presence of all the protons should be 36. This peak is accompanied by satellite signals due to proton-tin couplings which has J-values $J_{^{1}H-^{117}Sn}$ = 56.2 Hz and $J_{^{1}H-^{119}Sn}$ = 58.0 Hz. Besides the major peak from anion **1**, there is a peak associated with $[Me_3SnCl_2]^{1-}$ at 0.62 ppm which has integration value of less than 2.[17] The integration value was normalized to 24 protons on γ–carbon atoms in tetrapropyl ammonium observed at 0.95 ppm. Once reaction (**1**) started, the ^{1}H shift due to the terminal Me_3Sn- in $(Pr^{n}_{4}N)_2$**1** completely disappeared while three new peaks appeared at 0.39 – 0.43 ppm and all of which carried ^{1}H-$^{117/119}$Sn coupled peaks ($J_{^{1}H-^{117}Sn}$ = 55 Hz and $J_{^{1}H-^{119}Sn}$ = 58 Hz) (Figure3.1). The multiple peaks disappeared in 3 days. The integration value of $[Me_3SnCl_2]^{1-}$ increased to 24. Since this value did not sum to 31, it implies that some Me_3Sn- related compounds precipitated from solution. This is different than the case of pure $(Pr^{n}_{4}N)_2$**1** in CD_3CN over the same time frame.

The reaction (**2**) also followed a similar trend (Figure 3.2). The final integration value of $[Me_3SnCl_2]^{1-}$ was close to that found for reaction (**1**). These two reactions took a nearly identical reaction path as that observed for the reaction of $(Pr^n_4N)_2$**1** with $GaCl_3$ as measured by ^{1}H-NMR spectroscopy. The reaction (**3**) produced an unidentified peak at 1.2 ppm ($J_{^1H\text{-}^{117}Sn}$ = 81.0 Hz and $J_{^1H\text{-}^{119}Sn}$ = 83.8 Hz) besides the trimethyltin chloride peak near 0.6 ppm (Figure 3.3). The $J_{^1H\text{-}^{119}Sn}$ constants associated with Bi–$SnMe_3$ are found at 45 Hz in the literature,[18] so the possibility that the Bi–Sn bonds are found in the unknown peak is unlikely. The $J_{^1H\text{-}^{117/119}Sn}$ constants for $[Me_2SnCl_3]^{1-}$ are reported as 84.5 and 88.5 Hz,[19] and 88.9 Hz for $J_{^1H\text{-}^{119}Sn}$ in another report,[20] which are close to those found for reaction (**3**). It is likely that $[Me_2SnCl_3]^{1-}$ is the product.

The sum of the final integration values from the two proton-tin coupled peaks exceeded the initial value of 31. This implies that the actual integration value of $Pr^n_4N^+$ must have been lower because of polymeric product. The spectra of reactions (**4**) and (**5**) revealed an unshifted peak of terminal Me_3Sn– from compound **1** right after the reaction except the integration value was significantly lower < 13 (Figure 3.4 and 3.5). It completely disappeared for the reaction (**4**) in a day and nearly disappeared for the reaction (**5**) after 3 days. The total integration of proton-tin coupled peaks was smaller than the pure spectrum of **1** which implies a precipitation of product. The detail of ^{1}H shifts and $J_{^1H\text{-}^{117/119}Sn}$ assignments are listed in Table 3.1 – 3.5. In sum, the ^{1}H-NMR spectra collected for reactions (**1**) – (**5**) all indicate that dechlorostannylation of

anion **1** occurs in the presence of the Lewis acids $AlCl_3$, the neutral metal halides $InCl_3$ and $BiCl_3$ as well as with the anions of $[Bi_2Cl_9]^{3-}$ and $[GaCl_4]^{1-}$.

ICP-OES Spectrometry on Solid Products from Reaction (1) – (5)

The elemental analysis of the solid products found from the reaction (**1**) – (**5**) were studied by ICP-OES spectrometry. The results are presented in Table 3.6. All these reactions monitored on ^{1}H-NMR have shown these reactions with compound **1** undergo elimination of Me_3Sn terminal groups analogous to the case demonstrated for $GaCl_3$.

Comparing the reactions with Lewis acids ($AlCl_3$ and $InCl_3$), the precipitate from the reaction (**2**) had significantly higher relative abundance of In as opposed to that from the reaction (**1**) with 1.4 Al while the Bi and Sn were the same for both cases. A possible reason might be the reaction (**2**) produced a polymer with majority of repeating units with In atoms, possibly through bridging chlorides. The reaction (**1**) may have proceeded by chloride abstraction by $AlCl_3$ and produced $[AlCl_4]^{1-}$ anions, which stayed in the solution. As a result, a minimal Al content was found in the precipitate.

Reaction (**3**) and (**4**) with $BiCl_3$ and $[Bi_2Cl_9]^{3-}$, respectively, gave comparable results. The relative abundance of Sn with zero and 0.4 were found from the reaction (**3**) and (**4**), respectively. Reaction of compound **1** led by bismuth chlorides complexes favors the formation of trimethylstannyl chlorides as demonstrated by ^{1}H-NMR spectra. For the case of reaction (**5**), the precipitate contained no Ga, which suggested a gallium complex was still in the

solution. This evidence suggests that $[GaCl_4]^{1-}$ induces the formation of a polymeric product containing Bi and Sn as opposed the reaction observed with $GaCl_3$ in Chapter 2.

Work continues on growing single crystals of the products of reactions (**1**) – (**5**) to fully understand the scope of this chemistry. These structures would elucidate the nature of the bonding in these products.

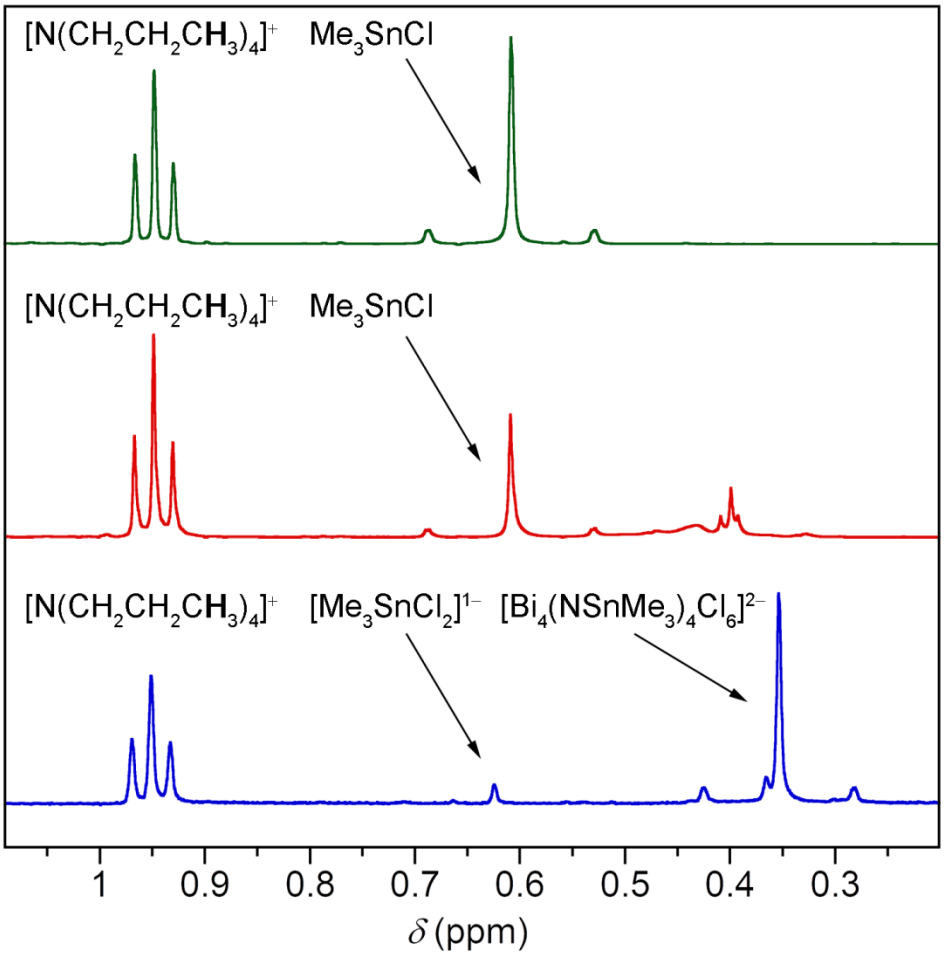

Figure 3.1. ^{1}H-NMR spectra of $(Pr^{n}_{4}N)_2$**1** + 6$AlCl_3$ in CD_3CN. $(Pr^{n}_{4}N)_2$**1** (blue), 10 min after addition of $AlCl_3$ (red), and after 3 days (green).

Table 3.1. Chemical shifts and coupling constants of tin-complexes after the reaction of $(Pr^{n}{}_{4}N)_{2}$**1** and $AlCl_{3}$.

Chemical Shift (ppm)	Types of Coupling	Coupling Constant and Elapsed Time	
		10 min	3 day
0.39	$J_{^{1}H-^{119}Sn}$ (Hz)	57.73	Not observed
	$J_{^{1}H-^{117}Sn}$ (Hz)	55.30	Not observed
0.40	$J_{^{1}H-^{119}Sn}$ (Hz)	57.63	Not observed
	$J_{^{1}H-^{117}Sn}$ (Hz)	55.29	Not observed
0.43	$J_{^{1}H-^{119}Sn}$ (Hz)	57.93	Not observed
	$J_{^{1}H-^{117}Sn}$ (Hz)	55.41	Not observed
0.61	$J_{^{1}H-^{119}Sn}$ (Hz)	64.35	64.10
	$J_{^{1}H-^{117}Sn}$ (Hz)	61.76	62.11

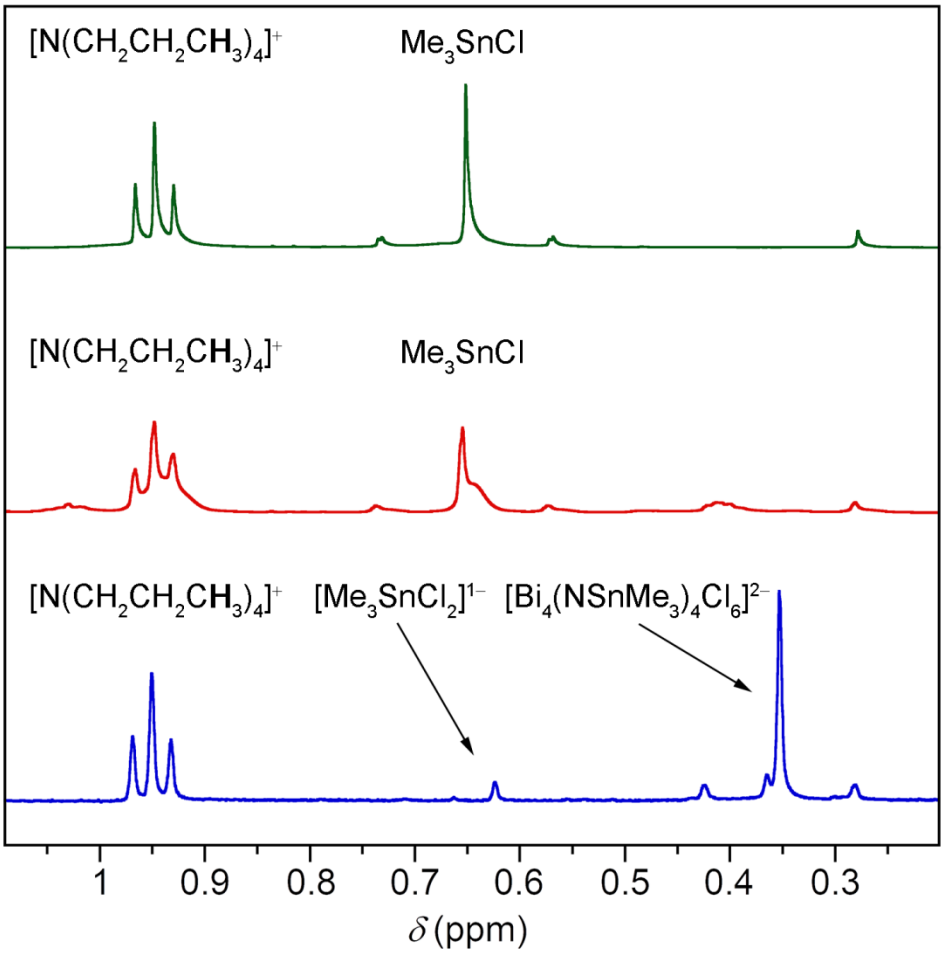

Figure 3.2. ^{1}H-NMR spectra of $(Pr^{n}_{4}N)_2$**1** + 6$InCl_3$ in CD_3CN. $(Pr^{n}_{4}N)_2$**1** (blue), 10 min after addition of $InCl_3$ (red), and after 3 days (green).

Table 3.2. Chemical shifts and coupling constants of tin-complexes after the reaction of $(Pr^{n}{}_{4}N)_{2}$**1** and $InCl_{3}$.

Chemical Shift (ppm)	Types of Coupling	Coupling Constant and Elapsed Time	
		10 min	3 day
0.66	$J_{^{1}H-^{119}Sn}$ (Hz)	66.33	66.52
	$J_{^{1}H-^{117}Sn}$ (Hz)	64.40	63.70

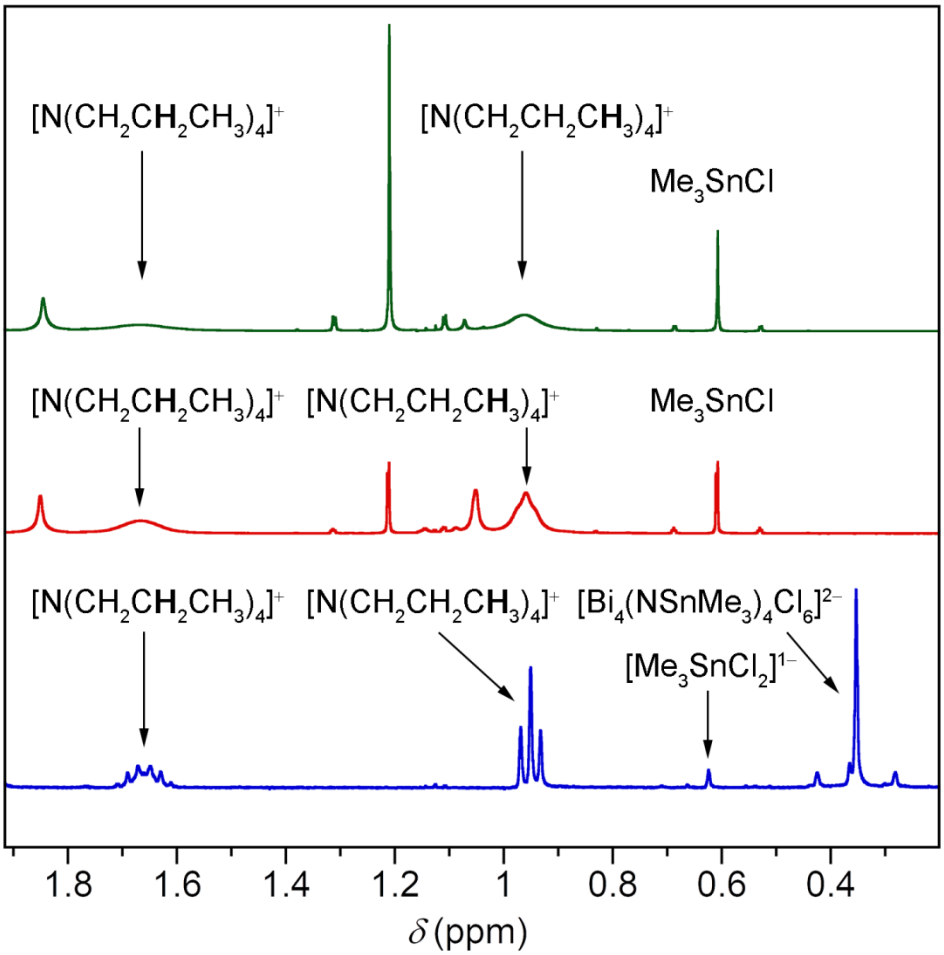

Figure 3.3. ^{1}H-NMR spectra of $(Pr^{n}_{4}N)_2$**1** + 6$BiCl_3$ in CD_3CN. $(Pr^{n}_{4}N)_2$**1** (blue), 10 min after addition of $BiCl_3$ (red), and after 1 day (green).

Table 3.3. Chemical shifts and coupling constants of tin-complexes after the reaction of $(Pr^n{}_4N)_2$**1** and $BiCl_3$.

Chemical Shift (ppm)	Types of Coupling	Coupling Constant and Elapsed Time	
		10 min	1 day
0.61	$J_{^1H-^{119}Sn}$ (Hz)	65.72	64.47
	$J_{^1H-^{117}Sn}$ (Hz)	63.09	61.67
1.2	$J_{^1H-^{119}Sn}$ (Hz)	83.83	82.75
	$J_{^1H-^{117}Sn}$ (Hz)	81.00	79.13

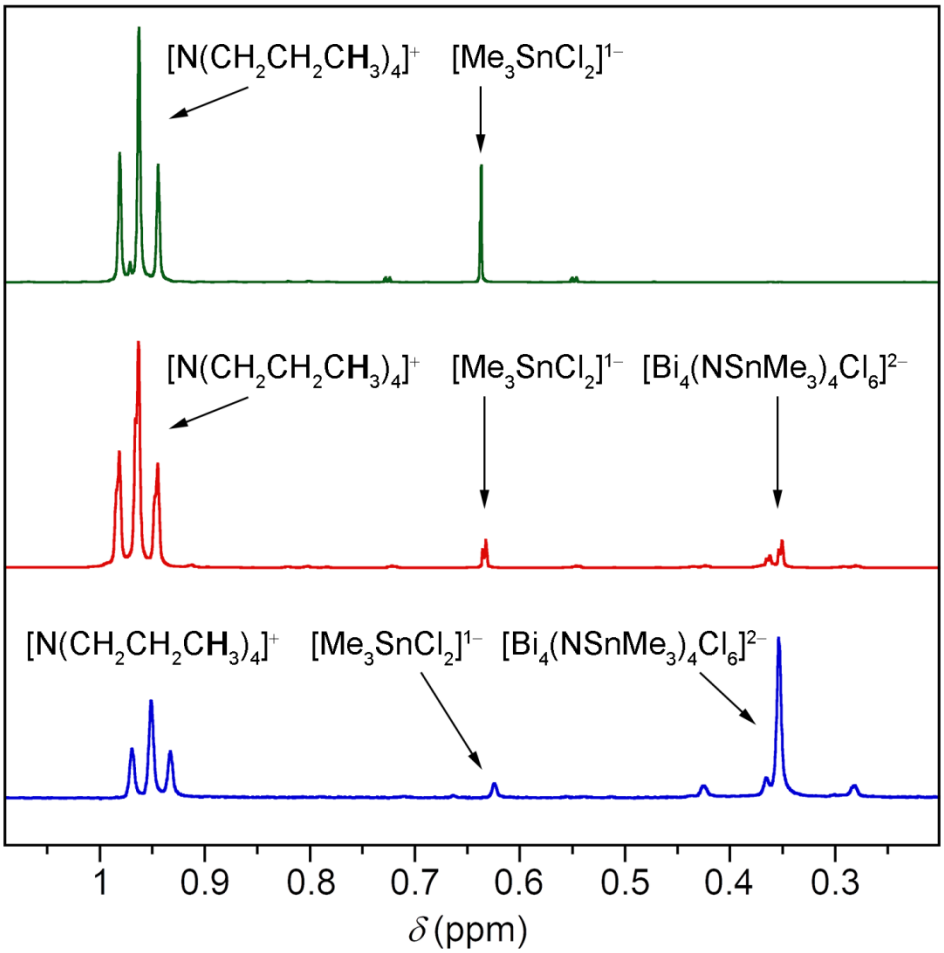

Figure 3.4. ^{1}H-NMR spectra of $(Pr^{n}{}_4N)_2$**1** + 3$(Pr^{n}{}_4N)_3[Bi_2Cl_9]$ in CD_3CN. $(Pr^{n}{}_4N)_2$**1** (blue), 20 min after addition of $[Bi_2Cl_9]^{3-}$ (red), and after 1 day (green).

Table 3.4. Chemical shifts and coupling constants of tin-complexes after the reaction of $(Pr^n{}_4N)_2$**1** and $(Pr^n{}_4N)_3[Bi_2Cl_9]$.

Chemical Shift (ppm)	Types of Coupling	Coupling Constant and Elapsed Time	
		20 min	1 day
0.35	$J_{^1H\text{-}^{119}Sn}$ (Hz)	59.71	Not observed
	$J_{^1H\text{-}^{117}Sn}$ (Hz)	57.17	Not observed
0.63	$J_{^1H\text{-}^{119}Sn}$ (Hz)	72.98	72.62
	$J_{^1H\text{-}^{117}Sn}$ (Hz)	70.14	69.39

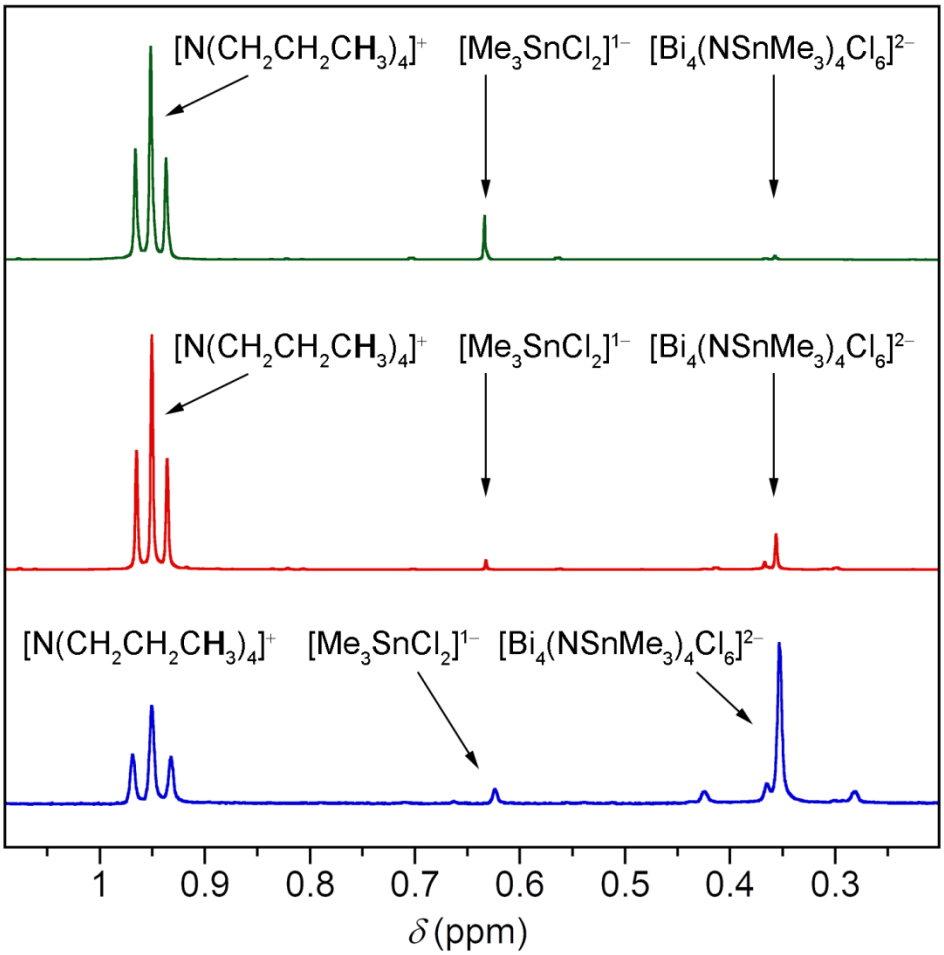

Figure 3.5. ^{1}H-NMR spectra of $(Pr^{n}_{4}N)_2$**1** + 6$(Pr^{n}_{4}N)[GaCl_4]$ in CD_3CN. $(Pr^{n}_{4}N)_2$**1** (blue), 10 min after addition of $[GaCl_4]^{1-}$ (red), and after 3 days (green).

Table 3.5. Chemical shifts and coupling constants of tin-complexes after the reaction of $(Pr^n{}_4N)_2$**1** and $(Pr^n{}_4N)[GaCl_4]$.

Chemical Shift (ppm)	Types of Coupling	Coupling Constant and Elapsed Time	
		10 min	3 day
0.36	$J_{^1H\text{-}^{119}Sn}$ (Hz)	58.37	58.38
	$J_{^1H\text{-}^{117}Sn}$ (Hz)	55.97	55.96
0.63	$J_{^1H\text{-}^{119}Sn}$ (Hz)	70.97	71.16
	$J_{^1H\text{-}^{117}Sn}$ (Hz)	67.75	68.06

Table 3.6. Relative abundance of elements in solids isolated from reactions (**1**) – (**5**) determined by ICP-OES spectroscopy.

Reaction	Elements	Relative Abundance
(**1**)	Al	1.4
	Bi	4
	Sn	1
(**2**)	In	10
	Bi	4
	Sn	1
(**3**)	Bi	4
	Sn	0
(**4**)	Bi	4
	Sn	0.4
(**5**)	Ga	0
	Bi	4
	Sn	4

Proposed Reaction Paths of (1) – (5)

The formation of Me_3SnCl from pure cubane **1** in CD_3CN suggests a pathway for the exchange of Me_3Sn groups involving the intermediate shown in scheme 3.7. Presumably, dehalostannylation affords a strongly basic nitrogen site which can then form an adduct with Lewis acids, ECl_3 (E = Ga, Al, In), (Scheme 3.8). Another possible initial step of these metal-exchanges may be attributed to the equilibrium process of $(Pr^n{}_4N)_2$**1** in solution (Scheme 3.2). The addition of a Lewis acid to the solution will strongly favor the adduct formation. The reaction then proceeds until the remaining nitrogen sites are capped by the Lewis acids.

Furthermore, neutral metal halides, which contain In and Bi atoms, could be used as to abstract chloride ions from anion **1** (Scheme 3.9). Due to the expanded octet rule, those large metals can bear increased number of bonds. Plus, neutral metal halides could proceed to an anionic form in presence of a counter ion. These factors can imply that one equivalent of metal halide atom can abstract one or more chlorides. This initial abstraction of chloride ion(s) can destabilize the structure of compound **1** which can then lead to an elimination of Me_3SnCl through intramolecular reaction. Conversely, the halide-rich anionic metal halides, $[Bi_2Cl_9]^{3-}$, may favor the Cl^- ion reacting with terminal Me_3Sn–moieties to eliminate Me_3SnCl from compound **1** (Scheme 3.10). If the coordination sites of metal halides are saturated, their metal atoms could be susceptible to lowering the coordination number by losing a chloride ion. As a result, this could in turn promote the abstraction of chlorides surrounding the

cubane to restore the coordination number of bismuth such that the molecular formula of $[Bi_2Cl_9]^{3-}$ is regained.

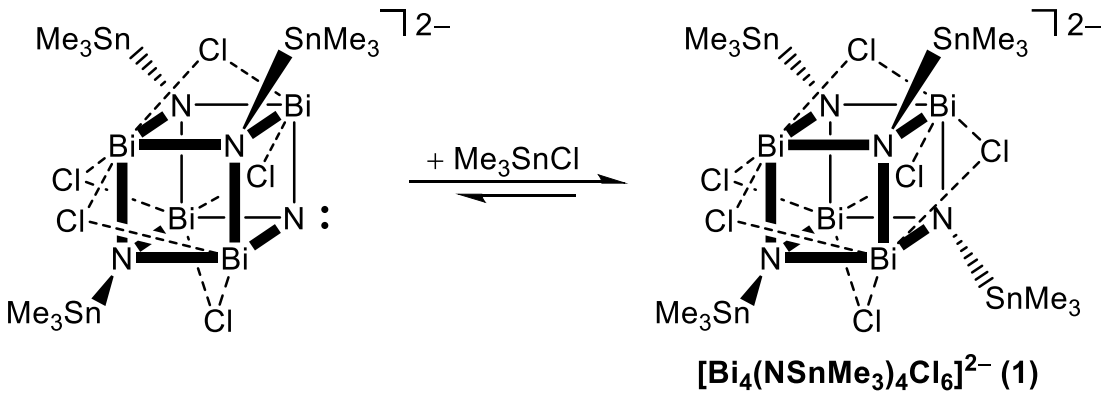

Scheme 3.7. Equilibrium process of ($Pr^n_4N)_2$**1** through intramolecular dehalostannylation

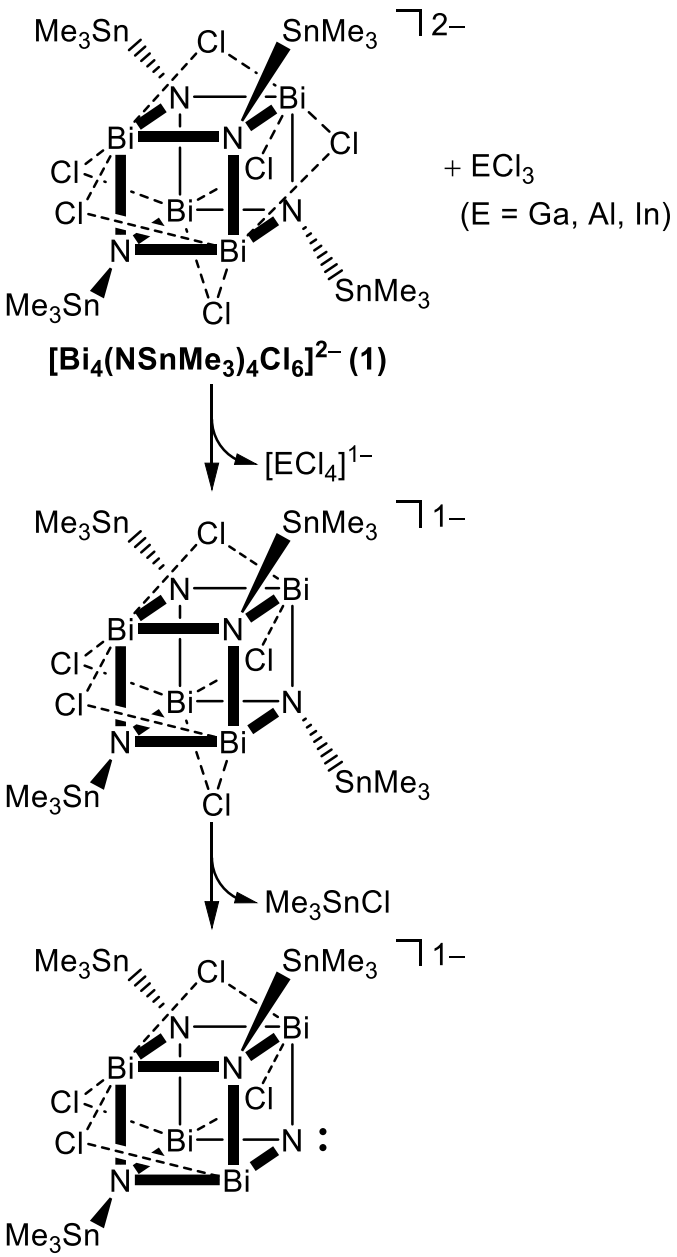

Scheme 3.8. A chloride ion abstraction from ($Pr^n_4N)_2$**1** in a reaction of Lewis acids followed by intramolecular dehalostannylation.

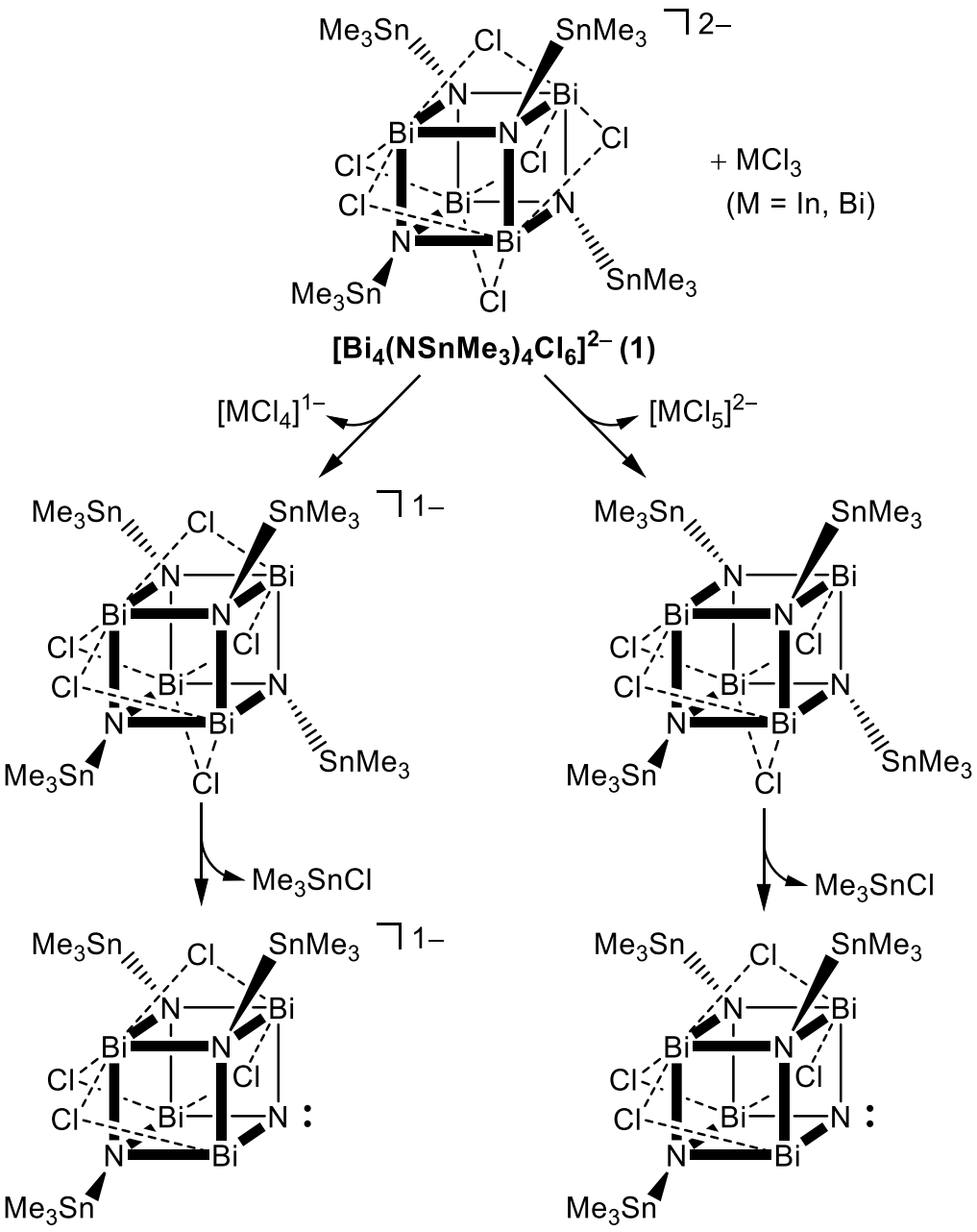

Scheme 3.9. Abstraction of chloride ion(s) from ($Pr^n_4N)_2$**1** heavy metal chlorides followed by intramolecular dehalostannylation.

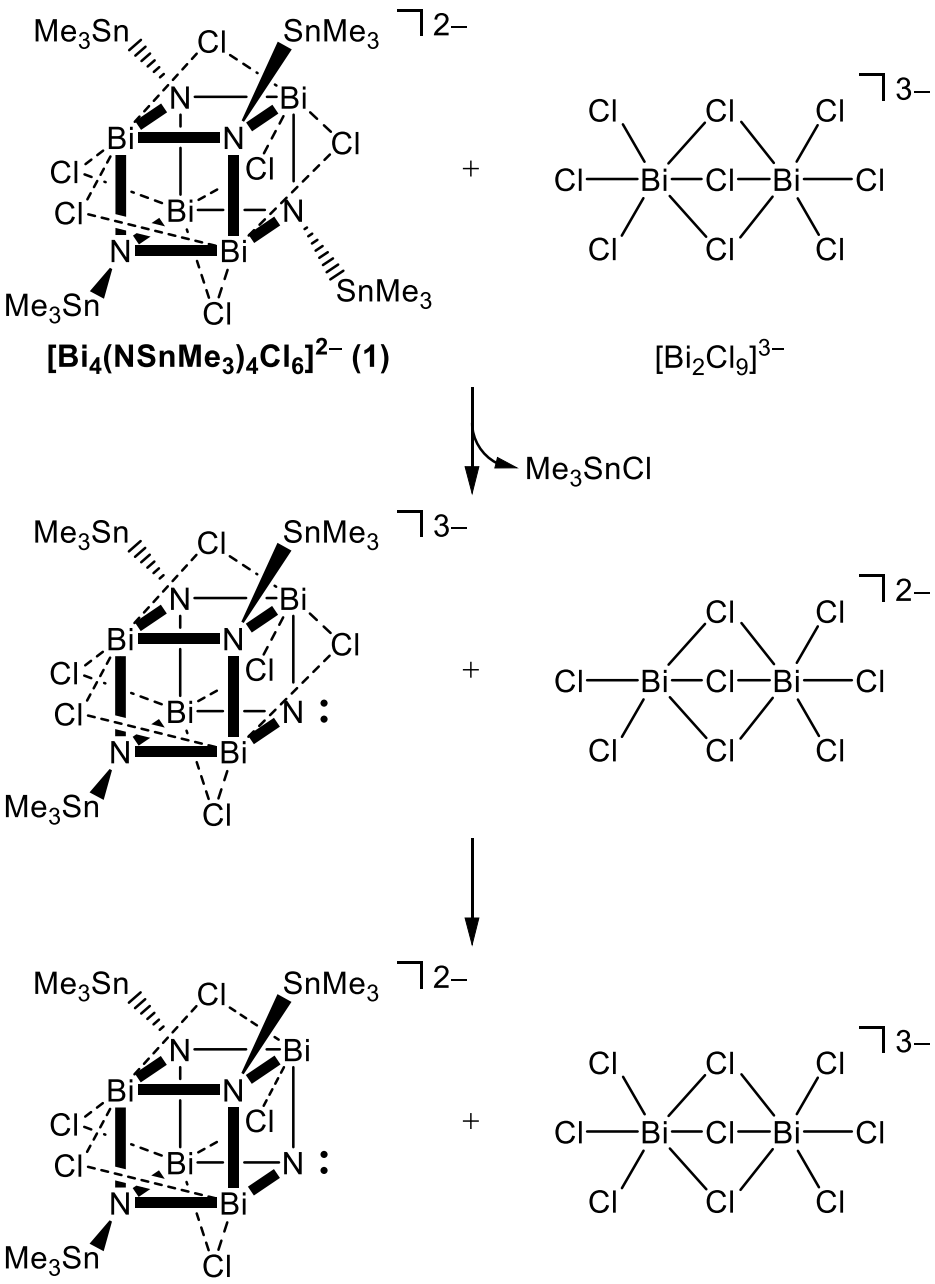

Scheme 3.10. Intermolecular dehalostannylation followed by abstraction of a chloride ion from $(Pr^{n}{}_{4}N)_2$**1** by anionic metal chloride.

Conclusion

The series of reactions monitored by ^{1}H-NMR spectroscopy between anion **1** and the metal chlorides ($AlCl_3$, $InCl_3$, $BiCl_3$, $[Bi_2Cl_9]^{3-}$, and $[GaCl_4]^{1-}$) demonstrate that trimethylstannyl groups can be removed to form new compounds in the presence of these metals. Thus, we conclude the presence of both terminal Me_3Sn- and chloride ions within the $[Bi_4(NSnMe_3)_4Cl_6]^{2-}$ anion gives unique reactivity towards a variety of metal chlorides including strong Lewis acids, heavy metal chlorides, and anionic metal chlorides. The observations from these results indicate that the reactions could be initiated by three factors: (1) abstraction of chlorides, (2) formation of $Me_3SnCl/[Me_3SnCl_2]^{1-}$ through dehalostannylation, and (3) adduct formation through equilibrium process on the anionic nitrogen sites. It is exciting that the metal-exchange process observed in the synthesis of $[B_4N_4(GaCl_3)_4]$ can be extended to several other metal halide species. Further work will include obtaining single crystals of the other metal-exchanged cubanes and attempting to link multiple cubanes via various bridging atoms. The presence of the intermediate in scheme 3.3 leads one to consider the exchange of R_3Sn- groups to generate clusters with bulkier groups on the tin to help stabilize the cluster.

Acknowledgements

We thank Dr. Laurance Beauvais, Brendan Crabb, and Merna Shoukry at Point Loma University for the ICP-OES data collection.

References

1. Bruno, I. J.; Cole, J. C.; Edgington, P. R.; Kessler, M.; Macrae, C. F.; McCabe, P.; Pearson, J.; Taylor, R. *Acta Crystallogr., Sect. B: Struct. Sci.* **2002**, *58*, 389.

2. Bickley, J. F.; Bond, A. D.; García, F.; Jantos, K.; Lawson, G. T.; McPartlin, M.; Steiner, A.; Wright, D. S. *J. Chem. Soc., Dalton Trans.* **2002**, 4629.

3. Decker, A.; Fenske, D.; Maczek, K. *Angew. Chem., Int. Ed. Engl.* **1996**, *35*, 2863.

4. Eichler, J. F.; Just, O.; Rees, W. S. *Inorg. Chem.* **2006**, *45*, 6706.

5. Veith, M.; Opsölder, M.; Zimmer, M.; Huch, V. *Eur. J. Inorg. Chem.* **2000**, 1143.

6. Kataria, J.; Mayer, P.; Vasisht, S. K.; Venugopalan, P. *J. Organomet. Chem.* **2009**, *694*, 2252.

7. Eichler, J. F.; Just, O.; Rees, W. S. In *Modern Aspects of Main Group Chemistry*; ACS Symposium Series; American Chemical Society, **2005**; Vol. 917, pp 122.

8. Kühner, S.; Kuhnle, R.; Hausen, H.-D.; Weidlein, J. *Z. Anorg. Allg. Chem.* **1997**, *623*, 25.

9. Choquette, D. M.; Timm, M. J.; Hobbs, J. L.; Nicholson, T. M.; Olmstead, M. M.; Planalp, R. P. *Inorg. Chem.* **1993**, *32*, 2600.

10. Fuchs, A.; Kaifer, E.; Himmel, H.-J. *Eur. J. Inorg. Chem.* **2008**, 41.

11. Pan, C.-L.; Chen, W.; Su, S.; Pan, Y.-S.; Wang, J. *Dalton Trans.* **2011**, *40*, 7941.

12. Monakhov, K. Yu.; Zessin, T.; Linti, G. *Eur. J. Inorg. Chem.* **2010**, 3212.

13. Ciani, G.; Moret, M.; Fumagalli, A.; Martinengo, S. *J. Organomet. Chem.* **1989**, *362*, 291.

14. Stark, J. L.; Harms, B.; Guzman-Jimenez, I.; Whitmire, K. H.; Gautier, R.; Halet, J.-F.; Saillard, J.-Y. *J. Am. Chem. Soc.* **1999**, *121*, 4409.

15. Beck, J.; Schlüter, S.; Zotov, N. *Z. Anorg. Allg. Chem.* **2004**, *630*, 2512.

16. Beck, J.; Dolg, M.; Schlüter, S. *Angew. Chem. Int. Ed.* **2001**, *40*, 2287.

17. Wilson, R. J.; Jones, J. R.; Bennett, M. V. *Chem. Commun.* **2013**, *49*, 5049.

18. Becker, G.; Rößler, M. *Z. Naturforsch., B: Chem. Sci.* **1982**, *37*, 91.

19. Diasse-Sarr, A.; Barry, A. H.; Diop, L.; Toscano, R. A.; Mahieu, B. *C.R. Chim.* **2007**, *10*, 469.

20. Das, M. K.; Buckle, J.; Harrison, P. G. *Inorg. Chim. Acta.* **1972**, *6*, 17.

Chapter 4: Preliminary Investigation of Bismuth-Nitrogen Clusters as Precursors to Materials

Introduction

Single-source precursors (SSPs) have been recognized as important reaction intermediates that can produce materials with specific properties for applications, for example, sensors, solar cells, optoelectronics, refractory materials, thermoelectrics, etc.[1–10] The applications of bismuth-nitride materials are underrepresented, yet these materials are candidates for hot-carrier solar cells[11] or as components of other applications.[12,13] The ideal sizes of these materials lie in the nano scale.[14] We have synthesized two novel bismuth-nitrogen containing compounds $(Pr^{n}{}_4N)_2[Bi_4(NSnMe_3)_4Cl_6]$, $(Pr^{n}{}_4N)_2$**1** and $[Bi_4N_4(GaCl_3)_4]$ (**2**) (Scheme 4.1) that may serve as single-source precursors.

This chapter is dedicated to preliminary studies on synthesizing bismuth-nitride nanomaterials using $(Pr^{n}{}_4N)_2$**1** and **2** as precursors in hot injection experiments (Figure 4.1). The hot injection experiment is generally conducted by rapidly introducing a precursor solution into a stirred coordinating solvent at a hot temperature.[15–20] The motif of the precursor molecule initiates the nucleation with the support of the heat while the coordinating solvent prevents the aggregation during the particle growth. The resulting particles are found in nanometer sizes if the experiment is carried out successfully. The products from these experiments differed from the molecular compounds **1** and **2** in distinct ways. While a variety of reaction conditions can be employed other than those presented in this chapter, the purpose of this initial investigation is to provide a guide for future work.

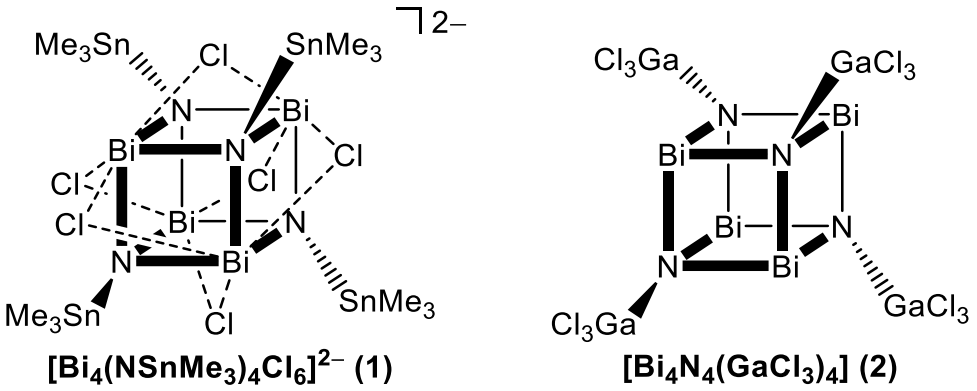

$[Bi_4(NSnMe_3)_4Cl_6]^{2-}$ (1) **$[Bi_4N_4(GaCl_3)_4]$ (2)**

Scheme 4.1. Bismuth-nitrogen clusters: $(Pr^n{}_4N)_2[Bi_4(NSnMe_3)_4Cl_6]$, $(Pr^n{}_4N)_2$**1**, and $[Bi_4N_4(GaCl_3)_4]$ (**2**).

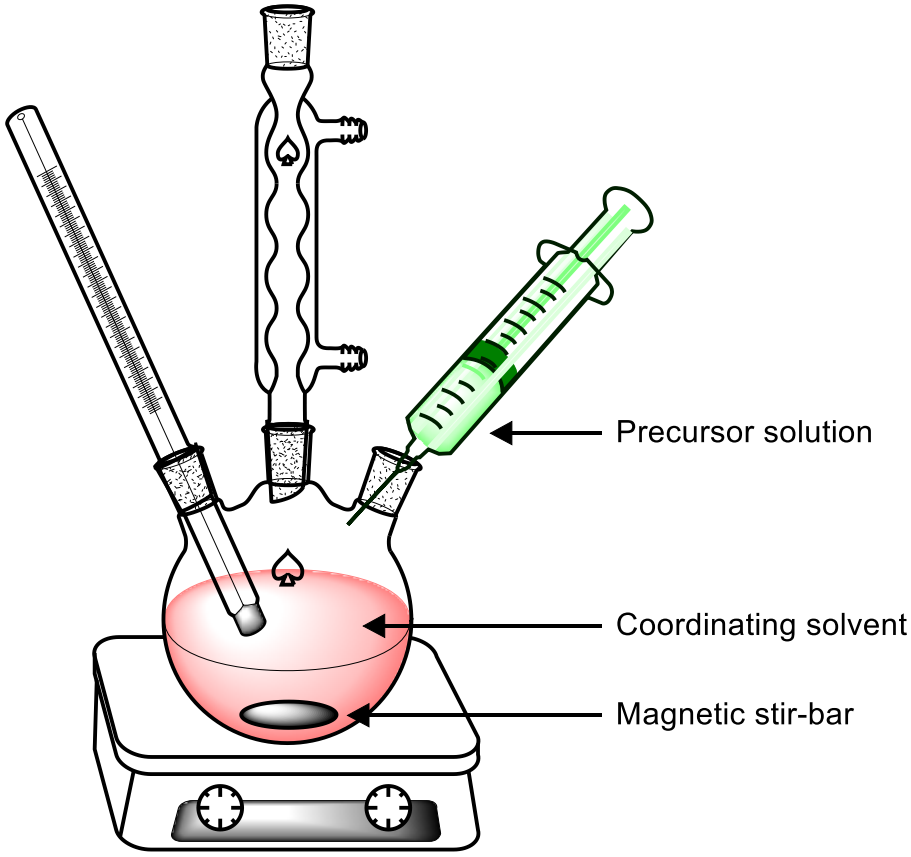

Figure 4.1. A typical apparatus used for hot injection experiments.

Experimental Section

General Concerns

Acetonitrile (MeCN) was purchased from Burdick and Jackson, hexane, diethyl ether (Et_2O), tetrahydrofuran (THF), dichloromethane (CH_2Cl_2), toluene, dimethyl sulfoxide (DMSO), ethylene diamine, propionitrile, and benzene were purchased from EMD and were stored over dried 4 Å molecular sieves for at least 18 h before use. Hexadecylamine (HDA) was purchased from Sigma-Aldrich. All reagents were stored in a nitrogen atmosphere. All other manipulations were handled in a nitrogen-filled drybox.

Preparation of Compounds

The syntheses of $(Pr^n_4N)_2[Bi_4(NSnMe_3)_4Cl_6]$, $(Pr^n_4N)_2$**1**, and $[Bi_4N_4(GaCl_3)_4]$ (**2**) are described in Chapter 2 (See Chapter 2 Experimental Section).

Characterization Methods

Diffuse reflectance spectra were recorded on a Jasco V-670 UV-Vis-NIR spectrophotometer equipped with a 60 mm integrating sphere. The background scan was taken with a nylon filter. A pulverized solid sample was evenly spread on a nylon filter for the sample scan. The powder X-ray diffraction (PXRD) patterns were collected on a Malvern Panalytical X'Pert Pro diffractometer using a Cu-K_α X-ray radiation source. The experimentally found diffraction pattern

was referenced to literature reports by using HighScore software. The scanning electron microscopy (SEM) images were collected on a FEI Quana 450 FEG Scanning Electron Microscope. The energy dispersive X-ray spectrometry (EDX) data was obtained by using an Oxford INCA Energy Dispersive Spectrometer with 50 mm^2 SDD crystal. The spectrum calibration was performed with a silicon wafer prior to data collection. Samples were placed on a carbon conductive tape affixed on an aluminum stub.

Preparation of Hot Injection Experiments

(1) Reaction of $(Pr^n_4N)_2$1 with HDA at 180 °C. Solid hexadecylamine (HDA) (4.5 g, 19. mmol) in a 100-mL three-neck round bottom flask was heated to 180 °C. An orange solution of $(Pr^n_4N)_2$**1** (0.082 g, 0.038 mmol) in 3.1 mL MeCN loaded into a syringe was rapidly injected into the liquid-phase HDA under vigorous stirring. The temperature dropped to ~80 °C and the solution became murky brown. The solution was heated at 180 °C for 18 h and the resulting solution appeared to be a murky black slurry. A 20 mL volume of hexane was added to the solution. The slurry was filtered on a fritted Büchner funnel and washed with successive aliquots of hexane (3 x 3 mL). The powder was washed with Et_2O (2 x 3 mL) and dried *in vacuo* overnight to afford 0.059 g of a black powder.

(2) Reaction of $(Pr^n_4N)_2$1 with HDA at 80 °C. Solid HDA (5.4 g, 22. mmol) in a 100-mL three-neck round bottom flask was heated to 80 °C. An

orange solution of ($Pr^n_4N)_2$**1** (0.11 g, 0.052 mmol) in 2.9 mL MeCN was loaded in a syringe and rapidly injected into the liquid-phase HDA under vigorous stirring. The temperature dropped to 67 °C and the solution became a clear, bright yellow color. The solution was heated at 80 °C for 21 h and the resulting solution was a murky light-yellow color. A 30 mL volume of hexane was added to the solution and excess HDA was allowed to dissolve overnight. The slurry was filtered on a fritted Büchner funnel and the solid product was washed with hexane (5 x 5 mL) and Et_2O (3 x 5 mL). The yellow solid was dried *in vacuo* overnight to afford 0.17 g.

(3) Reaction of [$Bi_4N_4(GaCl_3)_4$] (2) with HDA at 80 °C. Solid HDA (5.2 g, 22. mmol) in a 100-mL three-neck round bottom flask was heated to 80 °C. A pale green solution of **2** (0.070 g, 0.044 mmol) in 3.3 mL MeCN was loaded into a syringe and rapidly injected into a liquid-phase HDA under vigorous stirring. The temperature dropped to 64 °C and the solution became a murky white color. The solution was heated at 80 °C for 18 h with no visible change to the solution. A 50 mL volume of hexane was added to the solution. The slurry was filtered on a fritted Büchner funnel and the solid product was washed with hexane (5 x 5 mL) and Et_2O (3 x 5 mL). The white solid was dried *in vacuo* overnight to afford 0.16 g.

Results and Discussion

Properties of Product from Reaction (1)

Reaction of orange $(Pr^n_4N)_2$**1** in MeCN reacts with HDA at 180 °C to yield a brownish yellow solution. At 180 °C, the solution changes from an orange solution to a white murky foam. After the foam settles, a black powder was found along with a white solid. The product was washed with hexane to eliminate excess HDA (white powder) leaving only a black powder. PXRD analysis on the black powder reveals that it is metallic bismuth (Figure 4.2).[21] Thus, compound **1** is thermolabile when the reaction of (**1**) was carried out at 180 °C in the presence of the surfactant hexadecylamine (HDA). The reduction to bismuth metal may proceed through the protonation of the nitride because the surfactant is a primary amine. Similar reactions have been used to synthesize metal nanoparticles using HDA as a reducing agent.[22,23] If this hypothesis is correct, the use of aprotic surfactants would be the next approach to try.

Properties of Product from Reaction (2)

The reaction temperature was reduced to 80 °C in reaction (**2**). As opposed to reaction (**1**), reaction (**2**) resulted in a light-yellow solid, which appeared to have close resemblance of the color of compound **1**. The solubility of this product was tested in the common solvents found in the drybox: MeCN, Et_2O, THF, hexane, CH_2Cl_2, toluene, DMSO, ethylene diamine, propionitrile,

and benzene. None of these could dissolve the solid. The diffuse reflectance UV-Vis spectra of the resulting solid exhibited an absorption maxima at 340 nm, which tailed towards 600 nm while compound **1** had a peak at 313 nm and a shoulder at 454 nm (Figure 4.3). The peak remained exactly the same upon exposure to air for 24 h. This was a distinct feature compared to compound **1**, which was air-sensitive (See Chapter 2). The normalized spectra of compound **1** and the product from reaction (**2**) are clearly not the same; however, the color of the product was similar (Figure 4.4).

Electron microscopy revealed that the majority of the product particles range from 2 to 10 μm with irregular shapes (Figures 4.5). A small fraction of the product are circular particles of approximately 1 μm diameter (Figures 4.6). Those larger particles appeared to be composed of aggregates of smaller individual particles which were bound to each other. The EDX spectrum indicated the presence of the elements found in compound **1**, Bi, Cl, N, and Sn (Figure 4.7). The contribution of the tin peak was found close to the noise level. This could imply the elimination of Me_3SnCl during the reaction. The source of oxygen peak could be because of the presence of oxygen atoms in the carbon conductive tape which was used to mount the particles (Figure 4.8).

Properties of Product from Reaction (3)

Reaction (**3**) was carried out using $[Bi_4N_4(GaCl_3)_4]$ (**2**) and was performed at 80 °C similar to the reaction method used for reaction (**2**), producing a white solid. The solubility was tested with common solvents found in the drybox:

MeCN, Et_2O, THF, hexane, CH_2Cl_2, toluene, DMSO, ethylene diamine, propionitrile, and benzene. None of these could dissolve the solid. The diffuse reflectance UV-Vis spectra showed two main peaks: 276 nm (primary) and 299 nm (secondary) (Figure 4.9). The peak at 299 nm slightly became larger than that at 276 nm upon exposure to air for 24 h. Otherwise, the post-exposure spectrum appeared to be the same as the initial one. The comparison of normalized spectra between compound **2** and the product from reaction (**3**) had a distinct feature in the absorption range from 340 to 440 nm (Figure 4.10). For the case of compound **2**, the maximum peak was found at 320 nm and the shoulder peak at 410 nm. The absence of strong absorption in the visible region resulted in the white color of reaction (**3**) product.

The SEM image revealed that majority of particles found in the product ranged between 1 to 10 μm sizes with irregular shapes (Figure 4.11). These large particles were composed of aggregates of smaller particles. These findings are similar to those observed for reaction (**2**). The EDX spectrum exhibited the elements found in **2** (Figure 4.12). The source of oxygen peak could be attributed to the carbon conductive tape used to mount the particles, the same explanation given to the product of reaction (**2**).

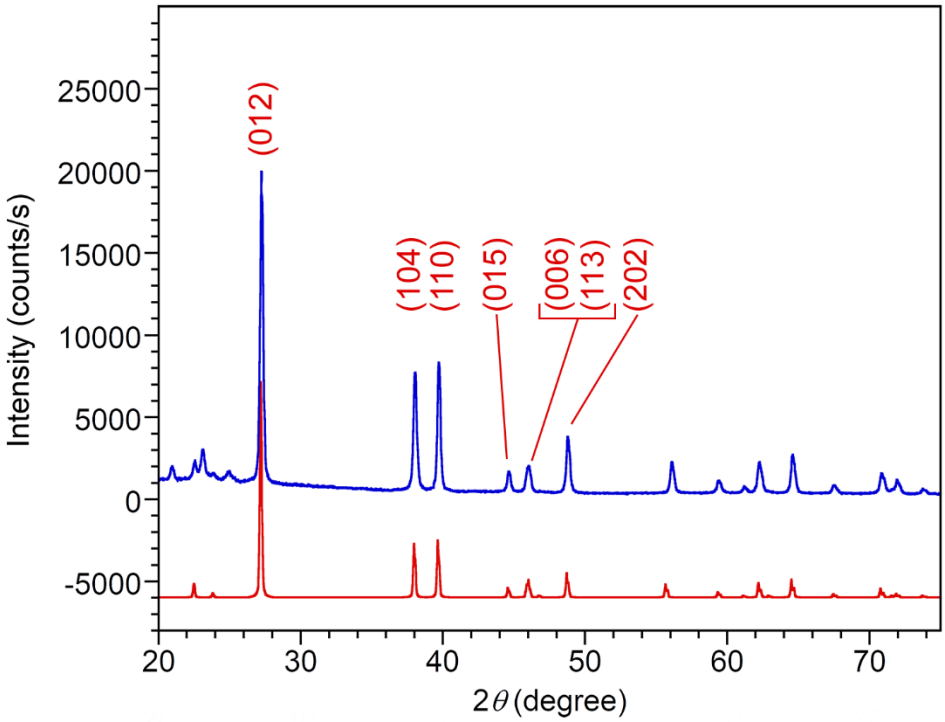

Figure 4.2. Powder X-ray diffraction pattern of the product from the reaction of $(Pr^{n}{}_{4}N)_2$**1** and HDA at 180 °C (blue). Reference: metallic bismuth (red).

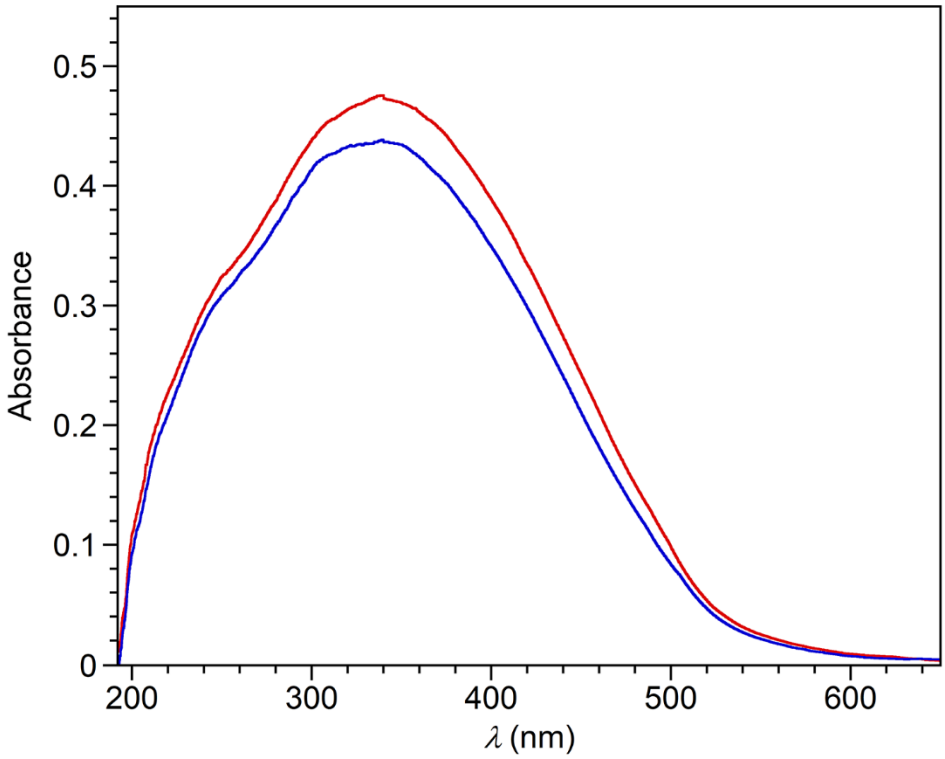

Figure 4.3. Diffuse reflectance UV-Vis spectra of the product from the reaction of $(Pr^{n}{}_{4}N)_{2}$**1** and HDA at 80 °C (red) and after-exposure to air for 24 h (blue).

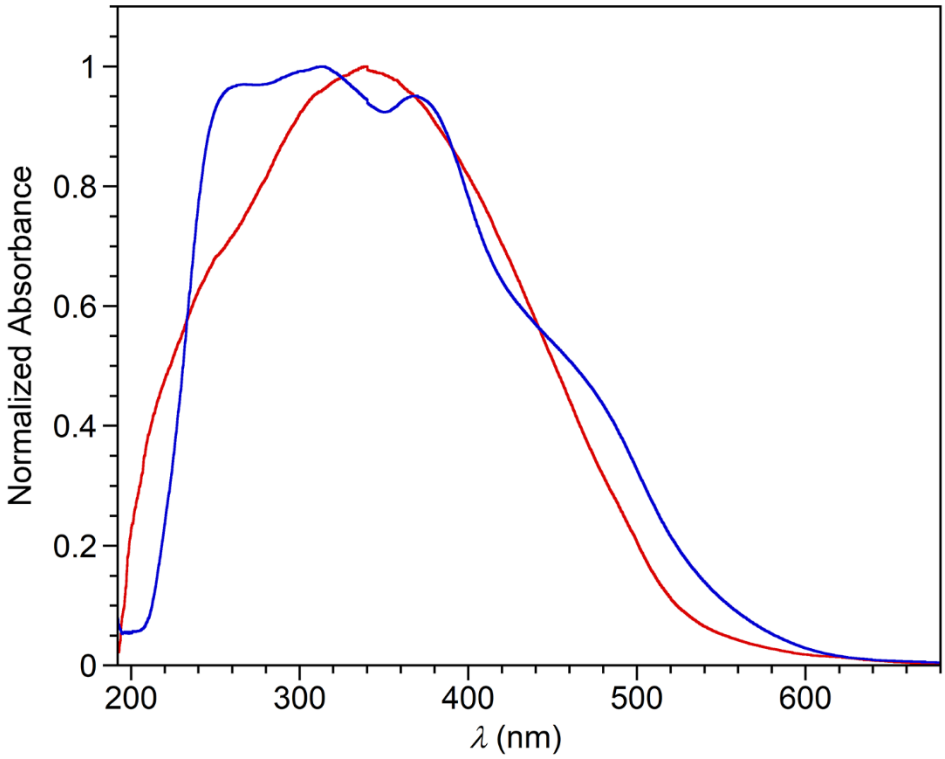

Figure 4.4. Diffuse reflectance UV-Vis spectrum of the product from the reaction of $(Pr^{n}{}_{4}N)_2$**1** and HDA at 80 °C (red). The spectrum of the starting material $(Pr^{n}{}_{4}N)_2$**1** (blue) is shown for comparison.

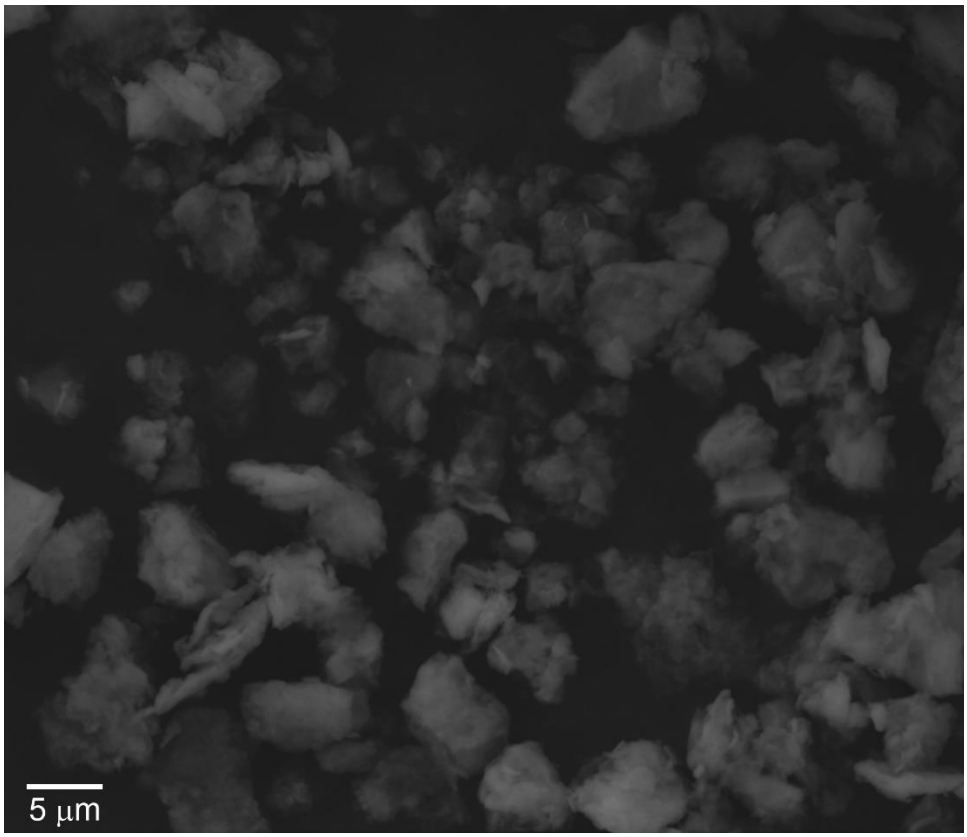

Figure 4.5. SEM image of average size particles in the product from the reaction of $(Pr^{n}{}_{4}N)_2$**1** and HDA at 80 °C.

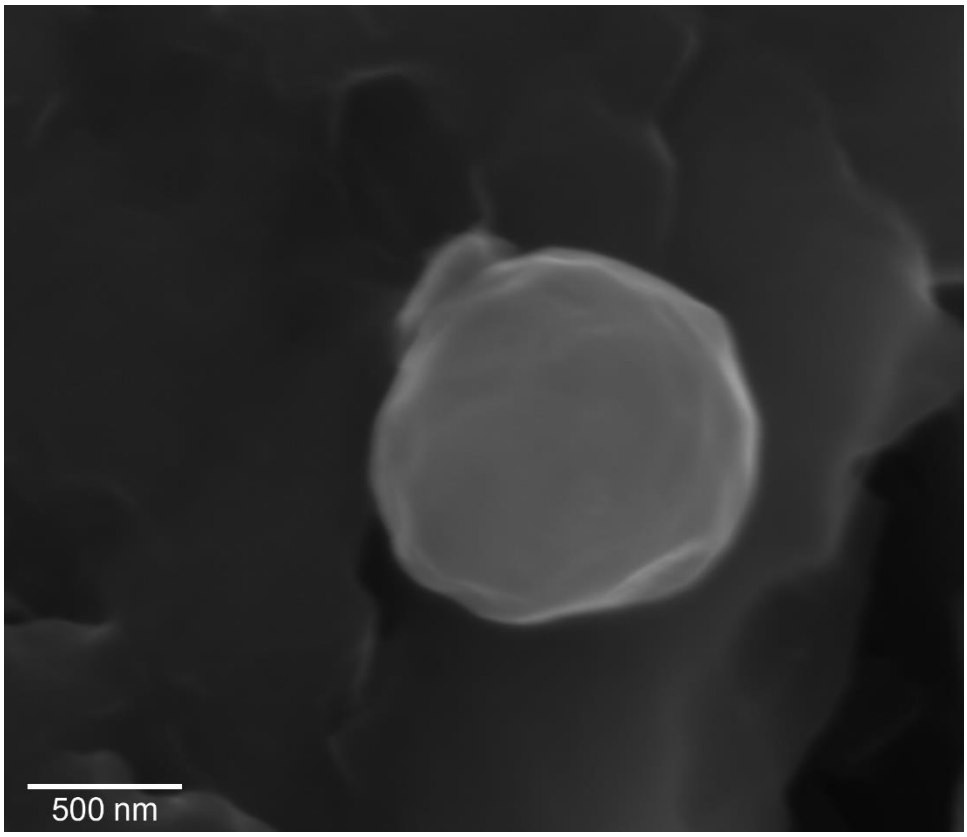

Figure 4.6. SEM image of a small particle product from the reaction of $(Pr^{n}{}_{4}N)_{2}$**1** and HDA at 80 °C.

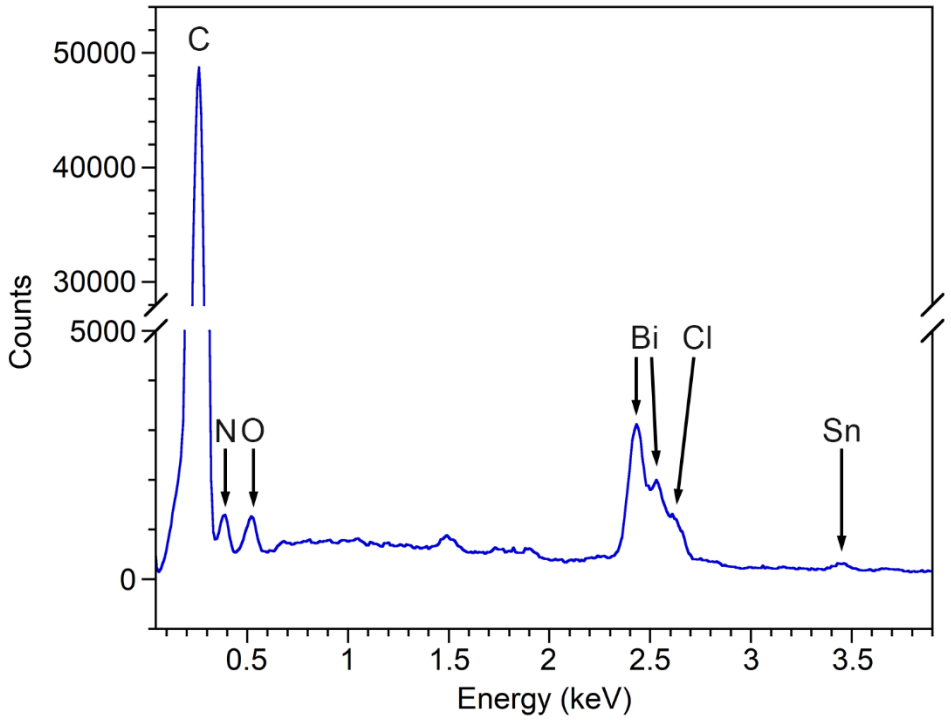

Figure 4.7. EDX spectrum of the product from the reaction of $(Pr^{n}{}_{4}N)_2$**1** and HDA at 80 °C.

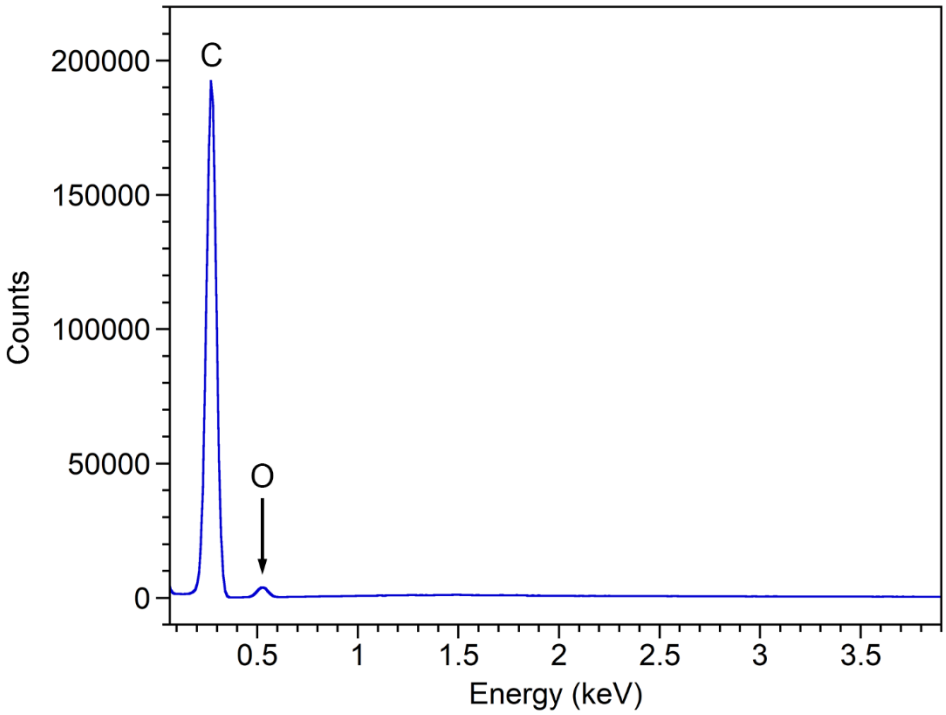

Figure 4.8. EDX spectrum of a carbon tape used to mount the sample.

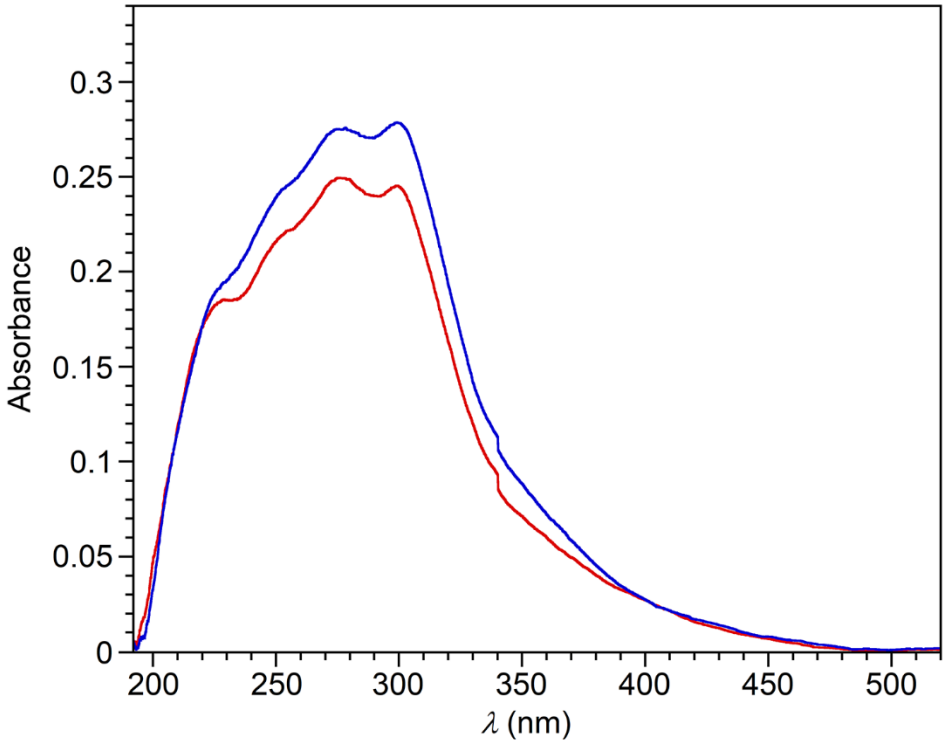

Figure 4.9. Diffuse reflectance UV-Vis spectra of the product from the reaction of compound **2** and HDA at 80 °C (red) and after exposure to air for 24 h (blue).

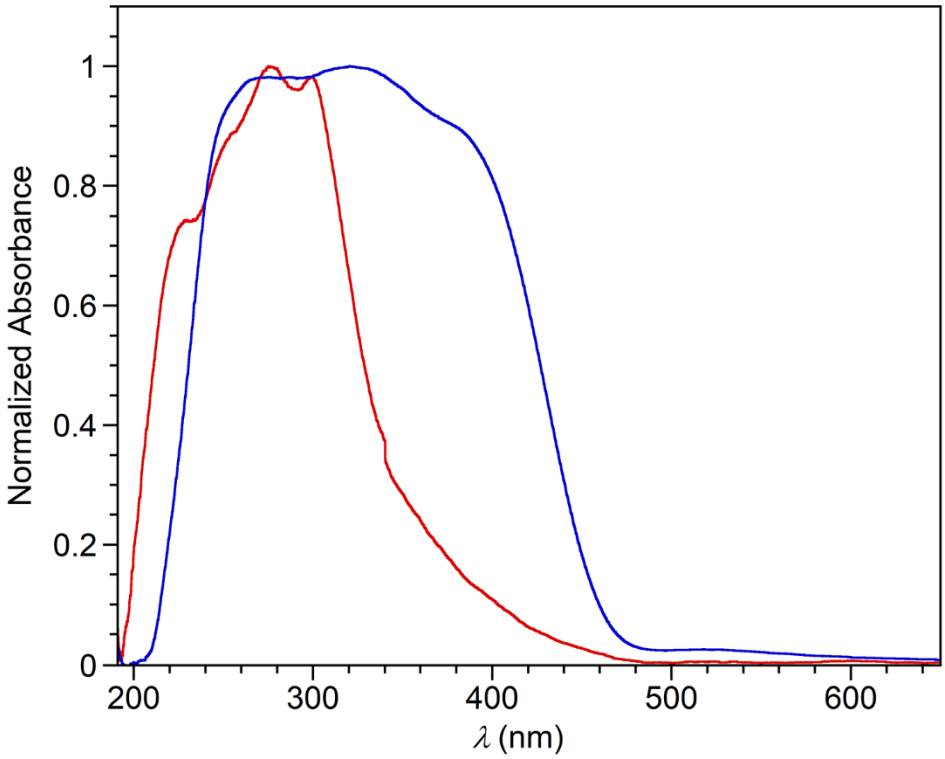

Figure 4.10. Diffuse reflectance UV-Vis spectrum of the product from the reaction of compound **2** and HDA at 80 °C (red). The spectrum of the starting material compound **2** (blue) is shown for comparison.

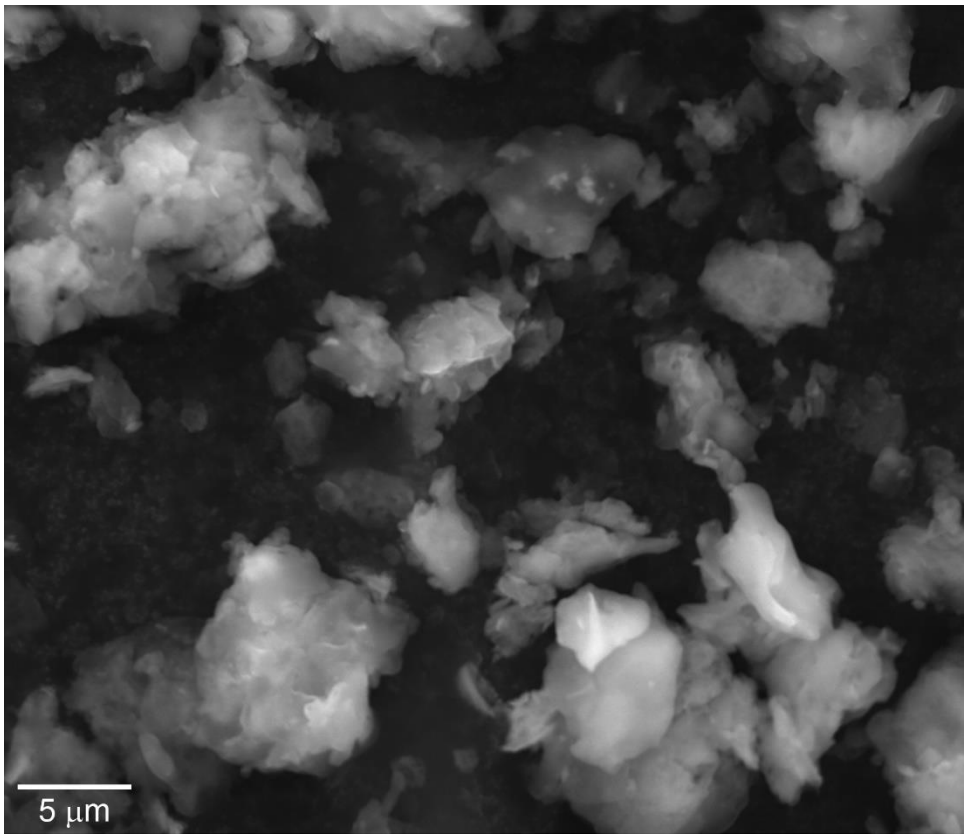

Figure 4.11. SEM image of average size particles from the product from the reaction of compound **2** and HDA.

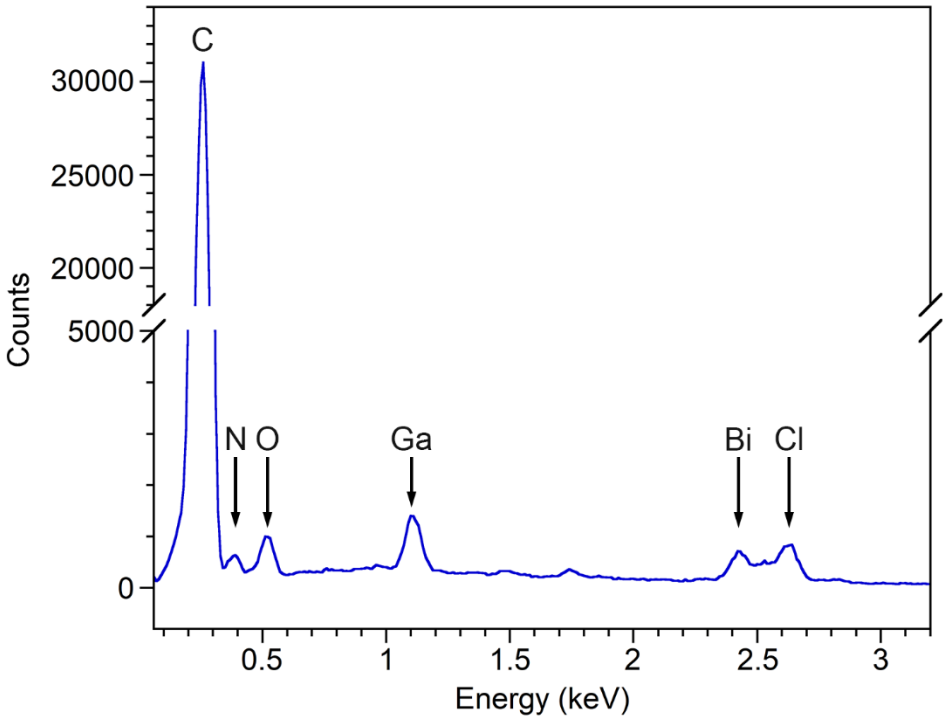

Figure 4.12. EDX spectrum of a particle product from the reaction of compound **2** and HDA.

Conclusion

The cubane $(Pr^n_4N)_2[Bi_4(NSnMe_3)_4Cl_6]$, $(Pr^n_4N)_2$**1** was used for a hot injection experiment in the presence of the surfactant hexadecylamine (HDA). Compound **1** was thermolabile when the reaction was conducted at 180 °C. The decomposition product of metallic bismuth was confirmed by the powder X-ray diffraction. The primary amine HDA may have reacted with the nitride in compound **1**, leading to reduction of bismuth to metal. When the reaction was performed at 80 °C, diffuse reflectance UV-Vis spectroscopy showed the air-stability of the product as opposed to the air-sensitive nature of **1**. The same reaction scheme at 80 °C was used for $[Bi_4N_4(GaCl_3)_4]$ (**2**). Similar to the result for compound **1**, the product was air-stable by diffuse reflectance UV-Vis spectroscopy as opposed to the air-sensitive nature of **2**. The particle products of reaction (**2**) and (**3**) had sizes ranging from 1 to 10 μm. Further modification in the procedure by changing the conditions (e.g. concentrations, reaction time, cooling rate, etc.) will help understand whether the particle size can be reduced to the nano-size and the properties will depend on the sizes. In addition, use of an aprotic surfactant such as trihexadecylamine may avoid the decomposition of the nitride ion of the cubane.

Acknowledgements

We would like to thank Dr. Laurence Beauvais for the use of the diffuse reflectance spectrometer. We thank Dr. Steven Barlow for assistance with SEM and EDX data collection, and SDSU Department of Geological Sciences for the use of powder X-ray diffractometer.

References

1. Malik, M. A.; Afzaal, M.; O'Brien, P. *Chem. Rev.* **2010**, *110*, 4417.

2. van Embden, J.; Chesman, A. S. R.; Jasieniak, J. J. *Chem. Mater.* **2015**, *27*, 2246.

3. He, G.; Shynkaruk, O.; Lui, M. W.; Rivard, E. *Chem. Rev.* **2014**, *114*, 7815.

4. Knapp, C. E.; Carmalt, C. J. *Chem. Soc. Rev.* **2016**, *45*, 1036.

5. Lewis, D. J.; Kevin, P.; Bakr, O.; Muryn, C. A.; Malik, M. A.; O'Brien, P. *Inorg. Chem. Front.* **2014**, *1*, 577.

6. Masala, O.; Seshadri, R. *Annu. Rev. Mater. Res.* **2004**, *34*, 41.

7. Reiss, P.; Carrière, M.; Lincheneau, C.; Vaure, L.; Tamang, S. *Chem. Rev.* **2016**, *116*, 10731.

8. Seisenbaeva, G. A.; Kessler, V. G. *Nanoscale.* **2014**, *6*, 6229.

9. Shi, W.; Song, S.; Zhang, H. *Chem. Soc. Rev.* **2013**, *42*, 5714.

10. Wang, F.; Richards, V. N.; Shields, S. P.; Buhro, W. E. *Chem. Mater.* **2014**, *26*, 5.

11. König, D.; Casalenuovo, K.; Takeda, Y.; Conibeer, G.; Guillemoles, J. F.; Patterson, R.; Huang, L. M.; Green, M. A. *Physica E.* **2010**, *42*, 2862.

12. Gäbler, F.; Kirchner, M.; Schnelle, W.; Schwarz, U.; Schmitt, M.; Rosner, H.; Niewa, R. *Z. Anorg. Allg. Chem.* **2004**, *630*, 2292.

13. Sun, Y.; Chen, X.-Q.; Yunoki, S.; Li, D.; Li, Y. *Phys. Rev. Lett.* **2010**, *105*, 216406.

14. Nozik, A. J. *Annu. Rev. Phys. Chem.* **2001**, *52*, 193.

15. Murray, C. B.; Norris, D. J.; Bawendi, M. G. *J. Am. Chem. Soc.* **1993**, *115*, 8706.

16. Murray, C. B.; Kagan, C. R.; Bawendi, M. G. *Annu. Rev. Mater. Sci.* **2000**, *30*, 545.

17. de Mello Donegá, C.; Liljeroth, P.; Vanmaekelbergh, D. *Small.* **2005**, *1*, 1152.

18. Park, J.; Joo, J.; Kwon, S. G.; Jang, Y.; Hyeon, T. *Angew. Chem. Int. Ed.* **2007**, *46*, 4630.

19. Williams, J. V.; Kotov, N. A.; Savage, P. E. *Ind. Eng. Chem. Res.* **2009**, *48*, 4316.

20. Timonen, J. V. I.; Seppälä, E. T.; Ikkala, O.; Ras, R. H. A. *Angew. Chem. Int. Ed.* **2011**, *50*, 2080.

21. Cucka, P.; Barrett, C. S. *Acta Cryst.* **1962**, *15*, 865.

22. Meffre, A.; Lachaize, S.; Gatel, C.; Respaud, M.; Chaudret, B. *J. Mater. Chem.* **2011**, *21*, 13464.

23. Hou, X.; Zhang, X.; Fang, Y.; Chen, S.; Li, N.; Zhou, Q. *J. Nanopart. Res.* **2011**, *13*, 1929.

Chapter 5: A New Route to a Puzzling Bismuth Phosphorus Compound

Introduction

In the interest of developing a better understanding of bismuth materials, we investigated the synthesis and structure of bismuth phosphide (BiP) materials. The only reported compound with this composition was prepared by reaction of bismuth trichloride and tris(trimethylstannyl) phosphine; however, its structure was not determined (Scheme 5.1).[1,2] The elemental data indicated an atomic ratio of Bi:P that was close to 1:1. Other elements, such as C, H, Si, and Cl, were also found. This could indicate the presence of surface species, but without structural characterization, the existence of $Cl_2Bi-P(SiMe_3)_2$ or $ClBi-PSiMe_3$ polymers or a mixture of elemental Bi, P, and byproducts cannot be excluded.

Molecules containing metal-phosphide (M−P) bonds are uncommon. Tris(trimethylsilyl) phosphine has been utilized in the synthesis of molecules containing an Al−P bond: $tmp_2AlP(SiMe_3)_2$ (tmp = 2,2,6,6-tetramethyl-piperidino),[3] and, it is logical to assume that it can serve as a source for forming other M−P bonds. The examples of M−P bond formation are found in Group III metal complexes (M = Al, Ga, In): Al−P: $[H_2AlP(SiMe_3)_2]_3$;[4] Ga−P: $[Et_2GaP(SiMe_3)_2]_2$,[5] $[Me_2GaP(SiMe_3)_2]_2$;[6] In−P: $[(Me_3SiCH_2)_2InP(SiMe_3)_2]_2$,[7] $[(Me_3SiCH_2)_2In]_2(\mu\text{-}P(SiMe_3)_2)(\mu\text{-}Cl)$,[7] and $[Ph_2InP(SiMe_3)_2]_2$.[8] All of these syntheses involve dehydrosilylation or dehalosilylation which brings concomitant production of $[(Me_3Si)_2P]^-$ and metal cation intermediates. There have been several indium-phosphorus (In−P) oligomers where $(Me_3Si)_3P$ was

used as a means to form indium-phosphido complexes. Some of the dimeric complexes to note are $[Me_2InP(SiMe_3)_2]_2$,[9,10] $[Ph_2InP(SiMe_3)_2]_2$,[8] $[(PhCH_2)_2InP(SiMe_3)_2]_2$,[11] $[Cp^*(Cl)In(\mu\text{-}P(SiMe_3)_2]_2$,[12] and $[Me(Me_3CCH_2)InP(SiMe_3)_2]_2$.[13] In these reactions, bulky substituents on the indium atoms stabilize the product and prevent side reactions. There is an example of a heterobimetallic cubane, $[\{Cp(CO)_3Mo\}_4In_4(PSiMe_3)_4]$,[14] where $(Cp(CO)_3Mo)$ moieties were substituted on indium sites. The driving force in the syntheses of these examples was dehalosilylation.

Relevant molecules that are similar to this project are bismuth-phosphide and bismuth-phosphido clusters: $[P\{BiClCH(SiMe_3)_2\}_3]$ (**3**) and $[P_2\{BiClCH(SiMe_3)_2\}_4]$ (**4**) (Scheme 5.2).[15] A lithiated organosilylphosphide was used as a precursor to form a bond with Lewis acidic bismuth atoms via a dehalosilylation mechanism. The size of the substituents on the silyl group is a key factor for determining if the product is monomeric, as in **3,** or dimeric, as observed in **4**.

Besides investigating alternative approaches for synthesizing BiP, we would like to make a molecular BiP cluster which can serve as a single source precursor for nano and bulk materials. Our preliminary result was that the black powder produced in the reaction of $BiCl_3$ and $(Me_3Si)_3P$ may lead to a mixture of elemental bismuth, phosphorus, and a mixture of byproducts. Perhaps the product contains Zintl ions as these types of ligand-free and ligand-stabilized anionic cage clusters are found in Group 14 and 15.[16] The characterization that has been attempted thus far resulted in an intractable solid.

We demonstrated that the anionic bismuth chloride complex $[Bi_2Cl_9]^{3-}$ reacts with tris(trimethylstannyl) amine in the formation of $[Bi_4(NSnMe_3)_4Cl_6]^{2-}$ and the oligomer (See Chapter 2), and, thus, we sought to investigate the reactivity of $[Bi_2Cl_9]^{3-}$ with $(Me_3Si)_3P$ (Scheme 5.3). In this chapter, we report a synthesis of a BiP product and its characterization by powder X-ray diffraction, diffuse reflectance UV-Vis spectroscopy, and transmission electron microscopy. As part of this project, the bismuth halide compounds Mes_2BiCl (**1**) and $[MesBi(\mu\text{-}Cl)]_2$ (**2**) (Mes = 2,4,6-trimethylphenyl) were structurally characterized. The presence of halides in these complexes are meant to promote dehalosilylation in the reaction with $(Me_3Si)_3P$ and the bulky mesityl-groups will inhibit polymerization.

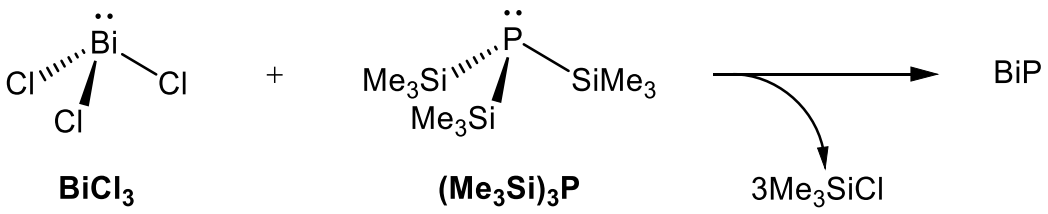

Scheme 5.1. Proposed reaction scheme attempted to produce bismuth-phosphide in the previous report.

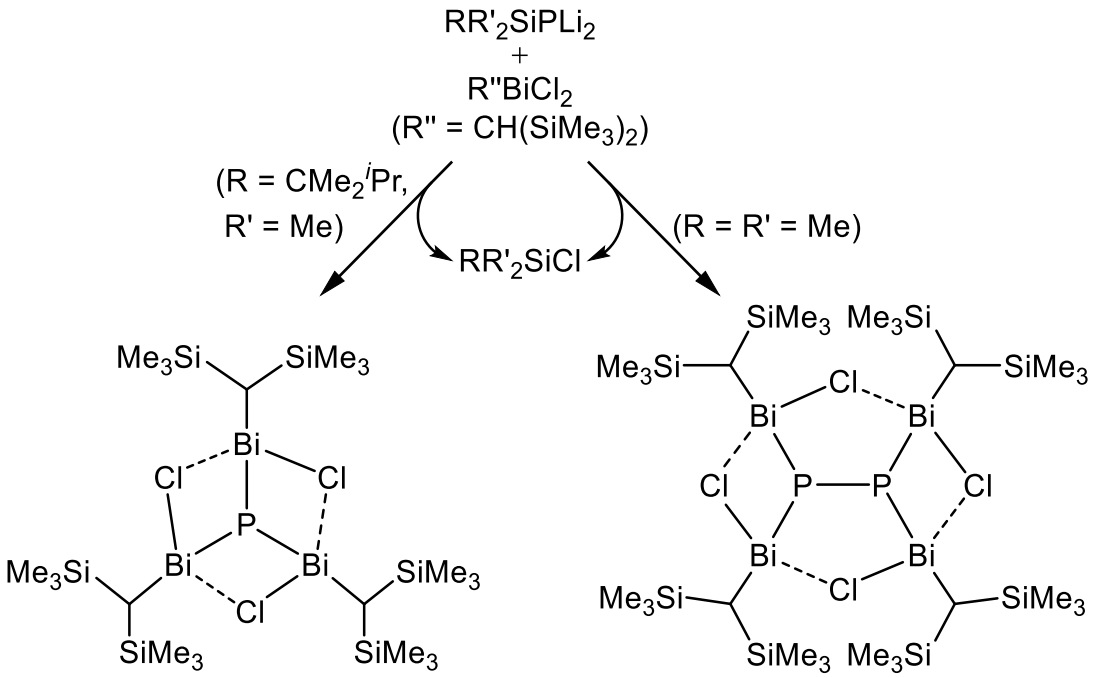

Scheme 5.2. Examples of dehalosilylation reaction in formation of bismuth-phosphide (**3**) and -imide (**4**) complexes.

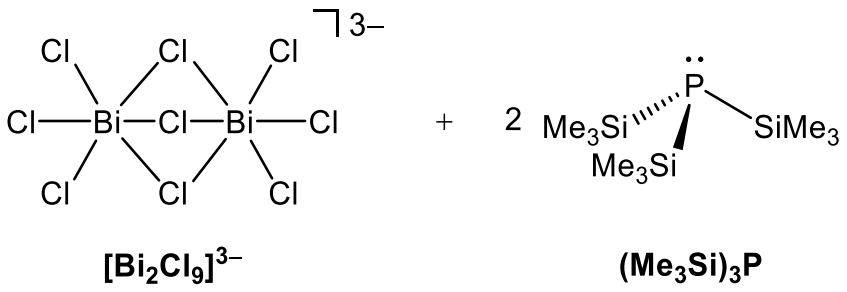

Scheme 5.3. Our approach for producing a bismuth-phosphide product.

Experimental Section

Preparation of Compounds

All operations were carried out using standard glove box and Schlenk techniques with an N_2 atmosphere unless otherwise noted. The compounds $(Me_3Si)_3P$ and $BiCl_3$ were purchased from Strem and Alfa Aesar respectively and used as received. A preparation of $(Et_4N)_3[Bi_2Cl_9]$ is given in Appendix. Mes_2BiCl (**1**) and $[MesBi(\mu\text{-}Cl)]_2$ (**2**) were synthesized according to literature procedure and were recrystallized from hot toluene.[17] Elemental analysis was performed at Columbia Analytical Services in Tucson, AZ.

(1) Reaction of $[Bi_2Cl_9]^{3-}$ and $(Me_3Si)_3P$. A solution of $(Me_3Si)_3P$ (0.036 g, 0.14 mmol) in 3.5 mL of THF was added to a solution of $(Et_4N)_3[Bi_2Cl_9]$ in (0.079 g, 0.070 mmol) in 8.8 mL of MeCN. A few drops of the phosphine turned the colorless solution to yellow and addition of the remaining phosphine resulted in a precipitation of a black powder. The reaction mixture was stirred for 90 min. The precipitate was washed successive aliquots of MeCN (3 x 5 mL) and Et_2O (3 x 3 mL) and was dried *in vacuo* overnight. The reaction afforded 0.028 mg (0.012 mmol, 82%). Elemental analysis: C, 2.58; H, 0.45; N, 0.25; Bi, 80.86; P, 12.14.

Single Crystal X-ray Diffraction Experiment

Paratone oil and nylon loops were purchased from Hampton Research. A single crystal was selected under a polarized light microscope and mounted on a nylon loop with paratone oil. The data collection was performed by using a Bruker Apex II diffractometer with a CCD detector equipped with a molybdenum sealed-tube X-ray source (λ = 0.71073 Å). The crystal was left under a cryo-temperature throughout the data collection. A scan rate of 0.5 deg/frame was used. The optimal strategy for collecting X-ray diffraction data was generated by Apex 2 software. The reflections were integrated by SAINT program and were scaled by SADABS program. Space groups were assigned using SHELXTL.[18] The structure was solved by ShelXS with a direct method and was refined by ShelXL with a least-squares method on Olex2 software.[19] The hydrogen atoms were assigned to the ideal positions on carbon atoms. All pertinent crystallographic data are summarized in Table 5.1. Selected bond lengths and angles are presented in Table 5.2 – 5.3.

Table 5.1. Crystallographic data for Mes_2BiCl (**1**) and $[MesBiCl(\mu\text{-}Cl)]_2$ (**2**).

	1	**2**
formula	$C_{18}H_{22}BiCl$	$C_{18}H_{22}Bi_2Cl_4$
formula weight, g/mol	482.78	798.11
T, K	240	100
crystal system	Monoclinic	Tetragonal
space group	$P2_1$	$I4_1/a$
a, Å	8.7026(5)	21.0283(11)
b, Å	9.3049(5)	21.0283(11)
c, Å	10.7411(6)	9.9591(6)
α, deg	90	90
β, deg	100.5876(12)	90
γ, deg	90	90
V, Å^3	854.97(8)	4403.8(5)
Z	2	8
crystal color	yellow	colorless
ρ_{calc}, g/cm^3	1.875	2.408
2θ range, deg	6.47 to 69.942	5.958 to 63.02
GOF (F^2)	0.868	1.087
R_1/wR_2, %	1.72/3.69	2.53/5.50
largest peak/hole (e$^-$/Å^3)	0.95/−0.63	0.95/−1.39
Flack x parameter	0.016(4)	

Other Characterization Methods

Diffuse reflectance spectra were collected on a Jasco V-670 UV-Vis-NIR spectrophotometer equipped with a 60 mm integrating sphere. The background scan was taken with a nylon filter. A pulverized solid sample was evenly spread on a nylon filter for the sample scan. Powder X-ray diffraction was performed with a Malvern Panalytical X'Pert Pro diffractometer with a Cu-K_α X-ray radiation source. The experimentally found peaks were referenced to previous reports on HighScore software. Transmission electron microscopy (TEM) micrographs were collected on FEI Tecnai 12 Transmission Electron Microscope. Formvar coated copper grids were used to hold the specimen. The accelerating voltage of the TEM was 120 kV. Particle size analysis was done using ImageJ software.

Results and Discussion

(1) Reaction of $[Bi_2Cl_9]^{3-}$ and $(Me_3Si)_3P$

The solid of $(Et_4N)_3[Bi_2Cl_9]$ is prepared in a similar manner as $(Pr^n{}_4N)_3[Bi_2Cl_9]$ (See Appendix). Addition of a tetrahydrofuran (THF) solution of $(Me_3Si)_3P$ into an acetonitrile (MeCN) solution of $(Et_4N)_3[Bi_2Cl_9]$ in a ratio of 1:2 results in a yellow color after addition of a few droplets of phosphine, and black powder precipitate forms thereafter (Scheme 5.4). The appearance does not change further until the end of the reaction in 90 min. The black powder is purified by washing successively with MeCN and diethyl ether. The solid is dried overnight *in vacuo*. The resulting dried solid affords 82% yield (assuming BiP product).

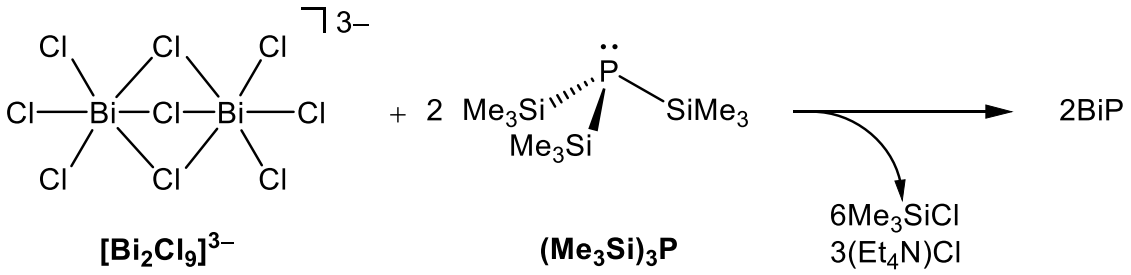

Scheme 5.4. Proposed reaction of producing bismuth-phosphide.

Properties of $[Bi_2Cl_9]^{3-}$ and $(Me_3Si)_3P$ Product

A diffuse reflectance UV-Vis-NIR spectrum of the Bi-P product reveals a broad absorption extending from 250 nm all the way to near-IR region (Figure 5.1) consistent with its black color. Because of the geometry and layout of the

X-ray diffractometer available to us, PXRD samples were mounted on glass slides and exposed to air before data collection. Upon exposure to air, the samples began to smoke and the powder took on a more rust colored hue. The PXRD data exhibits peaks that are referenced to metallic bismuth (Figure 5.2).[20] It is not clear that the Bi metal forms before or after exposure to air. Once the sample was left under aerobic conditions for 24 h color was lost from the sample. PXRD after this time revealed the presence of phosphorus in the form of bismuth phosphate hydrate (Figure 5.3).[21] Metallic bismuth found in the previous scan is still present. The TEM micrograph of the black powder with minimal exposure to air shows a cluster of semi-spherical particles (Figure 5.4). Smaller clusters are straightforward for size measurement as each individual particle is distinguishable, and a typical example is represented (Figure 5.5). The characterization of sizes on each particle finds the average size of 11.9 nm with a standard deviation of 1.6 nm. These particle sizes are distinct from the particles prepared from the reaction of $BiCl_3$ and $(Me_3Si)_3P$, which ranged between ~1 to 100 μm.[1] Further investigation is necessary to determine the nature of the black solid obtained from the reaction presented in scheme 5.4. The compound is air sensitive and the particle size of the powder obtained from scheme 5.4 is smaller. Like the sample found by Carmalt *et al.*, the elemental analysis of our samples had basically a 1:1 mole ratio of Bi:P. A structural analysis of reaction product of $[Bi_2Cl_9]^{3-}$ and $(Me_3Si)_3P$ is yet to be resolved. The powder X-ray diffraction data did not find the diffraction pattern of new species. It may be that BiP as prepared is amorphous and contaminated with Bi

metal based on PXRD. However, the PXRD data was not acquired in capillaries to prevent exposure to air. Crystalline bismuth phosphate hydrate was found in the sample stored in air for 24 h. If the bismuth-phosphide solid is amorphous, then extended X-ray absorption fine-structure (EXAFS) could reveal structural information. This technique relies on the X-ray absorption attributed to the influence by neighboring atoms and allows the elucidation for chemical and physical state of the atom such as oxidation state, coordination number, bond distances, and identity of any ligands.[22–28]

The EXAFS data interpretation of an unknown structure requires comparison with model structures consisting of atom types and bonds which are similar to proposed structure. The deconvolution can be approached by building a correlation on structural similarities between the models and the unknown. It is reasonable to collect the structural information consisting of a wide variety of analogues, so it would build the library of data necessary for deducing the structure. These selected model compounds include: $[P\{BiClCH(SiMe_3)_2\}_3]$ (**3**),[15] $[P_2\{BiClCH(SiMe_3)_2\}_4]$ (**4**),[15] $[^tBuPh_2SiP\{BiClCH(SiMe_3)_2\}_2]$ (**5**),[15] $[Bi_2(PSiPh_2{}^tBu)_4]$ (**6**),[29] and $[BiP(SiPh_2{}^tBu)_2]_2$ (**7**) (Scheme 5.5).[29] The structural characteristics of these compounds are closely related to those used for the reaction of $[Bi_2Cl_9]^{3-}$ and $(Me_3Si)_3P$, so they should be good models. This initial examination by the EXAFS will be a reasonable attempt that could lead to the structural solution.

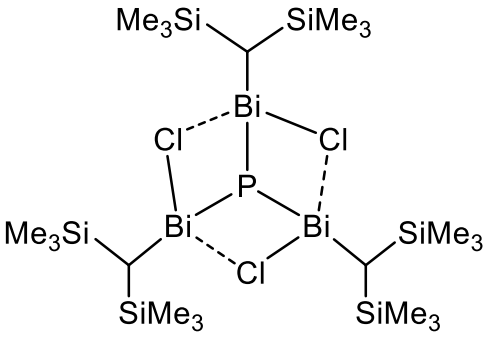

[P{BiClCH(SiMe$_3$)$_2$}$_3$]
3

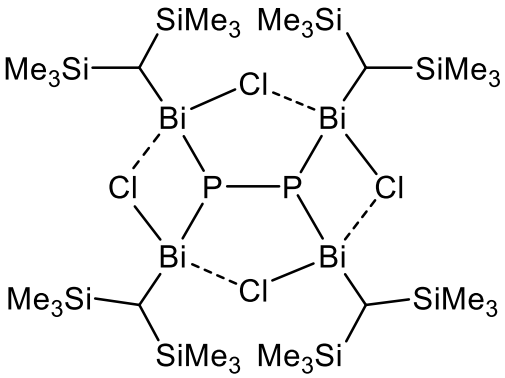

[P$_2${BiClCH(SiMe$_3$)$_2$}$_4$]
4

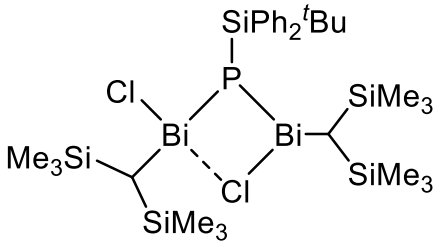

[^{t}BuPh$_2$SiP{BiClCH(SiMe$_3$)$_2$}$_2$]
5

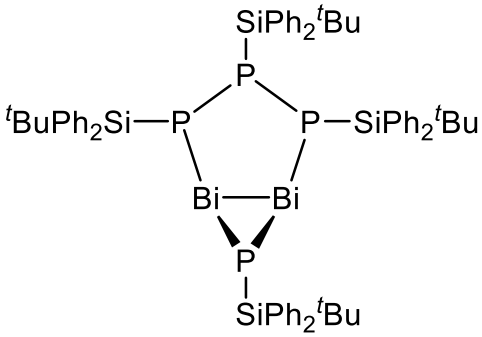

[Bi$_2$(PSiPh$_2$^{t}Bu)$_4$]
6

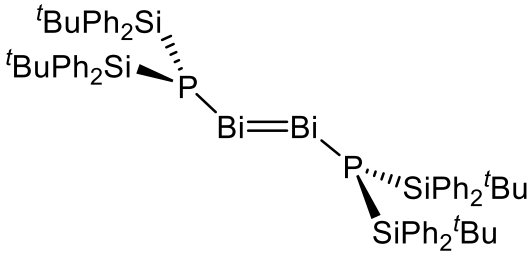

[BiP(SiPh$_2$^{t}Bu)$_2$]$_2$
7

Scheme 5.5. Model structures to be used for EXAFS analysis.

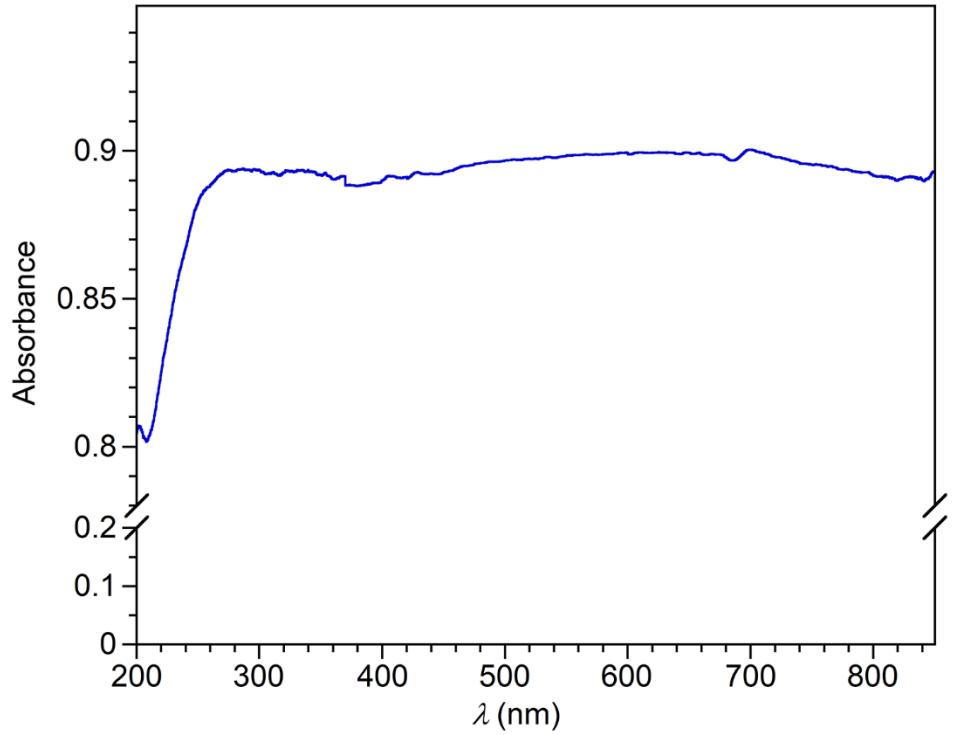

Figure 5.1. Diffuse reflectance UV-Vis spectrum of the product from reaction of $[Bi_2Cl_9]^{3-}$ and $(Me_3Si)_3P$. The spectrum was collected in the absence of air.

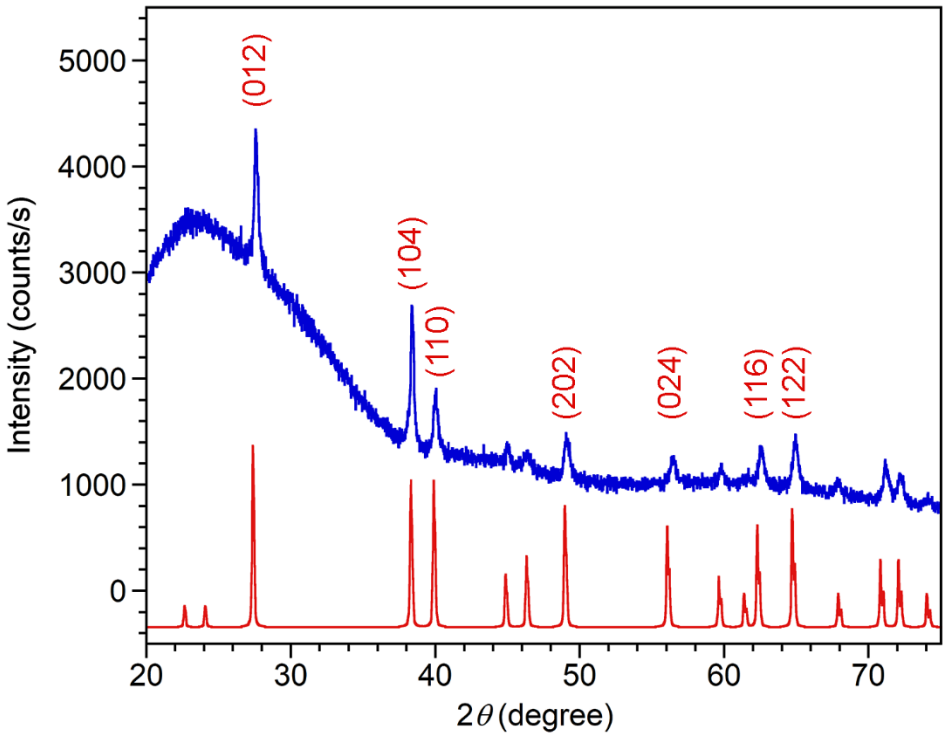

Figure 5.2. Powder X-ray diffraction data of the fine black powder obtained from the reaction of $[Bi_2Cl_9]^{3-}$ and $(Me_3Si)_3P$ (blue). Reference metallic bismuth (red).

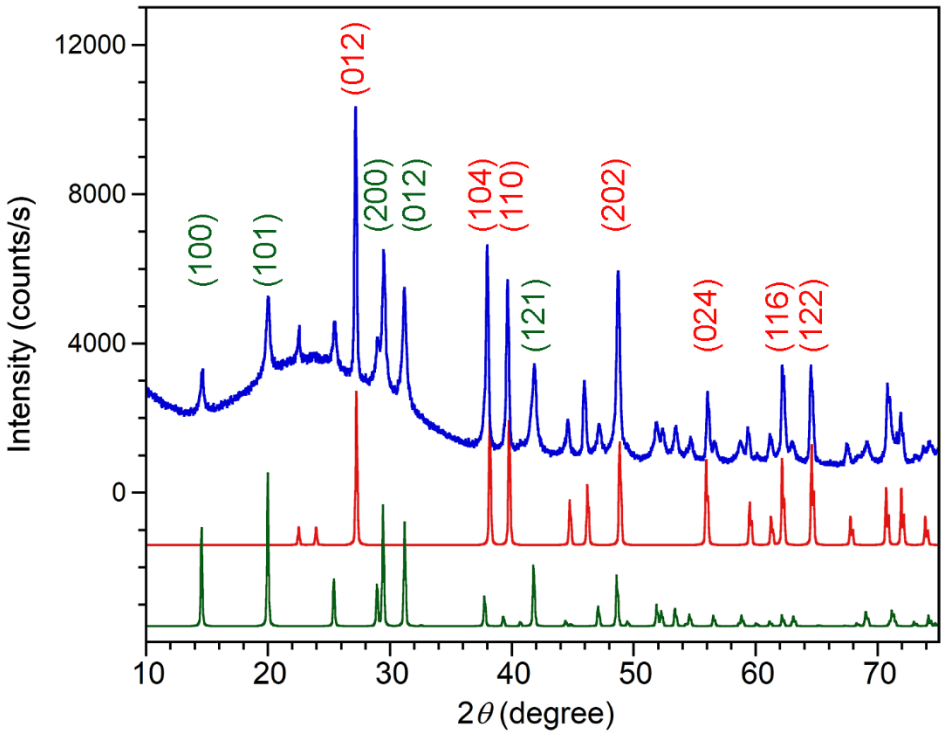

Figure 5.3. Powder X-ray diffraction data of the black powder after 24 h under aerobic conditions (blue). Reference: metallic bismuth (red); bismuth phosphate hydrate (green).

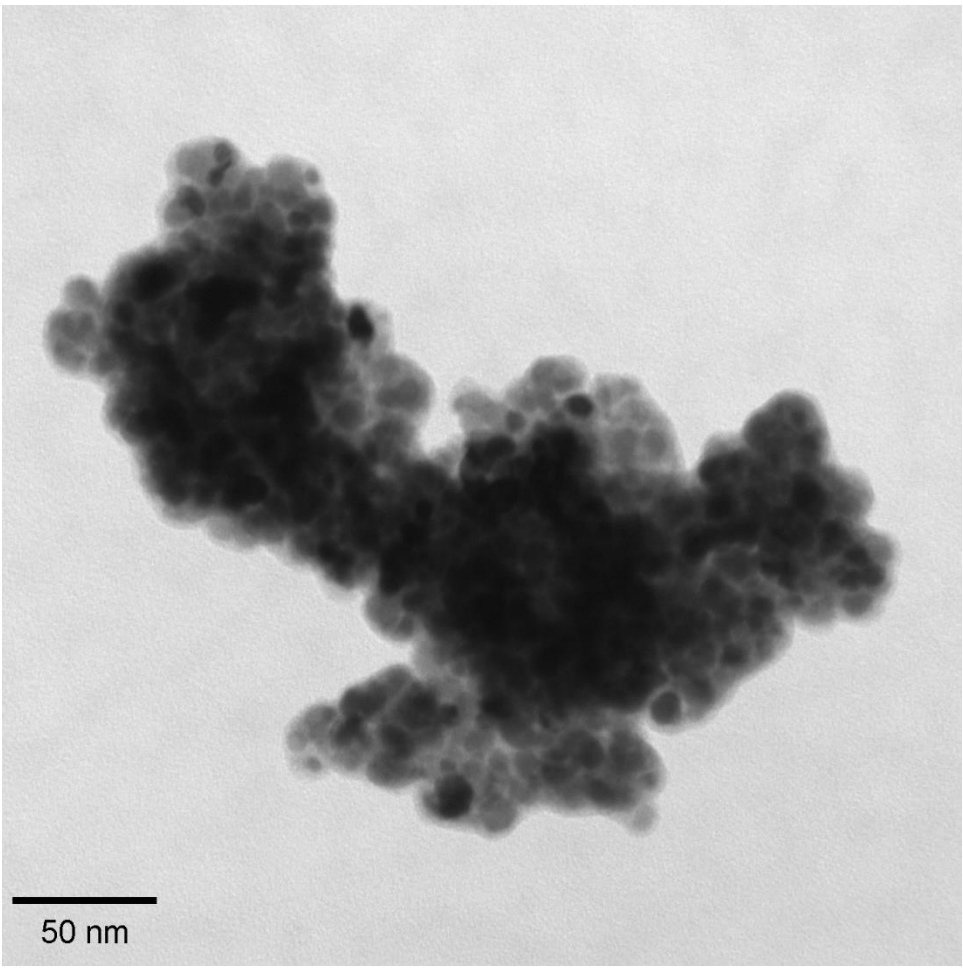

Figure 5.4. TEM micrograph of the black powder produced from the reaction of $[Bi_2Cl_9]^{3-}$ and $(Me_3Si)_3P$.

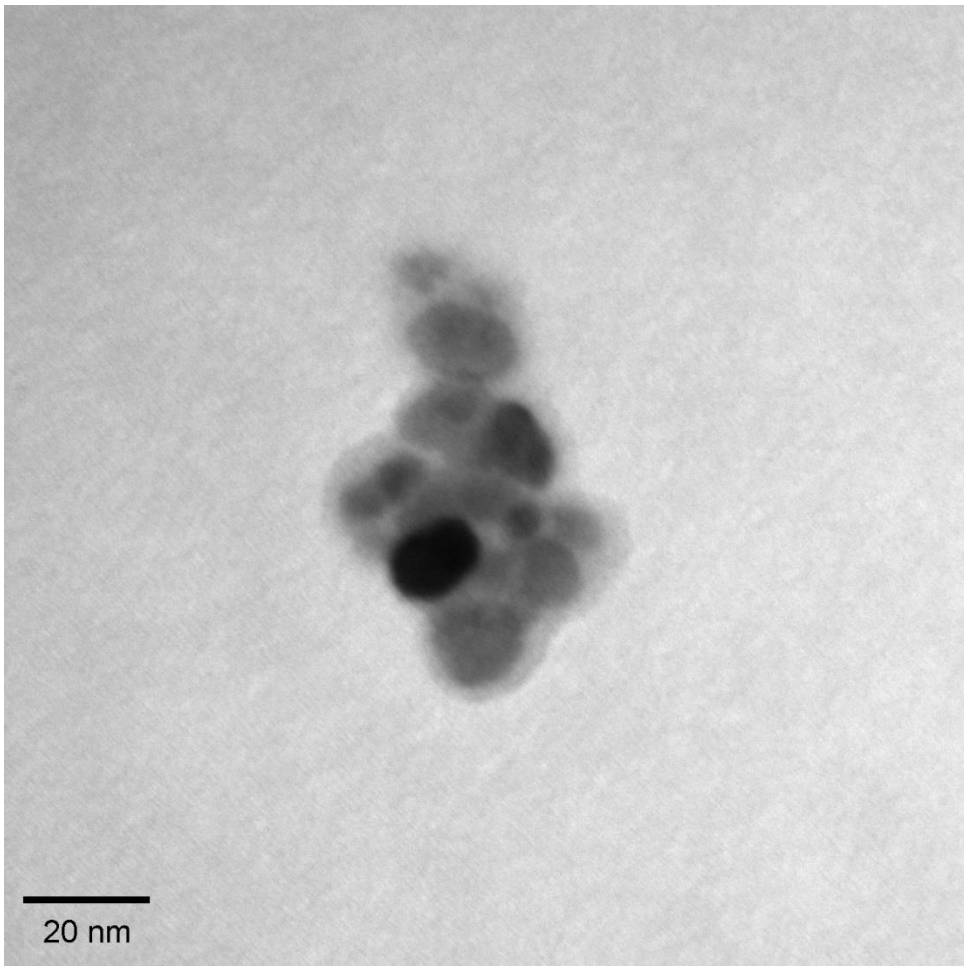

Figure 5.5. TEM micrograph of the black powder from a different spot.

Structure of (1)

A neutral complex **1** crystallizes in a monoclinic space group $P2_1$ one formula unit in the asymmetric unit. The bismuth centre adopts a trigonal pyramidal geometry (Figure 5.6). The chlorine atom resides asymmetrically with respect to the two mesityl rings. The bond angles of Cl1–Bi1–C1 and Cl1–Bi1–C10 are found at 89.74(8)° and 104.69(8)°, respectively. The ring containing C1–C9 is distorted to minimize the steric hindrance around C7 and Cl1. The close contacts between Cl1···C7 and Cl1···C18 are 3.481(5) Å and 3.397(4) Å, respectively. This type of distortion is also found in a closely related structure, R^a_2BiCl (R^a = 2,4,6-tris(trifluoromethyl)phenyl).[30] The two bond angles surrounding the Bi atom (Cl–Bi–C) in R^a_2BiCl are 87.8(2)° and 99.5(2)°. The mean Bi–C bond lengths found in **1** is 2.271(12) which are slightly shorter by ~0.1 Å than R^a_2BiCl. On the other hand, the Bi–Cl bond length is longer by ~0.1 Å. These deviations are minimal.

In the crystal packing, the chlorine atoms make a long-range interaction with a bismuth atom in an adjacent molecule in 3.9196(9) Å. This type of Bi···Cl intermolecular interactions has been found in [CH_3BiCl_2(bipy)] (bipy = 2,2-bipyridine) which are in the interatomic distances of 3.639(33) Å and 3.945(52) Å.[31] These ranges are within the sum of Bi and Cl van der Waals radii which is 4.03 Å (Bi: 2.22 Å; Cl: 1.81 Å).[32,33]

There is an isostructural compound, dimesitylbismuth(III) bromide, Mes_2BiBr, in the literature.[34] The only noticeable deviation from structure **1** is the interatomic distance of Bi–Br, which is ~0.16 Å longer owing to the larger

atomic size of bromide in the periodic trend. The interatomic distances of bismuth and carbon atom from two mesityl groups are 2.268(12) and 2.270(10) Å, which is the same for the structure of **2.** The distortion on mesityl rings are also observed in Mes_2BiBr. One of the Br–Bi–C bond angles is reported as 89.4(3)° and the other with 106.4(3)°. The substantial differences are not observed compared to **1**.

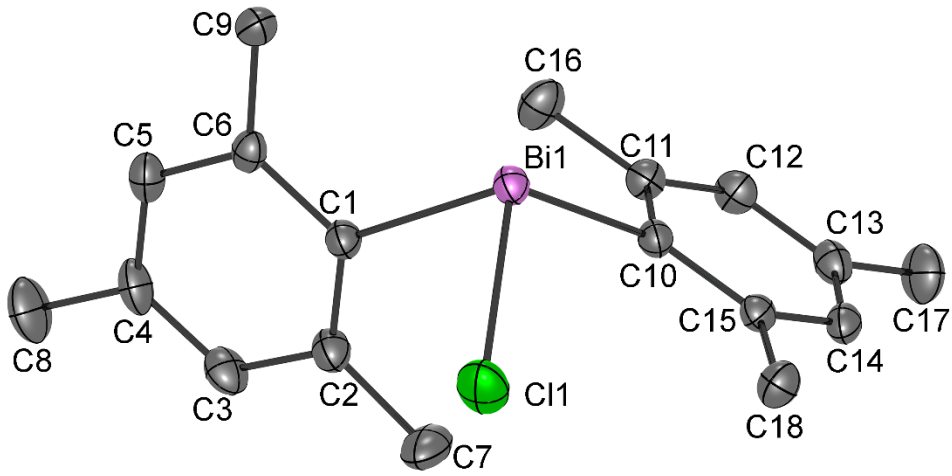

Figure 5.6. The X-ray crystal structure of **1**. The thermal ellipsoids are plotted at 50% probability level. The H atoms are omitted for clarity.

Table 5.2. Selected bond lengths (Å) and angles (°) for **1**. (Ar = aromatic; Me = methyl).

Bi–Cl	2.5352(8)	C1–Bi1–Cl1	89.74(8)
Bi–C mean	2.271(12)	C10–Bi1–Cl1	104.69(8)
C_{Ar}–C_{Ar} mean	1.398(9)	C1–Bi1–C10	97.81(11)
C_{Ar}–C_{Me} mean	1.507(5)	Bi–C1–C2	124.5(2)
C_{Ar}–C_{Ar}–C_{Ar} mean	120.0(15)	Bi–C1–C6	115.0(2)
C_{Ar}–C_{Ar}–C_{Me} mean	120.6(20)	Bi–C10–C11	116.6(2)
		Bi–C10–C15	122.9(2)

Structure of (2)

The neutral complex **2** crystallizes in the tetragonal space group $I4_1/a$ with a half of the formula unit defining the asymmetric unit (Figure 5.7a). The dimeric form is generated by the symmetry transformations (–x, 1–y, –z) and is related to the asymmetric unit by the inversion center on Cl2–Cl2' axis (Figure 5.7b). These two subunits are linked through bridging chlorides Cl2/Cl2'. The bismuth centre Bi1 adopts a seesaw geometry where Cl1 and Cl2' reside on the axial positions and C1 and Cl2 on the equatorial positions (For Bi1', Cl1' and Cl2 on axial; C1' and Cl2' on equatorial position) (Figure 5.8).

The geometrical parameters of mesityl (Mes) groups are consistent with the findings from the structure of (**1**): C_{Ar}–C_{Ar} 1.397(13) Å; C_{Ar}–C_{Me} 1.505(10) Å; C_{Ar}–C_{Ar}–C_{Ar} 120.0(21)°; C_{Ar}–C_{Ar}–C_{Me} 120.9(27)°. A plane of Mes-substituent is situated in a fashion which staggers between Cl1–Bi1–Cl2 as evidenced by the bond angles of C1–Bi1–Cl1 (93.8(1)°) and C1–Bi1–Cl2 (97.7(1))°. The steric crowd arises from the methyl groups on Mes-substituent is reduced in this manner.

The bridging chlorides (Cl2/Cl2') found in the structure are asymmetrically bound to the bismuth atoms: Bi1–Cl_{short} 2.54(1) Å; Bi1–Cl_{long} 3.095(1) Å. This type of asymmetric bonding scheme in Bi–(μ-Cl) commonly occurs in bismuth halide complexes as discussed in chapter 2 for the structure of $[Bi_4(NSnMe_3)_4Cl_6]^{2-}$. In the crystal packing, a coordination of chlorine atoms towards bismuth atoms in adjacent molecules are found in the range of 3.269(1)

Å. The distance is within the sum of van der Waals radii of 4.03 Å (Bi: 2.22 Å; Cl: 1.81 Å), so we conclude these atoms experience an intermolecular interaction.[32,33]

Mesitylbismuth(III) dibromide, $MesBiBr_2$, is found in the literature is closely related to the structure **2**.[17] These two structures possess a halide atom(s) that bridges to another molecular unit. The structure **2** is bridged through two chlorines which forms a dimer while $MesBiBr_2$ displays an extended solid through one bromide bridging to another. The bridging bromide bonds to bismuth atoms asymmetrically: $Bi–Br_{short}$ 2.808(3) Å and $Bi–Br_{long}$ 3.022(3) Å. The short is longer by 0.3 Å and the long is approximately the same compared to $Bi–Cl_{short/long}$. The bond angle formed by $C–Bi–Br_{terminal}$ is 106.8(7)° as opposed to 93.86(10)° in C1–Bi1–Cl1. The reason to account for the large deviation is the greater steric congestion towards one of the methyl groups on mesityl substituent due to the presence of bromide.

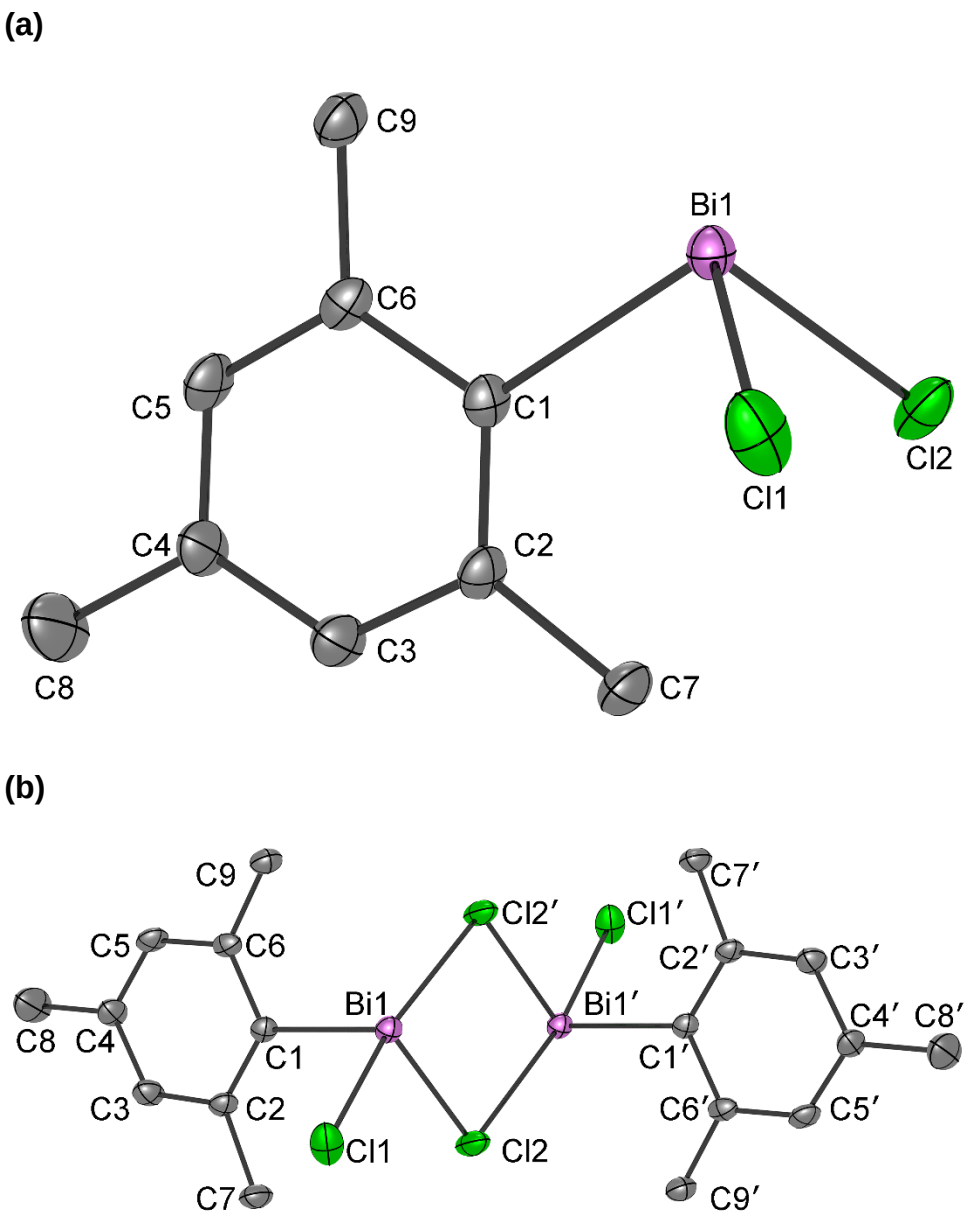

Figure 5.7. Asymmetric unit of complex **2** in the X-ray crystal structure (a) and the dimeric form of **2** (b). The thermal ellipsoids are plotted at 50% probability level. Hydrogen atoms are omitted for clarity. Symmetry transformations used to generate equivalent atoms: –x, 1–y, –z.

Table 5.3. Selected bond lengths (Å) and angles (°) for **2**. (Ar = aromatic; Me = methyl).

$Bi1–Cl_{short}$	2.540(10)	Bi1–C1–C2	125.0(3)
$Bi1–Cl_{long}$	3.0955(10)	Bi1–C1–C6	114.4(3)
Bi1–C	2.254(4)	C1–Bi1–Cl1	93.86(10)
Bi1–Bi1'	4.3686(6)	C1–Bi1–Cl2'	91.11(10)
$C_{Ar}–C_{Ar}$ mean	1.397(13)	C1–Bi1–Cl2	97.71(10)
$C_{Ar}–C_{Me}$ mean	1.505(10)	Cl1–Bi1–Cl2	95.07(4)
$C_{Ar}–C_{Ar}–C_{Ar}$ mean	120.0(21)	Bi1–Cl2–Bi1'	101.03(3)
$C_{Ar}–C_{Ar}–C_{Me}$ mean	120.9(27)	Cl1–Bi1–Cl2'	172.72(3)
		Cl2–Bi1–Cl2'	78.97(3)

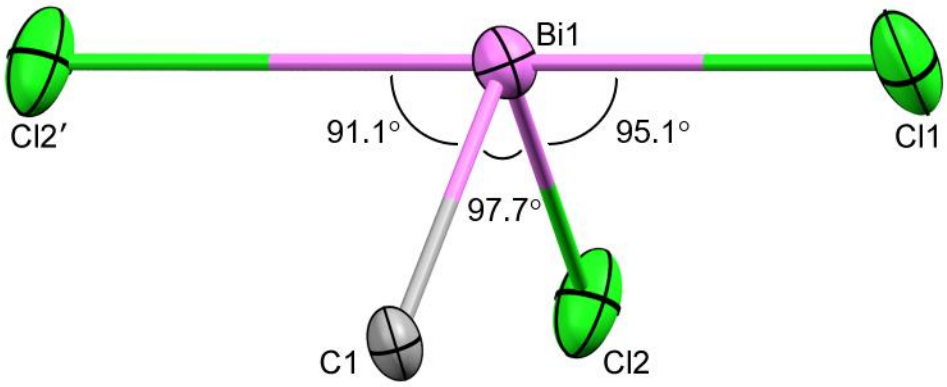

Figure 5.8. Selective atoms showing a seesaw geometry at Bi1 centre in X-ray crystal structure of **2**. The thermal ellipsoids are plotted at 50% probability level.

Conclusion

The reaction of $[Bi_2Cl_9]^{3-}$ and $(Me_3Si)_3P$ in solution resulted in a precipitation of black powder which is similar to the BiP compound previously reported from the reaction of neutral $BiCl_3$ and $(Me_3Si)_3P$. The elemental analysis is consistent with a 1:1 mole ratio of Bi:P. This powder absorbs spectroscopic range of UV-Vis-NIR in a solid state. The powder X-ray diffraction shows a presence of metallic bismuth in as-prepared sample after exposure to air for 20 min, and bismuth phosphate hydrate after 24 h left under air. The powder sample is very fine (10 – 15 nm range) as TEM micrographs show, and the particles sizes are significantly smaller than those synthesized from $BiCl_3$. EXAFS studies of BiP material obtained using $[Bi_2Cl_9]^{3-}$ and $BiCl_3$ can be compared. Compounds with the bonding motifs reported in 2009 may shed light on the nature of the bonding in these intractable solids.

Additionally, two complexes whose structures were previously uncharacterized, Mes_2BiCl (**1**) and $[MesBi(\mu\text{-}Cl)]_2$ (**2**) were structurally elucidated by single-crystal X-ray diffraction. These are potential precursors to compounds containing Bi-P bonds.

Acknowledgement

Chapter 5 contains material that is currently being prepared for publication. Yamamoto, N.; Nash, A. G.; Baker, S.; Bennett, M. V. “Investigation of the Reactivity of $[Bi_2Cl_9]^{3-}$ with $(Me_3Si)_3P$”. *Manuscript in preparation*. The dissertation author was the primary researcher for the data presented. Aaron Nash began investigating the reaction of $[Bi_2Cl_9]^{3-}$ with $(Me_3Si)_3P$. I would like to thank Dr. Beauvais for the use of diffuse reflectance spectrophotometer, Aaron Nash and Stig Baker for growing crystals of arylbismuth halide complexes, and SDSU Department of Geological Sciences for the use of powder X-ray diffractometer.

References

1. Carmalt, C. J.; Cowley, A. H.; Hector, A. L.; Norman, N. C.; Parkin, I. P. *J. Chem. Soc., Chem. Commun.* 1994, 1987.

2. Allen, G. C.; Carmalt, C. J.; Cowley, A. H.; Hector, A. L.; Kamepalli, S.; Lawson, Y. G.; Norman, N. C.; Parkin, I. P.; Pickard, L. K. *Chem. Mater.* 1997, *9*, 1385.

3. Habereder, T.; Nöth, H.; Paine, R. T. *Eur. J. Inorg. Chem.* 2007, *2007*, 4298.

4. Janik, J. F.; Wells, R. L.; White, P. S. *Inorg. Chem.* 1998, *37*, 3561.

5. Jouet, R. J.; Wells, R. L.; Rheingold, A. L.; Incarvito, C. D. *J. Organomet. Chem.* 2000, *601*, 191.

6. Wiedmann, D.; Hausen, H.-D.; Weidlein, J. *Z. Anorg. Allg. Chem.* 1995, *621*, 1351.

7. Wells, R. L.; McPhail, A. T.; Self, M. F. *Organometallics.* 1992, *11*, 221.

8. Wells, R. L.; McPhail, A. T.; Jones, L. J.; Self, M. F. *Polyhedron.* 1993, *12*, 141.

9. Stuczynski, S. M.; Opila, R. L.; Marsh, P.; Brennan, J. G.; Steigerwald, M. L. *Chem. Mater.* 1991, *3*, 379.

10. Thomas, F.; Schulz, S.; Nieger, M. *Z. Anorg. Allg. Chem.* 2002, *628*, 235.

11. Banerjee, C.; Hughes, D. L.; Bochmann, M.; Nann, T. *Dalton Trans.* 2012, *41*, 7244.

12. Douglas, Trevor.; Theopold, K. H. *Inorg. Chem.* 1991, *30*, 594.

13. Wells, R. L.; McPhail, A. T.; Self, M. F. *Organometallics.* 1993, *12*, 3363.

14. App, U.; Merzweiler, K. *Z. Anorg. Allg. Chem.* 1995, *621*, 1731.

15. von Hänisch, C.; Stahl, S. *Z. Anorg. Allg. Chem.* 2009, *635*, 2230.

16. Scharfe, S.; Kraus, F.; Stegmaier, S.; Schier, A.; Fässler, T. F. *Angew. Chem. Int. Ed.* 2011, *50*, 3630.

17. Becker, G.; Egner, J.; Meiser, M.; Mundt, O.; Weidlein, J. *Z. Anorg. Allg. Chem.* 1997, *623*, 941.

18. Sheldrick, G. M. *Acta Crystallogr., Sect. A: Found. Crystallogr.* 2008, *64*, 112.

19. Dolomanov, O. V.; Bourhis, L. J.; Gildea, R. J.; Howard, J. A. K.; Puschmann, H. *J. Appl. Crystallogr.* 2009, *42*, 339.

20. Davey, W. P. *Phys. Rev.* 1925, *25*, 753.

21. Romero, B.; Bruque, S.; Aranda, M. A. G.; Iglesias, J. E. *Inorg. Chem.* 1994, *33*, 1869.

22. Alexeev, O.; Gates, B. C. *Top. Catal.* 2000, *10*, 273.

23. Gurman, S. J. *J. Mater. Sci.* 1982, *17*, 1541.

24. Hayes, T. M.; Boyce, J. B. In *Solid State Physics*; Ehrenreich, H.; Seitz, F.; Turnbull, D., Eds.; Academic Press, 1983; Vol. 37, pp 173.

25. Lee, P. A.; Citrin, P. H.; Eisenberger, P.; Kincaid, B. M. *Rev. Mod. Phys.* 1981, *53*, 769.

26. Manaila, R.; Macovei, D. *J. Non-Cryst. Solids.* 1987, *90*, 383.

27. Scott, R. A. In *Methods in Enzymology*; Academic Press, 1985; Vol. 117, pp 414.

28. Wong, J. *Mater. Sci. Eng.* 1986, *80*, 107.

29. von Hänisch, C.; Nikolova, D. *Eur. J. Inorg. Chem.* 2006, *2006*, 4770.

30. Whitmire, K. H.; Labahn, D.; Roesky, H. W.; Noltemeyer, M.; Sheldrick, G. M. *J. Organomet. Chem.* 1991, *402*, 55.

31. Althaus, H.; Breunig, H. J.; Lork, E. *Organometallics.* 2001, *20*, 586.

32. Batsanov, S. S. *Inorg. Mater.* 2001, *37*, 15.

33. Bondi, A. *J. Phys. Chem.* 1964, *68*, 441.

34. Ebert, K. H.; Schulz, R. E.; Breunig, H. J.; Silvestru, C.; Haiduc, I. *J. Organomet. Chem.* 1994, *470*, 93.

Chapter 6: Seedless, One-Pot Synthesis of Near-Infrared Absorbing Silver Nanoparticles

Introduction

Silver nanoparticles of tunable size and shape can be produced in solution by a variety of chemical methods. In most basic and applied studies, the solvent is water. Broadly speaking, the nanoparticles are produced by the reduction of silver ions in the presence of a capping agent (a ligand or a polymer) that binds to the surface and stabilizes the nanoparticles either electrostatically or sterically, so that they do not aggregate upon collision. The simplest approaches yield nanospheres in the 5 to 20 nm diameter range. In the Turkevich method, citrate acts as both the reducing agent and capping agent, and the aqueous solution must be heated to near boiling in order to initiate the reduction.[1] A more rapid way of producing silver nanospheres is to reduce silver ions by sodium borohydride in the presence of a capping agent, most commonly citrate.[2,3]

Silver nanoparticles having shapes other than spheres can also be prepared by adjusting the reagents and reaction conditions. Triangles, cubes, hexagons, rods, tetrahedra, as well as more complex shapes such as core-shell and flower-like structures have been made.[4,5] Here we will focus on the simplest shape, the triangle, because 1) the synthesis is simple and fast, and 2) its optical properties are tunable and suitable for the solar cell application discussed in Chapter 7.

The key to producing the nanotriangles is careful control of the reaction conditions so that a suitable balance between growth kinetics and

thermodynamics is achieved. As the nanoparticles begin to grow, different crystal facets are formed and exposed to the surroundings. If a ligand can bind preferentially to a particular facet, this facet could then be blocked from binding to incoming silver atoms. Growth of the nanoparticle would then occur on facets that are less protected, resulting in anisotropic shapes.[6] The degree of anisotropy would be expected to depend on the rate of ligands colliding, binding, and optimally orienting themselves on the surface, relative to the rate of collision and binding of silver atoms with the surface. This mechanism of anisotropic growth is consistent with experiment (although direct proof is lacking) as well as Density Functional Theory calculations of citric acid binding to silver surfaces by Kilin *et al*.[7] Their work concluded that citric acid binds more strongly to Ag(111) surfaces compared to Ag(100) surfaces. This is due to a better matching of the spacing between citric acid's carboxylic acid groups with the spacing between the silver atoms of a (111) surface compared to a (100) surface. The better matching leads to the formation of four weak bonds between a citric acid molecule and the Ag(111) surface versus two weak bonds with the Ag(100) surface. Thus, growth on the (111) surface of a nanoparticle is inhibited while growth on the (100) surface is favored. Since the basic structural motif of a (111) surface is a triangle of closest-packed atoms, triangular nanoplates are produced in which the top and bottom surfaces are (111) and the edges are (100) (or perhaps other Miller Index planes).

The synthesis of silver nanotriangles usually follows either seeded or seedless approaches. In the seeded case, small silver nanoparticles (often

spheres) are first synthesized.[8] These “seeds” are then transferred to a second reaction mixture containing silver ions, ligands, and a reducing agent. The seeds serve as nucleation sites for larger nanoparticles and tend to outcompete any newly formed small clusters in the growth. Triangles are formed by the mechanism discussed in the previous paragraph.

In the seedless approaches, only a single reaction mixture is used, and the balance between growth kinetics and thermodynamics is achieved by having simultaneous chemical reduction and oxidative dissolution. Zhang *et al.* found that when sodium borohydride was added to an aqueous solution containing sodium citrate, silver nitrate, and hydrogen peroxide, the resulting nanoparticles were triangular nanoplates.[9] By increasing the concentration of the hydrogen peroxide, the size of the nanoplates could be increased. They explained their results using a modified version of the mechanism in the previous paragraph. As usual, the borohydride induces the formation of small nanoparticles, and those presenting larger (111) facets will be stabilized by the citrate. Nanoparticles having larger fractions of other facets will tend to be oxidatively dissolved by the peroxide, leaving silver ions that can once again be reduced and potentially added to the growing edges of the triangular nanoplates. The nanoplates thus grow at the expense of small clusters.

The ability to synthesize silver nanoparticles of different sizes and shapes is important in optical applications. This is because the optical properties of silver nanoparticles are strongly dependent on their size and shape. As the size of a nanoparticle becomes bigger, the plasmon resonance

wavelength becomes longer. In a qualitative sense, this can be understood because as the extent of motion of electrons in a physical system becomes larger, the energy levels of the electrons decrease and become closer together. The particle-in-a-box model provides the simplest link between the size of a system and the energy levels of the particle. In the 1-dimensional case, the energy levels are given by $E_n = n^2h^2/(8mL^2)$, where n is the quantum number, h is Planck's constant, m is the mass of the particle, and L is the length of the box in which the particle moves.[10] The separation between neighboring energy levels is $(2n+1)h^2/(8mL^2)$, so $\Delta E \alpha 1/L^2$ or $\lambda \alpha L^2$. This relation for the resonance wavelength is very approximate since it is based on the 1-dimensional particle-in-a-box model, but it does predict trends in the resonance wavelength as a function of the size of the nanoparticle.

In this chapter, a seedless, one-pot method is presented for synthesizing silver nanotriangles whose size can be controlled. The plasmon resonance can therefore be tuned throughout the visible range and into the near-infrared. Because the main application of these nanoparticles will be in binding them to solar cells to enhance photovoltaic performance, the requirements on their properties are that:

- they absorb or scatter light in spectral regions where solar cells do not absorb well (red and infrared)
- they are stable at room temperature for long periods of time
- the capping agents are easily displaced to enable facile binding of the nanoparticles to surfaces

- the synthesis is simple, involves as few reagents as possible, and is scalable to produce a large quantity of nanoparticles

To the best of our knowledge, while many procedures exist for producing silver nanoparticles that meet some of these requirements, none of them meet all of the criteria.

The method we developed is based on the scheme reported by Zhang *et al.* (discussed above) in which sodium borohydride was added to an aqueous solution containing sodium citrate, silver nitrate, and hydrogen peroxide. Their main conclusion was that the concentration of H_2O_2 dictated the silver nanoplates' final absorption maxima, which ranged from the visible to the near-IR spectral region. The more H_2O_2 used, the more the peak shifted to the red. One drawback which they discuss was that the near-IR absorbing nanoplates disintegrated after several hours. To avoid this problem, they tried two approaches. First, they found that the addition of polyvinylpyrrolidone (PVP) in the reaction mixture helped preserve the nanoplates, presumably by binding to the nanoplates as a robust steric capping agent. Second, they reduced the concentration of H_2O_2 by half and were able to produce stable red to near-IR absorbing nanoparticles, but the extinction of these nanoparticles was not high enough to fill in the absorption range where silicon solar cells do not absorb the light efficiently.

The method of Zhang *et al.* almost meets the four requirements listed above, but the rapid dissolution of the near-IR absorbing nanoplates as well as the inability to absorb significantly past 900 nm are significant problems for our

solar cell application (the near-IR absorbing nanoplates are precisely the ones we are most interested in using). The addition of PVP to solve the problem introduces a large, polymeric capping agent that inhibits binding to surfaces and is therefore undesirable for our application. The principal goal in our work, therefore, is to overcome the dissolution problem without using bulky ligands.

Dissolution of the near-IR-absorbing silver nanoplates can possibly be explained by excess H_2O_2 that may remain in the post-reaction solution. We hypothesize that reaction conditions, having the same reagents but different stoichiometric ratios, exist that would leave little or no excess H_2O_2. The near-IR-absorbing nanoplates would be stable while having the easily displaced citrate as a capping agent. After presenting our synthetic procedure, characterization of the optical and morphological properties will be given, using UV-Vis-NIR spectroscopy, dynamic light scattering (DLS), and transmission electron microscopy (TEM).

Experimental Section

Chemicals and Materials

Silver nitrate ($AgNO_3$, 99.5%+), sodium borohydride ($NaBH_4$, 99%+), and 200 proof ethanol (EtOH, 99.5%+) were purchased from Acros Organics. Sodium borohydride solid was stored in a N_2-filled drybox. Once taken out of the drybox, it was stored in a vacuum desiccator, and the vial was flushed with N_2 gas after each use. After five uses, a new batch was brought from the drybox.

Trisodium citrate dihydrate ($Na_3C_6H_5O_7$, or Na_3Cit, 99%+) and hydrogen peroxide (H_2O_2, 30 wt % or ca. 9.79 M) were purchased from Fisher Scientific. The hydrogen peroxide solution was stored in 4 °C refrigerator. Formvar/carbon 300 mesh copper grids were purchased from Ted Pella, Inc.

Preparation of Reagents

Aqueous solutions of 5 mM $AgNO_3$ and 50 mM Na_3Cit were prepared in 100 mL volumetric flasks and then stored in the dark. A solution of 5 mM Na_3Cit was prepared by diluting 50 mM Na_3Cit stock solution in a 100 mL volumetric flask. A 0.675 M H_2O_2 solution was prepared by adding 2 mL of 30% H_2O_2 to 27 mL of deionized (DI) water and then stored in 4 °C refrigerator. For the synthesis of yellow AgNPs, a 0.45 mM solution of $NaBH_4$ was prepared by serious dilution. First, 17 mg of $NaBH_4$ solid was added to 100 mL of DI water to make a 4.5 mM solution, followed by vigorous shaking for 10 s. Then, 1 mL of the solution was added to 9 mL DI water to make the 0.45 mM solution. This final solution was vigorously shaken for 10 s. The rapid mixing was needed because $NaBH_4$ reacts with water, thus, degrading the BH_4^-. For the synthesis of the triangular-shaped AgNP samples, a 100 mM of $NaBH_4$ solution was prepared by adding 19 mg of $NaBH_4$ solid to 5 mL of DI water. As above, the solution was vigorously shaken for 10s.

Preparation of Silver Nanoparticles

Triangular AgNPs were synthesized at ambient temperature, air, and room light conditions. The general reaction scheme involves mixing of the Na_3Cit, $AgNO_3$, and H_2O_2 solutions and vigorously stirring, followed by reducing the stirring rate and adding the $NaBH_4$ solution. Specific steps of the procedure will be now given, with the solution that ultimately turned orange being used as an example. Details will be provided they are critical in determining the final properties of the nanoparticles. First, 13.18 mL of DI water was added to a 20 mL scintillation vial. The stirring rate was made vigorous (the bottom of the vortex was slightly above the magnetic stirbar). Then, 0.45 mL of the 50 mM Na_3Cit stock solution was added to the DI water, followed by adding 0.80 mL of the 5 mM $AgNO_3$ stock solution dropwise. The dropwise addition is important in order to minimize production of trisilver citrate, which is relatively insoluble in water (solubility = 0.56 mM).[11] Next, 0.42 mL of 0.675 mM H_2O_2 solution was added, and the mixture was continued to be vigorously stirred for 10 minutes. Then, the solution was slowly stirred for 3 minutes. During this 3 minute period, the 100 mM $NaBH_4$ was prepared. A 0.15 mL aliquot of the 100 mM $NaBH_4$ solution was rapidly injected into the slowly stirred solution, leading to a change in the color of the solution from colorless to yellow. After 30 s of induction time, a rapid color change to orange took place. The solution was allowed to stir for another 5 minutes. Due to the light-sensitive nature of AgNPs, the samples were stored in the dark immediately after each experiment and at room temperature unless the experiment required storage in a 4 °C refrigerator.

To make the different colored nanoparticle solutions, the concentration of $AgNO_3$ was varied while the concentrations of Na_3Cit, H_2O_2, and $NaBH_4$ were held constant. The induction time became longer when the initial $AgNO_3$ concentration decreased. For example, the pale blue AgNPs had the longest induction time, which was 8 minutes. As a comparison with the triangular AgNPs, spherical yellow AgNPs were prepared. First, 13.55 mL of DI water was added to a 20 mL scintillation vial. The stirring rate was made vigorous (the bottom of the vortex was slightly above the magnetic stirbar). Then, 0.30 mL of the 5 mM Na_3Cit stock solution was added to the DI water, followed by adding 0.30 mL of the 5 mM $AgNO_3$ stock solution dropwise. Lastly, 0.85 mL of the 0.45 mM $NaBH_4$ solution was added dropwise to the mixture, resulting in a yellow color. The stirring was stopped after 1 minute. The reaction conditions for all the AgNP solutions are listed in Table 6.1. The reaction volume was fixed at 15 mL for all the AgNP solutions. The concentrations of reagents referred to in the caption are concentrations prior to the initiation of the reaction.

Table 6.1. List of concentrations of reagents for synthesizing each color of AgNP solution.

Color	Na_3Cit, mM	$AgNO_3$, mM	$NaBH_4$, mM	H_2O_2, mM
Yellow	0.100	0.100	0.0255	Not used
Orange	1.50	0.267	1.00	19.0
Red	1.50	0.200	1.00	19.0
Wine Red	1.50	0.167	1.00	19.0
Purple	1.50	0.133	1.00	19.0
Violet	1.50	0.100	1.00	19.0
Blue	1.50	0.078	1.00	19.0
Light Blue	1.50	0.050	1.00	19.0
Pale Blue	1.50	0.017	1.00	19.0

Characterization of the Nanoparticles

UV-Vis-NIR spectroscopy. UV-Visible-NearIR extinction spectra were collected on a Jasco V-670 spectrometer equipped with a temperature controller (EHC-746). The temperature was set to 23.0 °C. Quartz cuvettes of 1 cm pathlength were used in all measurements. The background for all samples was recorded with DI water. The orange, red, and wine red AgNP solutions were diluted by half with DI water due to their high absorbances.

Dynamic Light Scattering. The size and distribution of the nanoparticles were studied using a Malvern Zetasizer Nano-ZS dynamic light scattering instrument whose light source is a 633 nm solid-state laser. A sample volume of 100 μL was loaded into a disposable plastic polystyrene cuvette (Malvern ZEN0040) An equilibration time of 30 seconds was selected to allow the temperature to stabilize at 25.0 °C, and in preliminary measurements, the instrument automatically optimized the number of scans needed and the focal point of the laser in the sample. The final measurements were then recorded.

Transmission Electron Microscopy. The morphology and size distribution were analyzed by using a Tecnai T12 transmission electron microscope (TEM). A 2 μL AgNP solution was mixed with 8 μL 200 proof ethanol on a small piece of parafilm by retracting and dispensing the mixture multiple times. The mixing of EtOH allowed quick drying of the droplets on the TEM grids. One μL was pipetted from this mixture and then loaded onto a formvar/carbon-coated

copper grid (Ted Pella 01753-F) and left in the dark to dry. After 15 minutes, the grid was washed by immersing it in 200 μL of DI water that had been pipetted onto the parafilm. Excess water on the grid was blotted off from the side with a small piece of filter paper. The grid was left in air in the dark until it was completely dry. For the light blue and pale blue AgNPs, this staining process was repeated two more times because these solutions were dilute. The accelerating voltage of the TEM was 120 kV.

Centrifugation. Narrowing of the size distribution of the blue and pale blue silver nanoparticles was achieved by centrifugation with an Eppendorf 5430 Centrifuge. For both samples, 1.2 mL of the solutions was added to each of six 1.5 mL centrifuge tube. In the case of the blue AgNPs, a speed of 10,000 or 17,500 rpm for 15 min was used, while in the pale blue AgNPs case, a speed of 5000 rpm was used. The topmost 0.5 mL layer from each supernatant was first transferred to a 20 mL scintillation vial, and then 30 μL of each pellet was transferred to another vial that contained 7.02 mL of 1.5 mM Na_3Cit to achieve the same concentration of Na_3Cit as in the original nanoparticle samples.

Results and Discussion

Dependence of Solution Color on [Ag^+]

The size and shape distributions of the nanoparticles were determined by the relative concentrations of the reactants. In particular, we found that varying the $AgNO_3$ concentration while maintaining the concentrations of other reagents constant was a straightforward and reliable method of altering the size and shape of the nanoparticles (and therefore their color). The concentrations of all the reagents were given in Table 6.1. The resulting solutions are shown in Figure 6.1. The solutions starting from orange and proceeding to pale blue all contained H_2O_2 and decreasing concentrations of $AgNO_3$. The yellow nanoparticle solution on the left is included as a comparison and did not contain H_2O_2. The corresponding UV-Vis-NIR spectra are shown in Figure 6.2. The intensities are normalized in order to simplify a comparison of the peak positions. The normalization factors are given in the caption of the figure.

[Ag^+] 100 267 200 167 133 100 78 50 17 (μM)

Figure 6.1. Yellow, orange, red, wine red, purple, violet, blue, light blue, and pale blue AgNPs synthesized in the lab (left to right).

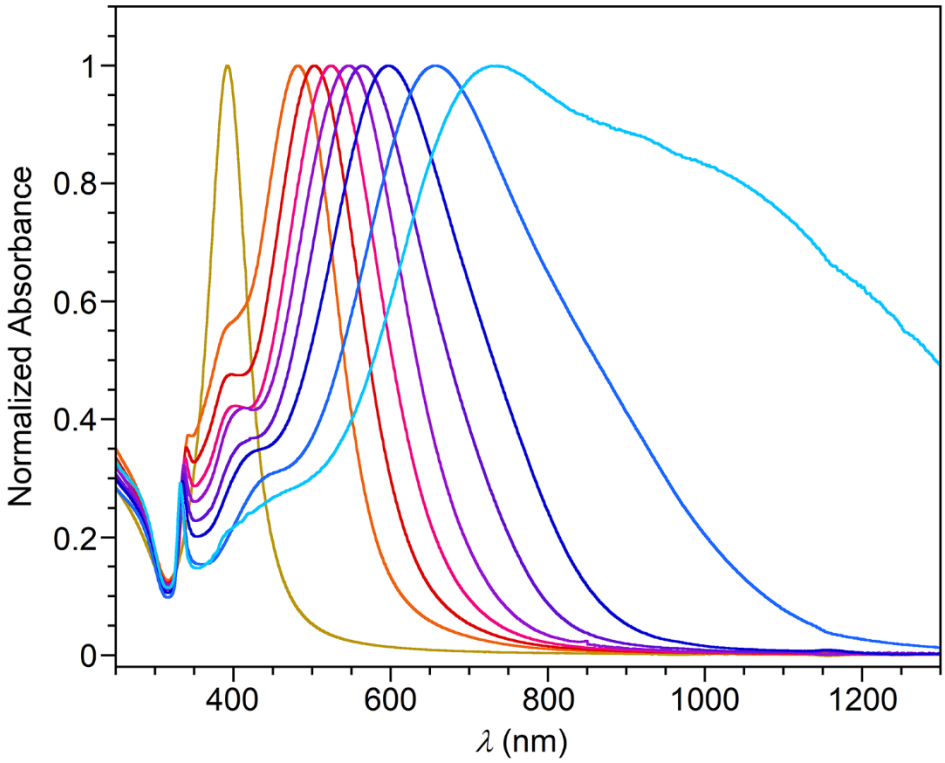

Figure 6.2. Solution UV-Vis-NIR spectrum of silver nanoparticles. Data was collected after 1 day the samples were made. One of four replicates from each color is shown. The color of each line represents each AgNP solution. Normalization factor: yellow (x 1.1), orange (x 0.84), red (x 1.1), wine red (x 1.3), purple (x 0.80), violet (x 1.1), blue (x 1.3), light blue (x 2.1), and pale blue (x 7.6).

The assignment of peaks in the UV-Vis-NIR spectra of triangular silver nanoplates was given by Kelly *et al*.[12] The major peak arises from in-plane dipole resonance mode, while the shoulder peak in the 400 - 430 nm range is due to in-plane quadrupole resonance mode. The sharp low wavelength peak at 335 nm is due to out-of-plane quadrupole resonance mode

Size and Shape of Silver Nanoparticles

The size and shape were determined by TEM analysis. Figure 6.3 shows TEM micrographs for the nanoparticles from the solutions in Figure 6.1. These micrographs show that the silver nanoplates with absorption peaks between 480 and 570 nm (orange to violet) were composed of a mixture of spherical, irregular, and triangular shapes while the solutions having peaks above 570 nm contained well-defined triangular shapes. Statistical measurements of the edge lengths showed that as the color red-shifted, the size distribution became broader (Table 6.2). This finding was consistent with the dynamic light scattering data, as will be described later in this section.

The size distributions from TEM can also be illustrated by histograms. Figure 6.4 shows histograms of blue and pale blue samples. The distributions are asymmetric, skewed towards the larger sizes, particularly for the pale blue case. The broadness of the pale blue distribution is likely to be the cause of the broad peak in the UV-Vis-NIR spectrum. The simulations of the spectrum based on the size distribution in Figure 6.4b are consistent with this explanation.[13]

The thickness of the triangular nanoparticles in the blue and pale blue samples was also able to be determined by TEM. Prior to imaging, it was necessary to centrifuge the nanoparticle solutions, so the particles could stack to each other. The stacking enabled the nanoparticles to bind perpendicular with respect to the plane of the TEM grid, as shown in Figure 6.5. The measured thicknesses of these nanoparticles were 5.5±0.3 and 7.0±0.4 nm for blue and pale blue samples, respectively. The aspect ratio (edge

length/thickness) are thus approximately 5:1 for the blue and 9:1 for the pale blue samples. These micrographs also show that these nanoparticles were flat plates as opposed to prisms.

Dynamic light scattering (DLS) was used as a quick and approximate diagnostic method of measuring the size distributions. Figure 6.6 shows DLS distributions for all of the samples studied from yellow to pale blue. Although quantitative agreement with the size and width of the TEM distributions is not expected (because DLS analysis involves a number of approximations, such as spherical particles), the peak and the width of the DLS distributions followed the trends found by TEM.

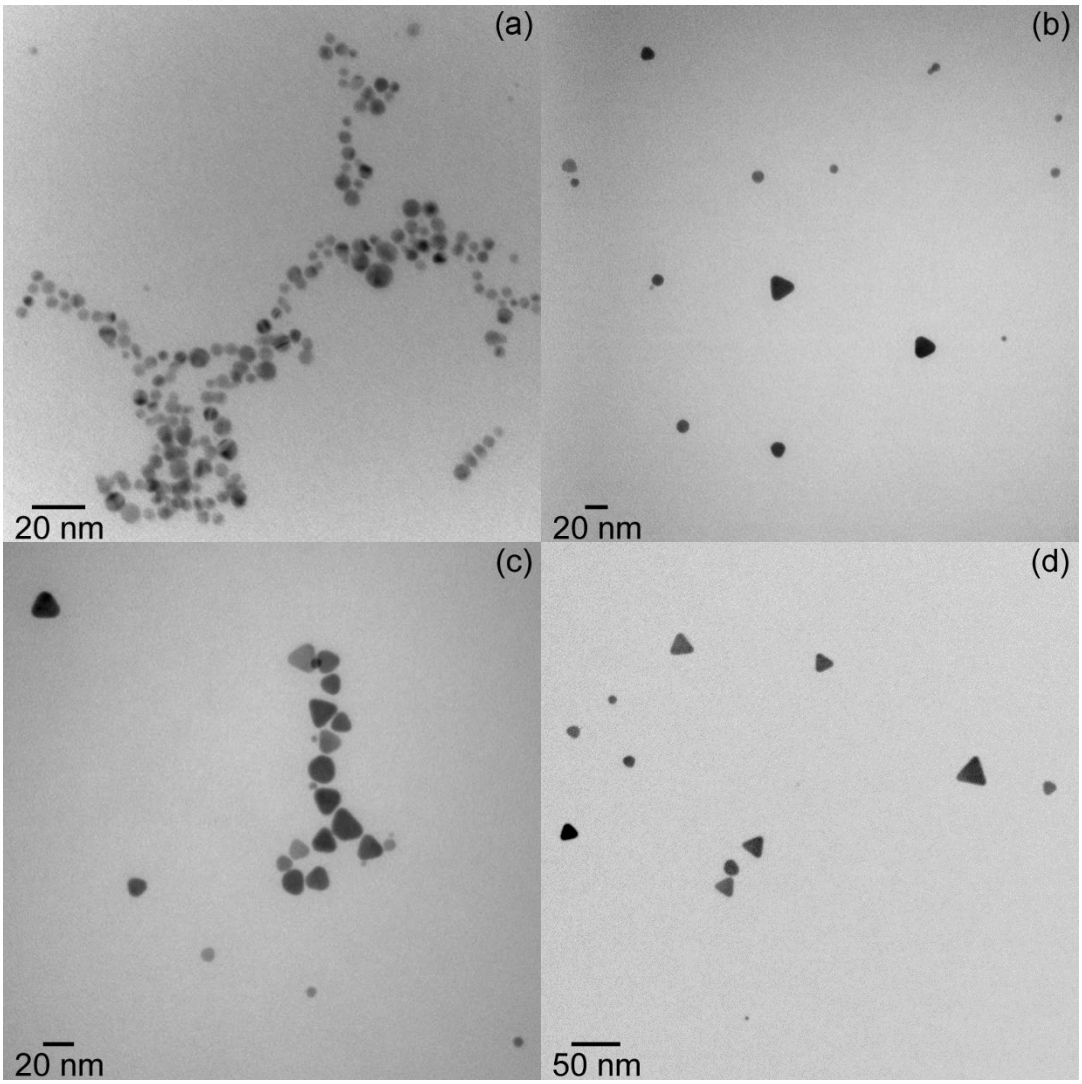

Figure 6.3. TEM micrographs of AgNPs representing each color made: (a) yellow (b) orange (c) red (d) wine-red.

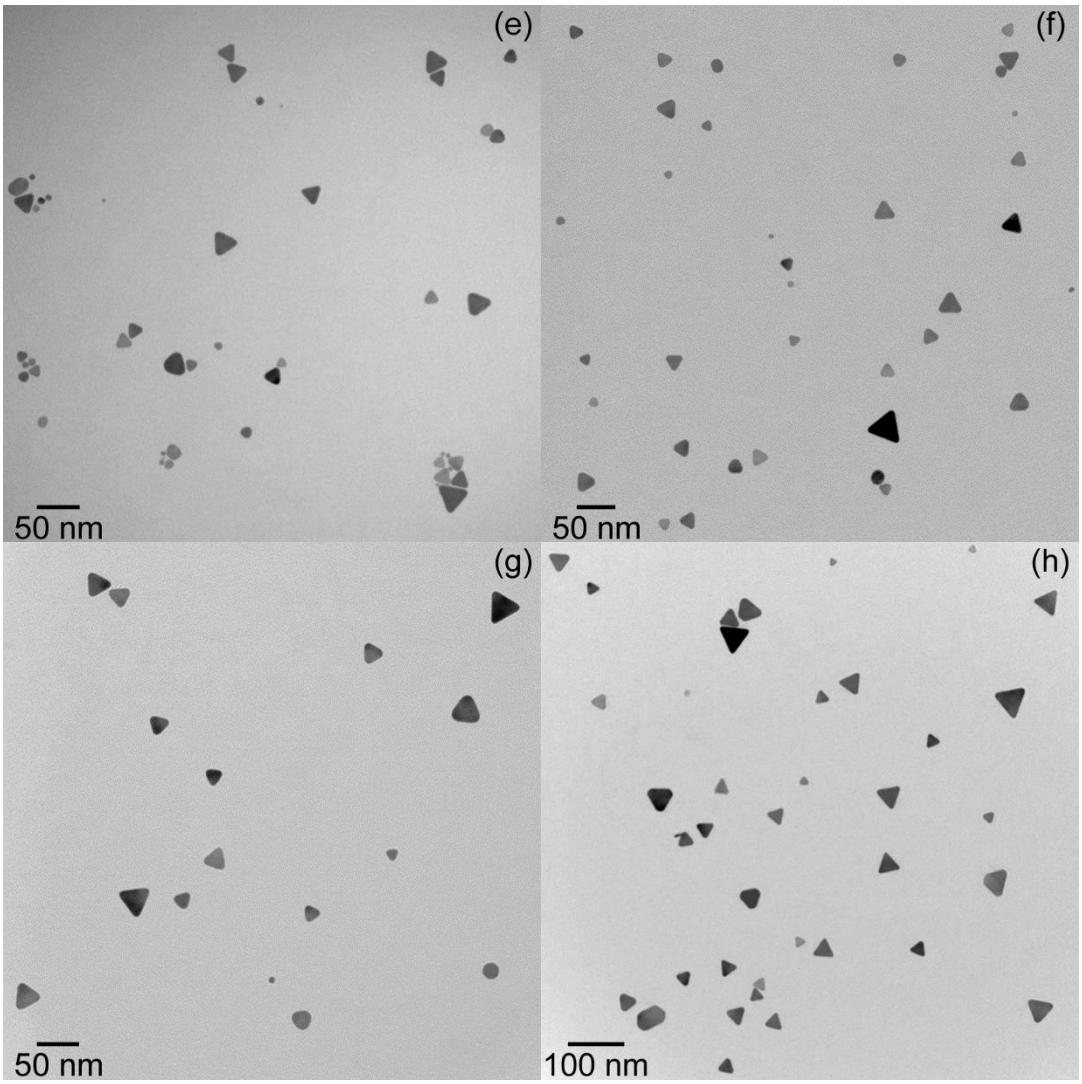

Figure 6.3 (cont.). TEM micrographs of AgNPs representing each color made: (e) purple (f) violet (g) blue (h) light blue.

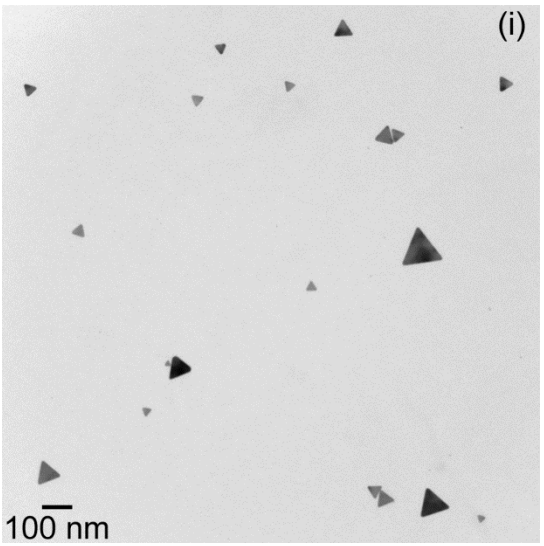

Figure 6.3 (cont.). TEM micrographs of AgNPs representing each color made: (i) pale blue.

Table 6.2. Average, standard deviation, and number of measurements (in parentheses) of edge lengths of AgNPs measured by TEM.

Color	Yellow	Orange	Red	Wine Red	Purple
Size, nm	6±2 (115)	19±6 (57)	21±6 (33)	22±7 (40)	24±7 (61)
Color	Violet	Blue	Light Blue	Pale Blue	
Size, nm	26±8 (47)	29±10 (164)	38±15 (65)	66±54 (214)	

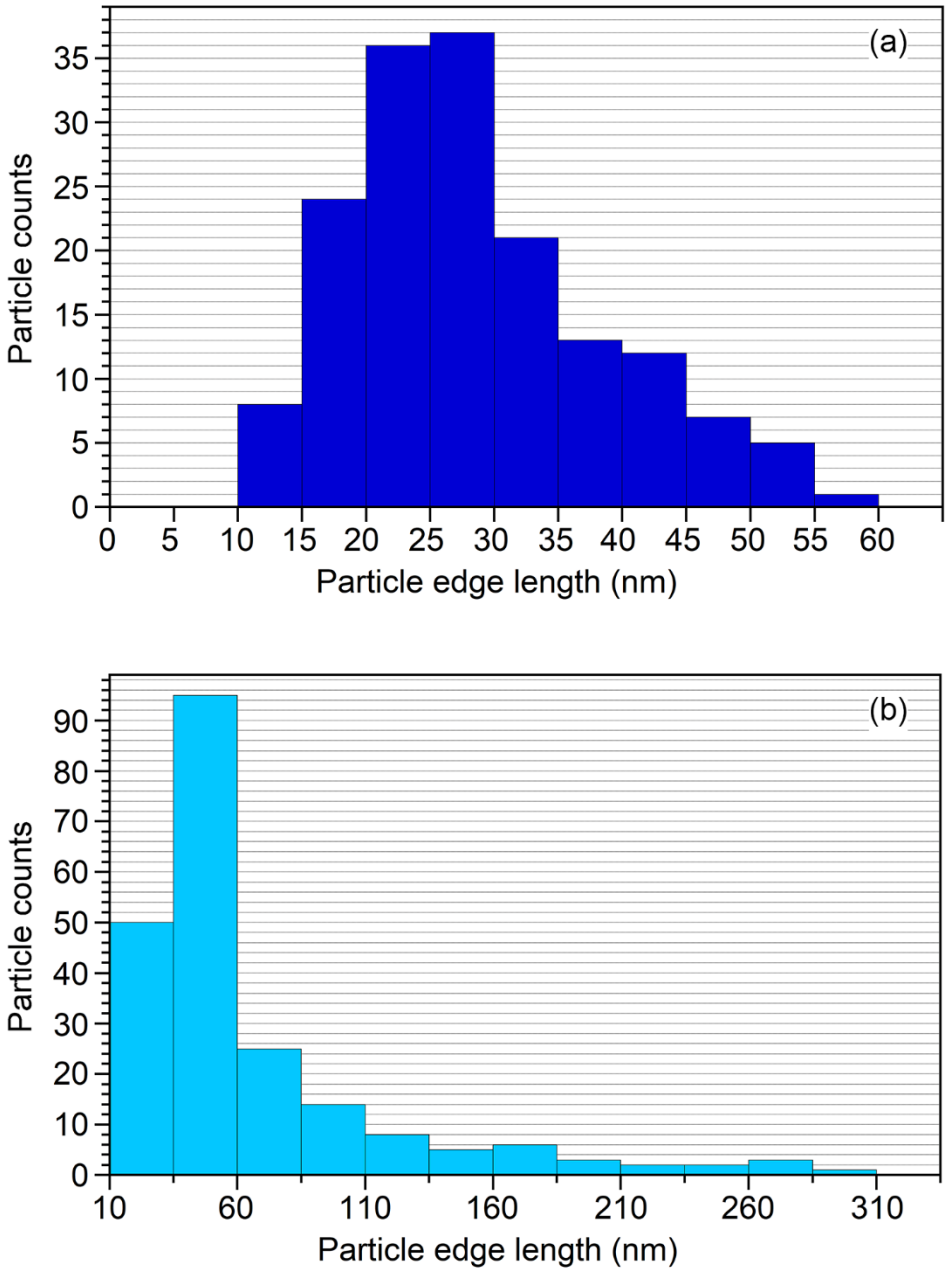

Figure 6.4. Statistical analysis of edge lengths of (a) blue and (b) pale blue AgNPs based on TEM micrographs

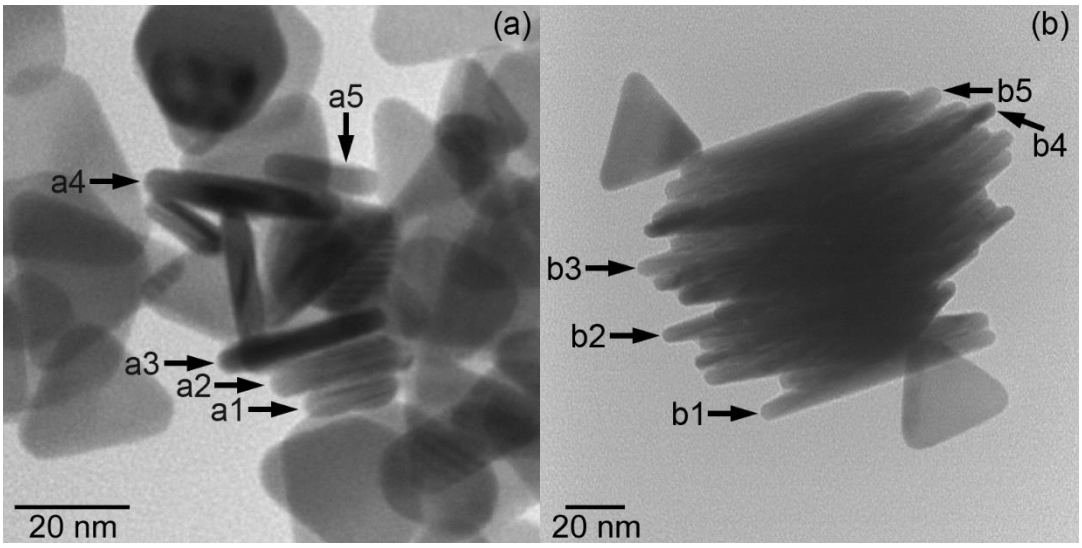

Figure 6.5. Thickness analysis worked on TEM micrographs of blue AgNPs (a) and pale blue AgNPs (b). Measured thickness: a1 to a5: 5.1, 5.8, 5.5, 5.8, 5.2 nm. b1 to b5: 7.1, 6.5, 6.7, 7.0, 7.6 nm.

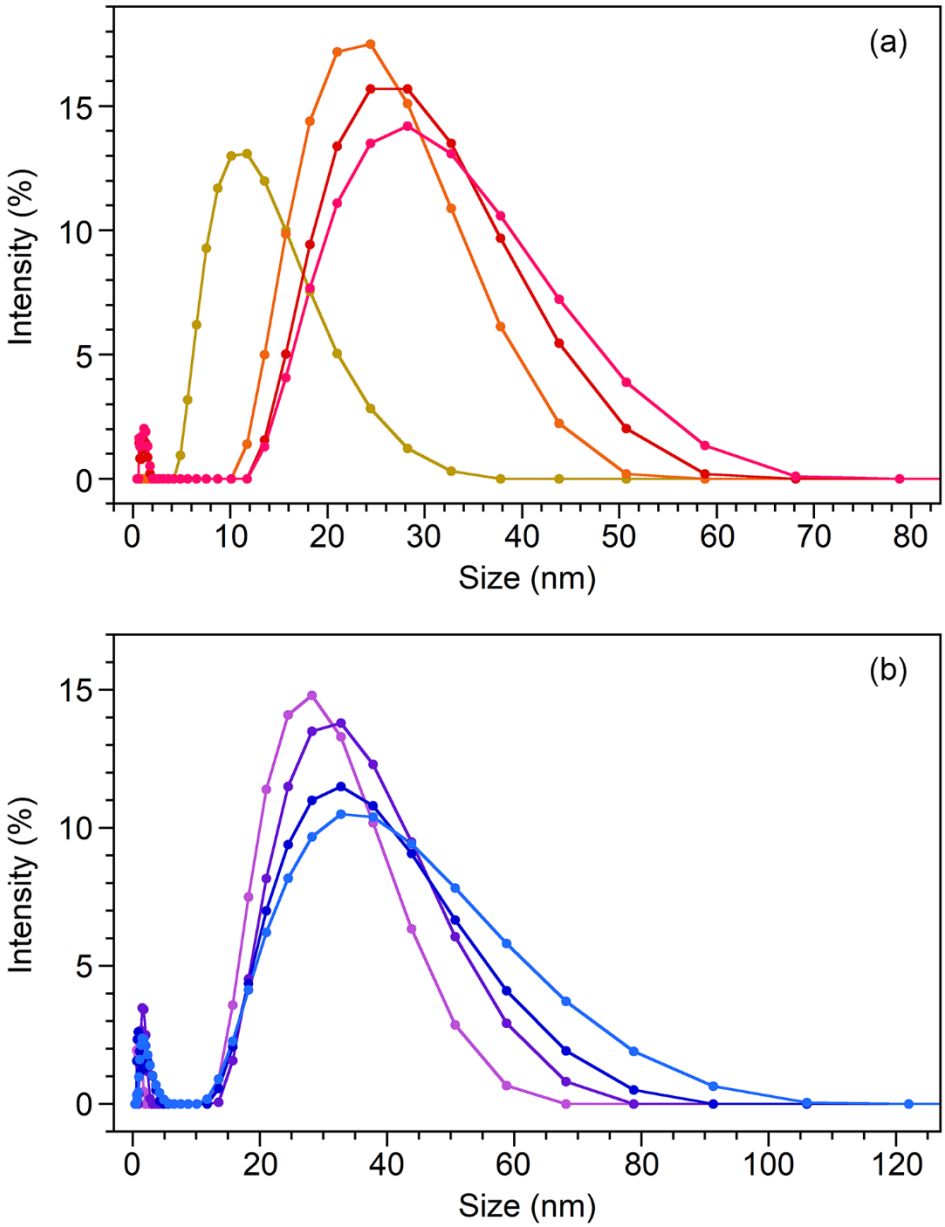

Figure 6.6. DLS spectra on 1 day old AgNP solutions. One of the four replicate samples was selected for the figures. The color of spectrum represents the color of AgNP solutions: (a) yellow, orange, red, wine red. (b) purple, violet, blue, light blue.

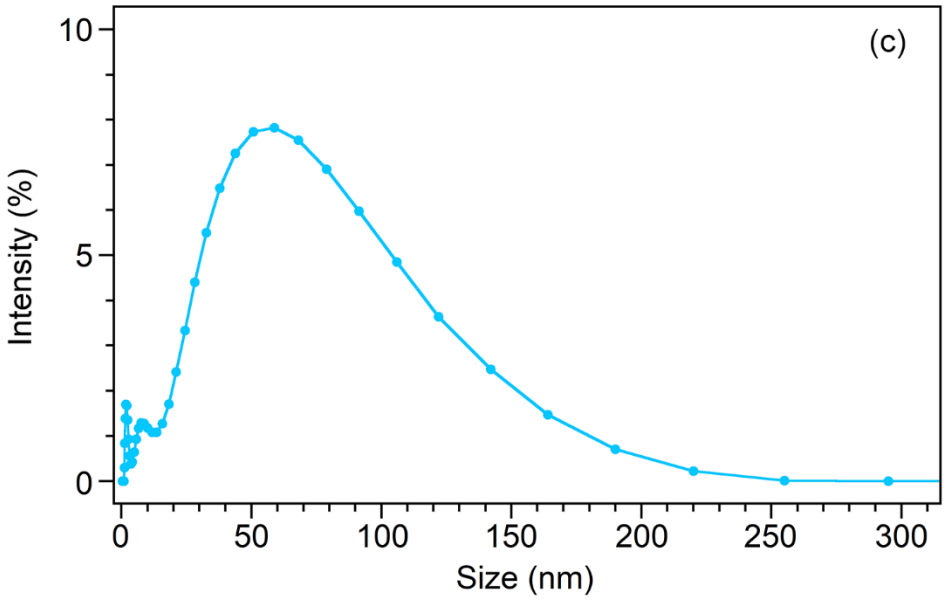

Figure 6.6 (cont.). DLS spectra on 1 day old AgNP solutions. One of the four replicate samples was selected for the figures. The color of spectrum represents the color of AgNP solutions: (c) pale blue.

Reproducibility and Stability of Silver Nanoparticle Samples

The reproducibility of colors and spectra was assessed by repeating the synthesis of each solution four times. The peak positions, λ_{max}, of four replicates for each color are summarized in Table 6.3. The last column shows the average and standard deviation of λ_{max} for each sample. The deviations are rather small for each sample. It is important to note that the procedure should be followed closely because a small deviation in, for example, stirring rate or concentrations can result in inconsistent shift of the peaks.

Table 6.3. Summary of λ_{max} found from four replicates of AgNPs prepared for each color. Units are in nm.

Color	λ_{max1}	λ_{max2}	λ_{max3}	λ_{max4}	$\lambda_{max,\ ave\ (std.)}$
Yellow	392	392	392	393	392(0)
Orange	483	471	485	482	480(5)
Red	503	494	501	504	500(4)
Wine Red	522	541	513	524	525(10)
Purple	546	554	561	551	553(5)
Violet	564	564	564	563	564(0)
Blue	597	594	598	596	596(1)
Light Blue	657	649	656	648	653(4)
Pale Blue	738	733	778	726	743(20)

In addition to the testing the reproducibility, the stability of the nanoparticles over time was investigated. Four replicates of each sample were stored at room temperature in the dark for 30 days. UV-Vis-NIR spectra and dynamic light scattering measurements were recorded 1 day, 3 days, 7 days, and 30 days after the reaction was completed. The peak wavelength for each sample blue-shifted by an average of 10 - 15 nm during the 30 days, except for the yellow AgNPs, whose peak wavelength red-shifted by 1 nm (Figure 6.7). In similar work by Zhang *et al*., larger AgNP nanoplates that absorb with peak wavelength 600 nm could be produced by increasing $[H_2O_2]$.[9] However, when $[H_2O_2]$ = 20 mM, the nanoparticles degraded after several hours. We speculate that the higher stability of our nanoparticles is attributed to the lower concentration of $AgNO_3$ used in our work. Lower population of nanoparticles

enables faster dissolution of the AgNPs into Ag^+ by H_2O_2. These ions will then be reduced by $NaBH_4$. This process will continue until the growth starts to dominate, so that a minimum amount of H_2O_2 is left after the reaction. This explanation is consistent with the work of Zhang and Li who found that when H_2O_2 was added to previously prepared silver nanoparticles, the UV-Vis-NIR absorbance decreased.[14] This study implies that excess H_2O_2 that remains in solution can cause dissolution of AgNPs.

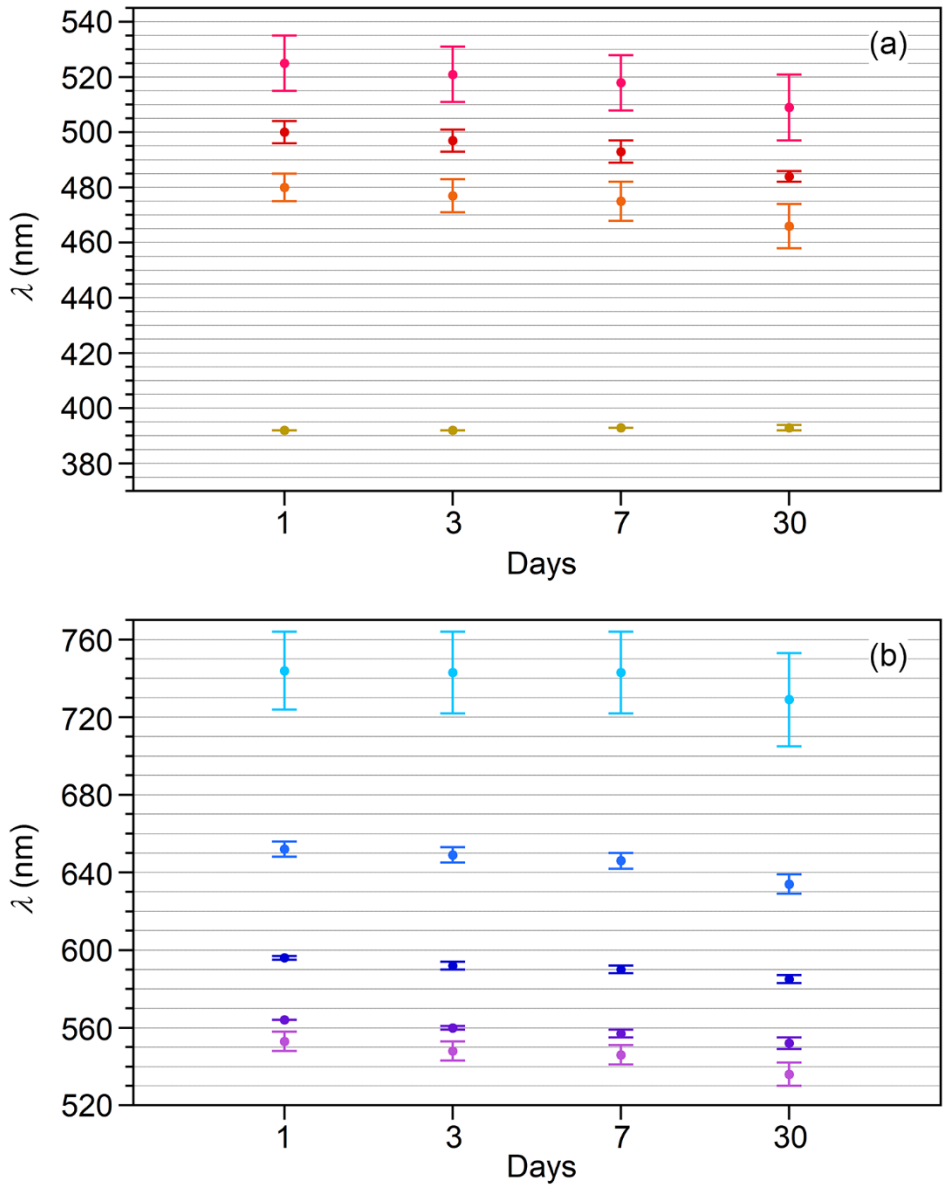

Figure 6.7. Stability of AgNP solutions monitored at measured λ_{max} for 30 days. Each data point represents the average and the standard deviation of four replicates. The color of data point corresponds to the color of AgNP solutions: (a) yellow, orange, red, wine red. (b) purple, violet, blue, light blue, pale blue.

Dynamic light scattering measurements of the four replicates measured over 30 days agreed with the stability assessed by UV-Vis-NIR spectroscopy. Figure 6.8 shows the sizes of the nanoparticles (mode of the DLS intensity distributions) in each of the different colored solutions. The sizes were consistent to within a few nanometers over 30 days, except for the yellow nanoparticles which increased from about 14 to 22 nm in diameter.

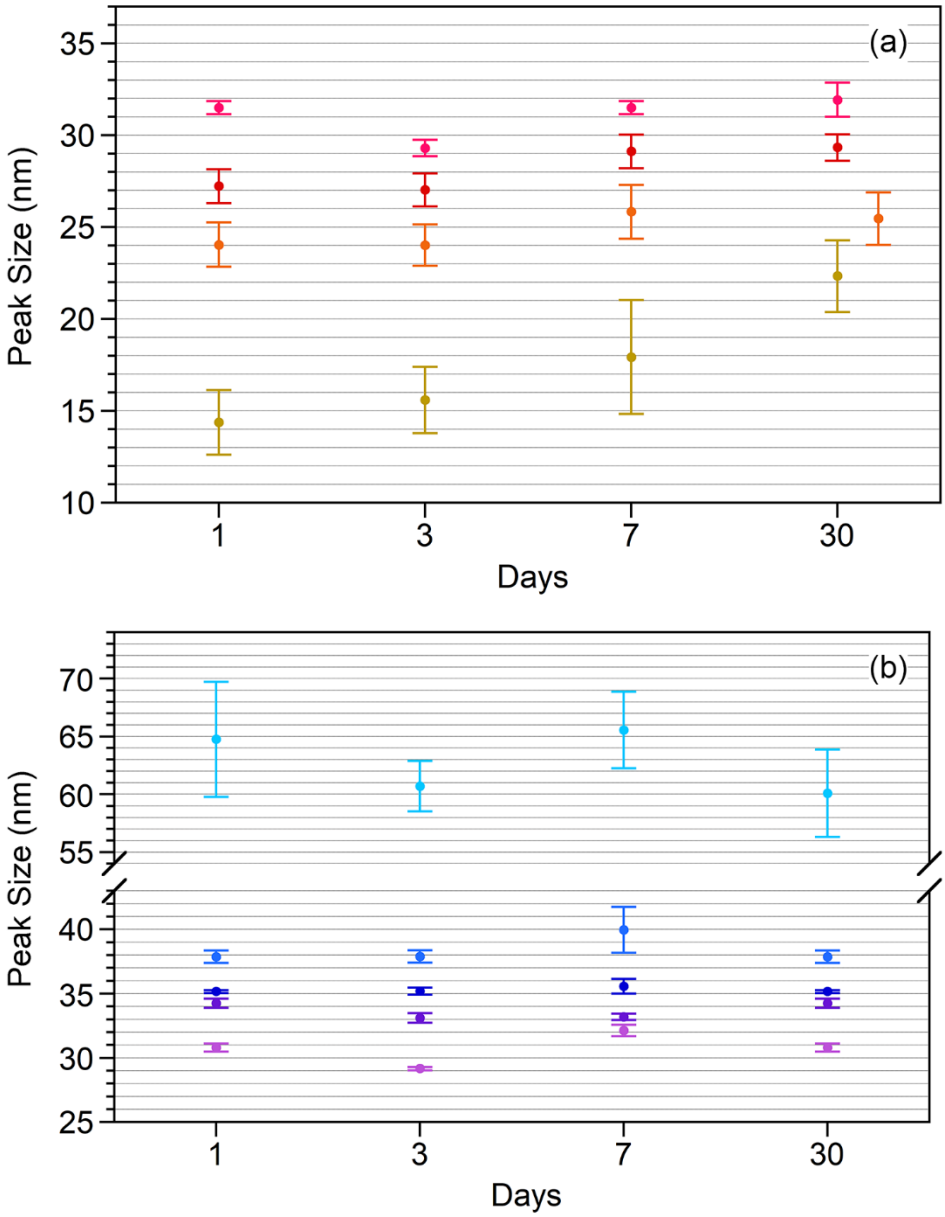

Figure 6.8. AgNP peak sizes determined from the DLS intensity distributions, measured over 30 days. The error bars are based on the averages of the four replicates (not on the width of the size distribution). The data point for the orange AgNP solution at 30 days was offset for clarity. The colors of the data points represent colors of the AgNP solutions: (a) yellow, orange, red, wine red. (b) purple, violet, blue, light blue, pale blue.

The stability of the nanoparticles as a function of storage temperature was also studied. UV-Vis-NIR spectroscopy was used to monitor the nanoparticles at room temperature and 4 °C (Figure 6.9). Spectra of the blue AgNP solution were recorded several times over 30 days. Initially, the blue nanoparticle solution was synthesized at room temperature, and the spectrum was recorded. This room temperature sample was meant to be the experimental control. This solution was then split in half; one was stored at room temperature and the other at 4 °C. On the seventh day, the nanoparticle solution stored at 4 °C was split in half; one was stored at room temperature and the other at 4 °C. The second splitting was done for the following reason. The active reagents such as borohydride and hydrogen peroxide have most likely been consumed by this point, so it is possible that the nanoparticle solution is now stable. If that is the case, the absorption peak should be constant, even if the nanoparticle solution is now stored at room temperature. In fact, the solution which was left at room temperature after the seventh day changed the most and blue-shifted by 28 nm after 30 days while the control and the sample stored at 4 °C blue-shifted by ~18 nm. For this reason, room temperature storage is preferred when the long-term storage of these nanoparticle solutions is considered.

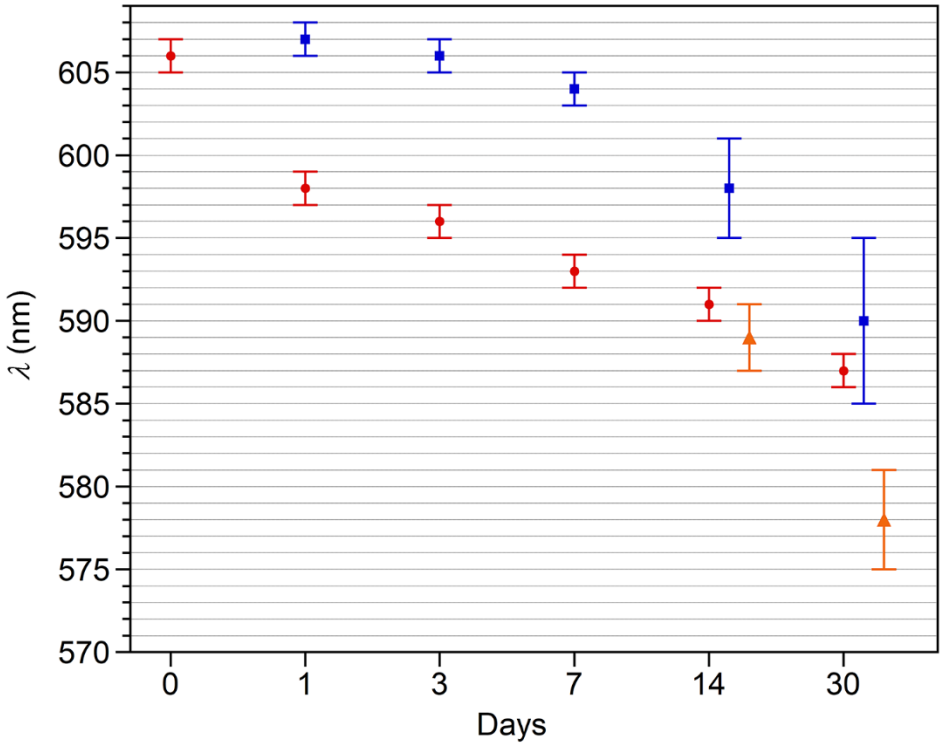

Figure 6.9. Storing temperature effect of blue AgNP solutions monitored at measured λ_{max} for 30 days. Each data point represents the average and the standard deviation of triplicate samples. AgNP solutions stored at r.t. in dark (red). Storage in 4 °C fridge (blue). AgNP solutions stored in 4 °C split into new vials and left at r.t. in dark after 7 days (orange). The data points on 14 and 30 days were offset for the clarity.

Size Separation of Silver Nanoparticles by Centrifugation

Centrifugation was employed to verify that the nanoparticles could be separated by their size. Based on the TEM and dynamic light scattering studies, the blue, light blue, and pale blue AgNPs had rather broad size distributions. For the purpose of the solar cell application discussed in Chapter 7, these broad size distributions may be advantageous because the scattering and absorption of the light covers a broad wavelength range. Nonetheless, we would like to demonstrate that we can separate the nanoparticles by size in case that is needed. For example, Figure 6.10 shows the results of centrifuging the blue nanoparticle solutions at 10,000 and 17,500 rpm. In the 10,000 rpm case, the size separation is more noticeable because both the supernatant and the solution made from the pellet are both different in color from the original solution. In the 17,500 rpm case, the solution made from the pellet resembles the original solution.

Figure 6.10. Supernatant of the blue AgNP solution, a solution with the pellet re-dispersed in 1.5 mM Na_3Cit, and the as-prepared AgNP solution (left to right). Centrifugation for 15 minutes at (a) 10,000 rpm and (b) 17,500 rpm.

This visual conclusion is confirmed by UV-Vis-NIR spectroscopy and TEM for the blue AgNP solution. Figure 6.11a shows the UV-Vis-NIR spectra of supernatant, re-dispersed pellet, and the original samples for the 10,000 rpm case and Figure 6.11b for 17,500 rpm case. The peak position, width, and absorbance are given in Table 6.4. Figure 6.12 shows the TEM micrographs of each sample solution prepared from the centrifugation studies. A summary of the TEM size analyses is given in Table 6.5. The finding from this study, even without having optimized centrifugation conditions, is that size separation could be more efficiently achieved at the slower speed.

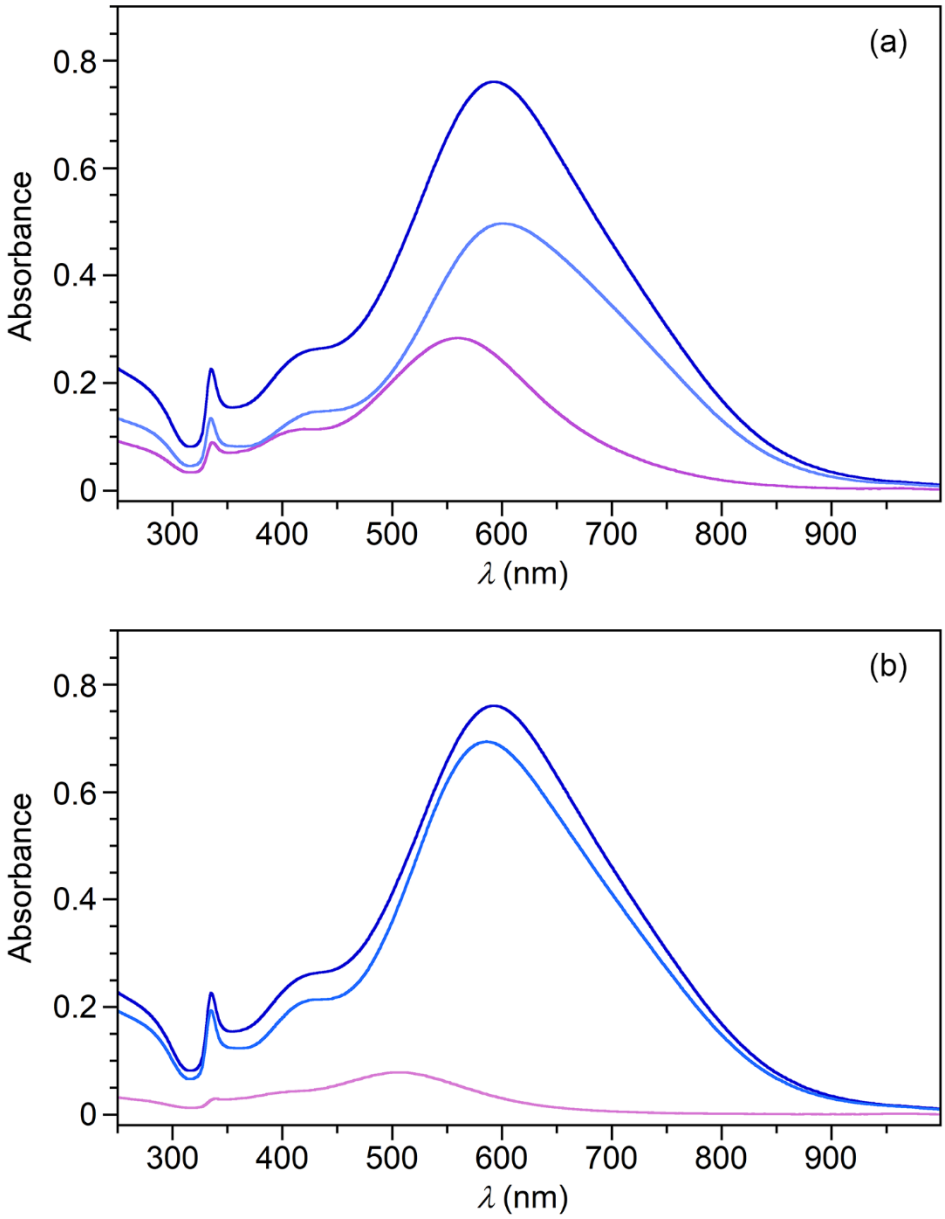

Figure 6.11. Solution UV-Vis-NIR spectra of the blue AgNP solution centrifuged at (a) 10,000 rpm for 15 min: as-prepared AgNP solution (blue), pellet re-dispersed in 1.5 mM Na_3Cit (light blue), and supernatant (purple), and (b) 17,500 rpm for 15 min: as-prepared AgNP solution (blue), pellet re-dispersed in 1.5 mM Na_3Cit (light blue), and supernatant (pink).

Table 6.4. The peak position, absorbance, and width (Full Width at Half Maximum) of as-prepared blue AgNP solution, and the blue AgNP solution centrifuged at 10,000 rpm and 17,500 rpm.

	As-prepared	10,000 rpm		17,500 rpm	
	Blue AgNPs	Pellet	Supernatant	Pellet	Supernatant
λ_{max}, nm	593	600	558	586	506
Absorbance	0.76	0.50	0.28	0.69	0.079
FWHM, nm	230	234	185	223	193

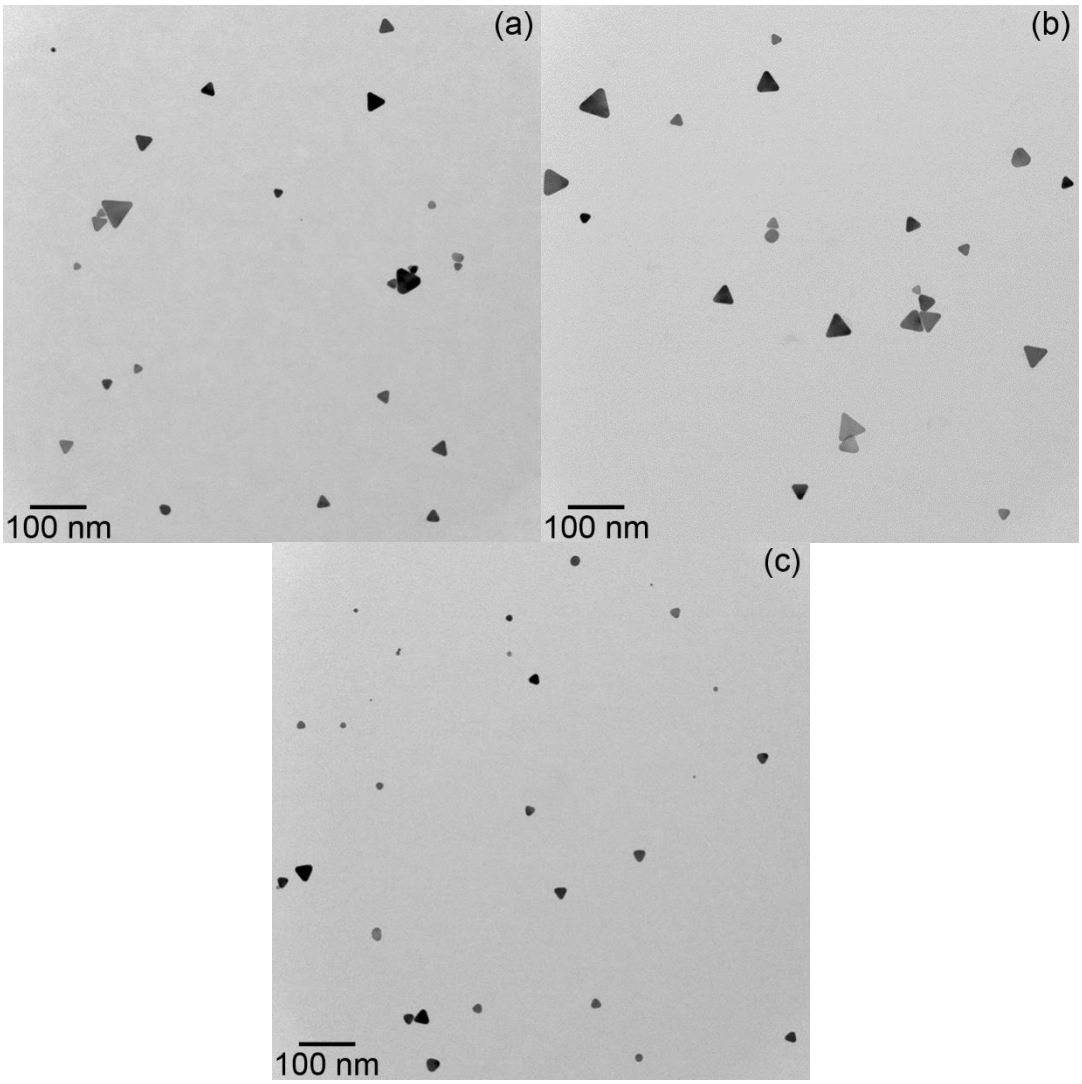

Figure 6.12. TEM micrographs of the blue AgNP samples centrifuged for 15 minutes at 10,000 rpm: (a) uncentrifuged original (b) pellet (c) supernatant.

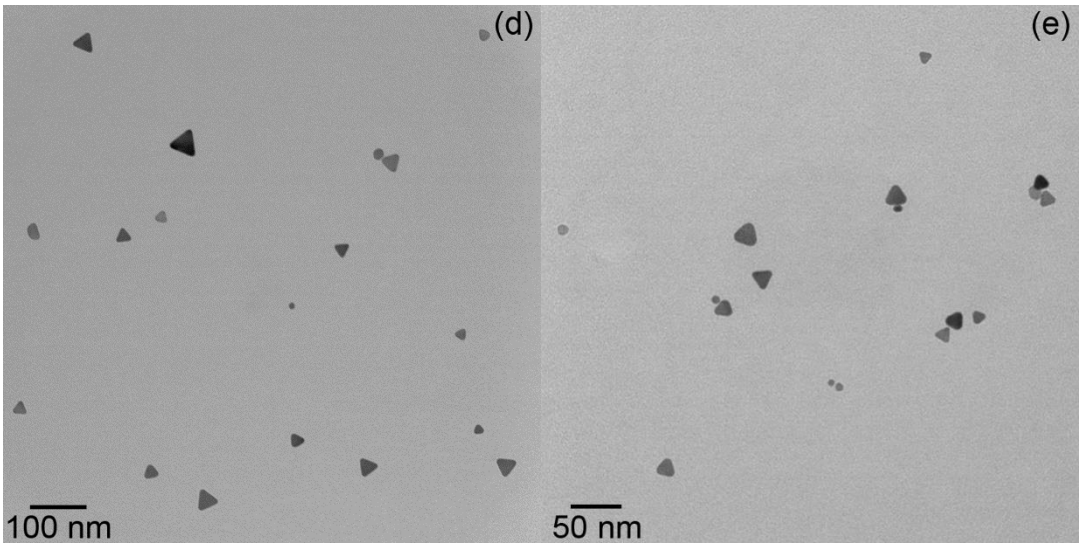

Figure 6.12 (cont.). TEM micrographs of the blue AgNP samples centrifuged for 15 minutes at 17,500 rpm: (d) pellet (e) supernatant.

Table 6.5. Average and standard deviation of measured edge lengths of AgNPs by TEM. Comparison between as-prepared blue AgNPs and centrifuged solutions.

	As-prepared	10,000 rpm		17,500 rpm	
	Blue AgNPs	Pellet	Supernatant	Pellet	Supernatant
Size, nm	29(10)	37(13)	26(8)	32(10)	17(5)

Scaling up of Blue and Pale Blue AgNP Reactions

The results presented thus far showed that we have successfully developed a synthetic scheme for producing stable silver nanoparticles that are capped by the weakly bound and small citrate ligand. The red and near IR absorbing solutions are of the greatest interest for our practical application of solar cell enhancement. An issue is that these nanoparticle solutions were made using the lowest $AgNO_3$ concentrations, and thus the nanoparticle populations are low. To overcome this problem, scaling up the synthesis would be desirable. This may appear straightforward, yet adopting the synthetic technique from the 15 mL reaction and simply increasing the volumes of all reagents (a total volume of 100 mL) did not result in the exact reproduction of the 15 mL results. The issue appears to be that the final reagent added ($NaBH_4$) does not spread fast enough throughout the solution when the reaction mixture is stirred slowly. Increasing the speed of stirring solved this problem. The scaling up scheme was successful as evidenced by the UV-Vis-NIR spectra of the blue and pale blue AgNP solutions compared to those from the 15 mL reactions (Figure 6.13).

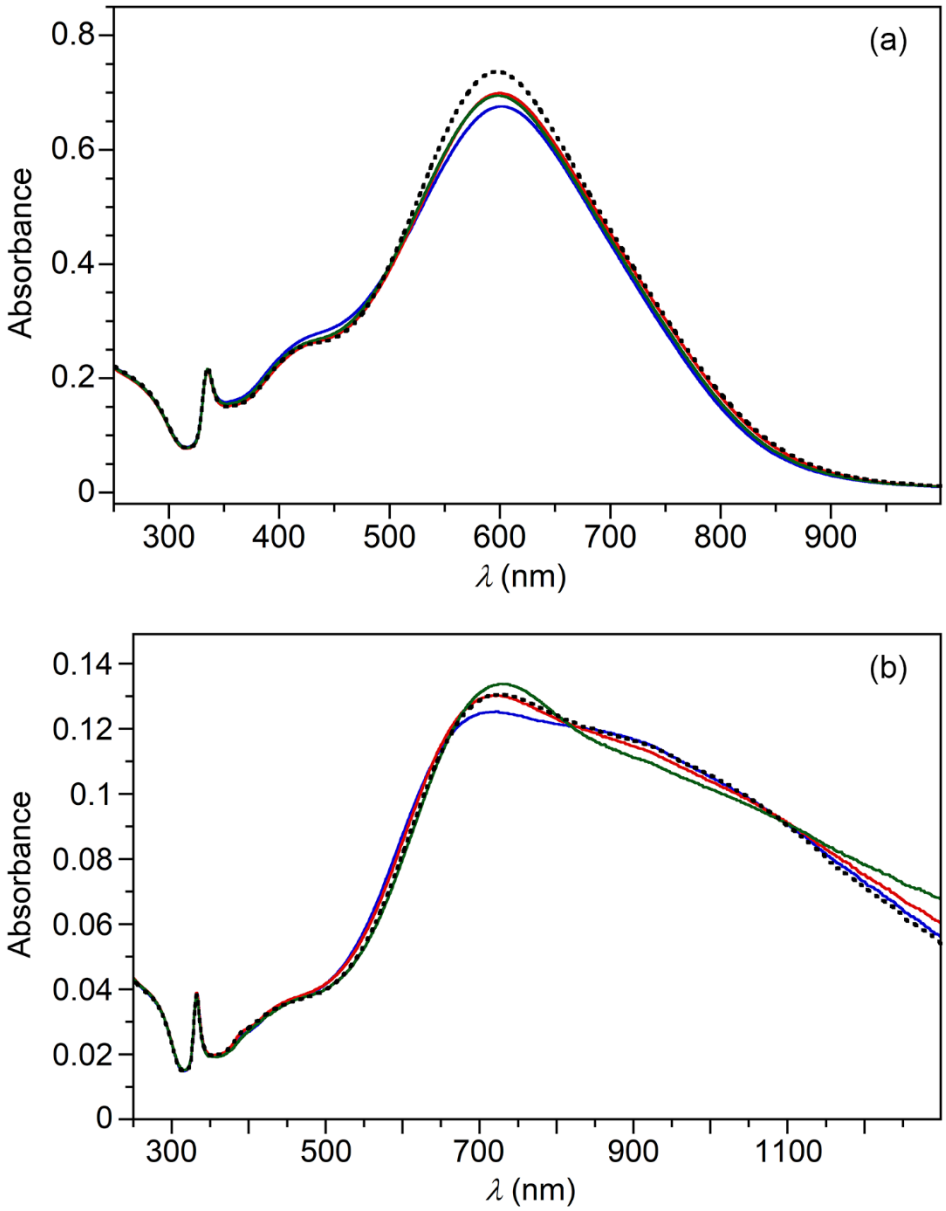

Figure 6.13. Solution UV-Vis-NIR spectrum of (a) blue AgNPs ($\lambda_{max,\ ave}$ = 599) and (b) pale blue AgNPs ($\lambda_{max,\ ave}$ = 725 nm) prepared in a 100 mL reaction scale. The different colored spectra represent each trial of three replicates, respectively. The dotted line shows a spectrum from 15 mL reaction scale for each colored solution.

Comments on the Reaction Mechanism

The studies presented above focused on the synthesis of the triangular nanoplates. Future work to investigate the mechanism is planned in the research group, so at this point, only a few preliminary and speculative comments regarding the mechanism will be given. In particular, the question of why lower Ag^+ reactant concentrations lead to larger nanoplates with sharper vertices will be briefly discussed. Nucleation and growth theory as applied to nanoparticle formation provides a basic context, although we hope to add specific molecular details to the mechanistic picture.[15] At low [Ag^+], the initial growth rate of the nanoparticles is expected to be slow, because oxidative dissolution by hydrogen peroxide competes with the formation of small silver complexes by collisions of silver atoms. Note that for the pale blue solution, which contains the largest nanoplates, the initial [Ag^+] and [H_2O_2] are the following: [Ag^+] = 17 μM while [H_2O_2] = 19 mM; see Table 6.1. Once a few nanoparticles form by random chance and citrate preferentially caps their (111) facets, growth of these nanoparticles will likely dominate over formation of new silver clusters if the sticking probability of an atom colliding with the nanoparticle is greater than the binding probability of two colliding atoms. Because of the low [Ag^+], the new silver atom on the nanoparticle will have time to diffuse and find a thermodynamically favorable position, which would be on an unprotected edge of the nanoparticle. The growth of the nanoparticle in this low [Ag^+] range would thus be under thermodynamic control, and the triangular motif of the atoms on the (111) surface would dictate the triangular shape of the nanoparticle.

Conclusion

The synthesis of silver nanoparticles that absorb and scatter light throughout the visible and near-infrared region was developed by a one-pot, seedless approach under ambient conditions. This straightforward method produces nanoparticles that are not only reproducible in size and shapes but also stable for over 30 days. Another advantage is that the capping agent, citrate, is small and loosely bound and therefore easily displaced when binding to surfaces. These features are appealing because they are suitable for light harvesting applications such as solar cells. In addition, the reaction scheme can be scaled up to 100 mL volume with only a minor modification in stirring rate when the sodium borohydride is introduced to the reaction mixture.

Acknowledgements

Chapter 6 contains material that is currently being prepared for publication. Yamamoto, N.; Torres, M. Z.; Harris, D.; Pullman, D. P. “Seedless, one-pot synthesis of infrared-absorbing silver nanoparticles”. *Manuscript in preparation*. The dissertation author was the primary researcher for the data presented. I thank a fellow graduate student in Dr. Pullman’s group, Martha Torres, for her contribution in the computational calculations, which will be included in the manuscript, to aid in the interpretation of silver nanoparticles I have prepared. Debra Harris is an undergraduate researcher who patiently adhered to my guidance to prepare the nanoparticles and assessed the

reproducibility. Besides chemistry, she is very talented at cleaning and organizing the lab neatly. I would like to thank PURE Bioscience of El Cajon, CA for partial support of this work.

References

1. Turkevich, J.; Stevenson, P. C.; Hillier, J. *Spec. Discuss. Faraday Soc. Special.* **1951**, *11*, 55.

2. Creighton, J. A.; Blatchford, C. G.; Albrecht, M. G. *J. Chem. Soc., Faraday Trans. 2.* **1979**, *75*, 790.

3. Lee, P. C.; Meisel, D. *J. Phys. Chem.* **1982**, *86*, 3391.

4. Xia, Y.; Xiong, Y.; Lim, B.; Skrabalak, S. E. *Angew. Chem. Int. Ed.* **2008**, *48*, 60.

5. Zhang, T.; Song, Y.-J.; Zhang, X.-Y.; Wu, J.-Y. *Sensors.* **2014**, *14*, 5860.

6. Sun, Y.; Xia, Y. *Science.* **2002**, *298*, 2176.

7. Kilin, D. S.; Prezhdo, O. V.; Xia, Y. *Chem. Phys. Lett.* **2008**, *458*, 113.

8. Parnklang, T.; Lertvachirapaiboon, C.; Pienpinijtham, P.; Wongravee, K.; Thammacharoen, C.; Ekgasit, S. *RSC Adv.* **2013**, *3*, 12886.

9. Zhang, Q.; Li, N.; Goebl, J.; Lu, Z.; Yin, Y. *J. Am. Chem. Soc.* **2011**, *133*, 18931.

10. Atkins, P.W.; De Paula, J. *Physical Chemistry, 10th ed.*; W.H. Freeman and Company: New York, **2014**.

11. Silver Citrate. https://www.rsc.org/Merck-Index (accessed 4/4/2019).

12. Kelly, K. L.; Coronado, E.; Zhao, L. L.; Schatz, G. C. *J. Phys. Chem. B.* **2003**, *107*, 668.

13. Torres, M. Z. Unpublished work.

14. Zhang, L.; Li, L. *Anal. Methods.* **2016**, *8*, 6691.

15. Polte, J. *CrystEngComm.* **2015**, *17*, 6809.

Chapter 7: Application of Near Infrared Absorbing Silver Nanoparticles Towards Solar Cell Enhancement

Introduction

The photoresponse of silicon solar cells to sunlight is due mostly to absorption of visible and near-UV radiation. Since the band gap of silicon is 1.1 eV, silicon can in principle absorb near-infrared (near-IR) light up 1100 nm; however, between 700 nm and 1100 nm, the absorption coefficient decreases by a factor of 500.[1] Thus, a large fraction of the near-IR portion of the sun's spectrum is wasted. In the past decade, research groups have improved the response to near-IR radiation by incorporating metal or semiconducting nanoparticles into silicon solar cells.[2–21] Generally, the rationale is that the nanoparticles can help trap and/or couple the incident radiation into the solar cell by virtue of the strong surface plasmon resonance of the nanoparticles (i.e., the strong collective oscillation of electrons induced by incident radiation). Silver nanoparticles possess an exceptionally intense resonance[22–24] and therefore have been the nanoparticles of choice in most "plasmonic solar cell" studies. Excitation of the plasmon resonance generates an enormous, spatially concentrated near-field (i.e., the oscillating electric field in the region surrounding the nanoparticles).[22] It is this field that is mostly responsible for the phenomenon of surface-enhanced Raman Spectroscopy, in which the Raman signal of molecules bound to the surface of a metal nanoparticle can be dramatically increased (sometimes by a factor up to 10^6) compared to the Raman signal of molecules in solution.[25–28] Moreover, as shown and discussed in Chapter 6, the resonant wavelength for silver nanoparticles can be tuned

throughout the visible and near-IR regions straightforwardly by changing the size and shape of the nanoparticles.

The challenge is to construct a solar cell such that the energy absorbed by the nanoparticles is efficiently transferred to the solar cell. In most studies thus far, the nanoparticles have either been embedded within the cell (near the p-n junction or at the backplane) or have been deposited on the surface of the cell. In the latter case, the nanoparticles are in direct contact with the surface or with a thin dielectric layer (~10 – 30 nm, typically silicon dioxide or silicon nitride) that electrically isolates the nanoparticles from the cell. The presence of the dielectric layer limits the undesired effect of electron-hole pair recombination that can occur when the nanoparticle is in direct contact with the solar cell.[5]

Plasmonic solar cells with dielectric layer thicknesses below a few nanometers are promising and are the focus of the present work for the following reason. Since the amplitude of the near-field decreases rapidly with distance from the nanoparticle (e.g., $1/r^3$ for the dipole field),[6] placing the nanoparticles within 1 nm of the solar cell's surface could potentially lead to significant gains in solar cell efficiency. The chemistry-based method we will use to create atomically thin isolation layers differs from prior attempts by other groups, which used expensive vacuum deposition methods that often have problems in making uniform ultrathin layers.

Our strategy for enhancing the performance of thin-film solar cells is to modify the surface with short linker molecules which can then bind to the silver nanoparticles. The length of the linker molecule can be altered so that the

dependence of the photoresponse on the distance between the nanoparticles and the surface can be studied. In Chapter 6, we presented a new method of preparing silver nanoparticles that absorb and scatter red and near-infrared light absorbing. These are the nanoparticles we intend to use for the solar cell application. In this chapter, we present the synthesis of a short linker molecule, 4-aminobenzene diazonium (4-ABD), that will be used to functionalize the surface. Ultimately, we would like to test the photo-response of the silver nanoparticle modified solar cells when they are exposed to the sunlight. The purpose of this chapter is to present preliminary results that will lay the foundation for this research topic.

Since much of this chapter focuses on the synthesis of 4-ABD, a brief background of the diazonium chemistry will be given. Aryl diazonium compounds have been used for surface modifications on a variety of substrates.[29–31] These substrates include silicon, gold, graphene, carbon nanotube, nanoparticles, etc. During the attachment process to the surface, the diazonium moiety is displaced, generating N_2, and the aryl group binds to the surface. Besides the diazo group, the aryl group can carry a second functional group which can then be used to bind to another species such as nanoparticles (Scheme 7.1). Two strategies have been employed for binding the aryl diazonium compound to the surfaces: 1) electrochemical reduction and 2) spontaneous reduction. In the electrochemical approach, the potential energy supplied from the electrode promotes the dissociation of the diazo group to form N_2 gas. This leaves behind a reactive aryl radical which can then covalently

attach to the surface. Studies have also shown that spontaneous reduction of aryl diazonium compounds can take place on various substrates. The advantage of the spontaneous reaction is that the surface modification can be achieved by a simple immersion of the substrate into a solution of aryl diazonium salts. Silicon surfaces are among those that have been studied. For the attachment to work, silicon surfaces must be covered by a silicon hydride layer. Since as-purchased silicon wafers are covered by a native oxide layer that is unreactive toward the diazonium salt, the surface must first be etched and hydrogenated by hydrofluoric acid.

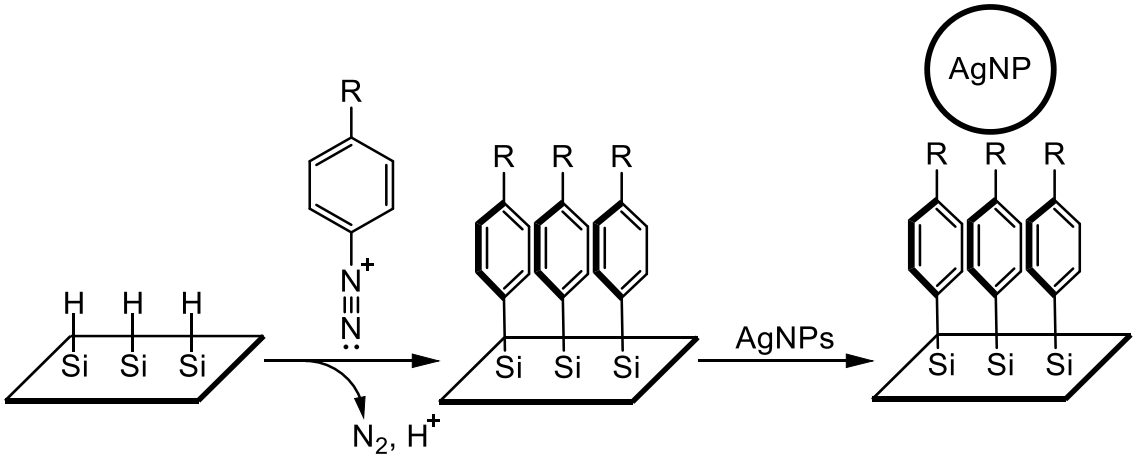

Scheme 7.1. Reaction steps to the attachment of the silver nanoparticles on aryl diazonium modified silicon wafer surface.

In terms of the selection of a functional group on the aryl diazonium that bind to the silver nanoparticles, an amine group was chosen for our first approach. This choice was made because amine groups are known to bind strongly to silver nanoparticles, as confirmed by surface-enhanced Raman spectroscopy.[32,33]

Experimental Section

Chemicals and Materials

Acetone (99.7%), methanol (MeOH, 99.9%), diethyl ether (Et_2O, 99.9%), fluoroboric acid (HBF_4, 48 – 50%), 6 N hydrochloric acid (HCl), sodium nitrite ($NaNO_2$, 99%), and trichloroethylene (99.9%) were purchased from Fisher Scientific. Dimethyl sulfoxide-d_6 (DMSO-d_6; D, 99.9%) was purchased from Cambridge Isotope Laboratories, Inc. Hydrofluoric acid (HF, 48 – 51%) was purchased from Acros Organics and *p*-phenylenediamine (98%+) from TCI. Silicon(100) wafers that are single-side polished (diam. 100 mm, 500 – 550 mm thickness, p-type (boron doped), resistivity 1 – 30 Ω·cm) were purchased from Ultrasil Corporation.

Preparation of Reagents

A diluted 10% HF solution was prepared by addition of 4 mL 48 – 51% HF solution into 16 mL DI water in a 30 mL high density polyethylene bottle

(HDPE). A solution of 8.4 M $NaNO_2$ was prepared by dissolving 5.88 g $NaNO_2$ (85.2 mmol) solid in 10 mL DI water.

Preparation of Samples

4-Aminobenzenediazonium tetrafluoroborate, 4-ABD·BF_4. 4-ABD·BF_4 was synthesized in 1955 by Whetsel *et al.*,[34] but we have developed a simpler route based on the scheme employed for the synthesis of benzenediazonium tetrafluoroborate.[35] A 10 mL volume of DI water was added to 0.865 g *p*-phenylenediamine (8.00 mmol) in a 50 mL beaker immersed in an ice bath. 1.67 mL of 6 M HCl (10 mmol) was slowly added to the slurry while stirring. 0.752 mL of $NaNO_2$ solution (8.50 mmol) was added dropwise into the mixture. An ice cold 1.03 mL 50% HBF_4 was added to the reaction mixture, which was left stirring for 30 minutes. The solid was collected on a piece of filter paper placed on a Büchner funnel under vacuum. The residue was washed successively with ice water (3 x 5 mL), MeOH (3 x 5 mL), and Et_2O (3 x 5 mL). The solid was allowed to dry under air in the dark. The solid product was stored in 4 °C refrigerator. ^{1}H-NMR (DMSO-d_6): 6.8 ppm (d, ^3J = 9.4 Hz, 2H); 8.1 ppm (d, ^3J = 9.3 Hz, 2H); 8.3 ppm (s, 2H). Infrared spectrum (cm^{-1}): 3461, 3370, 3262, 3108, 2185, 1648, 1586, 1367, 1013, 833, 701.

Degreased Silicon Wafer. Silicon samples 1.5 x 5.0 cm in size were cut from a p-type Si(100) wafer and rinsed under a running DI water tap. After drying, the wafer was successively cleaned in scintillation vials containing 18

mL of (1) trichloroethylene, (2) acetone, and (3) methanol. In each step of the cleaning, the vials were placed on a shaker for 3 minutes. The samples were rinsed with DI water in between each rinse. The cleaned wafer was flushed with DI water, dried under flowing nitrogen gas, and stored in a vial.

Hydrogen-Terminated Silicon Wafer. The degreased silicon wafer was immersed into 20 mL of 10% HF solution in a 30 mL HDPE bottle. The bottle was vigorously stirred on a vortexing device for 2 minutes. The resulting wafer was quickly immersed into two separate beakers carrying DI water and dried under flowing nitrogen gas. Infrared spectrum (cm^{-1}): 2143, 2112, 2082.

Characterization Methods

^{1}H-NMR Spectroscopy. ^{1}H-NMR data collection was carried out on a 400 MHz Varian VNMRS at 30 °C.

Contact Angle Measurements. The contact angle instrument was constructed in the Pullman lab and consists of a side-mounted digital microscope attached to an XYZ translation stage, a sample stage whose height and orientation could be adjusted, and a rear LED light for illuminating the sample. For a contact angle measurement, a 10 μL droplet of DI water was placed on the silicon sample with a micropipette. An image of the droplet was then captured by the side-mount microscope.

Germanium-ATR FTIR (Ge-ATR FTIR). The spectra for silicon samples were collected on ThermoFisher Scientific Nicolet iS50 FTIR Spectrometer equipped with VariGATR Grazing Angle Ge-ATR accessory manufactured by Harrick Scientific Products Inc., and a MCT-A detector. A homemade housing was mounted on the VariGATR to allow nitrogen purging of the sample and the Ge-ATR crystal. The instrument was purged with pure nitrogen gas for 1 h prior to the use and was continued to be purged during the data collection. The background reference spectrum for degreased silicon samples was air while the background reference spectrum for hydrogen-terminated silicon samples was the degreased silicon sample. A total of 1024 scans was taken. The spectral resolution was 4 cm^{-1}.

Diamond-ATR FTIR. The FTIR spectrum of the synthesized diazonium salt was collected on a second spectrometer, a ThermoFisher Scientific Nicolet iS5 FTIR Spectrometer equipped with a diamond ATR accessory. This spectrometer was used instead of the iS50 to avoid damaging the Ge ATR crystal with the diazonium salt crystals. The background reference spectrum was air. A total of 64 scans was taken. The spectral resolution was 4 cm^{-1}.

Results and Discussion

Synthesis of 4-ABD·BF_4

Addition of DI water to solid *p*-phenylenediamine results in pale pink slurry. Addition of HCl into the slurry produces a purple colored solution for the first 30 s and a light brown color thereafter. Addition of $NaNO_2$ solution into the mixture makes the color dark green. Addition of HBF_4 solution produces a foamy brown precipitate. Washing the precipitate with iced water, MeOH, and Et_2O affords a light brown solid in a 35% yield.

Properties of 4-ABD·BF_4

The ^{1}H-NMR spectrum collected in DMSO-d_6 shows a peak with chemical shift at 8.3 ppm and an integration value of two. This peak originates from the protons attached to the amine group (Figure 7.1). Two doublet peaks are observed in the aromatic region at 6.8 and 8.1 ppm with the coupling constants of ^3J = 9.4 and 9.3 Hz, respectively. These imply that these protons are in the ortho-position, and non-equivalent substituents are attached to the aromatic ring. The product is pure based on the NMR spectrum. The FTIR spectrum confirms the presence of the N≡N stretch at 2185 cm^{-1}, which is the indicative peak of the diazonium functional group (Figure 7.2). This peak matches with a previous report in the literature.[34] The peak at 833 cm^{-1} is the C–H out-of-plane bending mode, which corresponds to a *para*-substituted aromatic compound.

Properties of Hydrogen-terminated Silicon Wafer

The appearance of H-terminated silicon samples is visually the same as the as-received wafers, which have a native oxide coating. The FTIR spectrum taken on a Ge-ATR crystal shows indicative peaks of silicon-monohydride at 2082 cm^{-1}, silicon-dihydride at 2112 cm^{-1}, and silicon-trihydride at 2143 cm^{-1}, respectively (Figure 7.3). These peaks match with a previous report in the literature.[36] The H-terminated silicon surface is hydrophobic. This is evidenced by the contact angle measurement. First, the contact angle on a degreased silicon sample was measured. As Figure 7.4 shows, this sample had an angle of 17.0°, indicating a hydrophilic surface. The H-terminated silicon wafer had an angle of 81.0°.

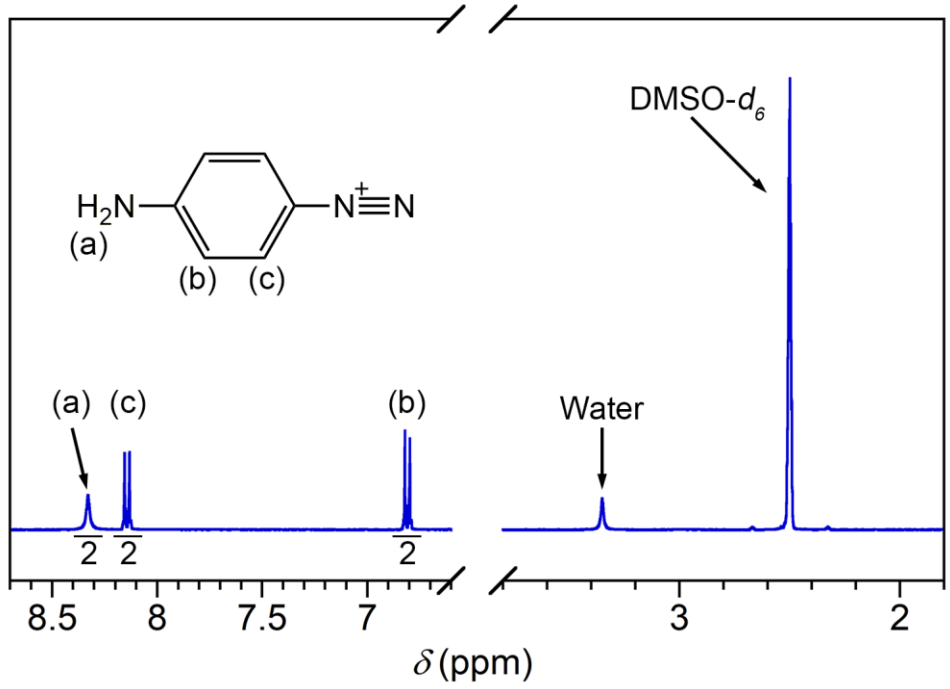

Figure 7.1. ^{1}H-NMR spectrum of 4-ABD·BF_4 in DMSO-d_6.

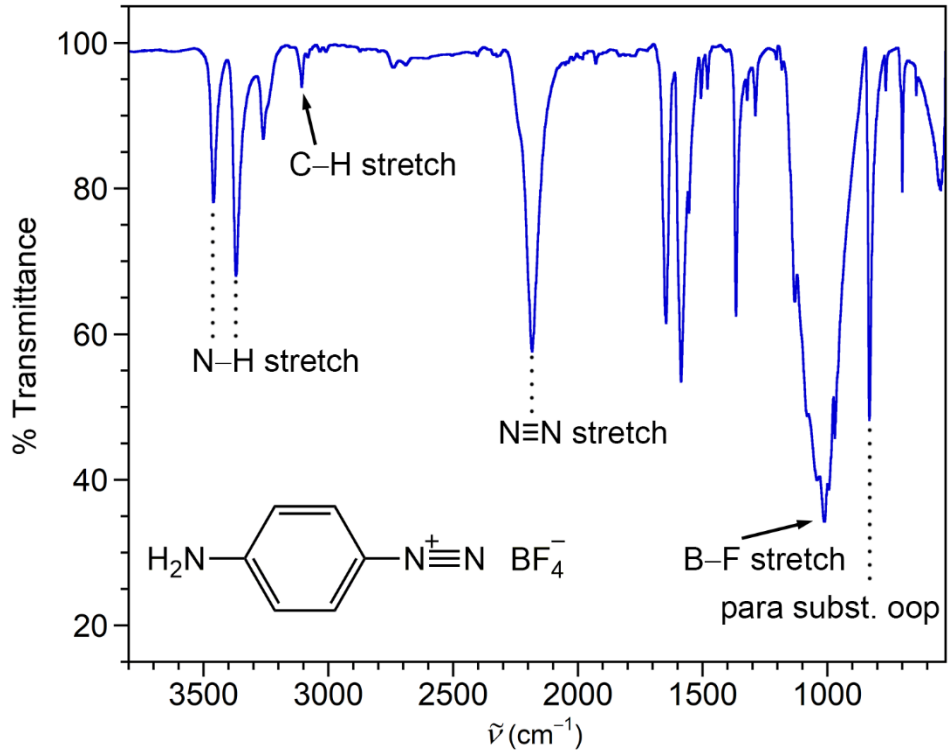

Figure 7.2. FTIR spectrum of 4-ABD·BF_4 solid.

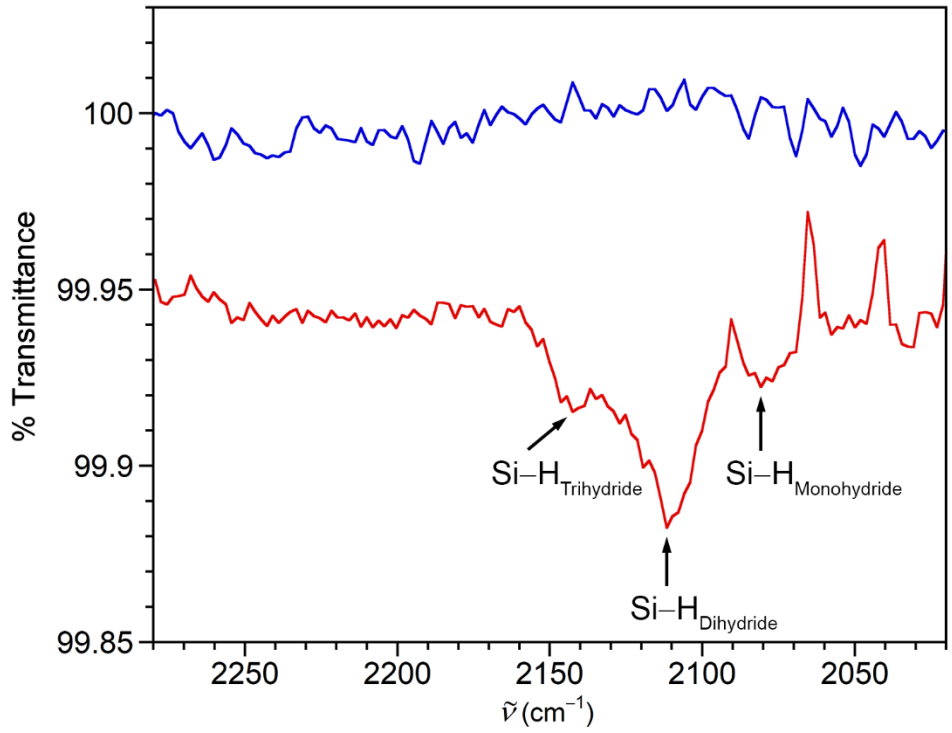

Figure 7.3. FTIR spectra of degreased silicon wafer (blue), and hydride-terminated silicon wafer (red).

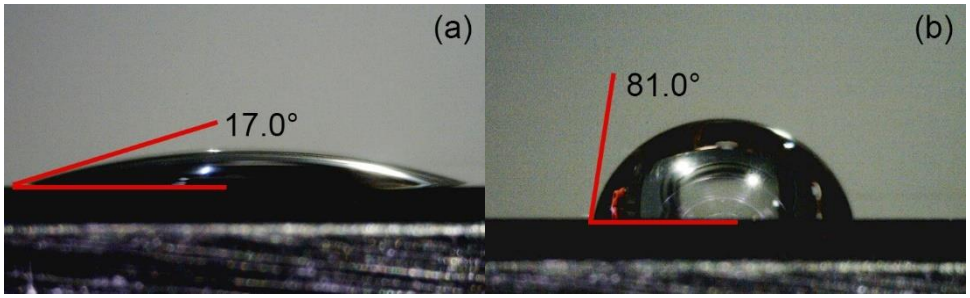

Figure 7.4. Contact angle measurements on (a) degreased silicon wafer and (b) hydride-terminated silicon wafer. A 10 μL DI water droplet was placed for both wafers.

Conclusion and Future Work

The aryl diazonium salt, 4-aminobenzenediazonium tetrafluoroborate, was prepared and will be used for attachment on the silicon wafer. Once the attachment has been achieved and confirmed by FTIR spectroscopy and contact angle measurements, the aryl group modified silicon wafer will be immersed in a pale blue silver nanoparticle solution which is prepared by the scheme described in Chapter 6. The presence of silver nanoparticles on the silicon wafer will be confirmed by scanning electron microscopy (SEM) and UV-visible reflectance spectroscopy. As a comparison and a control, as-received cleaned wafer will be treated with the silver nanoparticle solution and will be examined with the same characterization techniques.

Ultimately, this scheme, which is tested on the silicon sample as a mimic, will be employed on silicon solar cells. The solar cell performance will then be assessed by measuring the current-voltage curve when illuminating with a full-spectrum solar simulator as well as wavelength-selectable sources.

References

1. Green, M. A. *Sol. Energy Mater. Sol. Cells.* **2008**, *92*, 1305.

2. Atwater, H. A.; Polman, A. *Nat. Mater.* **2010**, *9*, 205.

3. Pillai, S.; Catchpole, K. R.; Trupke, T.; Green, M. A. *J. Appl. Phys.* **2007**, *101*, 093105.

4. Hu, L.; Chen, G. *Nano Lett.* **2007**, *7*, 3249.

5. Moulin, E.; Sukmanowski, J.; Luo, P.; Carius, R.; Royer, F. X.; Stiebig, H. *J. Non-Cryst. Solids.* **2008**, *354*, 2488.

6. Hägglund, C.; Zäch, M.; Petersson, G.; Kasemo, B. *Appl. Phys. Lett.* **2008**, *92*, 053110.

7. Catchpole, K. R.; Polman, A. *Opt. Express.* **2008**, *16*, 21793.

8. Temple, T. L.; Mahanama, G. D. K.; Reehal, H. S.; Bagnall, D. M. *Sol. Energy Mater. Sol. Cells.* **2009**, *93*, 1978.

9. Li, J.; Yu, H.; Wong, S. M.; Zhang, G.; Sun, X.; Lo, P. G.-Q.; Kwong, D. -L. *Appl. Phys. Lett.* **2009**, *95*, 033102.

10. Akimov, Y. A.; Koh, W. S. *Nanotechnology.* **2010**, *21*, 235201.

11. Akimov, Yu. A.; Koh, W. S.; Sian, S. Y.; Ren, S. *Appl. Phys. Lett.* **2010**, *96*, 073111.

12. Krasnov, A. *Sol. Energy Mater. Sol. Cells.* **2010**, *94*, 1648.

13. Wang, W.; Wu, S.; Reinhardt, K.; Lu, Y.; Chen, S. *Nano Lett.* **2010**, *10*, 2012.

14. Ouyang, Z.; Pillai, S.; Beck, F.; Kunz, O.; Varlamov, S.; Catchpole, K. R.; Campbell, P.; Green, M. A. *Appl. Phys. Lett.* **2010**, *96*, 261109.

15. Ferry, V. E.; Verschuuren, M. A.; Li, H. B. T.; Verhagen, E.; Walters, R. J.; Schropp, R. E. I.; Atwater, H. A.; Polman, A. *Opt. Express.* **2010**, *18*, A237.

16. Madzharov, D.; Dewan, R.; Knipp, D. *Opt. Express.* **2011**, *19*, A95.

17. Akimov, Y. A.; Koh, W. S. *Plasmonics.* **2011**, *6*, 155.

18. Temple, T. L.; Bagnall, D. M. *Appl. Phys. Lett.* **2011**, *109*, 084343.

19. Zhang, Y.; Ouyang, Z.; Stokes, N.; Jia, B.; Shi, Z.; Gu, M. *Appl. Phys. Lett.* **2012**, *100*, 151101.

20. Jang, Y. H.; Jang, Y. J.; Kim, S.; Quan, L. N.; Chung, K.; Kim, D. H. *Chem. Rev.* **2016**, *116*, 14982.

21. Mandal, P.; Sharma, S. *Renewable Sustainable Energy Rev.* **2016**, *65*, 537.

22. Evanoff, D. D.; Chumanov, G. *J. Phys. Chem. B.* **2004**, *108*, 13957.

23. Kelly, K. L.; Coronado, E.; Zhao, L. L.; Schatz, G. C. *J. Phys. Chem. B.* **2003**, *107*, 668.

24. Hao, E.; Schatz, G. C. *J. Chem. Phys.* **2004**, *120*, 357.

25. Albrecht, M. G.; Creighton, J. A. *J. Am. Chem. Soc.* **1977**, *99*, 5215.

26. Jeanmaire, D. L.; Van Duyne, R. P. *J. Electroanal. Chem. Interfacial Electrochem.* **1977**, *84*, 1.

27. Brus, L. *Acc. Chem. Res.* **2008**, *41*, 1742.

28. Camden, J. P.; Dieringer, J. A.; Zhao, J.; Van Duyne, R. P. *Acc. Chem. Res.* **2008**, *41*, 1653.

29. Pinson, J.; Podvorica, F. *Chem. Soc. Rev.* **2005**, *34*, 429.

30. Mahouche-Chergui, S.; Gam-Derouich, S.; Mangeney, C.; Chehimi, M. M. *Chem. Soc. Rev.* **2011**, *40*, 4143.

31. Assresahegn, B. D.; Brousse, T.; Bélanger, D. *Carbon.* **2015**, *92*, 362.

32. Davies, R. A.; Chong, N. S.; Ooi, B. G. *Optics and Photonics Journal.* **2013**, *03*, 13.

33. Chong, N. S.; Donthula, K.; Davies, R. A.; Ilsley, W. H.; Ooi, B. G. *Vib. Spectrosc.* **2015**, *81*, 22.

34. Whetsel, K. B.; Hawkins, G. F.; Johnson, F. E. *J. Am. Chem. Soc.* **1956**, *78*, 3360.

35. Flood, D. T. *Org. Synth.* **1933**, *13*, 46.

36. Chabal, Y. J.; Higashi, G. S.; Raghavachari, K.; Burrows, V. A. *J. Vac. Sci. Technol. A.* **1989**, *7*, 2104.

Appendix: Preparation of Bismuth Chloride Anionic Salts, $[Bi_2Cl_9]^{3-}$

Preparation of Compounds

All the reactions were handled in a nitrogen-filled drybox. The sample was dried on Schlenk line *in vacuo*. Acetonitrile (MeCN), purchased from Burdick and Jackson, and diethyl ether (Et_2O), purchased from EMD were stored over activated 4 Å molecular sieves in the drybox. The salts (Pr^n_4N)Cl (Acros Organics, 94%), (Et_4N)Cl·H_2O (Alfa Aesar, 98%) were dried *in vacuo* at 100 ºC before being stored in the drybox.

(Pr^n_4N)$_3$[Bi_2Cl_9]. A solution of $BiCl_3$ (2.0 g, 6.2 mmol) in 15.5 mL of MeCN and a solution of (Pr^n_4N)Cl (2.1 g, 9.3 mmol) in 19.5 mL were split in a half to a new vial, respectively. Each vial containing (Pr^n_4N)Cl was added dropwise to each $BiCl_3$ solution under magnetic stirring, resulting in a colorless solution. The reaction was left under stir overnight. A trace amount of undissolved white particles was filtered off through a nylon filter paper on a Hirsch funnel by vacuum filtration. The filtrate was placed in two separate small jars and sealed in a large jar filled with Et_2O to promote vapor diffusion, respectively. Colorless crystals were found after 5 days. The crystals were grinded in a fine powder on a mortar-and-pestle and was washed with successive THF (3 x 10 mL) and Et_2O (3 x 10 mL) on a nylon filter paper on a Hirsch funnel by vacuum filtration. The solid was dried *in vacuo* overnight to afford 3.7 g (92. %).

$(Et_4N)_3[Bi_2Cl_9]$. A solution of $BiCl_3$ (0.51 g, 1.6 mmol) in 6.0 mL of MeCN and a solution of $(Et_4N)Cl$ (0.41 g, 2.5 mmol) in 8.0 mL of MeCN were prepared. A solution of $(Et_4N)Cl$ was added dropwise to $BiCl_3$ solution under magnetic stirring, resulting in a colorless solution. The reaction was left under stir overnight. The product solution was filtered through celite. The filtrate was set up for recrystallization by Et_2O vapor diffusion into the product solution. Colorless crystals were found after 4 days. The crystals were grinded in a fine powder on a mortar-and-pestle and was washed with successive Et_2O (3 x 10 mL) on a fritted Buchner funnel. The solid was dried *in vacuo* overnight to afford 0.41 g (45. %).